Universität Stuttgart

Forefront engineering of nitrogen-vacancy centers in diamond for quantum technologies

Von der Fakultät 8 Mathematik und Physik der Universität
Stuttgart zur Erlangung der Würde eines Doktors der
Naturwissenschaften (Dr. rer. nat.) genehmigte Abhandlung

Vorgelegt von
Felipe Fávaro de Oliveira
aus Curitiba, Brasilien

Hauptberichter: Prof. Dr. Jörg Wrachtrup
Mitberichter: Prof. Dr. Peter Michler

Tag der Mündlichen Prüfung: 19.07.2017

3. Physikalisches Institut
Universität Stuttgart

2017

Forefront engineering of nitrogen-vacancy centers in diamond for quantum technologies

Von der Fakultät 8 Mathematik und Physik der Universität
Stuttgart zur Erlangung der Würde eines Doktors der
Naturwissenschaften (Dr. rer. nat.) genehmigte Abhandlung

Vorgelegt von

Felipe Fávaro de Oliveira

aus Curitiba, Brasilien

Hauptberichter: Prof. Dr. Jörg Wrachtrup
Mitberichter: Prof. Dr. Peter Michler

Tag der Mündlichen Prüfung: 19.07.2017

3. Physikalisches Institut
Universität Stuttgart

2017

Abstract

The revolution being led by the next generation of quantum technologies. Since the beginning of the 20th century, the rise of quantum physics has revolutionized the human comprehension of the universe. At that time, several experimental observations pushed physicists to think outside the classical Newtonian mechanics and electromagnetism theories. For instance, the pioneer study of the electromagnetic radiation of a blackbody by several scientists such as Max Planck and Lord Rayleigh is considered by many the first gearing event that challenged the so-called classical physical concepts of light and matter. The following breakthrough works involving the wave-particle duality concept to explain the particle-like behavior of electromagnetic waves and the photoelectric effect have then led to the foundations of quantum mechanics. Although very controversial at that time, quantum mechanics began to expand and gain further grounds after the mathematical formulation developed by Ervin Schrödinger in 1926 [1] and subsequent studies. Yet, since that time, a question has intrigued scientists from many different research fields: can the concepts of quantum mechanics be somehow implemented in something feasible (i.e. a device) for the long benefit of the society? The answer came quickly by the development of a ground-breaking first-generation of quantum technologies such as the laser and the global positioning system (GPS), which are devices based primarily on the quantum principle of coherence. These events resulted in quantum physics to be evolved from essentially a conceptual framework, to provide new inspirations for realistic technological applications.

A particular field that has always been of broad interest is the capability of store, transmit and process information. With the rise of the industrial applications of semiconductor technology, especially the development of silicon-based micro-electronic devices in the late 1950s [2], the digitally-encoded type of information became popular and widely-spread within many different areas. Recent advances in micro- and nano-structuring, and a rapid progress in the material synthesis and development of new platforms led to a continuous increase of transmission speed and storage capacity of information in modern devices. Since the invention of integrated circuits, Moore's law [3] has reasonably predicted the time evolution related to the density of electronic components that can be packed on a

chip (and the related cost) due to the advances in the information processing efficiency (clock speed rate) and fabrication processes of micro-electronic devices. In the past few years, however, the fundamental limitation on this time-development became more evident and realistically closer to be reached: ultimately, the miniaturization of electronic devices will be limited by the finite size of atoms (for example, single-atom transistors [4]) and the corresponding heat dissipation of the integrated circuits.

To tackle this limitation, the idea of developing a so-called quantum computer [5] shades light on a new generation of technological implementations of quantum physics. In this case, technological development goes far beyond than packing more and more components to silicon chips, supporting a vast and entirely new research area. In a classical computer, units of information are stored in a physical system that can assume two distinct states (classical bits: 0 or 1) such as the local magnetization of a material. Information processing (e.g. computation) is then performed by events that change the state configuration of individual strings of bits, governed by a given set of instructions (e.g. an algorithm). Analogously, in the case of a quantum computer, units of information are represented by quantum systems (qubits) that can assume two distinct states ($|0\rangle$ and $|1\rangle$), as well as any arbitrary superposition of these states (that is, $[\alpha |0\rangle + \beta |1\rangle]$, satisfying $|\alpha|^2 + |\beta|^2 = 1$). The computation is performed by a given set of logical operations, corresponding to the time evolution of the system state under certain conditions (that is, unitary transformations acting on the qubit state). A variety of quantum systems have been explored as potential qubits, including single photons [6, 7], trapped ions [8–10] and atoms [11, 12], and solid-state systems [13–16].

Triggered by the rapidly-evolving capabilities to engineer and experimentally manipulate these different types of qubits, several research areas exploring their quantum mechanical properties have emerged. Among others, the nano-scale sensing of physical quantities using spin impurities in solid-state systems (hereinafter referred to as quantum sensing) is of particular interest of this work and will be briefly explored below. The so-called quantum sensor (that is, the qubit that is sensitive to a particular physical quantity) makes the use of its vulnerability to the environment to its advantage. The strong sensitivity of the qubit spin to external perturbations couples it to target systems and, therefore, can be used to measure quantities of interest through e.g. the corresponding qubit coherence. As an adaptation of the basic criteria for applicable qubits in quantum computation proposed by DiVincenzo [5], a quantum system must fulfill the following basic requirements to be implemented as a quantum sensor. First, the quantum system must have discrete, individually-addressable energy levels (usually represented by $|0\rangle$ and $|1\rangle$). Second, the initialization of the quantum system into a specific en-

ergy state and the evolved state read-out must be feasible, with high reciprocal fidelity. Third, coherent manipulation between the quantum system energy states must be possible by e.g. time-dependent fields. Fourth, the quantum system must be sensitive to a relevant physical quantity via e.g. Stark and Zeeman effects for the cases of interactions with electric and magnetic fields, respectively.

The intrinsic physical properties determines the superiority of some quantum systems in comparison to others for specific applications. Hence, the choice of a system for a particular quantum sensing application must be based essentially on the system response to the desired measurable physical quantity. Moreover, the quality of the quantum system must be considered, which depends on the relation between the interaction strength with the target system and the accumulation of unwanted noise. Another decisive parameter is the system size due to basic geometric constrains. Eventually, spin impurities in solids are primary candidates for quantum sensing of magnetic and electric fields with high sensitivity and atomic-like spatial resolution. Up to date, these miniaturized sensors have provided vital insights in the nano-world, with a level of details that could never be achieved by their classical competitors. The state-of-the-art types of quantum sensors and specific applications are reviewed in literature, e.g. in Refs. [17, 18].

The negatively-charged nitrogen-vacancy (NV) center in diamond is the main quantum system investigated in this work. It is an exceptional and versatile atomic-sized spin system, consisting of a substitutional nitrogen atom and an adjacent lattice vacancy in diamond [19]. Recent advances in material engineering resulted in the controlled synthesis of diamond crystals with high degree of purity and exceptional crystalline quality (that is, low concentration of impurities and lattice defects [20, 21]). Hence, NV centers hosted in ultra-pure diamond substrates behave as well-isolated spin systems that fulfill the previously-described requisites for a viable qubit in quantum sensing applications. The NV center electron spin combines a paramagnetic spin ground state to a very bright optical transition [19]. As a consequence, spin-selective intersystem crossing enables the optical readout of the ground state spin on a single-site level [22]. Moreover, NV centers in diamond can be operated at room temperature, which opens a much broader (and probably more simplified) class of nano-sensing and imaging applications.

The robustness and homogeneity of the diamond lattice structure up to the boundary atomic layers (that is, the crystal surface) allows NV centers to be stable within a few nanometers of depth [23] and even to be hosted within diamond nanocrystals [24–26]. This is a remarkable characteristic of diamond and NV centers, which allows a strong magnetic dipolar coupling of NV centers (sensors) to e.g. target external spins, scaling with the inverse of their cubic relative distance [17,

27–31]. In order to fulfill the requirements of different applications, NV centers can be deliberately created in diamond using different techniques such as electron irradiation [22, 32] and ion implantation [33, 34]. One relevant technological aspect is the dependence of the optical and spin properties of created NV centers on their corresponding depth within the host diamond crystal. Several studies have experimentally addressed this aspect [35–37], showing that NV centers suffer from degraded properties as they become closer to the diamond surface. For instance, NV centers hosted in ultra-pure diamond bulk materials show spin coherence times of $\sim$ ms [20], whereas for near-surface NV centers these values are depleted to the $\sim$ µs range [36]. Eventually, these results highlight the importance of controlling the defect-environment of created NV centers for further advances in NV center-based quantum technologies.

The presented work takes as starting gear the available methods for the creation of NV centers in diamond and their concomitant advantages and limitations. The main framework of this Thesis is based on a central challenge in quantum technologies: the improvement of the quantum properties of spin impurities in solid-state host materials by exploring relevant material science aspects. Although this work is focused on diamond, the presented results also have a broader implication for other solid-state materials such as silicon carbide (SiC) [38] and rare-earth doped crystals [39]. Both qualitative and quantitative aspects of the formation and dynamics of lattice damages and spin impurities in diamond are investigated by combining experimental results to numerical calculations. Moreover, novel techniques for the improved engineering of NV centers are proposed, paving the way for the next-generation of quantum devices using implanted spin impurities in solid-state systems.

Often, electric and magnetic field fluctuations deteriorate the optical, spin and charge transport properties of semiconductor materials, especially in the vicinity of surfaces and interfaces [40–43]. In the case of diamond, the origin of these features are mainly surface carbon dangling bonds [44–46] and paramagnetic surface states (e.g. surface spins) [47, 48]. In the presented work, the diamond surface morphology and chemical composition are investigated in close connection to the properties of near-surface NV centers. Typical treatments such as thermal annealing induce phase-transitions at the diamond surface such as thermally-induced graphitization [49]. The top layers of diamond are hence highly defective, which results in induced electronic states in the band gap within the near-surface diamond region that strongly influence the quantum performance of NV centers. This is further aggravated in the case of diamond exposure to i.e. capacitively-coupled plasma treatments due to the strong ion bombardment of the substrate surface [50–53]. A key experimental challenge is the development of a method to remove diamond

surface layers and thus to bring NV centers at the nanometer proximity to the diamond surface, while preserving their optical and spin properties.

To this aim, this work presents the controlled etching of diamond using a novel oxygen inductively-coupled plasma (ICP) process. Importantly, the resulting nanometer etching rate with high reproducibility and selectivity makes the developed process suitable for diamond structuring techniques towards quantum sensing applications [54–57], where compatibility with near-surface NV centers is a requirement. No traces of plasma-induced damages to the etched diamond surface could be detected by X-ray photoelectron spectroscopy (XPS) and confocal microscopy techniques. The exposure of different diamond substrates to the developed plasma process shows no plasma-induced quenching, and shows enhanced spin properties of very shallow NV centers (depths of $< 4\,\mathrm{nm}$). The availability of such fabrication tool is one of the key roadblocks in this Thesis to develop novel platforms for the engineering of near-surface NV centers with augmented properties.

Next, the work is focused on a well-established creation technique of NV centers: the nitrogen implantation of diamond followed by high-temperature thermal annealing [33, 34]. So far, this method results in the best spatial positioning accuracy of NV centers in diamond, a feature that is extremely relevant in applications based on i.e. ordered arrays of near-surface spin-defects [58]. Experimental investigations of the creation of NV centers by this method (and several others such as ion irradiation [59–63]) reveal that, in general terms, alternative paths of vacancy recombination in diamond during the thermal annealing process completely limit the creation efficiency of NV centers. Vacancy-related paramagnetic spins are foreseen as a strong source of spin decoherence of NV centers, especially in the nanometer vicinity of the diamond surface. Remarkably, up to date, there is no available method to suppress the formation of such lattice defects during the thermal annealing process of implanted diamond substrates.

Aspiring to change this paradigm, a novel method to tailor the formation dynamics of such implantation-induced defects is presented in this work. This comprises the implantation of nitrogen atoms into the induced space-charge layer of free injected holes in an ultra-pure diamond substrate, generated by a nanometer-thin boron-doped diamond layer on the substrate surface. Under high temperatures, such a structure behaves similarly as a planar p^{+}-n abrupt junction of semiconductor physics. The induced excess of free charge carriers within the implanted region of the substrate changes the charge-state of lattice defects, with concomitant changes in their diffusion and recombination behavior. Under such conditions, the formation of vacancy-related paramagnetic spin defects is strongly sup-

pressed, as confirmed by a detailed analysis of the spin noise environment sensed by near-surface NV centers. As a result, tenfold-improved spin coherence times and twofold-improved formation yield of NV centers are achieved by the developed method. The presented experimental results are further supported by numerical simulations of the formation and evolution of implantation-induced spin defects, analyzed within single implanted ion sites.

Alternatively, these results are also utilized to investigate an optimized architecture of a thin (δ) profile of NV centers at the diamond surface for quantum sensing applications. This is based on the techniques of nitrogen doping of diamond during the chemical vapor deposition (CVD) process [64–68] and post helium ion irradiation [60, 63]. Importantly, the optimum engineering of such a structure requires quantitative knowledge of the activation of NV centers by irradiation-induced vacancies during thermal annealing. To this aim, the depth distribution profiles of near-surface helium-induced NV centers (and related optically-active helium defects) are investigated by plasma step-etching and confocal microscopy techniques. These results provide insights into the efficiency of vacancy diffusion as well as alternative recombination paths concurrent to the formation of NV centers. In contrast to the common belief, the range of efficient formation of NV centers is limited to approximately $10 - 15$ nm (in radius) around the initial helium ion track positions in the diamond lattice. Accordingly, NV centers are shown to be created with a high efficiency ($\sim 15\%$) only within the atomic distribution profile of irradiated atoms. Related limitations of the helium irradiation technique are also investigated for the case of helium irradiation with high fluences ($> 10^{12}$ atoms.cm^{-2}).

The experimental results reveal that the formation of vacancy-related defects within the irradiated region of the substrate are responsible for the observed saturation in the formation efficiency as well as for a sub-surface suppression effect in the corresponding distribution profile of NV centers for increasing ion fluence. Simple analytical estimations further provide quantitative insights on these effects. At the end, the acquired knowledge is utilized to experimentally realize the proposed optimized architecture of the δ-profile of NV centers directly at the diamond surface. NV centers hosted within the fabricated structure at depths of < 5 nm demonstrate tenfold-improved spin coherence times in comparison to conventional nitrogen implantation technique corresponding to similar depths. Moreover, benchmark quantum sensing measurements are presented by sensing electron spins embedded within a film at the diamond surface, further highlighting the potential of this method for the detection of external spins with augmented sensitivity.

Thesis outline. In Chapter 1, basic features of diamond as a spin-host material are briefly introduced, together with the definition of the spin system under study. Chapter 2 presents a short overview of the available methods for the targeted creation of NV centers in diamond. Particular features, as well as the advantages and limitations of each method are also discussed. Chapter 3 addresses the diamond surface and its influence on the properties of NV centers. The surface physical and chemical compositions are analyzed in details after the substrate exposure to different treatments. A novel plasma process is proposed and its concomitant characteristics are investigated, aiming to bring NV centers closer to the diamond surface while importantly preserving their properties. Chapter 4 starts with an investigation of the nitrogen ion implantation technique in diamond. Numerical simulations using Molecular Dynamics and kinetic Monte Carlo methods, as well as analytical calculations are utilized to draw a definitive and broad picture of the formation of spin defects in diamond. The novel method of ion implantation within the space-charge layer induced in the ultra-pure region of a boron-doped structure is presented and the resulting effects on the formation dynamics of NV centers and vacancy-related defects are analyzed. Briefly, the foreseen impacts of the obtained results on the creation of coupled pairs of NV centers are discussed as well. Chapter 5 investigates an optimized architecture for the nitrogen δ-doping technique for NV center-based quantum sensing applications. Important aspects of the vacancy diffusion in diamond are investigated by the depth-profiling of NV centers and helium-related defects in diamond. The experimental realization of such a structure and quantum sensing benchmark measurements are presented. Finally, the utilized experimental setups and a variety of auxiliary methods are summarized in the Appendices.

Zusammenfassung

Die von der nächsten Generation der Quantentechnologie angeführte Revolution. Von Beginn des zwanzigsten Jahrhunderts an hat die Quantenphysik das menschliche Verständnis des Universums revolutioniert. Zu dieser Zeit haben mehrere experimentelle Beobachtungen Physiker dazu gezwungen, über die Grenzen der klassischen Newtonschen Mechanik und Maxwellschen Elektromagnetik hinaus zu denken. Die Pionierarbeiten zur elektromagnetischen Strahlung schwarzer Körper durch Wissenschaftler wie Max Planck und Lord Rayleigh wird beispielsweise von vielen als eine erste Infragestellung der sogenannten klassischen physikalischen Theorien über Licht und Materie angesehen. Die darauffolgenden bahnbrechenden Arbeiten zum Welle-Teilchen-Dualismus, welche das teilchenähnliche Verhalten von elektromagnetischen Wellen sowie den photoelektrischen Effekt beschreiben, haben dann die Grundlagen für die Quantenmechanik gelegt. Wenn auch zunächst sehr kontrovers diskutiert, hat sich die Quantenmechanik nach ihrer mathematischen Formulierung durch Erwin Schrödinger im Jahre 1926 [1] sowie durch weitere Studien entscheidend weiterentwickelt. Seit dieser Zeit hat eine Frage jedoch viele Wissenschaftler aus vielen unterschiedlichen Forschungsfeldern beschäftigt: Können die Effekte der Quantenmechanik in irgendeiner Weise zum nachhaltigen Wohle der Gesellschaft genutzt werden? Die Antwort auf diese Frage kam prompt durch die Einführung von bahnbrechenden Technologien wie dem Laser und dem globalen Positionierungssystem (GPS), welches beides Geräte sind die primär auf dem quantenmechanischen Konzept der Kohärenz basieren. Diese Entwicklungen führten dazu, dass sich die Quantenphysik von einem konzeptionellen Grundgerüst zu einer inspirierenden Basis für neuartige technologische Anwendungen weiterentwickelt hat.

Ein Anwendungsgebiet welches seit jeher großes Interesse genießt, ist die Fähigkeit Informationen zu speichern, zu übertragen und zu verarbeiten. Durch das Auftraten der industriellen Anwendungen der Halbleitertechnologie und insbesondere durch die Entwicklung von Silizium-basierten Mikrochips in den späten 1950er Jahren [2] hat sich die digitale Kodierung von Informationen in viele Bereiche ausgebreitet. Jüngste Fortschritte in der Mikro- und Nanostrukturierung von Materialen und die rapide Verbesserung der Materialsynthese führten zu einer

kontinuierlichen Erhöhung der Übertragungsgeschwindigkeit sowie der Speicherka-
pazität von Informationen in modernen Bauteilen. Seit der Erfindung von inte-
grierten Schaltkreisen, hat das Moorsche Gesetz [3] die zeitliche Entwicklung der
Dichte von elektronischen Bauteilen (und deren Kosten) welche in einen einzelnen
Chip integriert werden können erstaunlich verlässlich vorhergesagt. In den letzten
Jahren wurden jedoch die fundamentalen Grenzen dieser Entwicklung immer deut-
licher und scheinen immer näher zu rücken: letztendlich wird die Miniaturisierung
von elektronischen Bauteilen durch die endliche Größe eines einzelnen Atoms [4]
und die entsprechende Wärmeabgabe des integrierten Schaltkreises begrenzt sein.

Motiviert von dieser Grenze lässt die Entwicklung eines sogenannten Quan-
tencomputers [5] neues Licht auf eine neue Generation von technischen Imple-
mentierungen der Quantenphysik scheinen. In diesem Fall geht die technologi-
sche Entwicklung weit darüber hinaus lediglich mehr und mehr Schaltkreise auf
einem Siliziumchip unterzubringen, sondern eröffnet ein konzeptionell neues Feld
der Wissenschaft. In einem klassischen Computer sind Informationen in einem
physikalischen System mit zwei konkreten Zuständen (klassische Bits 0 oder 1),
wie beispielsweise der lokalen Magnetisierung eines Materials gespeichert. Infor-
mationsverarbeitung (z.B. Berechnungen) geschieht dann durch Vorgänge welche
den Zustand von einer Reihe von Bits gemäß festgelegten Anweisungen (z.B. Algo-
rithmen) verändern. Im Falle eines Quantencomputers sind die Informationsein-
heiten durch Quantensysteme (Qubits) realisiert welche zwei konkrete Zustände
($|0\rangle$ und $|1\rangle$) sowie jede beliebige Superposition dieser Zustände annehmen können
($[\alpha\,|0\rangle + \beta\,|1\rangle]$ mit der Bedingung $|\alpha|^2 + |\beta|^2 = 1$). Rechenvorgänge finden durch
eine Reihe von logischen Operationen entsprechend der zeitlichen Entwicklung der
Systems unter gewissen Bedingungen statt (Einheitstransformationen welche auf
den Zustand des Qubits wirken). Eine Vielzahl von Quantensystemen wie beispiel-
sweise einzelne Photonen [6, 7], gefangene Ionen [8–10] und Atome [11, 12] sowie
Festkörpersysteme [13–16] wurde auf deren Anwendung als potentielle Qubits hin
untersucht.

Ausgelöst durch die sich schnell entwickelnden Möglichkeiten diese unterschiedli-
chen Arten von Qubits zu erzeugen und experimentell zu manipulieren, sind mehre-
re neue wissenschaftliche Disziplinen entstanden die deren quantenmechanischen
Eigenschaften untersuchen. Für die vorliegende Arbeit ist unter anderem das Bes-
timmen von physikalischen Größen auf der Nanoskala mit Hilfe von Spin-Defekten
in Festkörpersystemen (hier als "Quantensensorik" bezeichnet) von besonderem
Interesse und wird daher im Folgenden kurz erläutert. Der sogenannte Quan-
tensensor, also ein Qubit welches auf eine bestimmte physikalische Größe sensitiv
ist, verwandelt seine Anfälligkeit auf äußere Einflüsse in einen Vorteil. Durch die
starke Sensitivität des Qubit Spins auf äußere Störungen wird es an das zu unter-

suchende System gekoppelt und kann daher benutzt werden um Messgrößen z.B. durch die damit verbundene Quantenkohärenz zu bestimmen. Analog zu den von DiVincenzo aufgestellten Eigenschaften die ein Quantensystem aufweisen muss um als Qubit in einem Quantencomputer Anwendung zu finden [5], lassen sich folgende Kriterien formulieren die ein Quantensystem erfüllen muss um als Quantensensor implementiert werden zu können. Zum einen muss das System diskrete, einzeln adressierbare Energiezustände aufweisen (üblicherweise als $|0\rangle$ und $|1\rangle$ bezeichnet). Zum anderen muss die Initialisierung des Quantensystems in einen spezifischen Energiezustand sowie das Auslesen des zeitlich entwickelten Zustandes mit hoher Genauigkeit und Reproduzierbarkeit möglich sein. Darüber hinaus muss die kohärente Manipulation zwischen den Energiezuständen des Quantensystems z.B. durch zeitabhängige Felder möglich sein. Letztlich muss das Quantensystem auf die relevanten physikalischen Größen sensitiv sein, wie beispielsweise Stark- oder Zeeman-Effekte für elektrische bzw. magnetische Felder.

Je nach spezifischer Anwendung sind auf Grund ihrer intrinsischen physikalischen Eigenschaften manche Quantensysteme besser geeignet als andere. Die Auswahl des jeweiligen Quantensystems basiert daher auf der Antwort des Systems auf die zu untersuchende Messgröße. Weiter muss die Qualität des Quantensystems, welche sich aus der Stärke der Wechselwirkung mit dem zu untersuchenden Systems sowie des parasitären Rauschens ergibt, hinterfragt werden. Ein weiterer Aspekt ist die Größe des Systems welche durch geometrische Rahmenbedingungen gegen ist. Schlussendlich sind Spin-Defekte in Festkörpern die primären Kandidaten für quantenmechanische Messungen von magnetischen und elektrischen Feldern mit hoher Sensitivität und atomarer räumlicher Auflösung. Bereits heute haben diese miniaturisierten Sensoren entscheidende Einblicke in die Nanowelt gegeben deren Detailreichtum mit klassischen Sensoren unerreichbar wäre. Der aktuelle Stand der Technik von unterschiedlichen Quantensensoren und deren spezifische Anwendungen sind in der Literatur zusammengefasst [17, 18].

Das negativ geladene Stickstoff-Fehlstellen Zentrum (engl.: nitrogen-vacancy center, NV center) in Diamant ist das in der vorliegenden Arbeit untersuchte Quantensystem. Es ist ein außergewöhnliches und vielseitiges atomares Spin-System, welches aus einem Stickstoffatom auf einem substitutionellen Gitterplatz und einer benachbarten Gitterfehlstelle im Diamant besteht [19]. Neue Fortschritte bei der Materialentwicklung ermöglichen die kontrollierte Synthese von Diamantkristallen mit einem hohen Maß an Reinheit und hervorragender kristalliner Qualität (d.h. niedrige Konzentration an Verunreinigungen und Gitterfehler [20, 21]). NV Zentren in solchen hoch-reinen Diamantsubstraten verhalten sich daher wie gut isolierte Spin-Systeme welche die zuvor beschriebenen Kriterien für die Anwendung von Qubits in der Quantensensorik erfüllen. Der Elektron-

spin des NV Zentrums verbindet einen paramagnetischen Spin-Grundzustand mit einem sehr hellen optischen Übergang [19]. Als Konsequenz ermöglicht das Spin-abhängige *Intersystem Crossing* ein optisches Auslesen des Spin-Grundzustandes von einem einzelnen Defekt [22]. Darüber hinaus können NV Zentren bei Raumtemperatur untersucht werden, was eine breitere (und wahrscheinlich auch einfachere) Anwendung in der Nano-Sensorik und bei bildgebenden Verfahren ermöglicht.

Die Robustheit und Gleichmäßigkeit der Diamantkristallstruktur bis hin zu der begrenzenden atomaren Schicht (d.h. der Kristalloberfläche) ermöglicht es, dass NV Zentren bereits wenige Nanometer unter der Oberfläche stabil sind [23] und selbst in Nanokristallen aus Diamant vorkommen [24–26]. Dies ist eine auffällige Eigenschaft von Diamant und NV Zentren, die eine starke Wechselwirkung zwischen NV Zentren (Sensoren) und D.h. externe Spins auf die Kristalloberfläche erlaubt, deren Stärke mit ihrer invertierten kubischen relativen Distanz skaliert [17, 27–31]. Um die Anforderungen unterschiedlicher Anwendungen zu erfüllen, können NV Zentren durch unterschiedliche Techniken wie Elektronenbestrahlung [22, 32] und Ionenimplantation [33, 34] kontrolliert erzeugt werden. Ein technologisch relevanter Aspekt ist dabei die Abhängigkeit der optischen Eigenschaften und der Spin-Kohärenz der erzeugten NV Zentren von deren Tiefe innerhalb des Diamantkristalls. Mehrere Arbeiten haben diesen Aspekt experimentell untersucht [35–37], mit dem Ergebnis, dass sich die optischen Eigenschaften der NV Zentren verschlechtern, je näher sie sich an der Diamantoberfläche befinden. Zum Beispiel haben NV Zentren weit innerhalb des hoch-reinen Diamanten eine Spinkohärenzzeit im Bereich von Millisekunden [20], wohingegen sich bei oberflächennahen NV Zentren dieser Wert auf Mikrosekunden verringert [36]. Diese Ergebnisse zeigen, dass die Kontrolle über die Umgebung der erzeugten NV Zentren bei der Weiterentwicklung von NV Zentren basierten Quantentechnologien von fundamentaler Bedeutung ist.

Die vorliegende Arbeit beginnt mit den derzeit verfügbaren Methoden zur Erzeugung von NV Zentren in Diamant sowie deren Vorteile und Limitierungen. Den allgemeinen Rahmen dieser Arbeit bildet eine der zentralen Herausforderungen der Quantentechnologie: Die Verbesserung der Eigenschaften von Spin-Defektzentren in Festkörpern durch relevante materialwissenschaftliche Aspekte. Auch wenn diese Arbeit sich auf Diamant fokussiert, sind die hier präsentierten Ergebnisse auch von weiterreichender Bedeutung beispielsweise für andere Festkörpersysteme wie Siliziumkarbid (SiC) [38] und mit seltenen Erden dotierte Kristalle [39]. Sowohl qualitative als auch quantitative Aspekte für die Bildung und Dynamik von Kristalldefekten und Spin-Verunreinigungen in Diamant werden durch eine Kombination von experimentellen Ergebnissen und numerischen Berechnungen untersucht. Darüber hinaus werden neue Techniken für die verbesser-

te Herstellung von NV Zentren vorgeschlagen, welche den Weg für die nächste Generation von Quantenbauteilen mit implantierten Spin-Defekten weisen.

Oftmals verschlechtern elektrische und magnetische Feldfluktuationen die optischen wie auch die Spin- und Ladungstransport-Eigenschaften von Halbleitern, insbesondere in der Umgebung von Oberflächen und Grenzflächen [40–43]. Im Fall von Diamant sind die Ursprünge dieser Fluktuationen hauptsächlich nicht-gesättigte Kohlenstoffbindungen an der Oberfläche [44–46] sowie paramagnetische Oberflächenzustände (Oberflächenspins) [47, 48]. In der vorliegenden Arbeit wurde der Einfluss der Morphologie der Diamantoberfläche sowie deren chemische Zusammensetzung auf die Eigenschaften von oberflächennahen NV Zentren hin untersucht. Typische Behandlungsmethoden wie thermisches Ausheizen verursachen Phasenübergänge an der Diamantoberfläche wie termisch induzierte Graphitisierung [49]. Die obersten atomaren Lagen des Diamanten sind daher sehr reich an Defekten, was zur Bildung von elektronischen Zuständen in der Bandlücke nahe der Diamantoberfläche führt, welche die quantenmechanische Leistungsfähigkeit der NV Zentren stark beeinflusst. Dies wird durch die Behandlung der Diamantoberfläche mit beispielsweise kapazitiv gekoppeltem Plasma wegen des heftigen Ionenbeschusses der Oberfläche weiter verschlimmert [50–53]. Eine zentrale Herausforderung ist die Entwicklung von Methoden zur Entfernung der Diamantgrenzschicht um NV Zentren bis auf wenige Nanometer an die Oberfläche zu bringen ohne dabei ihre optischen Eigenschaften oder deren Spin-Kohärenz zu kompromittieren.

Zu diesem Ziel präsentiert diese Arbeit ein kontrolliertes Sauerstoff-Ätzverfahren für Diamant unter Zuhilfenahme eines neuartigen, auf induktiv gekoppeltem Plasma (ICP) basierenden Prozesses. Wichtig ist dabei, dass die nanometer-präzise Ätzrate äußerst reproduzierbar und selektiv ist, was den entwickelten Prozess für die Strukturierung von Diamanten in Hinblick auf quantensensorische Anwendungen interessant macht [54–57], da hier die Kompatibilität mit oberflächennahen NV Zentren eine wichtige Rolle spielt. An der geätzten Diamantoberfläche konnten keine Zeichen von plasma-induzierten Schäden mit Hilfe von Röntgenphotoelektronenspektroskopie (XPS) oder konfokaler Mikroskopie festgestellt werden. Die Plasmabehandlung von unterschiedlichen Diamantsubstraten durch den hier entwickelten Prozess zeigt kein plasma-induziertes Auslöschen der NV-Fluoreszenz jedoch sogar eine Verbesserung der Spin-Eigenschaften von besonders oberflächennahen NV Zentren (Tiefe < 4 nm). Die Verfügbarkeit solcher Werkzeuge ist einer der Meilensteine dieser Arbeit um neue Plattformen für die Weiterentwicklung von oberflächennahen NV Zentren zu schaffen.

Zunächst konzentriert sich diese Arbeit auf eine bereits gut etablierte Meth-

F. F. de Oliveira

ode zur Herstellung von NV Zentren: Die Implantation von Stickstoff in Diamant gefolgt von thermischen Ausheizen bei hohen Temperaturen [33, 34]. Bislang besitzt diese Methode die höchste räumliche Präzision bei der Positionierung von NV Zentren in Diamant, was bei Anwendungen von beispielsweise geordneten Feldern von oberflächennahen Spin-Defekten eine wichtige Rolle spielt [58]. Experimentelle Untersuchungen über die Erzeugung von NV Zentren durch diese Methode (und mehreren anderen Methoden wie Ionenbestrahlung [59–63]) zeigen, dass allgemein gesprochen, alternative Prozesse der Fehlstellen-Rekombination im Diamant während des thermischen Ausheizungsprozesses das effektive Erzeugen von NV Zentren limitieren. Mit Fehlstellen in Verbindung stehende paramagnetischen Spins gelten als starke Quelle von Dekohärenz für den Spin des NV Zentrums, selbst in der Umgebung von wenigen Nanometer an der Diamantoberfläche. Erstaunlicherweise ist bis heute keine Methode bekannt mit Hilfe derer sich die Ausbildung solcher Gitterdefekte während des thermischen Ausheizens von implantieren Diamantsubstraten unterdrücken lässt.

Motiviert durch diesen Umstand wird in dieser Arbeit eine neue Methode vorgestellt, mit Hilfe derer sich die Dynamik bei der Bildung solcher implantationsinduzierten Defekte beeinflussen lässt. Dies beinhaltet die Implantation von Stickstoffatomen in die induzierte Raumladungszone der freien injizierten Löcher welche in eine nanometerdicke Schicht von Bor-dotiertem Diamant auf der Oberfläche eines hoch-reinen Diamantsubstrats generiert wurden. Bei hohen Temperaturen verhält sich eine solche Struktur ähnlich wie ein planarer p^+-n übergang in der Halbleiterphysik. Der Überschuss an freien Ladungsträgern innerhalb der implantierten Region des Substrates verändert den Ladungszustand der Gitterdefekten, was wiederum deren Diffusions- und Rekombinationsverhalten beeinflusst. Unter diesen Umständen ist die Bildung von paramagnetischen Spins welche aus Fehlstellen resultieren deutlich unterdrückt, was durch die detaillierte Untersuchung des Spin-Rauschens in der Umgebung von oberflächennahen NV Zentren nachgewiesen werden kann. Als Ergebnis konnte eine Verbesserung der Spinkohärenzzeit um einen Faktor Zehn und eine Verdopplung der Ausbeute bei der Bildung von NV Zentren nachwiesen werden. Die präsentierten experimentellen Ergebnisse sind weiterhin durch numerische Simulationen der Bildung und zeitlichen Entwicklung von implantationsinduzierten Spin-Defekten belegt, welche an einzelnen Implantationsstellen ausgewertet werden.

Alternativ werden diese Ergebnisse außerdem dazu benutzt, eine optimierte Architektur von einem dünnen (δ) Profil von NV Zentren an der Diamantoberfläche für quantensensorische Anwendungen zu untersuchen. Dies basiert auf der Dotierung des Diamanten mit Stickstoff während der chemischen Gasphasenabscheidung [64–68] gefolgt von der Bestrahlung des Diamanten mit Heliumionen [60,

F. F. de Oliveira

63]. Wichtig hierbei ist, dass die Optimierung solcher Strukturen die quantitative Kenntnis der Aktivierung der NV Zentren durch bestrahlungsinduzierte Fehlstellen während des thermischen Ausheizprozesses voraussetzt. Mit diesem Ziel wurde die Tiefenverteilung von oberflächennahen, heliuminduzierten NV Zentren (und verwandten optisch aktiven Heliumdefekten) mit Hilfe von schrittweisem Plasmaätzen und konfokaler Mikroskopie untersucht. Diese Ergebnisse liefern Einblicke in die Effizient der Fehlstellendiffusion sowie in alternative Rekombinationswege welche gleichzeitig mit der Entstehung von NV Zentren stattfinden. Im Gegensatz zur vorherrschenden Meinung, ist der Bereich für die effektive Bildung von NV Zentren auf einen Korridor mit Radius von etwa $10 - 15$ nm um die Spur der Heliumionen im Diamantgitter begrenzt. Entsprechend konnte gezeigt werden, dass NV Zentren mit hoher Effizienz ($\sim 15\%$) nur innerhalb der atomaren Verteilung der eingestrahlten Atome gebildet werden. Limitierungen der Helium-Bestrahlungsmethode für den Fall von hohen Teilchenfluenzen ($> 10^{12}$ Atome.cm^{-2}) wurden ebenfalls untersucht.

Ergebnisse zeigen, dass die Bildung von Defekten welche innerhalb der bestrahlten Region des Substrates durch Fehlstellen hervorgerufen werden für die beobachtete Sättigung der Bildungseffizient sowie für eine Verringerung der Verteilung von NV Zentren unter der Oberfläche bei hohen Teilchenfluenzen verantwortlich sind. Einfache analytische Abschätzungen geben quantitative Einblicke in diese Effekte. Schlussendlich fließen all diese Erkenntnisse in die experimentelle Realisierung einer optimierten Architektur eines δ-Profils von NV Zentren direkt an der Diamantoberfläche ein. NV Zentren innerhalb dieser Struktur zeigen bei einer Tiefe von < 5 nm eine etwa zehnfach höhere Spinkohärenz im Vergleich zu NV Zentren welche durch herkömmliche Stickstoffimplantation in ähnlicher Tiefe erzeugt wurden. Darüber hinaus werden Benchmark Tests für die Quantensensorik gezeigt, bei denen Elektronenspin welche auf der Diamantoberfläche abgeschieden wurden nachgewiesen werden, was nochmals das Potential dieser Methode für die Detektion externer Spins mit verbesserter Sensivitüt unterstreicht.

Aufbau der Arbeit. In Kapitel 1 wird Diamant als Wirtsmaterial für Spin-Defekte zusammen mit der Definition des untersuchten Spin-Systems eingeführt. Kapitel 2 beinhaltet einen kurzen Überblick über die derzeit verfügbaren Methoden um bewusst NV Zentren in Diamant zu erzeugen. Besondere Eigenschaften sowie Vorteile und Limitierungen der einzelnen Methoden werden erläutert. Kapitel 3 handelt von der Diamantoberfläche und ihrem Einfluss auf die Eigenschaften von NV Zentren. Der physikalische und chemische Aufbau der Oberfläche nach deren Behandlung durch unterschiedliche Prozesse wird im Detail analysiert. Ein neuartiger Plasmaprozess wir vorgestellt und untersucht mit dem Ziel, NV Zentren näher an die Diamantoberfläche zu bringen und dabei ihre Eigenschaft zu erhalten. Kapi-

F. F. de Oliveira

tel 4 beginnt mit einer Untersuchung der Stickstoffionen-Implantationstechnik in Diamant. Numerische Molekulardynamiksimulationen und kinetische Monte Carlo Methoden sowie analytische Berechnungen werden benutzt um eine belastbare und weitreichende Vorstellung von der Bildung von Spin-Defekten in Diamant zu schaffen. Die neue Methode der Ionenimplantation innerhalb der Raumladungslage der hoch-reinen Region einer Bor-dotierten Struktur wird präsentiert und die daraus resultierenden Auswirkungen auf die Bildung und Dynamik von NV Zentren und anderen Fehlstellen-Zentren wird analysiert. Der Implikationen dieser Ergebnisse auf die Erzeugung von gekoppelten Paaren von NV Zentren wird ebenfalls kurz erörtert. Kapitel 5 untersucht eine optimierte Architektur für die δ-Dotierung von Diamant basierend auf Anwendungen in der Quantensensorik. Wichtige Aspekte der Fehlstellen-Diffusion in Diamant werden durch die Bestimmung der Tiefenverteilung von NV Zentren und anderen Helium-Defektzentren untersucht. The experimental realization of such a structure and quantum sensing benchmark measurements are presented. Die experimentelle Realisierung einer solchen Struktur sowie quantensensorische Benchmark Test werden gezeigt. Zuletzt werden die verwendeten experimentellen Aufbauten und eine Vielzahl von unterstützenden Methoden in den Appendizes zusammengefasst.

Acknowledgements

Moving from another country into Germany to do a Ph.D. has been since the idea's first steps extremely challenging, difficult, and at the same time, very rewarding. The concomitant results of these last five years that are written in this Thesis were only possible due to the contributions of outstanding people both in the personal and professional aspects of my life.

First and foremost, I would like to thank **Prof. Dr. J. Wrachtrup** for allowing me to enter into an amazing and resourceful research environment, where I felt very welcomed and encouraged. I am very thankful for the infinite discussions that we had, the great given insights and critical eyes of expertise that he provided over my research. It is a personal pleasure and an honor to have his name on my Ph.D. Thesis, and I will take his enthusiasm and perseverance as an example for my professional life. Moreover, I also thank very much **Prof. Dr. P. Michler** for being the second supervisor and **Prof. Dr. G. Wunner** for being the Chairman of the Ph.D. exam.

Without any hesitation, I must say that my achievements would not be possible without **Dr. A. Denisenko**. I will always be grateful for having worked under his co-supervision and being able to primarily execute many exciting research projects that were born in his office. His mentoring, guidance and endless efforts (and persistence) have provided the ground stacks throughout my whole Ph.D. research. Additionally, the taught experimental skills provided me the tools needed for the execution of my research and therefore are very much appreciated. Thank you Andrej! I could not have done this without you.

I cannot thank enough for the many external collaborations that were established during my research, being one of the key-points of the presented results. As follows, there is a list of acknowledgements for my collaborators from all around the world.

Greiner, **Matthias Widmann**, **Torsten Rendler**, **Thomas Oeckinghaus**, **Dr. T. Häberle** and **Farida Shagieva**. Thank you all for always being there when I needed!

For the technical support and the help with legal things I highly acknowledge **Ms. Claudia Unger** and **Mr. Stephan Hirschmann**. For the organization of our work environment and great chats I thank **Ms. Spajic**. You really help to hold the institute in one piece and provide a vital support for everyone!

Last but not least, I would like to acknowledge the people that were present in the backstage of my research, being the pillars holding my personal life.

First of all, I would like to generally thank my whole family (and my in-laws) for supporting and encouraging me to overcome challenges that I never thought would be possible. Being abroad, approximately 10000 km from home, family and old friends, has not been easy, but I truly feel them with me. This energy keeps pushing me forward in a strong pace. I really believe that most of what I have achieved and the values that I have must be acknowledged to people that surrounded me during my life. Shortly, but emphatic, thank you from the deepest part of my heart!

Particularly, I would like to thank my mother, **Carla Glade Fávaro**, for being the most incredible person that I know. Her passed values of family and hard working are the wheels of my life. I cannot thank you enough for the intense support, kindness and affection that you have for me.

There is one particular person that deserves an acknowledgement as long as this Thesis: my wife **Alessandra Ferreira Moreira**. She has literally jumped into a new journey with me when coming to Germany. During the last five years, she indeed was the person who hold everything together. She resisted through infinite late days - weekends - holidays of working, no vacation and shortage of money and incredibly: with the most beautiful smile. She is the kindest person I know and an explicit example of how love can change everything. Moreover, she gave birth to a miracle named **Gabriel**, who has been teaching me how magnificent is the task of being a father. Every single word written in this document is dedicated to you two.

I could not forget to briefly say thank you for my Brazilian friends in Germany. They made me feel home and helped me to go through an infinite number of situations. Thank you for the Brazilian touch given to my life in Germany!

Contents

List of Figures

List of Abbreviations

AC	Alternating current
AFM	Atomic force microscopy
AOM	Acousto-optic modulator
APD	Avalanche photo-diode
CBM	Conduction band minimum
CPMG	Carr-Purcell-Meiboom-Gill
CTRIM	Crystal-TRIM
CVD	Chemical vapor deposition
CW	Continuous wave
DC	Direct current
DEER	Double electron-electron resonance
EPR	Electron paramagnetic resonance
ESEEM	Electron spin echo envelope modulation
ESR	Electron spin resonance
fcc	Face-centered cubic
FFT	Fast Fourier transform
FID	Free induction decay
FPGA	Field-programmable gate array
FWHM	Full width at half maximum
GeV	Germanium-vacancy
HPHT	High-pressure high-temperature
ICP	Inductively coupled plasma
IMD	ITAP molecular dynamics
IMFP	Inelastic mean free path
IR	Infrared
keV	Kilo-electron Volts
KMC	Kinetic Monte Carlo
MD	Molecular dynamics
MEMS	Micro-Electro-Mechanical Systems
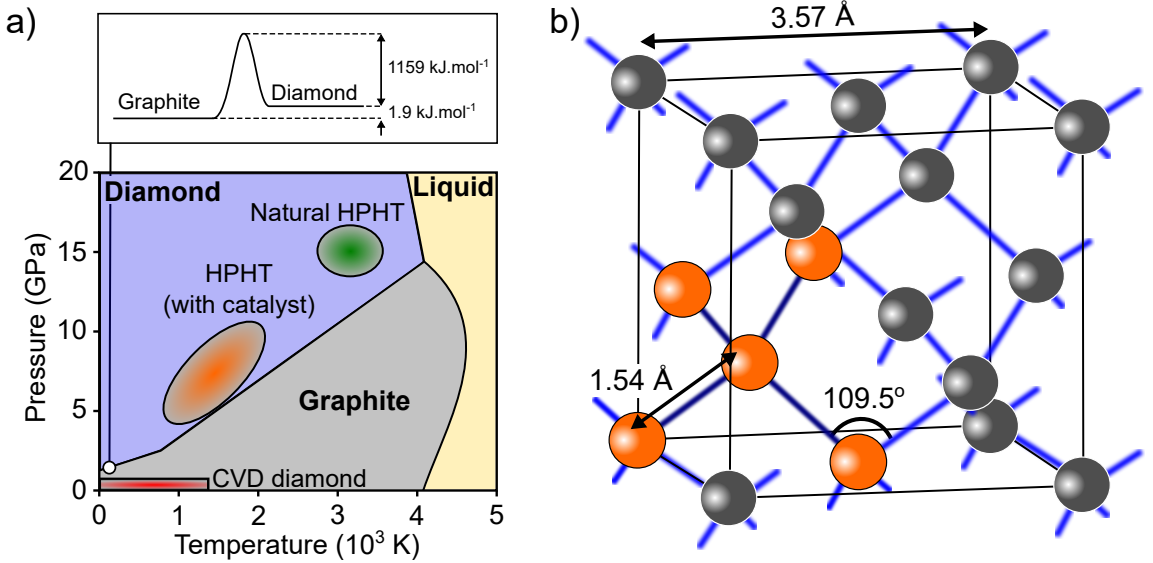
MeV	Mega-electron Volts
MHD	Magnetohydrodynamics
MIBK	Methyl isobutyl ketone
MRI	Magnetic Resonance Imaging
NA	Numerical aperture
NMR	Nuclear Magnetic Resonance
NV	Nitrogen-vacancy
ODMR	Optically detected magnetic resonance
PKA	Primary knock-on atom
PMMA	Polymethyl methacrylate
ppb	Parts per billion
ppm	Parts per million
PSF	Point spread function
RF	Radio frequency
RIE	Reactive ion etching
RMS	Root mean square
RT	Room temperature
sccm	Standard cubic centimeters per minute
SiC	Silicon carbide
SIMS	Secondary ion mass spectroscopy
SiV	Silicon-vacancy
SNR	Signal-to-noise ratio
SRIM	Stopping and range of ions in matter
STP	Standard temperature and pressure
TEM	Transmission electron microscope
UV	Ultraviolet
VBM	Valence band maximum
WCO	Wet chemical oxidation
XPS	X-ray photoelectron spectroscopy
ZBL	Ziegler-Biersack-Littmark
ZPL	Zero-phonon line

1. Diamond as a host material of spin-impurities

As previously introduced, this work is mainly focused on the unique quantum properties of the negatively-charged NV center in diamond. In this sense, this Chapter starts with the introduction of diamond as a host material of spin impurities. The relevant material properties are briefly discussed, together with the main techniques used for the artificial synthesis of high-quality diamond substrates. Lastly, the NV center is introduced and a brief overview of its relevant properties is given in the context of quantum sensing applications.

1.1. The diamond material

Diamond is a very unique material, popularly known as beautiful and shiny gemstones. Far from their appearance, research and industrial applications primarily focus on the outstanding properties that different types of diamond exhibit. Figure 1.1 a) shows the pressure-temperature phase diagram of carbon. The natural formation of diamond occurs under extremely high pressure and high temperature conditions, ranging $10 - 15\,\mathrm{GPa}$ and $2000 - 3000°\mathrm{C}$, respectively [69]. These extreme conditions occur naturally within the mantle of Earth, at depths of $140\,\mathrm{km}$ up to $200\,\mathrm{km}$. Under standard temperature and pressure (STP) conditions, however, graphite is the stable allotrope (solid structure) of carbon, whereas diamond is meta-stable. Although diamond and graphite show only a subtle enthalpy difference of $\sim 1.9\,\mathrm{kJ.mol^{-1}}$, a high energy barrier for the inter-conversion process from diamond to graphite ($\approx 1159\,\mathrm{kJ.mol^{-1}}$ for the [111] crystal direction [70]) is present (see the upper part of figure 1.1 a). This means that diamond is considered as a perfectly stable material under STP conditions.

Figure 1.1.: Phase diagram of carbon and the diamond lattice structure. a) The pressure vs. temperature carbon phase diagram is shown for the allotropes of carbon, namely diamond and graphite (figure partially adapted from Refs. [69] and [71]). The pressure and temperature ranges of different diamond synthesis methods are also presented. In the upper part, the schematic energy diagram for the diamond-to-graphite phase transition is shown, with the corresponding enthalpy and activation energy values (not scaled). **b)** Schematic representation of the diamond lattice unit cell. The five orange spheres highlight the tetrahedral structure of the carbon bonds in diamond.

1.1.1. Bulk material properties
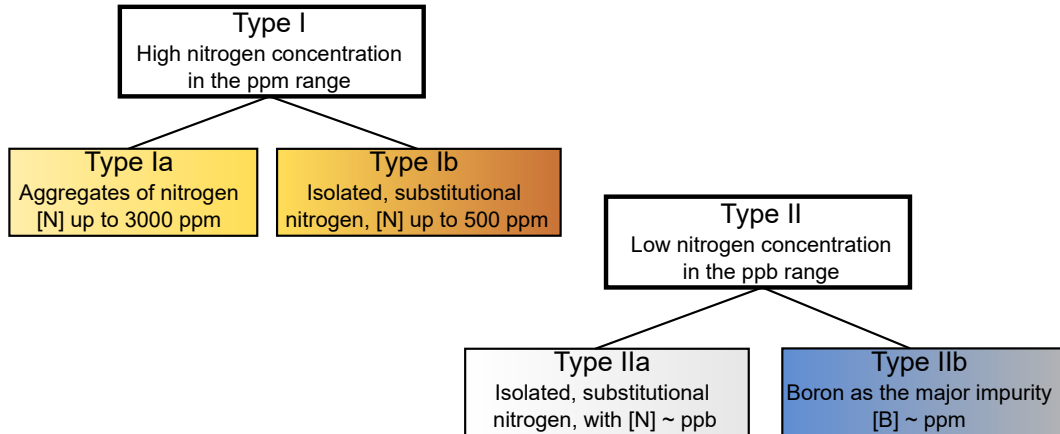
In its ground state, carbon atoms have six electrons and adopt the electronic configuration $1s^2 2s^2 2p^2$, where two core electrons occupy the 1s electronic shell and four valence electrons are equally distributed between the 2s and 2p electronic shells. During the formation of a crystal, carbon atoms are in excited states due to external perturbations. Under these conditions, orbital hybridization occurs in order to maximize the number of bonds available in the solid, thus minimizing the energy of individual chemical bonds. In the case of carbon atoms in diamond, the "s" and the three "p" orbitals mix, forming four sp^3 hybridized orbitals with a mutual angle of 109.5° in a tetrahedral geometry. One of the 2s valence electrons is then promoted to a 2p electronic shell, resulting in a $1s^2 2s^1 2p^3$ electronic configuration. The tetrahedral structure is hence imprinted on the highly-compact lattice configuration of diamond, with equal and strong binding energy among neighboring carbon atoms.

In the case of carbon atoms in graphite, the "s" and two "p" orbitals mix, forming three sp^2 hybridized orbitals with a mutual angle of 120° in a planar geometry perpendicular to the remaining "p" orbital. These three hybrid orbitals are responsible for σ-bonds (end-overlap between sp^2 hybridized orbitals) in graphite, whereas the perpendicular "p" orbitals form carbon π-bonds. Such a planar bonding configuration characterizes the layered structure of graphite, where the strong σ-bonds align carbon atoms within atomic-thin honeycomb-like monolayers that are, however, easily sheared from each other by breaking the weak inter-layer Van der Waals interactions. The strength of the σ-bonds has been responsible for the rapid expansion in the research of graphene (monolayers of carbon atoms arranged in the mentioned honeycomb-like structure) and related applications such as electrochemical and bio sensors [72].

Figure 1.1 b) shows a schematic representation of the resulting diamond lattice unit cell. The tetrahedral bond configuration is highlighted by the five orange spheres, each one representing an individual carbon atom. As mentioned, each carbon atom has four valence electrons that establish covalent bonds to four other neighbor carbon atoms, with an inter-atomic distance of 1.54Å (under STP). Diamond presents a face-centered cubic (fcc) lattice structure, with a lattice constant of 3.57Å. Such a bonding configuration can be further considered to discuss several material properties of diamond. For instance, the carbon-carbon covalent bond strength and the tetrahedral configuration are responsible for an extreme material hardness, giving to diamond the title of the hardest known bulk material (the value of 10 in the Mohs scale of hardness [73]). Furthermore, the high binding energy between carbon atoms also gives diamond an extreme chemical and irradiation inertness.

The closely-packed carbon atoms within the diamond lattice efficiently transfer heat via phonon-assisted propagation due to a high Debye temperature of 1860 K [74], resulting in an excellent thermal conductivity of 22 W.cm^{-1}.K^{-1} [75, 76]. Together with a high electrical breakdown field of 10^4 kV.cm^{-1} [75], the mentioned properties make diamond one of the most promising materials in industrial applications such as high-power electronic devices and tools for i.e. polishing, grinding and drilling [77].

Depending upon the growth environment, extrinsic impurity atoms can be incorporated to the diamond lattice. These impurities are per definition imperfections, or defects, which gives rise to i.e. particular optical absorption spectra corresponding to different levels and types of impurities [79]. Due to their similar atomic radii to carbon, the commonly-observed impurities in natural diamonds are nitrogen and boron atoms (and related complexes). During the crystal growth, these impurities

Figure 1.2.: Main classification categories of diamond. The main classification categories of diamond are shown. Individual color scales indicate the typical diamond color observed for each type. Denominations adapted from Ref. [78].

replace carbon lattice atoms with a minimum energy cost, resulting in a crystal with i.e low density of lattice dislocations and growth defects [80]. The nitrogen and boron impurity contents are the main criteria to classify diamonds into particular types, as summarized in figure 1.2.

Diamond substrates that present absorption lines in the infrared (IR) spectral range are assigned to the main Type I [78]. These diamonds present a yellow/brown coloration due to the presence of nitrogen aggregates (Type Ia) or single, substitutional nitrogen impurities - also known as P1 centers - (Type Ib) with relatively high concentrations, ranging up to several hundred parts per million (ppm). More than 98% of all natural diamonds fit within this category. These types of diamond can present an n-type conductivity due to the activation of nitrogen donor impurities, as discussed in details in Chapter 4.

In the absence of the characteristic IR absorption lines of nitrogen defects, diamond is assigned to the Type II [78]. Type IIa diamonds are the purest and the most rare in nature, presenting concentrations of nitrogen and boron impurities in the low parts per billion (ppb) range. Consequently, these diamond substrates are excellent insulators and are optically transparent from the ultraviolet (UV) to the far infrared (IR) ranges [79]. In this work, the utilized diamond substrates fit within this category. Type IIb diamonds present an excess of boron impurities, with concentrations ranging up to several hundred ppm. This type of diamond can present a p-type conductivity due to the activation of boron acceptor impurities, as also discussed in Chapter 4.

1.1.2. Growth methods

Due to the outstanding properties and economical relevance of diamond materials, major research efforts have been directed since the last century to the development of diamond syntheses techniques. Nowadays, these efforts have culminated in artificially-synthesized diamond substrates that possess properties comparable to the natural material. The main advantages of synthetic diamonds are the relatively-low production costs (in comparison to the search of natural gemstones) and the capability to precisely manipulate i.e. the dominant type and concentration of impurities to match the requirements of specific applications. Among several other methods, controlled high-pressure high-temperature (HPHT) and microwave plasma-enhanced chemical vapor deposition (CVD)[1] are the two most common and widely-adopted techniques for the synthesis of diamond crystals. These two methods will be briefly described in this section.

High-pressure high-temperature (HPHT) technique

As the name implies, this technique essentially simulates the geological pressure and temperature growth conditions of natural diamonds (see the phase diagram in figure 1.1 a). Generally, two approaches are utilized. The first approach, the so-called "direct method", involves the use of specially-designed equipment to subject a nominally pure carbon-containing sample (usually graphite, alternatively with an embedded diamond seed) to pressures in excess of $\sim 15\,$GPa and temperatures as high as $\sim 2000°$C [81]. In this sense, the synthesis of diamond occurs in a harsh environment, which is costly to be reproduced in laboratory conditions.

The second approach, the so-called "indirect" or "catalytic conversion method", utilizes a rather simplified equipment to subject the carbon-containing sample to pressure and temperature slightly below the natural growth conditions of diamond. The HPHT exposure is performed embedding the carbon-containing sample within a catalytic solution of, for example, transition metals such as copper and manganese [82]. Under HPHT conditions, a supersaturated carbon-containing chemical solution is formed, which results in the carbon crystallization as diamond with a reduced activation energy [82]. In this approach, pressure and temperature conditions ranging $\sim 5\,$GPa and $\sim 1200°$C [83], respectively, are typically utilized (see the phase diagram in figure 1.1 a).

---

[1]Microwave plasma-enhanced is one of the subcategories of diamond growth by CVD. There are several other subcategories such as hot filament CVD that will not be covered in this Chapter due to the resulting inferior quality of artificially-synthesized diamond substrates. Throughout this Thesis, for simplification, microwave plasma-enhanced chemical vapor deposition is generally referred to as CVD.

In both cases, the level of impurity incorporation in the grown diamond is rather high (typically hundreds of ppm), culminating mainly in the production of Type I diamond substrates (figure 1.2). This method is largely employed in diamond applications for e.g. drilling tools, where large-scale and relatively-low production costs are the priorities over the level of crystal purity. Nonetheless, the HPHT growth of high-quality Type IIa diamond substrates have recently become feasible with the use of highly-controlled catalysis environment [84]. In this Thesis, Type IIa HPHT diamond substrates are experimentally analyzed in section 5.1.3.

Microwave plasma-enhanced chemical vapor deposition (CVD) technique

An alternative growth method of synthetic diamonds is known as chemical vapor deposition [21, 85]. The development of this technique focused primarily on the concomitant flexibility of diamond growth both homoepitaxially (onto a diamond seed) and heteroepitaxially (onto a different material such as iridium [86]). The later has a significant impact on industrial applications of diamond such as material hard coating [87], a feature that cannot be achieved by the HPHT technique.

In the case of microwave plasma-enhanced CVD, a plasma is generated in the growth chamber (directly above the diamond seed) by heating a gas-mixture of molecular hydrogen (H_2) and methane (CH_4) using microwave irradiation. In this method, diamond growth takes place at considerably lower pressure and substrate temperature conditions ($\sim$ mbar and $\sim 1000°C$, respectively - see the phase diagram in figure 1.1 a). The growth of the diamond film occurs layer by layer due to the diffusion of highly-reactive hydrocarbon-related species from the plasma to the surface of the diamond seed. Importantly, the hydrogen plasma efficiently removes non-diamond carbon phases and stabilizes the growing diamond lattice. Further details on the growth mechanism of diamond by the CVD technique will be investigated in Chapter 5, section 5.3.2. By carefully adjusting the growth parameters, the synthesis of high-quality diamond films with large mono-crystalline sectors and low density of lattice dislocations is possible [21].

Particularly, the utilized gas-mixture in the CVD process provides an excellent control mechanism of the resulting diamond properties. In its natural abundance, carbon presents an isotope proportion of $\sim 98.9\%$ ^{12}C to $\sim 1.1\%$ ^{13}C. This feature is relevant to applications of diamond as a spin-impurity host material, since the ^{13}C isotope has a $\mathbf{I} = \frac{1}{2}$ nuclear spin, whereas the ^{12}C has no nuclear spin [88]. Hence, the introduction of isotopically-enriched CH_4 gas to the plasma gas-mixture can be used to manipulate the resulting ratio of carbon isotopes in the grown diamond film. This provides a path to control the corresponding spin environment

within the diamond lattice [88].

In general, the CVD technique results in a low level of contamination (that is, low amount of extrinsic atoms in diamond), allowing the growth of ultra-pure Type IIa diamond films with extremely low concentrations of nitrogen and boron impurities (values even below 1 ppb [89]). On the other side, the flexibility of the CVD technique also allows the intentional introduction of impurities into the grown diamond film, which facilitates the growth of high-quality *n*- and *p*-type diamond substrates [90]. This is performed by the addition of controlled concentrations of i.e. nitrogen and boron atoms in the plasma gas-mixture, respectively. The relevance of the controlled impurity incorporation during diamond CVD growth is a central feature of the fabricated diamond structures presented in Chapters 4 and 5.

1.1.3. Color centers in diamond

The complete saturation of carbon valence electrons in diamond results in a large indirect band gap of 5.47 eV at room temperature [76]. This makes diamond a well-suitable host material of optically-active defects, that is essentially, a host material of additional energy levels lying within its band gap. Eventually, defects with energy transitions that are within the visible light spectrum ($1.65 - 3.1$ eV) are known as *color centers*. This is due to the resulting colorful appearance of diamond substrates that contain relatively high concentrations of these defects.

Up to date, more than 500 color and/or paramagnetic centers have been identified in diamond [79]. Some of these defects exhibit unique quantum properties, being thus more thoroughly investigated than others. For example, the silicon-vacancy (SiV) center [91–93] and the germanium-vacancy (GeV) center [94] in diamond have been extensively investigated as platforms for i.e. quantum cryptography due to their extremely narrow-band optical emission spectra [94, 95]. On the other hand, the combination of a paramagnetic spin ground state and the optical polarization and readout processes makes the NV center an exceptional sensor of, for example, small magnetic fields, as explored below. Consequently, the NV center has been one of the most thoroughly reported spin impurities in diamond.

1.2. The nitrogen-vacancy center in diamond
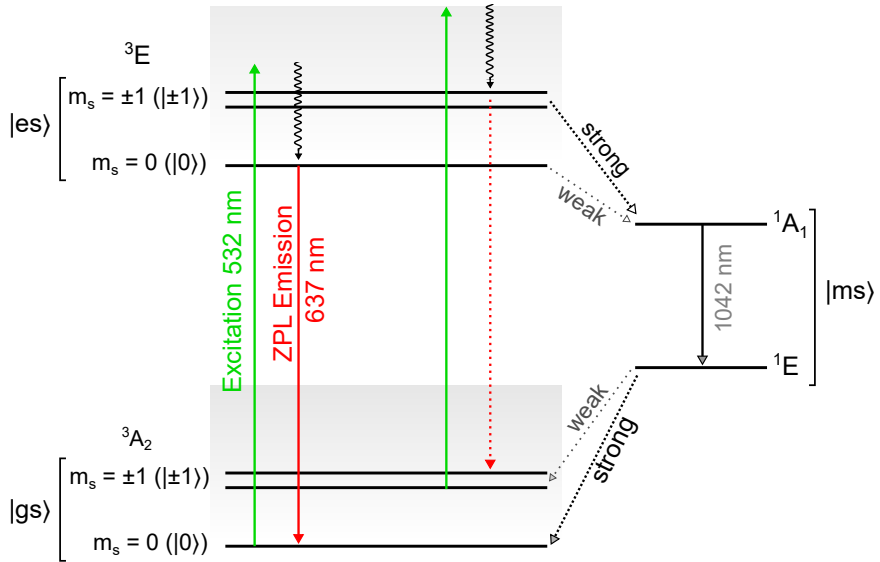
In 1976, Davies *et al.* reported on a strong optical band at 1.945 eV ($\sim$ 637 nm) observed in type Ib diamond substrates after the production of radiation-induced damages and subsequent high-temperature treatment [96]. For annealing temperatures above 600°C, an increase of the band intensity at 1.945 was observed simultaneously to the reduction of the optical band intensity at 1.673 eV ($\sim$ 751 nm), attributed to single lattice vacancies (GR1 centers [79]). Since type Ib diamonds present an excess of single substitutional nitrogen atoms, Davies *et al.* attributed this feature to the formation of lattice defects during thermal annealing, constituting of a trapped vacancy at or nearby to a single nitrogen atom site. This prediction was indeed correct and corresponds to the currently accepted physical structure of the NV center in diamond.

NV centers have a triagonal C_{3v} symmetry, with the nitrogen atom and the adjacent vacancy being localized along the defect $\langle 111 \rangle$ major symmetry axis [97]. Hence, the symmetry of the tetrahedral structure of the diamond lattice allows NV centers to be oriented along four possible crystallographic directions, namely $[111]$, $[\bar{1}\bar{1}1]$, $[1\bar{1}\bar{1}]$ and $[\bar{1}1\bar{1}]$. Generally, the four directions are equally populated in NV center-rich diamond substrates, but preferential alignment along one crystallographic direction has been observed in nitrogen-doped diamond films grown by the CVD technique [98]. Interestingly, the optical properties of NV centers are rather orientation-independent, whereas the relative position of the nitrogen atom and the vacancy can still be independently addressed [97].

1.2.1. Electronic structure

The electronic structure of the NV center is fundamentally determined by the nitrogen atom and the three carbon atoms adjacent to the vacancy [99]. The substitutional nitrogen atom has five valence electrons, from which three are shared with the neighboring carbon atoms. Each dangling bond of the carbon atoms surrounding the vacancy has one unpaired valence electron. Accordingly, the neutral NV center has 5 electron in total, characterizing a system with an electron spin of $S = \frac{1}{2}$ [100]. Depending upon the position of the Fermi level within the diamond lattice, however, different charge states of the NV center are observed [101, 102].

For instance, the presence of nearby donor impurities such as P1 centers in the diamond lattice results in the capture of another electron by a nearby NV

Figure 1.3.: The electronic energy levels of the NV center. A schematic representation of the electronic energy levels of the NV center is shown (solid-horizontal lines). The system comprises of a triplet ground state ($|gs\rangle$), a triplet excited state ($|es\rangle$) and a meta-stable state ($|ms\rangle$) - see text. The allowed optical transition between the $|gs\rangle$ and $|es\rangle$ is also shown (green and red arrows), with the corresponding ZPL emission at 637 nm. The wavy arrows represent photon relaxation into phonon sidebands of the diamond lattice. Optical spin polarization is possible by the intersystem crossing via the meta-stable state, which decays preferentially to the ground state $m_s = 0$ energy level (dotted lines represent the transition probabilities). Figure adapted from Ref. [103].

center[2], that is $NV^0 + P1^0 \rightarrow NV^- + P1^+$. The negatively-charged NV center has in total 6 electrons, delivering a system with an electron spin of $S = 1$. Among all possible charge-states, only the negatively-charged NV center presents a strong magneto-optical response and is hence responsible for the vast application field of NV centers as quantum sensors. In this sense, all presented experiments in this work are performed using negatively-charged NV centers and, for simplicity, the abbreviation *NV center* is used throughout the Thesis (unless the charge-state is specifically mentioned).

The electronic energy levels of the NV center can be well-described using a simple three level system [103, 105], as presented in figure 1.3. The model comprises of a ground state ($|gs\rangle$) spin triplet with $^3A_2$ symmetry, an excited state ($|es\rangle$)

---

[2]Theoretically, it would be possible for an NV center to lose another electron (having in total 4 electrons) due to the presence of acceptor impurities within the diamond lattice. This would characterize the positively-charged NV center. Its characterization lacks experimental confirmation, although recent progresses have been reported [104].

spin triplet with ^{3}E symmetry and a meta-stable intermediate state ($|ms\rangle$) that effectively comprises two singlet states with ^{1}A$_1$ and ^{3}E symmetries [103, 105, 106]. Due to spin-spin interactions between the two unpaired electrons in the $|gs\rangle$, a zero-field splitting of $D = 2.870$ GHz lifts the degeneracy between the $m_s = 0$ and $m_s = \pm 1$ spin sublevels[3]. This allows the manipulation of the $|gs\rangle$ spin sublevels using time-varying electromagnetic fields within the microwave frequency range, even in the absence of an external magnetic field [22].

1.2.2. Optical properties
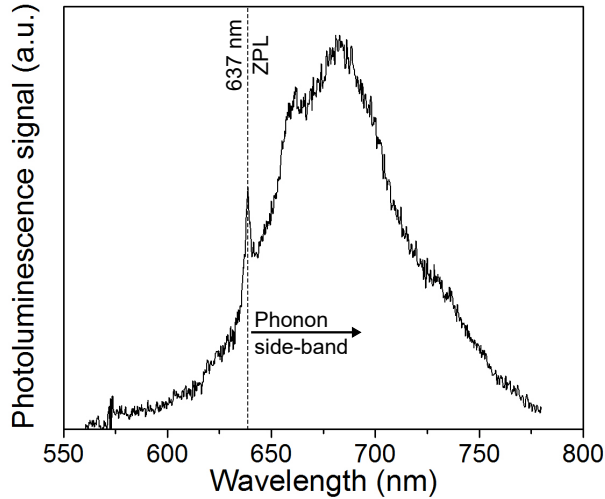
The NV center photoluminescence is characterized by a zero-phonon line (ZPL) emission at 637 nm of wavelength, as a result of the decay from the $|es\rangle$ to the $|gs\rangle$ levels (see figure 1.3). Figure 1.4 presents the characteristic photoluminescence spectrum of an NV center (excitation at 532 nm, see Appendix A.1). As it can be seen, only a small fraction of photons ($\approx 4\%$) is emitted into the ZPL. The majority of the emitted photons relax into phonon sidebands of the diamond lattice, with energies ranging up to ≈ 800 nm (with a maximum centered at ≈ 680 nm).

Under off-resonance illumination using, for example, green laser illumination (532 nm), the NV center experiences a spin-conserving transition from the ^{3}A$_2$ to the ^{3}E state (relaxing also into the phonon sidebands of the $|es\rangle$). From there, the NV center spin can decay back to the $|gs\rangle$ via two alternative channels [107, 108]. The first is the direct spin-conserving fluorescence decay (that is, for example, $|es\rangle$ $m_s = 0 \rightarrow |gs\rangle$ $m_s = 0$), which can be accompanied by photon relaxation into phonon side-bands. The second is the intersystem crossing through the intermediate singlet states $|ms\rangle$ (figure 1.3). The latter is assumed as a meta-stable state due to its long lifetime of approximately 250 ns, whereas the lifetime of the $|es\rangle$ spin states is in the range of a few ns [109]. Moreover, the transition between the singlet states can be both non-radiative or radiative, with a characteristic ZPL emission at 1042 nm [106].

In the case of the NV center, the probability of the spin to decay via the intersystem crossing is strongly spin state-dependent [107, 108]. For the $|es\rangle$ $m_s = 0$ state, intersystem crossing occurs with a negligible probability and the spin relaxes into the $|gs\rangle$ $m_s = 0$ state via radiative decay, as previously explained. In contrast, the decay from the $|es\rangle$ $m_s = \pm 1$ state occurs with similar probabilities either through radiative decay to the $|gs\rangle$ $m_s = \pm 1$ state or through intersystem

---

[3]Here, m_s represents the electron spin magnetic quantum number relative to the operator S_z - see below.

Figure 1.4.: Photoluminescence spectrum of the negatively-charged NV center. The characteristic photoluminescence spectrum of the negatively-charged NV center is shown (532 nm excitation wavelength). The ZPL emission at 637 nm can be easily identified, together with the broad phonon side-band.

crossing, decaying preferentially into the $|gs\rangle$ $m_s = 0$ state (see figure 1.3).

This feature results in the possibility of optical polarization and readout of the NV center spin state, importantly at room temperature. After several pumping cycles (e.g. illumination for a few µs), the spin population of the NV center is fully polarized into the $|gs\rangle$ $m_s = 0$ state with high fidelity ($> 90\%$ [110]). Moreover, since the lifetimes of the radiative and intersystem crossing decays are different, approximately 30% less photons are emitted when the NV center is initially excited from the $|gs\rangle$ $m_s = \pm 1$ state. Hence, a correlation between the spin state and the measured photoluminescence signal intensity can be performed.

The spin-state optical readout is performed during the applied laser pulse (few µs of duration) by recording the fluorescence response of the investigated NV center. This is only accomplished within the first ≈ 300 ns of the laser pulse due to the unavoidable optical initialization process of the spin in its $|gs\rangle$ $m_s = 0$ state under illumination and therefore the loss of the information, as previously described[4]. When combined to controlled microwave irradiation, these features allow the full control and the coherent manipulation of the NV center electron spin at single

---

[4]It should be noted that measurements are performed by accumulating the readout signal several times (in the order of 10000 repetitions under identical parameters) to increase the signal-to-noise ratio due to the low amount of collected photons at each measurement cycle. The readout laser pulse of the previous sequence is hence also utilized to re-initialize the spin state for the next measurement cycle.

sites.

1.2.3. The spin Hamiltonian

Due to the absence of spin-orbit coupling in the $|\text{gs}\rangle$, the Hamiltonian of the NV center electron spin is governed mainly by the zero-field splitting (H_{ZFS}), electron Zeeman interaction (H_{Z}) and spin-spin hyperfine interaction (H_{HF}) components [97]. In this case, the general form of the spin Hamiltonian in the corresponding $m_{\text{s}} = -1, 0, +1$ basis, where the z-axis is chosen to coincide with the NV center axis, can be written as[5]:

$$
\begin{aligned}
H &= H_{\text{ZFS}} + H_{\text{Z}} + H_{\text{HF}} \\
&= \underbrace{DS_{\text{z}}^2 - k_\perp E_{\text{x}}\left(S_{\text{x}}^2 - S_{\text{y}}^2\right) + k_\perp E_{\text{y}}\left(S_{\text{x}}S_{\text{y}} + S_{\text{y}}S_{\text{x}}\right)}_{ZFS} + \underbrace{\gamma_{\text{e}}B_{\text{z}}S_{\text{z}}}_{Z} + \underbrace{\mathbf{S}A\mathbf{I}}_{HF}. \quad (1.1)
\end{aligned}
$$

where D and $k_\perp E_{\text{x,y}}$ are the zero-field splitting parameters, $k_\perp = 170\,\text{kHz.µm.V}^{-1}$ is the electric susceptibility parameter [97], $E_{\text{x,y}}$ are the electric field transverse components, $S_{\text{x,y,z}}$ are the projections of the spin operator $\mathbf{S}$, $\gamma_{\text{e}} = g_{\text{e}}\mu_{\text{B}}/h \approx 2.80\,\text{MHz.G}^{-1}$ is the gyromagnetic ratio of the NV center electron spin (divided by 2π), μ_{B} is the Bohr magneton, $g_{\text{e}} \approx 2$ is the electron g-factor, and B_{z} is the component of the external magnetic field along the NV center axis[6]. A careful analysis of each component of the Hamiltonian gives further insights on the sensitivity of the NV center electron spin to certain physical quantities of interest, some of which are briefly highlighted below.

The axial zero-field splitting parameter $D = \frac{3}{2}D_{\text{z}} = 2.870\,\text{GHz}$, that is the axial component of the zero-field splitting diagonal tensor $\mathbf{D}$, is sensitive to temperature fluctuations [111–113], with a corresponding temperature dependency of $\sim dD/dT = -74.2\,\text{kHz.k}^{-1}$ [111]. Moreover, the transverse zero-field splitting parameters $k_\perp E_{\text{x,y}}$ represent the induced shift on the $|\text{gs}\rangle$ energy levels of the NV center electron spin due to lattice strain and electric fields [56, 97].

---

[5]Here, $\hbar = 1$ and hence the Hamiltonian has units of frequency.

[6]Magnetic field components perpendicular to the NV center axis result in the mixing of the original m_{s} levels into new eigenstates. In the presented work, only the magnetic field component along the NV center is relevant. Therefore, for simplicity, effects of $B_{\text{x,y}}$ are excluded from the analysis.

The electron Zeeman interaction corresponding to the magnetic field component along the NV center axis lifts the degeneracy of the $|gs\rangle$ $m_s = \pm 1$ spin states. This results in a symmetric splitting shift in the transition frequencies from the $|gs\rangle$ $m_s = 0$ to the $m_s = \pm 1$ energy levels. By taking into account the effect of the transverse components of the electric field ($E_\perp$), the spin transition frequencies are thus given by:

$$v_{\pm 1}\left(B_z\right) = D \pm \sqrt{\left(\gamma_e B_z\right)^2 + \left(E_\perp\right)^2}. \tag{1.2}$$

Clearly, the detection of external magnetic and electric fields, as well as strain by the NV center electron spin is in principle possible through the induced frequency shifts on the $m_s = \pm 1$ energy levels. This highlights the NV center as a potential nano-sensor in magnetometry and electrometry applications [18, 97, 114]. The sensitivity of spin-based magnetic field sensors is fundamentally limited by the associated quantum noise (statistical distribution of the measured spin projection) [114]. Moreover, the optical spin-state readout method is further limited by the photon shot-noise [115]. In the case of the NV center electron spin, typically $D \gg E_\perp$ [114]. Single NV centers are hence ultra sensitive atomic-size sensors of magnetic fields, which is the base building block to probe local electron paramagnetic resonance (EPR) and nuclear magnetic resonance (NMR) weak signals [27–29, 31]. The associated magnetic sensitivity (η) to AC fields generated by, for example, nearby external spins, is given by [114, 116]:

$$\eta = \frac{\pi\hbar}{2g_e\mu_B C\sqrt{IT_2}}. \tag{1.3}$$

As seen, the sensitivity depends on the collection efficiency (C) of emitted photons (with intensity I) by the NV center sensor. Diamond has a very high refraction index (~ 2.4), which causes most of the emitted photons to be reflected back into the diamond lattice at the diamond-air interface due to total internal reflection. This results into a generally poor collection efficiency (below 10%), which can be overcome by i.e. the fabrication of diamond photonic waveguides such as nanopillars [55]. Moreover, the magnetic sensitivity is ultimately limited by the spin coherence time (T_2) of the NV center electron spin, which will be further explored in section 1.3. Hence, the development of experimental techniques to increase the T_2 time of NV centers, and hence the AC magnetic sensitivity, is of primarily importance in quantum sensing applications, being one of the focuses of the presented work.

The hyperfine interaction with nuclear spins further highlights the NV center as a promising platform in the field of quantum information processing and compu-

tation. In equation 1.1, A is the hyperfine tensor and $\mathbf{I}$ represents the hyperfine-coupled nuclear spin. NV centers have a built-in nitrogen nuclear spin, which assumes values of $I = 1$ and $I = \frac{1}{2}$ for the ^{15}N and ^{14}N isotopes, respectively [117]. Moreover, hyperfine coupling of the NV center to ^{13}C nuclear spins is also observed, with a corresponding interaction strength that depends on their relative position in the diamond lattice [118]. Nuclear spins are much more robust memories due to their weak interaction with the environment and thus have much longer coherence times. Further details can be found in literature, in Refs. [15, 16, 119]
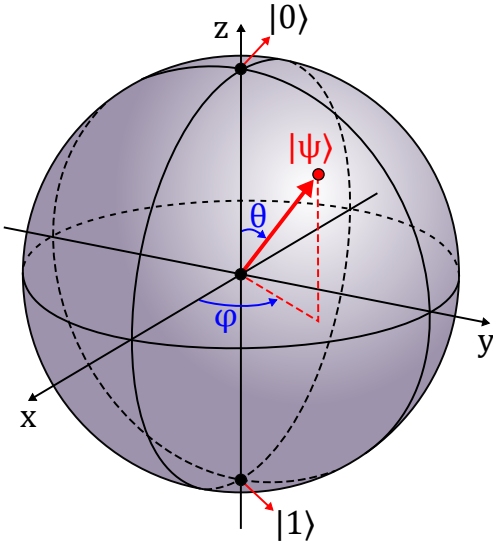
1.3. Coherent spin manipulation

In this section, the coherent manipulation of the NV center electron spin by electron spin resonance (ESR) technique and the relevant spin properties are investigated. In the presented spin experiments, the strength of the magnetic field applied along the NV center axis is sufficiently high to allow the v_{+1} and v_{-1} transition frequencies (equation 1.2) to be individually addressed. In this sense, the NV center can be considered as an effective two-level system, where the spin states $|0\rangle$ and $|1\rangle$ are defined as the $m_\mathrm{s} = 0$ and $m_\mathrm{s} = -1$ (or alternatively $m_\mathrm{s} = +1$) ground state spin sublevels, respectively.

The visualization of the spin state evolution is sometimes counter-intuitive, since the evolved spin state can assume linear combinations of the $|0\rangle$ and $|1\rangle$ states. In this regard, the Bloch sphere [120] presents a relatively simple interpretation for arbitrary spin states of a two-level system, as schematically shown in figure 1.5. The poles of the sphere represent the $|0\rangle$ and $|1\rangle$ states, whereas arbitrary linear combinations $|\psi\rangle = \alpha |0\rangle + \beta |1\rangle$, satisfying $|\alpha|^2 + |\beta|^2 = 1$, are points on the sphere surface defined by the angles θ, φ and the spin vector $|\psi\rangle$. Hence, any state of the system can be generally represented as:

$$|\psi\rangle = \cos\left(\frac{\theta}{2}\right) |0\rangle + \mathrm{e}^{i\varphi} \sin\left(\frac{\theta}{2}\right) |1\rangle \,. \qquad (1.4)$$
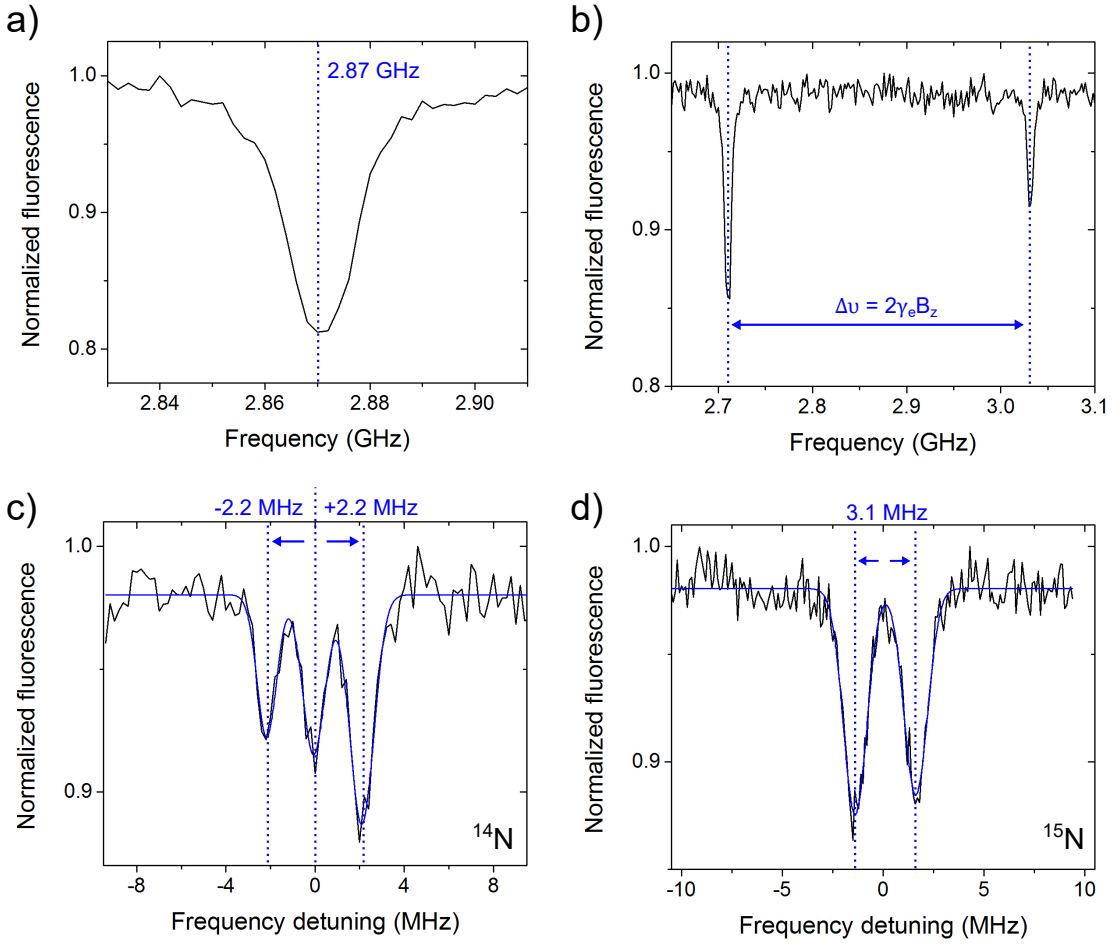
In the case of the NV center, the optical readout of the spin state represents the projection of $|\psi\rangle$ on the z-axis of the Bloch sphere, resulting on a measurable population of the $m_\mathrm{s} = 0$ ($|0\rangle$) or $m_\mathrm{s} = -1$ ($|1\rangle$) states. The coherent spin manipulation utilizing pulsed microwave fields result into rotations of the spin vector around the Bloch sphere, where the angle φ represents the rotation phase (also commonly referred to as the phase with respect to the microwave field).

Figure 1.5.: The Bloch sphere representation. The Bloch sphere representation of an effective two-level system is shown. The poles of the sphere are the $|0\rangle$ and $|1\rangle$ states, representing the $m_s = 0$ and $m_s = -1$ (or alternatively $m_s = +1$) ground state spin sublevels of the NV center in diamond, respectively. Linear combinations of states are represented by points on the surface of the Bloch sphere, defined by the angles θ and φ. Figure adapted from Ref. [121].

1.3.1. Optically detected magnetic resonance

To experimentally address the NV center spin transition frequencies (equation 1.2), relatively low intensity laser excitation and microwave irradiation can be utilized [22]. This technique is known as optically detected magnetic resonance (ODMR). Specifically, the constant application of a microwave field during illumination characterizes the continuous wave (CW) ODMR technique. The constant illumination of the NV center spin state under an applied off-resonance microwave field (that is, with a frequency different than $v_{\pm 1}$) leads to the optically-induced spin polarization into the $|gs\rangle$ $m_s = 0$ state. As a result, the decay occurs through the radiative transition from the $|es\rangle$ $m_s = 0$ level, that is, a bright fluorescence response. For an applied microwave field resonant to the ground state spin transition, a steady-state population transfer among the $|gs\rangle$ spin sublevels is achieved, depending upon the detuning of the the Rabi frequency (see below) and illumination intensity. In this case, intersystem crossing results into a decay with a reduced photoluminescence response. Hence, the NV center transition frequencies can be determined by sweeping the microwave frequency, while simultaneously monitoring its photoluminescence intensity under constant illumination.

Figure 1.6.: Optically detected magnetic resonance of a single NV center. a) The
CW optically detected magnetic resonance measurement of a single NV center is
presented in the absence of external magnetic field. The $m_s = \pm 1$ states are degen-
erated and both correspond to the transition frequency of the zero-field splitting,
that is $v_{\pm 1}\,(B_z = 0) = 2.870\,\text{GHz}$. **b)** In the case of an applied magnetic field of
$\approx 5.7\,\text{mT}$ along the NV center axis, the degeneracy is lifted. Consequently, the
$m_s = 0 \rightarrow m_s = \pm 1$ transitions can be individually addressed. **c)** and **d)** present
the pulsed optically detected magnetic resonance measurement of two single NV
centers, where the hyperfine splitting due to the ^{14}N and ^{15}N intrinsic nuclear
spins is observed, respectively.

If there is no magnetic field applied (and considering a negligible $E_\perp$), the spin
$m_s = \pm 1$ sublevels are degenerated. According to equation 1.2, the corresponding
CW ODMR spectrum shows a single transition frequency at the zero-field splitting
value, as exemplified in figure 1.6 a). A magnetic field along the NV center axis
lifts the degeneracy of the $m_s = \pm 1$ spin sublevels through the electron Zeeman
interaction. As exemplified in figure 1.6 b), the corresponding CW ODMR spec-

trum shows two individual transition frequencies, with a frequency separation of $\Delta v = 2\gamma_{\mathrm{e}}B_{\mathrm{z}}$ symmetric to the zero-field splitting frequency[7].

Due to the relatively high optical and microwave combined power, the CW ODMR spectrum suffers from inhomogeneous power broadening [122]. To overcome this issue, a pulsed scheme can be employed. In the simplest case, the NV center spin is optically initialized into the ground state $m_{\mathrm{s}} = 0$ sublevel and a resonant microwave pulse with a finite duration is applied to induce $m_{\mathrm{s}} = 0 \rightarrow m_{\mathrm{s}} = \pm 1$ population transfer within the ground state spin sublevels. For an optimum optical contrast, the pulse length should be optimized to induce a full transition between the mentioned states, that is a 180° rotation of the spin vector in the Bloch sphere representation. The microwave pulse is then followed by the optical readout of the spin state. The utilization of a relatively low microwave power (to avoid the previously-mentioned power broadening) allows the individual electron hyperfine-induced transitions to be probed. Figures 1.6 c) and d) show the pulsed ODMR spectra of two single NV centers that have ^{14}N ($I = 1$ system, 2.2 MHz frequency shift) and ^{15}N ($I = \frac{1}{2}$ system, 3.1 MHz frequency shift) intrinsic nuclear spins [117].
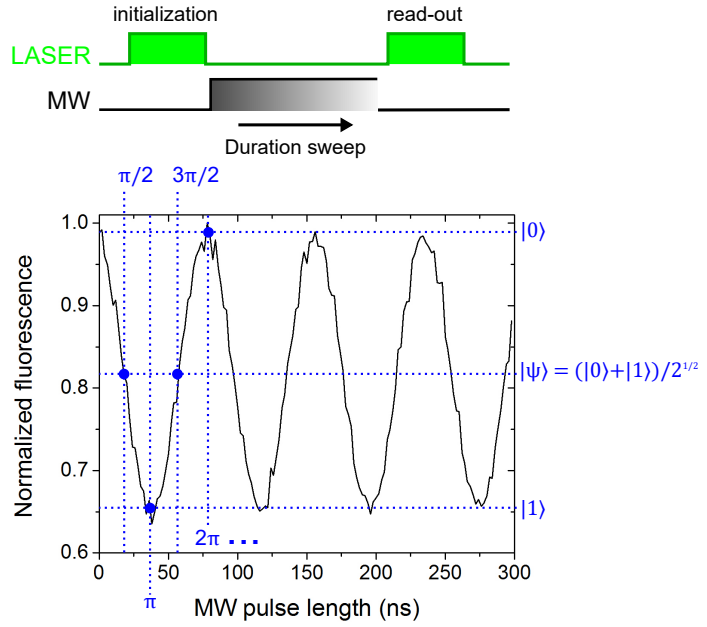
1.3.2. Rabi oscillations

As previously described, a resonant microwave field applied to an NV center can induce ground state spin transitions. The rotation angle of the spin vector in the Bloch sphere corresponding to the transfer of population between the two addressed energy levels (for example, $m_{\mathrm{s}} = 0 \leftrightarrow m_{\mathrm{s}} = -1$) depends however on the integrated field (microwave) applied to the NV center spin, that is the amplitude and duration of the microwave pulse. A constant variation of the field induces different rotation angles of the spin vector, e.g. coherent oscillations in the populations of the driven spin sublevels, known as Rabi oscillations.

The measurement sequence is shown in the upper part of figure 1.7. First, the NV center spin is initialized into the $|\mathrm{gs}\rangle$ $m_{\mathrm{s}} = 0$ sublevel by the laser pulse. Then, a resonant microwave pulse is applied to coherently transfer spin population between the driven ground state spin sublevels, where the resulting spin state is subsequently readout optically by a second laser pulse. As previously mentioned, the measurement of the spin population as a function of the microwave pulse length

---

[7]In the presented experiments, the alignment of the magnetic field along the NV center axis is performed by searching the position of the magnet that delivers the highest separation value between the transition frequencies, being symmetric to $D = 2.870\,\mathrm{GHz}$.

Figure 1.7.: Rabi oscillation measurement of a single NV center. In the upper part, the measurement sequence is presented. The variation in the duration of the resonant microwave pulse results into a change in the applied integrated microwave power to the NV center spin, which corresponds to oscillations in the NV center spin population.

results in oscillations, as evidenced in the lower part of figure 1.7.

Recalling the Bloch sphere notation, there are some specific microwave pulse lengths that should be highlighted. Considering that the spin is initialized at i.e. the north pole ($|0\rangle$) of the sphere, a $\pi/2$-pulse[8] brings the spin vector to the equator region of the sphere, corresponding to the superposition state $|\psi\rangle = \frac{1}{\sqrt{2}}(|0\rangle + |1\rangle)$. Similarly, a π-pulse brings the spin vector to the south pole of the sphere, corresponding to the complete population transfer from the $|0\rangle$ to $|1\rangle$ state. These specific rotations and further combinations will be relevant in different measurement sequences for the coherent manipulation of the NV center spin, as it will be described in the following sections.

---
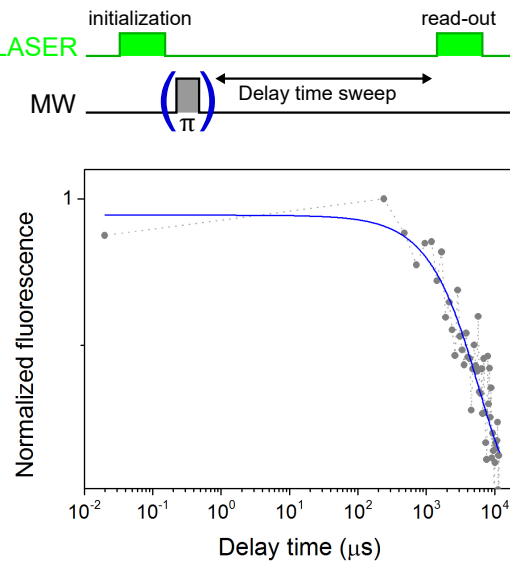
[8]Unless specified, all microwave pulses have a zero relative phase, representing rotations along one specific axis of the Bloch sphere.

1.3.3. Spin-lattice relaxation time

The characteristic time scale for a polarized NV center spin to decay into the thermally mixed state (e.g. the spin polarization under dark conditions) is known as the spin-lattice relaxation (T_1) time. In the case of NV centers hosted in bulk diamond, this decay is mainly induced by interactions with lattice phonons that induce stochastic population transfer among the ground state spin levels [123]. Due to a high Debye temperature, the density of phonon excitations in diamond is relatively low in comparison to most of solids. This fact results in T_1 times in the order of a few milliseconds at room temperature [65, 123–125]. Since this process is a phonon-assisted population decay, T_1 times are very sensitive to the temperature, reaching values of up to $\sim 170\,\text{s}$ at low temperature [123].

The measurement sequence is shown in the upper part of figure 1.8. The NV center electron spin is initialized into the ground state $m_\text{s} = 0$ sublevel by the first laser pulse and subsequently readout by a second laser pulse, applied after a

Figure 1.8.: Spin-lattice relaxation time measurement of a single NV center. In the upper part, the measurement sequence is presented. Two laser pulses (initialization and readout) are spaced by a delay time that is varied to obtain the time needed for the $m_\text{s} = 0$ spin sublevel to decay into the thermally mixed state. The resonant microwave π-pulse placed fixed after the initialization laser pulse is optional, corresponding to the measured time needed for the $m_\text{s} = -1$ spin sublevel to decay into the thermally mixed state (usually used as a reference to enhance the signal-to-noise ratio). The resulting decay of the spin population with increasing delay time is exemplified in the lower part of the figure. The blue line corresponds to the fit using equation 1.5.

variable delay time. Alternatively, a resonant microwave π-pulse can be applied in between the laser pulses to drive the $m_\mathrm{s} = 0 \to m_\mathrm{s} = -1$ transition, thus representing the readout of the spin population of the ground state $m_\mathrm{s} = -1$ sublevel. This is generally utilized for an enhanced signal-to-noise ratio, where the subtraction between these two measurements results in the rejection of common noise sources [123]. The population decay resulting from such a measurement is exemplified in the lower part of figure 1.8. Such a curve is fitted using an exponential decay in the form of [123, 124]:

$$C(t) = A \cdot \exp\left[-\frac{t}{T_1}\right] + Con, \tag{1.5}$$

where A and Con are fitting constants, t is the delay time between the laser pulses and T_1 is the described spin-lattice relaxation time. The NV center T_1 time is a good indicative of the crystalline lattice quality, since lattice dislocations result in additional phonon excitations and therefore further ways for the stochastic population transfer among the NV center ground state spin levels [126]. In this sense, the measured T_1 times of created NV center are used throughout this Thesis to evaluate the lattice quality of fabricated diamond substrates.

1.3.4. Free induction decay

The rotation of the spin state onto the equator of the Bloch sphere (e.g. the superposition state) by a unitary operation aligns the corresponding spin magnetization perpendicular to the NV center principal axis. In this case, the magnetization amplitude starts to rotate on the xy-plane of the Bloch sphere due to its sensitivity to small magnetic field fluctuations via electron Zeeman interactions. This is analogous to a phase accumulation[9] of the $|1\rangle$ spin state component relative to $|0\rangle$ represented by a phase angle φ, that is:

$$|\psi\rangle = \frac{1}{\sqrt{2}}\left(|0\rangle + |1\rangle\right) \to |\psi\rangle' = \frac{1}{\sqrt{2}}\left(|0\rangle + \mathrm{e}^{i\varphi}|1\rangle\right). \tag{1.6}$$

In the case of the NV center, the accumulated phase corresponds to time-varying fluctuations of the local magnetic field due to the dynamics of the surrounding spin bath. The accumulated phase depends however not only on the strength of

---

[9]The NV center ground state $m_\mathrm{s} = 0$ spin sublevel is not sensitive to electron Zeeman interaction.

the time-dependent magnetic field ($B(t)$), but also on the time (t) that the spin remains at the superposition state:

$$\varphi(t) = 2\pi\gamma_{\mathrm{e}} \int_0^t B(t)dt. \tag{1.7}$$
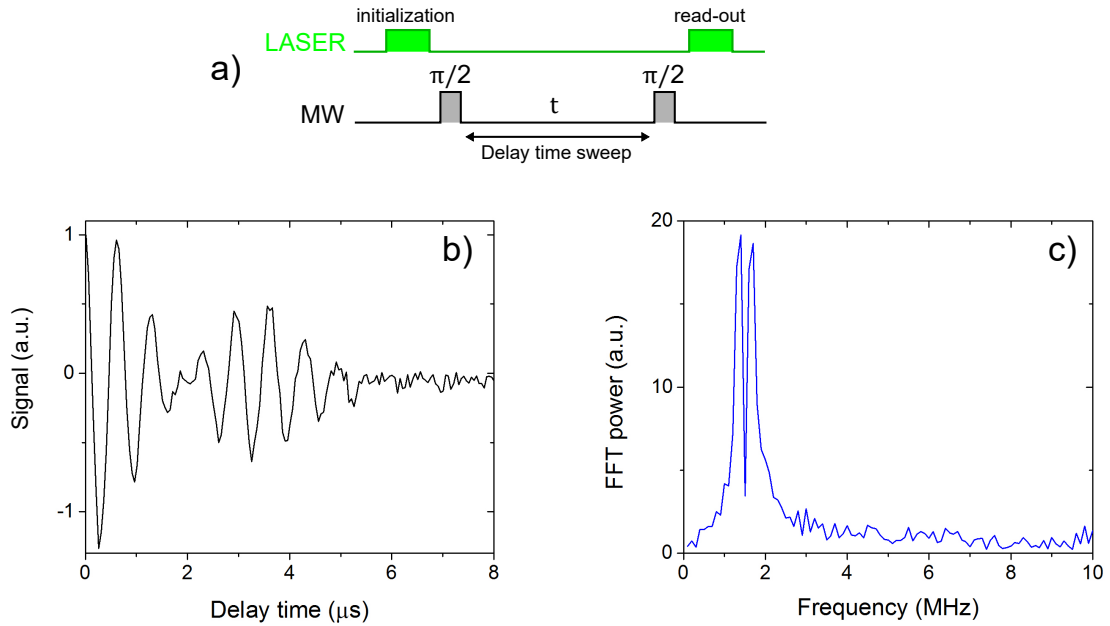
One can further subdivide the accumulated phase within two regimes. The first corresponds to $B(t)$ components that have constant strength and orientation over time (DC regime). This results into a uniform phase accumulation at every measurement cycle (e.g. coherent oscillations). The second corresponds to $B(t)$ components that fluctuate over time (AC regime). This results into an overall different net phase accumulation at each measurement cycle, generally resulting into a dephasing of the time-averaged measured magnetization. In the Bloch sphere representation, this would result into a reduction of the length of the spin vector. The time scale that defines such a decay is the spin dephasing (T_2^*) time.

The Ramsey, or free induction decay (FID) measurement sequence is presented in figure 1.9 a) [127]. Initially, the NV center spin is optically polarized into the ground state $m_{\mathrm{s}} = 0$ sublevel by the first laser pulse. Subsequently, a resonant microwave $\pi/2$-pulse creates a superposition state that evolves freely for a time t (according to equation 1.6). The evolved spin state is then projected into a measurable population difference by a second resonant microwave $\pi/2$-pulse (that is, projection onto the z-axis of the Bloch sphere) and optically readout[10], as previously explained.

Figure 1.9 b) exemplifies the resulting decay observed in an FID measurement, performed on a single NV center with an intrinsic ^{15}N nuclear spin. The coupling of the NV center electron spin to the nitrogen nuclear spin results into the observed beatings. Additionally, a decay of the overall signal contrast is observed due to the stochastic phase accumulation at each measurement cycle. The fast Fourier transform (FFT) of the signal clearly reveals the expected frequencies of the spin-spin hyperfine interaction with the nitrogen nuclear spin (Figure 1.9 c). The observed FID decay can be fitted using [128]:

---

[10]Two individual sequences are utilized to address the full polarization contrast at the spin readout process. One ends with a $\pi/2$-pulse, resulting in the rotation of the spin vector towards the south pole of the Bloch sphere ($|1\rangle$). The other ends with a $3\pi/2$-pulse, resulting in the rotation of the spin vector towards the north pole of the Bloch sphere ($|0\rangle$). The subtraction of these measurements results in a signal contrast ultimately limited by the ODMR contrast. In the presented results, such a measurement protocol (or simple adaptations of it) is adopted for all pulsed schemes with multiple microwave pulses.

Figure 1.9.: Free induction decay of a single NV center. a) The FID measurement
sequence is presented. Two laser pulses are used for the initialization and readout
of the spin state. In between, two microwave $\pi/2$-pulses are applied with a delay
time in between that is varied in order to represent different net accumulated
phases. **b)** The resulting FID decay of the spin population with increasing inter-
pulse delay time is exemplified for an NV center with an intrinsic ^{15}N nuclear spin.
The phase accumulation presents beatings due to the nitrogen nuclear spin and
a general exponential decay that characterizes the spin dephasing (T_2^*) time. For
this measurement, a magnetic field of $32\,$mT is applied along the NV center axis.
c) The fast Fourier transform (FFT) of the FID decay reveals the two frequencies
corresponding to the hyperfine coupling of the NV center electron spin to the
intrinsic ^{15}N nuclear spin. Figure adapted from Ref. [128].

$$C(t) = \exp\left(-\frac{t}{T_2^*}\right) \cdot \left[\sum_i A_i \cos\left(2\pi v_i t + \varphi_i\right)\right] + Con. \qquad (1.8)$$

Here, the exponential component represents the overall decay of the measured
fluorescence contrast and the sum term represents all possible spin-spin hyperfine
interaction components (i), with amplitude A_i, frequency v_i and phase φ_i (Con is
a fitting constant).

As previously mentioned, the T_2^* time is limited by the effective dipolar inter-
actions between the NV center and the surrounding spin bath. For instance, NV
centers hosted in ultra-pure diamond substrates with natural abundance of ^{13}C nu-
clear spins are limited with T_2^* times ranging a few microseconds [88]. Moreover,

diamond substrates with an abundance of P1 centers can lead to an additional spin dephasing and oscillation (beatings) components [127, 129]. The FID measurement scheme is very efficient for the detection of magnetic fields in the DC regime [20]. In the case of an AC magnetic field with a constant frequency, the accumulated phase during the free evolution time is in average zero due to the periodic change in its signal.

1.3.5. Spin coherence time

Alternatively to the FID, spin echo-based measurement schemes can be employed to similarly monitor the dephasing of the NV center electron spin state coupled to nearby spins, while simultaneously rejecting magnetic noise components of the environment within certain frequency regimes due to the phase refocusing of the echo. In this case, the characteristic time that defines the spin dephasing within this detection frame is known as spin-spin relaxation, or spin coherence (T_2) time.
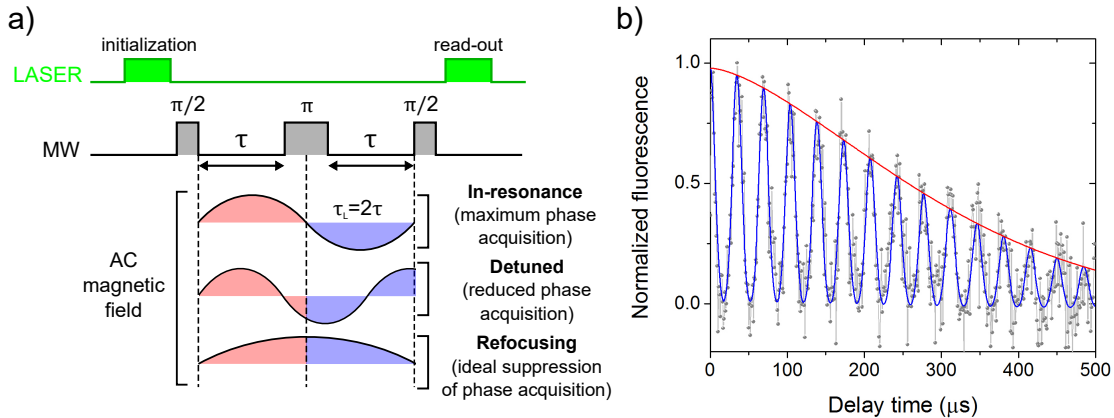
Its measurement is performed using the Hahn-echo sequence[11] [130], which is essentially an FID sequence with an additional π-pulse positioned symmetrically between the two $\pi/2$-pulses (see figure 1.10 a). During the first free evolution time, the surrounding spin bath causes a local magnetic field at the NV center position that induces the accumulation of a phase. The π-pulse rotates the NV center magnetization 180° along the yz-plane, which results into the inversion of the sign of the accumulated phase during the second free evolution time, that is the refocusing of the net accumulated phase. At the end, the accumulated phase is given by:

$$\varphi(t) = 2\pi\gamma_\mathrm{e} \left[\int_0^\tau B(t)dt - \int_\tau^{2\tau} B(t)dt \right].$$ (1.9)

From this, it becomes clear that the efficiency of phase refocusing depends on the relation between the AC magnetic field oscillation period (τ_L) and the free evolution time (2τ). As depicted in the lower part of figure 1.10 a), such a phase refocusing is very efficient for the cases of a DC and an AC magnetic field with $\tau_\mathrm{L} \gg \tau$. In contrast, this protocol is rather inefficient for higher frequencies of AC fields, which leads to a non-zero net phase accumulation. The Hahn-echo scheme

---

[11]In the case of the NV center, the readout of the spin state is conditioned to the projection of the magnetization onto the z-axis of the Bloch sphere. Hence, an adaptation of the original Hahn-echo sequence is utilized, with the addition of a second $\pi/2$-pulse at the anticipated position (time) of the spin echo formation (before the readout process).

Figure 1.10.: Spin coherence time (Hahn-echo scheme) measurement of a single NV center. a) The Hahn-echo measurement sequence is presented. Two laser pulses are used for the initialization and readout of the spin state. In between, two microwave $\pi/2$-pulses are applied, with an intermediate refocusing π-pulse (symmetric inter-pulse delays τ). Both inter-pulse spacings are varied simultaneously in order to represent different accumulation and/or refocusing of acquired phases. Three different frequency regimes of the AC magnetic field are shown (see text). **b)** The resulting spin coherence decay is exemplified for a single NV center hosted into an ultra-pure diamond substrate (magnetic field of $5.4\,\text{mT}$ is applied along the NV center axis). The measured spin population presents an overall decay, with a characteristic T_2 time. Together with this, collapses and revivals are observed due to the match between the inter-pulse spacing and half of the AC magnetic field oscillation period (τ_L) of weakly-coupled nearby ^{13}C nuclear spins (the schematic in-resonance and refocusing of the AC field for different frequency ranges is represented in the lower part of a). The blue-solid line represents the data fitting using equation 1.10 and the red-solid line represents the fit to a single exponential decay.

thus results into the loss of sensitivity to static and slowly-fluctuating fields, being not well suitable for DC magnetometry applications.

However, the phase refocusing allows the detection of AC magnetic fields with constant frequency (which would be the case of detecting i.e. external nuclear spins in nano-NMR experiments) via electron spin echo envelope modulation (ESEEM) [131]. For example, weakly-coupled nearby ^{13}C nuclear spins in the diamond lattice induce a magnetic field at the position of the NV center that oscillates with a frequency equal to their Larmor precession frequency. The spectroscopy of the NV center spin environment by ESEEM is performed by sweeping both inter-pulse delays simultaneously and recording the NV center fluorescence response, as previously described. Importantly, such a spectroscopy technique (using a variety of pulse sequences - see Appendix G) can also be used to detect other nuclear spin species located in the nanometer vicinity of the shallow NV center sensor, such as

protons on the diamond surface [27, 28].

When the inter-pulse spacing in the Hahn-echo sequence matches half of the oscillation period of the ^{13}C-induced magnetic field, the accumulated phase is maximized (*in-resonance* label in figure 1.10 a). This results into the rapid collapse of the NV center spin coherence, as observed in the measured coherence decay in figure 1.10 b). This collapse is rapidly followed by a revival of the spin coherence signal for increasing τ, since the accumulated net phase is reduced due to the refocusing process (*detuned* and *refocusing* labels in figure 1.10 a). Such a process is repeated for any subsequent delay time that obey $2\tau = N\tau_{\mathrm{L}}$, with $N = 1, 3, 5....$ Furthermore, the overall spin coherence signal contrast decays depending upon the corresponding T_2 time of the NV center (represented by the solid-red line in figure 1.10 b).

The observed decay can be fitted using (adapted from Ref. [23]):

$$C(t) = A \cdot \exp\left[-\left(\frac{t}{T_2}\right)^n\right] \sum_{i=0}^{N_{\mathrm{R}}} \exp\left[-\left(\frac{t - i\tau_r}{2\tau_c}\right)^2\right] + Con, \qquad (1.10)$$

where the first exponential term represents the main decay envelope, with the corresponding T_2 time, and the sum term represents the ESEEM modulation signal due to weakly-coupled ^{13}C nuclear spins in the diamond lattice (A and Con are fitting constants). Here, N_{R} is the observed number of revivals, τ_r is the corresponding revival periodicity, and τ_c is the fast initial decay related to the ESEEM modulation. The value of the exponent n depends on the nature of the dominant spin bath, assuming values of $1 \leqslant n \leqslant 3$ [23]. A slowly fluctuating nuclear spin bath leads to $n = 3$ (e.g. slow dephasing), whereas a rapidly fluctuating bath such as electron spins leads to $n = 1$ (e.g. fast dephasing).

The nature of the spin bath also has a major influence on the corresponding NV center T_2 time. For instance, NV centers hosted in ultra-pure diamond substrates with natural abundance of the ^{13}C isotope have fundamentally-limited T_2 times ranging $< 600\,\mu\text{s}$ due to spin-spin hyperfine interactions, showing a strong dependency on the ^{13}C concentration [88]. On the other hand, the depletion of the ^{13}C concentration to values of less than 0.3% leads to T_2 times ranging $\sim$ ms [20]. The influence of the spin bath on the spin properties of NV center becomes much more pronounced in the near surface region. Magnetic and electric field noise from the diamond surface deplete the T_2 times of nearby NV centers to the $\sim \mu\text{s}$ range, even in isotopically-purified materials [23]. As pointed in equation 1.3, however, long coherence times are highly desired in AC magnetometry applications using near-surface NV centers. Overcoming such a limitation is at the heart of this Thesis,

which is primarily focused on the development of experimental methods to deliver a reasonable device architecture based on NV centers with augmented quantum properties. The measured T_2 times are therefore utilized throughout the following Chapters as figure-of-merit values to evaluate the potential implementation of created NV centers in quantum sensing applications.

1.4. The diamond surface

The diamond surface plays an important role in the optical and spin properties of near-surface NV centers. There are mainly three aspects related to the diamond surface that influence these properties, namely i. the surface chemistry and physical structure, ii. the presence of sub-surface dislocation and defects due to e.g. polishing and plasma etching, and iii. magnetic and electric field noise from the surface spin bath. In this section, these aspects of the diamond surface are briefly described. All described aspects consider a diamond surface oriented along the [100] direction, the same as used in the presented experiments throughout the following Chapters.

1.4.1. Structure

In general, surface of solid materials are presented in several different configurations in order to minimize the surface energy, known as the material surface reconstruction. In this case, the surface reconstruction is heavily influenced by the chemical composition of the top material layers, as well as by any imperfections (i.e. dislocations) of the material lattice. In the case of diamond, an unreconstructed surface presents an atomic layer of carbon atoms, each having two dangling bonds. Since these unpaired electrons are highly unstable, an ideal carbon-terminated surface reconstructs by the formation of C=C π-bonds. Such a scenario is however unfeasible in practice due to the growth environment of diamond crystals.

As previously explained, diamond crystals grown by CVD technique using a plasma gas-mixture of CH_4 and H_2 are hydrogen-terminated [132]. The hydrogen termination reconstruction occurs mainly by the substitution of a π-bond to one C-H bond [45], resulting in an efficient covering of the diamond surface by hydrogen. In the case of a diamond surface exposed to air (or any oxidizing environment), an oxygen termination process takes place. Differently than hydrogen, carbon and oxygen atoms can bind and form different surface chemical compositions. Among

others, the most common are the formation of ketone (C=O), ether (C-O-C) and hydroxyl (C-OH) groups [133].
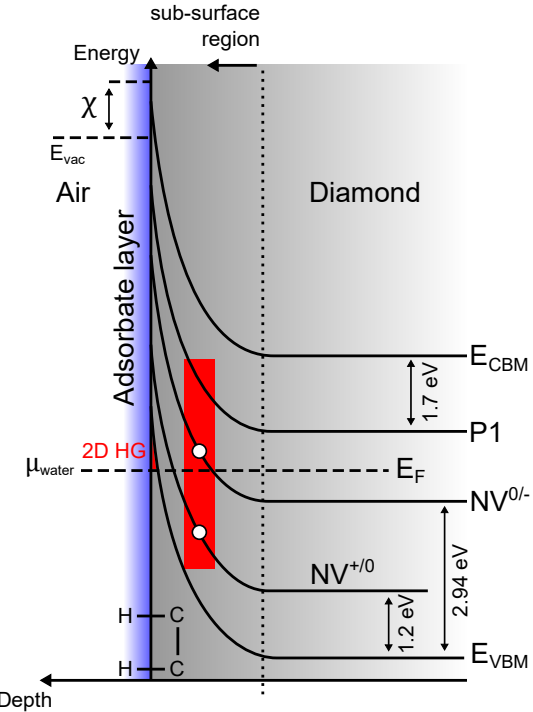
So far, these reconstruction paths assume a pristine sp^3 diamond structure. Different treatments such as ion implantation, high-temperature annealing and plasma etching may result into the formation of local sub-surface lattice defects, thus altering the surface reconstruction and even inducing material phase-transitions such as diamond graphitization.

1.4.2. Electronic band structure and termination

The chemical composition of the diamond surface governs the electronic band structure and band bending of the material within its sub-surface layers. Moreover, the surface reconstruction defines the surface dipole configuration, which determines the electron negativity of the material surface. Such a property is important since it defines if the reconstructed surface will behave as an insulator or as a conductor [134]. In the case of a hydrogen-terminated diamond surface, hydrogen atoms are less electronegative than carbon atoms. As seen in figure 1.11, individual C-H bonds create a band bending effect at the diamond surface due to the induced C-H dipole moments pointing towards the inside of the material, with the aid of a redox reaction between terminating hydrogen atoms and an adsorbed layer of i.e. water molecules [134]. Consequently, the Fermi level is pinned 50 meV below the valence band maximum (VBM), generating a hole accumulation layer in the valence band due to out-diffusion of electrons from the material [134]. Such a termination gives the diamond surface a negative electron affinity ($\chi \approx 1$ eV), thus leading to a *p*-type conductive diamond surface that can be used, for example, to actively control the charge state of NV centers [101, 102].

This is further evidenced in figure 1.11, where the charge transition levels of the NV center are also presented. This represents the capture or release of an electron by the NV center upon the level crossing with the Fermi level. The NV center charge transition levels NV$^{+/0}$ and NV$^{0/-}$ lie at 1.2 eV and 2.94 eV above the VBM, respectively. As approaching the hydrogen-terminated surface, the valence and conduction bands shift towards higher energy values, eventually leaving the Fermi level below the acceptor level of the negatively-charged NV center. If located in the nanometer vicinity of a hydrogen-terminated surface, NV centers are thus predominantly in the neutral or even positive charge states.

In contrast to this, oxygen atoms are more electronegative than carbon atoms, which generates a surface dipole pointing towards the outside of the material. The

Figure 1.11.: Band bending structure of a hydrogen-terminated diamond surface and the NV center charge transition levels. A schematic representation of the band bending structure of a hydrogen-terminated diamond surface is shown. Here, E_{vac} is the vacuum level, χ is the corresponding negative electron affinity. E_{VBM}, E_{CBM} and E_F are the valence band maximum, conduction band minimum and Fermi level, respectively. The chemical potential of the layer of adsorbates is given by μ_{water}. The formed 2D hole gas at the diamond surface responsible for the conductivity characteristic of the material is represented by the 2D HG. The charge transition levels including the different possible NV center charge states and the P1 center donor level are also shown. The white dots and the red highlighted region represent typical depths of near-surface NV centers. Figure adapted from Ref. [135].

different arrangements of carbon-oxygen bonds prevent the band bending in the close vicinity of the diamond surface and can result into a positive electron affinity of the diamond surface with a value that depends on the oxygen surface coverage. Negatively-charged NV centers in the nanometer vicinity of an oxygen-terminated diamond surface are therefore stable, as experimentally evidenced in several studies [124, 136].

2. Creation methods of NV centers in diamond

The rise of quantum technologies based on solid-state spin defects has highlighted diamond as one of the most promising host materials. As previously explored in section 1.1, great research efforts have been directed recently to the controlled growth of diamond, resulting in high-quality ultra-pure synthetic crystals. These advances have led to the observation of color centers in synthetic materials with optical and spin properties comparable to those from natural materials. Among other color centers, the NV center in diamond is a prime candidate for solid-state spin defect-based technologies, with successful demonstrations in a wide variety of research fields ranging from quantum information processing to quantum sensing.

Each particular quantum application presents unique constrains to the corresponding engineering technique of color centers. It is therefore difficult to establish a universal method that can be used to create e.g. NV centers upon the demands of all applications. Since all color centers are by definition impurities in the crystal lattice, the controlled engineering of NV centers matching specific requirements is a challenging experimental task. In most applications, an efficient architecture demands the positioning of NV centers with nanometer accuracy and high efficiency, while still retaining excellent spin and optical properties. The basic building blocks to create NV centers are evidently single vacancies and nitrogen impurities in the diamond lattice. Depending on the utilized method to create NV centers, the sources of these two components are either intrinsic to the crystal (i.e. incorporated during growth) or targeted-introduced in the lattice (by e.g. ion implantation).

The main employed methods to create NV centers in diamond are discussed in this Chapter. At first, the electron irradiation of diamond is presented. The results are further used to discuss optimized conditions for the vacancy diffusion in diamond during thermal annealing. Second, techniques based on the ion implantation method in diamond are presented. Within this category, the nitrogen implantation and ion irradiation techniques are discussed. The conversion efficiency from

nitrogen atoms to NV centers and the resulting properties of NV centers are briefly investigated. At the end, the creation of NV centers during the CVD growth of thin diamond films is discussed.

The results presented in this Chapter related to the ion irradiation and co-implantation techniques are published in F. Fávaro de Oliveira *et al.*, Physica Status Solidi (a) **213**, 8 (2016).
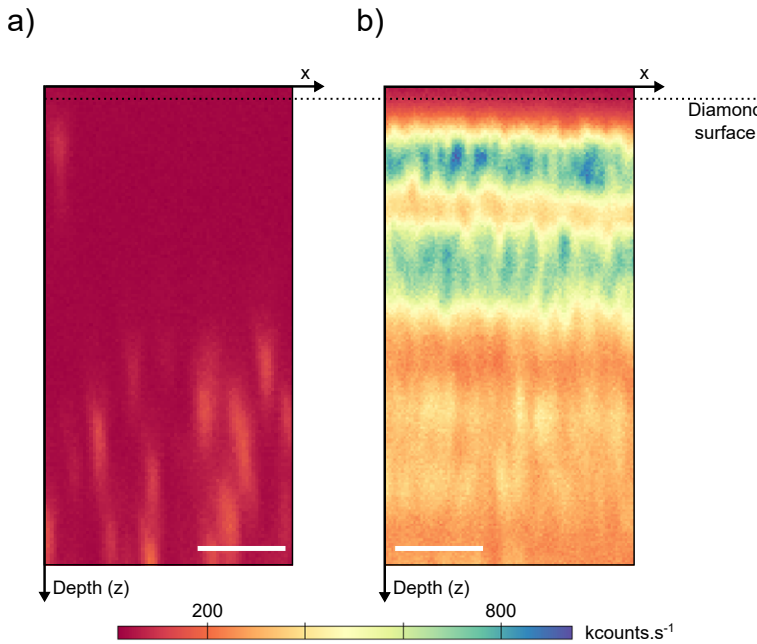
2.1. High-energy electron irradiation technique

The first reports on the creation of NV centers in nitrogen-containing diamond substrates were based on the conversion of intrinsic nitrogen impurities (incorporated during the crystal growth) into NV centers by irradiation-induced damages, followed by thermal annealing [22, 32]. The exposure of diamond to high-energy ($\sim$ MeV) electrons results in the displacement of carbon atoms with sufficient energy to break the carbon covalent bonds [32, 137]. Single vacancies in diamond have an activation energy of $\sim 2.3\,$eV and hence, become mobile in the lattice at temperatures above 600°C [138]. In this sense, a thermal treatment is a critical step due to two main reasons. First, the recombination of single vacancies and interstitial carbon atoms (also known as *Frenkel pairs*) rebuilds the diamond lattice, thus eliminating most of the irradiation-induced damages. Second, mobile vacancies in the diamond lattice can eventually be trapped by nitrogen impurities to finally form stable NV centers.

Due to their low mass, high-energy electrons can only transfer a small amount of energy to lattice carbon atoms. Comparatively, electron irradiation with an energy of 10 MeV creates in average 5 vacancies per electron with a corresponding penetration depth ranging up to $\sim$ 15 mm in diamond [137]. The first experiment presented to investigate this method utilizes two single-crystal [100]-oriented electronic-grade type IIa diamonds synthesized by Element Six [139]. The substrates are ultra-pure with a relatively homogeneous concentration of nitrogen impurities in the low-ppb range. Vacancies are created via electron irradiation with 10 MeV of energy and fluences of $10^{11}\,$cm^{-2} and $10^{16}\,$cm^{-2} for each substrate[1]. Afterwards, the diamond substrates are annealed at a temperature of 1000°C under vacuum condition ($< 10^{-6}\,$mbar) for eight hours (optimized annealing parameters will be discussed in the next section). The diamond surface oxidation is per-

---

[1] Collaboration with Dr. Bernd Abel, Leibniz-Institutes für Oberflächenmodifizierung e.V. (IOM) in Leipzig.

Figure 2.1.: Confocal microscopy depth-images of electron-irradiated diamonds. The resulting density of NV centers after electron irradiation with 10 MeV of energy followed by thermal annealing are shown in the confocal microscopy depth-images. The diamonds shown in a) and b) are irradiated with electron fluences of $10^{11}\,\text{cm}^{-2}$ and $10^{16}\,\text{cm}^{-2}$, respectively. The horizontal dashed line represents the position of the diamond surface. Scale bars show 3 µm.

formed by immersing the substrate in a mixture of sulfuric, nitric and perchloric acids (H_2SO_4:HNO_3:$HClO_4$, respectively) with a 1:1:1 ratio, at the corresponding boiling temperature for two hours. Such a method is hereinafter referred to as *wet chemical oxidation* (WCO) [49, 140].

Figures 2.1 a) and b) show the confocal microscopy depth-images of the two substrates irradiated with fluences of $10^{11}\,\text{cm}^{-2}$ and $10^{16}\,\text{cm}^{-2}$, respectively. As seen, NV centers are created in both diamonds, even tough the concentration of nitrogen impurities is low. A high conversion efficiency from nitrogen impurities to NV centers of approximately 50% is estimated from the density of NV centers in figure 2.1 b) (see Appendix E). Variations observed in the density of NV centers at different depths are attributed to a non-homogeneous incorporation of nitrogen atoms during the diamond growth process.

Irradiation with high electron fluences ($> 10^{16}\,\text{cm}^{-2}$) results in relatively homogeneous distributions of vacancies through the entire diamond crystal. Since individual electrons create only a few vacancies along their entire path, the dam-

age to the diamond lattice is minimized and NV centers are created in a relatively defect-free environment. Wide-field microscopy measurements[2] are used to address the spin properties of the NV centers in the diamond irradiated with the higher electron fluence (figure 2.1 b). An external magnetic field of $\sim 10\,\text{mT}$ is aligned to one of the possible orientations of NV centers. Spin coherence times are measured using the Hahn-echo scheme discussed in section 1.3.

Despite the high density of NV centers, T_2 times ranging $0.5\,\text{ms}$ are measured at different depth-regions of the investigated diamond. Accordingly, the performed measurements indicate that NV centers created by this technique have properties comparable to natural NV centers. The evident drawback of this method is the impossibility to control the spatial position of the created NV centers. Since vacancies are distributed through the entire depth penetration of electrons, the creation of NV centers occurs randomly within the whole irradiated volume.

2.1.1. Vacancy-related defects: optimized conditions for thermal annealing

The annealing time and temperature must be chosen carefully to optimize the treatment towards the highest formation efficiency of NV centers in diamond. Several investigations have utilized optical absorption and electron paramagnetic resonance (EPR) techniques to investigate the behavior of vacancy-related defects in irradiated diamonds subjected to high temperatures [78, 89]. As previously mentioned, diamond substrates that contain an abundance of single vacancies show the GR1 optical band with a ZPL at $\sim 1.673\,\text{eV}$ [79]. It has been demonstrated that thermal annealing at $\sim 400°\text{C}$ results in the rapid recombination of Frenkel pairs, which translates into a typical reduction of 20% in the GR1 optical signal [78]. As mentioned, the diffusion of vacancies in diamond starts to occur at temperatures higher than $600°\text{C}$. Within this temperature, the formation of NV centers and the elimination of irradiation-induced damages are extremely slow [89].

As discussed in Ref. [89], annealing at temperatures higher than $800°\text{C}$ for two hours leads to the complete disappearance of the GR1 optical signal and an efficient activation of NV centers. Importantly, substitutional nitrogen atoms in the diamond lattice are immobile in this temperature range [142, 143]. Within this temperature range, however, small vacancy chains are formed competitively to NV centers in the diamond lattice. For higher annealing temperatures ($>$ $1100°\text{C}$), the formation of higher-order vacancy complexes such as vacancy rings

---

[2]Courtesy of Florestan Ziem. Measurements performed similarly as in Ref. [141].

occurs with much higher probability [89]. Based on this, the utilized optimum annealing parameters throughout the presented experiments are exposure times longer than two hours, under high-vacuum condition and at temperatures ranging $900 - 1000°$C.

2.2. Ion implantation
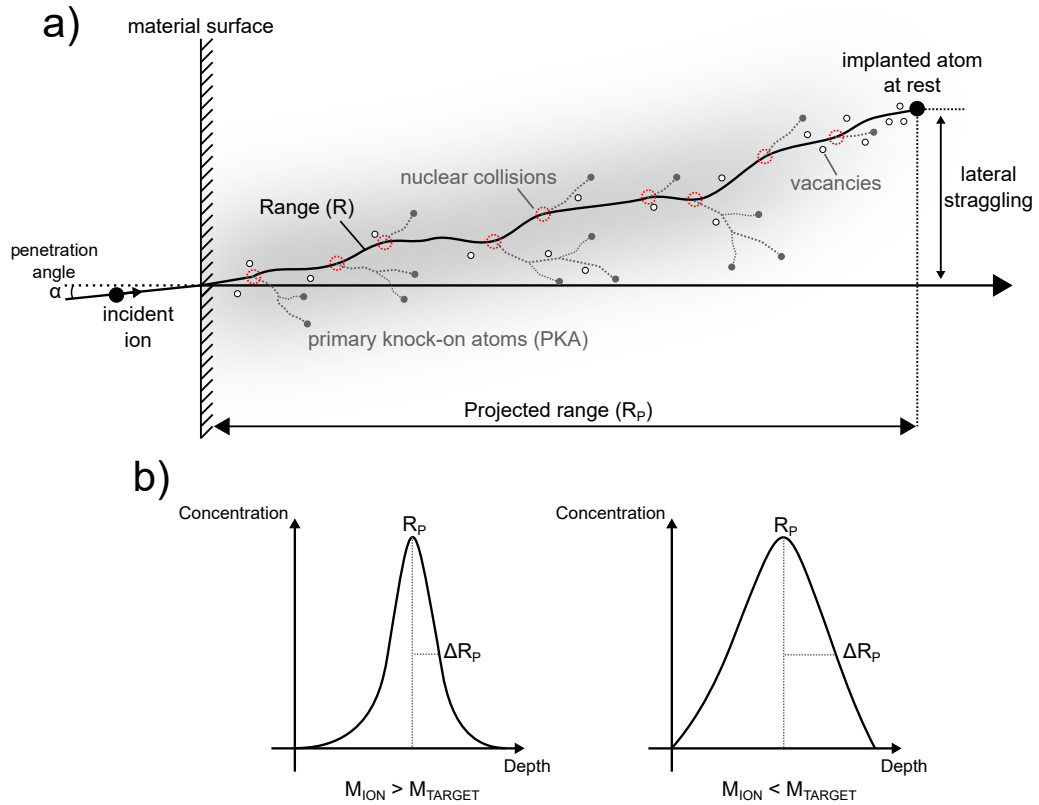
Several material properties such as optical absorption and conductivity can be modified by the intentional introduction of atomic impurities in a pure material. The use of high-energy ($>$ keV) ion beams enables the introduction of a wide variety of atoms independently of host material-implanted atom thermodynamic equilibrium factors [144]. Driven by the importance of shallow junctions in modern electronics, major efforts have been directed towards predicting the depth distribution and corresponding changes in a wide-range of material properties by the introduction of impurities.

2.2.1. Basic concepts

An ion penetrating a solid (target) gradually loses kinetic energy by undergoing through several collision events with the nuclei and electrons of the target lattice atoms. The mean traveled distance between collision events and the amount of energy lost per collision depend on e.g. the incident ion beam energy, the masses of implanted and target atoms, and the crystallographic structure of the target material [144]. The energy loss mechanism of implanted ions can be further classified into two categories: nuclear and electronic.

Nuclear collision events between the incident ion and target nuclei are characterized by large discrete amounts of energy loss, wherewith a significant angular deflection in the original trajectory of the implanted ion is observed. Moreover, nuclear collisions lead to lattice disorders around the ion path such as vacancies and interstitial atoms. This energy loss mechanism is predominant for the cases of ion implantation with relatively low energy (< 10 keV) and high atomic mass of the incident ion relative to the target atoms [144].

Collision events between the incident ion and the electronic cloud of target atoms are characterized by much smaller energy losses, with which a minimum deflection is observed in the original trajectory of the implanted ion. Furthermore, the lattice

Figure 2.2.: Schematic representation of the features related to a single ion implantation event. a) The resulting path of an implanted ion into a solid target material (with an incident angle α) is schematically shown. Primary knock-on atoms (PKA) represented by gray dots are lattice atoms that gain enough energy (through a primary collision with the incident ion) to displace further lattice atoms. Created lattice vacancies are represented by white dots. Relevant elements of interest are also shown, namely the penetration range (R), the projected range (R_P), and the ion lateral straggling of the implanted atom. **b)** The expected depth distribution of implanted atoms are schematically shown for the cases where the ion mass is larger (left side) and smaller (right side) than the target-atom mass. Figure adapted from Ref. [144].

disorder induced by such electronic collisions is considered to be negligible. This energy loss mechanism is predominant for the case of ion implantation with high energy ($> 100\,\mathrm{keV}$) and low atomic mass of the incident ion relatively to the target atoms [144]. Understanding the energy loss mechanism is therefore of fundamental importance not only to control the depth distribution of implanted atoms, but also to determine the nature and corresponding arrangement of the implantation-induced lattice damages.

Figure 2.2 a) shows a schematic representation of the path of an implanted ion

that undergoes through a series of collision events in a solid material. Nuclear collisions (red-dashed circles) give lattice atoms enough kinetic energy to displace further lattice atoms in a cascade-like effect (see gray small trajectories in figure 2.2 a). These energetic target-atoms are known as *primary knock-on atoms* (PKA) and are also responsible for the generation of lattice disorder [144]. When at rest, the implanted atom has traveled a distance in the target material defined by the *range* (R). Typically, the characterization of the implantation distribution is more accurately described by the *projected range* (R_{P}, the depth penetration of the incident ion) and the *lateral straggling* (planar deviation from the ion-penetration position).

Since collision events are stochastic processes, atoms implanted under the same experimental parameters present a statistically-broadened distribution of R_{P}. Figure 2.2 b) shows schematic representations of the projected range and its reciprocal standard deviation (ΔR_{P}). This value characterizes the uncertainty in the depth of implanted ions, which depends directly on the implantation energy and the ratio between the masses of the implanted and target atoms. As seen, sharper depth distributions are expected for the implantation of heavier atoms due to a larger energy-transfer cross-section [144]. The general form of the stopping depth distribution of implanted atoms corresponds to a Gaussian distribution function in the form of [144]:

$$ C(z) = \frac{\phi_{\mathrm{I}}}{(2\pi)^{1/2}\Delta R_{\mathrm{P}}} \exp\left[-\frac{1}{2}\left(\frac{z - R_{\mathrm{P}}}{\Delta R_{\mathrm{P}}} \right)^2 \right], \tag{2.1} $$

where ϕ_{I} and z are the ion fluence and the depth, respectively. Such a mathematical description is relevant for the utilized method to experimentally-extract the depth of NV centers by step-etching, as discussed in Appendix E.

The consideration of the crystallographic structure of the target material leads to the *ion channeling effect.* Incident ions that penetrate the material aligned to a crystal axis or plane travel a larger distance in the material before loosing energy through a nuclear collision event. In this case, the relative importance of nuclear to electronic energy losses is much smaller. Electronic interactions would hence act as a steering mechanism, keeping the implanted ion within the channeling route (i.e. trajectory along a crystal axis). Consequently, a deeper distribution of channeled ions in comparison to equation 2.1 and a reduced concentration of lattice disorder are expected. Therefore, the disadvantage of ion channeling is the unpredictability in the projected range of implanted atoms. To avoid this effect, an incident implantation angle of $\sim 7°$ can be used [144]. In this way, ions that
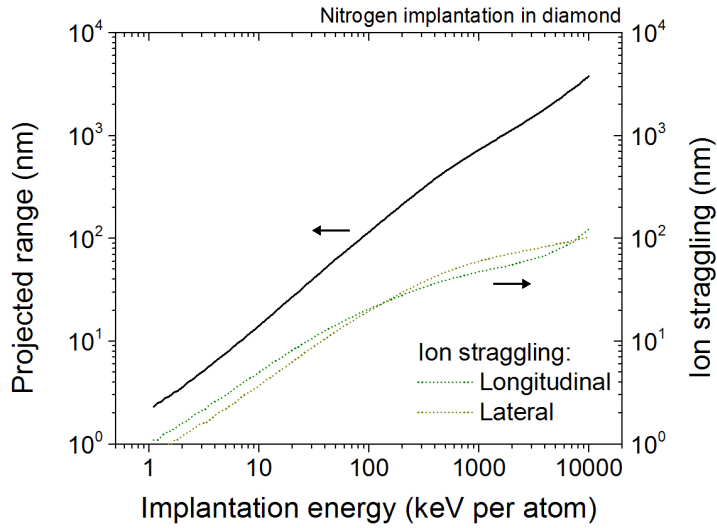
penetrate the material in a channeling route suffer from large trajectory oscillations (due to electronic collisions) and rapidly scatter out of the channel by a nuclear collision event.

Different software can be used to simulate the ion implantation for a variety of ion/target combinations. The Stopping and Range of Ions in Matter (SRIM) [145] makes the use of analytical and Monte Carlo calculations to provide e.g. the depth distributions of implanted atoms and lattice damages. This program considers the ion implantation in an amorphous material and thus does not take the channeling effect into account. A more complete software, the Crystal-TRIM (CTRIM) [146] incorporates the crystallographic structure of the target material into calculations. Consequently, the simulated depth distributions of implanted atoms and lattice damages include the ion channeling effect, thus reproducing a more realistic scenario. For a full analysis at the atomic scale, sophisticated simulation techniques such as Molecular Dynamics (MD) [147] are more appropriated. Since these methods usually consider all interatomic interactions between implanted and target atoms, their implementation is noticeably more complex and requires much more computational power than the previously-mentioned software.

2.2.2. Nitrogen implantation in diamond

Nitrogen implantation in ultra-pure diamond substrates has been widely utilized to create NV centers in a more controllable way [33–35, 148]. Implanted ions provide simultaneously nitrogen impurities and vacancies, which can be converted into NV centers by a subsequent thermal annealing treatment. As discussed in the last section, nitrogen atoms that penetrate the diamond lattice would suffer a series of collisions that deviate them from the original trajectory until they reach a rest position. This intrinsic uncertainty in the projected range of implanted atoms will be consequently imprinted on the position accuracy of the created NV centers.

Figure 2.3 presents a SRIM simulation of the projected range of implanted nitrogen atoms in diamond (R_P, black line) versus the implantation energy. In addition, the longitudinal (green-dotted line) and lateral (yellow-dotted line) ion straggling ranges are also presented. High-energy ($\sim$ MeV) nitrogen implantation in diamond results in a high formation yield of NV centers, reaching values of up to 50% [35, 148]. Moreover, the deep projected range ($\sim$ μm) leads to a broad spatial distribution of lattice defects along the path of implanted nitrogen ions (e.g. reduced local concentrations), which results in NV centers with optical and spin properties comparable to natural ones [89]. However, such high implantation energy results
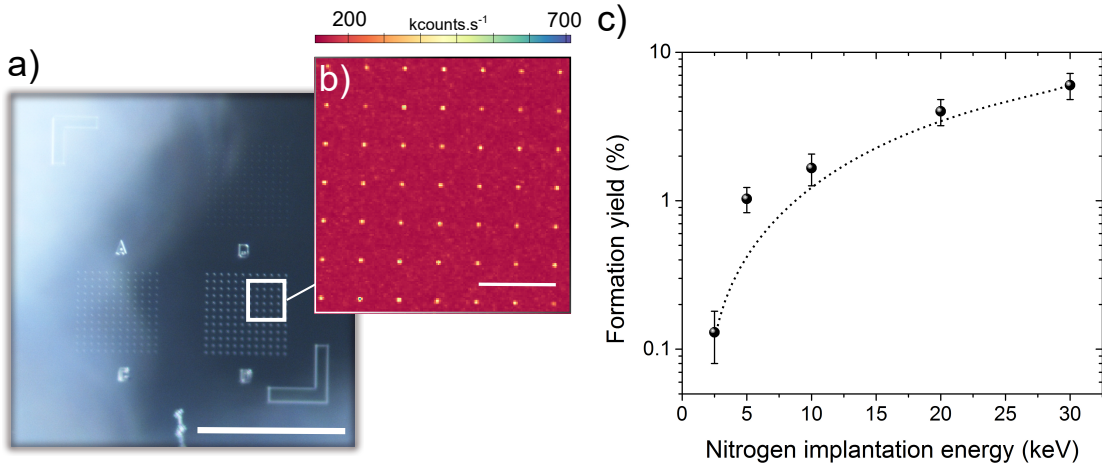
Figure 2.3.: Intrinsic limitation of the spatial accuracy of implanted nitrogen atoms in diamond by SRIM. The projected range (R_P, black line) and the respective ion straggling (longitudinal and lateral respectively represented by the green-dotted and yellow-dotted lines) are shown for different nitrogen implantation energies. The curves are simulated using the SRIM program. Figure adapted from Ref. [35].

in a large spatial positioning uncertainty of created NV centers. As seen in figure 2.3, both longitudinal and transverse ion straggling ranges reach several tenths of nanometers for implantation energies in the $\sim$ MeV range. In this case, the implementation of NV centers in e.g. quantum sensing of external spins is completely restrained.

In the case of lower implantation energies (< 10 keV), the spatial positioning accuracy of nitrogen atoms and ultimately of NV centers is in the range of $5-10$ nm (figure 2.3). Since the presented experiments in this thesis are focused within this energy range, a detailed analysis of the creation of NV centers by this method will be presented. We start by evaluating the formation yield of NV centers using a single-crystal [100]-oriented electronic-grade ultra-pure (nitrogen impurities in the low-ppb range) diamond synthesized by Element Six.

To improve the accuracy of the evaluation, a polymethyl methacrylate (PMMA) mask is patterned on the surface of the diamond by means of electron-beam lithography. First, a 50K 9% diluted PMMA solution is spin-coated on the diamond surface and backed at 160°C for four minutes, resulting in a final film thickness of $\sim$ 300 nm. Then, a 5 nm-thick anti-charging chromium layer is thermally-evaporated on the diamond surface. A Raith E-line machine is used to expose

Figure 2.4.: Investigation of the formation yield of NV centers by low-energy nitrogen implantation. a) Optical microscopy image of the PMMA mask containing apertures with 50 nm (upper arrays) and 100 nm (lower arrays) of diameter. Nitrogen atoms are implanted through these masks in order to calibrate the formation yield of NV centers. The scale bar represents 100 μm. **b)** Confocal microscopy image of the diamond region implanted with nitrogen ions at 2.5 keV of energy and fluence of 10^{13} cm^{-2} through the PMMA mask array with 100 nm apertures. Measurements are performed after the removal of the mask and subsequent thermal annealing. The number of NV centers in each aperture region is estimated either by photoluminescence intensity or second-order auto-correlation measurements ($g^2(\tau)$). The scale bar represents 10 μm. **c)** The calculated formation yield of NV centers via the above-described method is shown versus the nitrogen implantation energy. The dashed line is a guide to the eye.

selected regions of the mask to a focused electron beam with 20 keV of energy and exposure dose of 280 μC.cm^{-2}. The anti-charging layer is chemically removed and the patterns are developed by immersing the structure in a 1 : 3 mixture of methyl isobutyl ketone (MIBK) / isopropyl for two minutes at room temperature.

Figure 2.4 a) shows a dark-field optical microscopy image of the resulting mask. Arrays of apertures with 50 nm (upper) and 100 nm (lower) of diameter are used to limit the diamond surface exposure to the nitrogen ion beam. In this way, a more precise estimation on the number of implanted nitrogen atoms per surface area is obtained. Nitrogen atoms are then implanted in individual regions with 2.5, 5.0 and 10 keV using a home-built focused-ion beam setup (see Appendix A.2). Further implantation events using 20 and 30 keV of energy are performed using another implantor setup with a homogeneous ion beam[3]. For all implantation energies, the used ion fluences range from 10^{11} cm^{-2} up to 10^{13} cm^{-2}. After the nitrogen

---

[3]Collaboration with Dr. M. Schreck, Institut für Physik, Universität Augsburg.

implantation, the PMMA mask is removed using organic solvents and the diamond is annealed at a temperature of 950°C under vacuum condition ($< 10^{-6}$ mbar) for two hours. The diamond surface oxidation is performed by WCO treatment. At the end, created NV centers at individual regions are addressed by confocal microscopy technique, as described in Appendix A.1.

Figure 2.4 b) shows a confocal microscopy image of a region implanted with nitrogen ions at 2.5 keV of energy and fluence of 10^{13} cm^{-2} through the PMMA mask array with 100 nm apertures. As seen, NV centers are well localized within the aperture regions only. The statistical number of NV centers per aperture is obtained by comparing the photoluminescence signal intensity at each spot with the signal intensity of a single NV center created under similar conditions. This analysis is repeated for all implantation energies and ion fluences. For smaller numbers of NV centers within individual aperture regions, second-order auto-correlation measurements ($g^2(\tau)$) are also utilized. The experimentaly-estimated formation yield of NV centers versus the nitrogen implantation energy is shown in figure 2.4 c). First and foremost, the calculated values are in relatively good agreement with literature for all implantation energies [35]. As seen, the formation yield strongly decreases with decreasing implantation energy, especially for implantation energies below 10 keV.

Particularly, nitrogen implantation with 2.5 keV of energy results in a formation yield of $\sim 0.1\%$ for NV centers with expected depths of approximately 5 nm [145]. Furthermore, spin coherence times of created NV centers for all mentioned implantation energies are also measured. Following the observed behavior in the formation yield, the average T_2 times strongly decreases for decreasing implantation energy. In fact, NV centers created by nitrogen implantation with 2.5 keV of energy show T_2 times shorter than 5 µs in average. The nitrogen implantation technique will be revisited and further explored in Chapter 4.

2.2.3. Carbon and helium irradiation of diamond

So far, the two presented creation techniques could not completely fulfill the requirements for the creation of NV centers in a scalable architecture for e.g. quantum sensing applications. On one side, electron irradiation technique is based on the creation of lattice vacancies that efficiently convert nitrogen impurities into NV centers with outstanding properties, but completely lacks the spatial control of NV centers. On the other side, low-energy nitrogen implantation provides simultaneously nitrogen impurities and vacancies with a consequent nanometer-positioning

accuracy, but the method suffers from a low formation yield of NV centers with concomitant degraded properties.
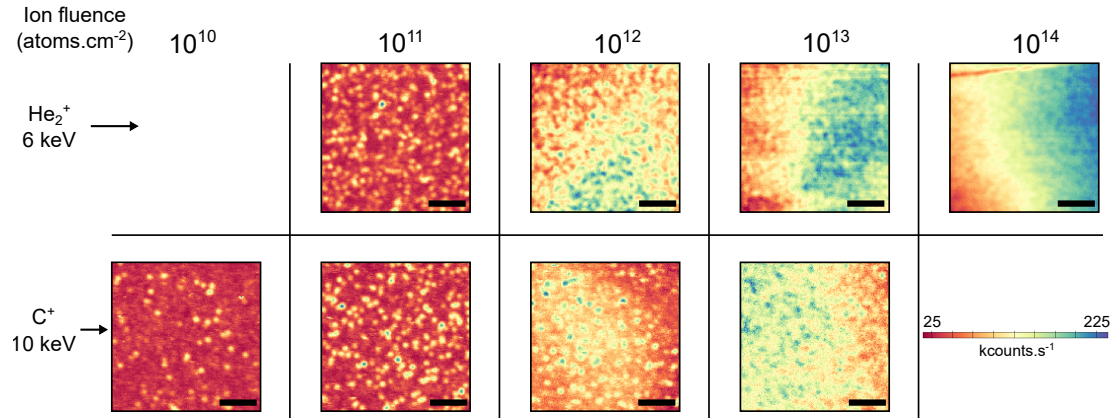
In order to overcome these obstacles, NV centers can be created by inert ion irradiation followed by high-temperature annealing [59–63]. This technique merges the best qualities of the two previously-described creation methods of NV centers. First, similarly as in electron irradiation, the formation of NV centers occurs at remote positions from the damaged region due to the ion impact, which leads to a reduced density of lattice defects in the near vicinity of NV centers. Second, the implantation of inert ions can be performed with similar spatial accuracy as in the case of direct nitrogen implantation. The spatial distribution of NV centers is therefore ultimately limited by the vacancy diffusion around the as-implanted ion tracks.

NV centers created by ion irradiation method are investigated utilizing a single-crystal [100]-oriented electronic-grade diamond synthesized by Element Six. This substrate has a homogeneous doping concentration of nitrogen impurities incorporated during the growth process in the low-ppb range [89]. Molecular helium (He_2^+) and carbon (C^+) ions are chosen for the irradiation of diamond and creation of vacancies. Molecular helium ions[4] are implanted in individual regions of the diamond substrate with 6.0 keV of energy and fluences ranging from 2×10^{11} atoms.cm^{-2} up to 2×10^{14} atoms.cm^{-2}. Carbon ions are implanted in individual regions of the diamond substrate with 10.0 keV of energy and fluences ranging from 10^{10} atoms.cm^{-2} up to 10^{13} atoms.cm^{-2}. All implantation events are performed using the described setup in Appendix A.2. The used energies are chosen in order to match the expected depth distributions of helium and carbon atoms in diamond [145, 146].

It should be highlighted that, according to SRIM simulations, carbon atoms produce in average ten times more vacancies per implanted atom than helium at the given energies. Therefore, the ion fluence ranges are chosen to allow a direct comparison between the two different ion sources (e.g. similar vacancy concentration ranges), whereas the damage threshold for diamond amorphization is not reached [149, 150]. For the diffusion of vacancies and the resulting creation of NV centers, the diamond substrate is then annealed at a temperature of 950°C under vacuum condition ($< 10^{-6}$ mbar) for two hours. Afterwards, the substrate is cleaned and oxygen-terminated by WCO treatment.

---
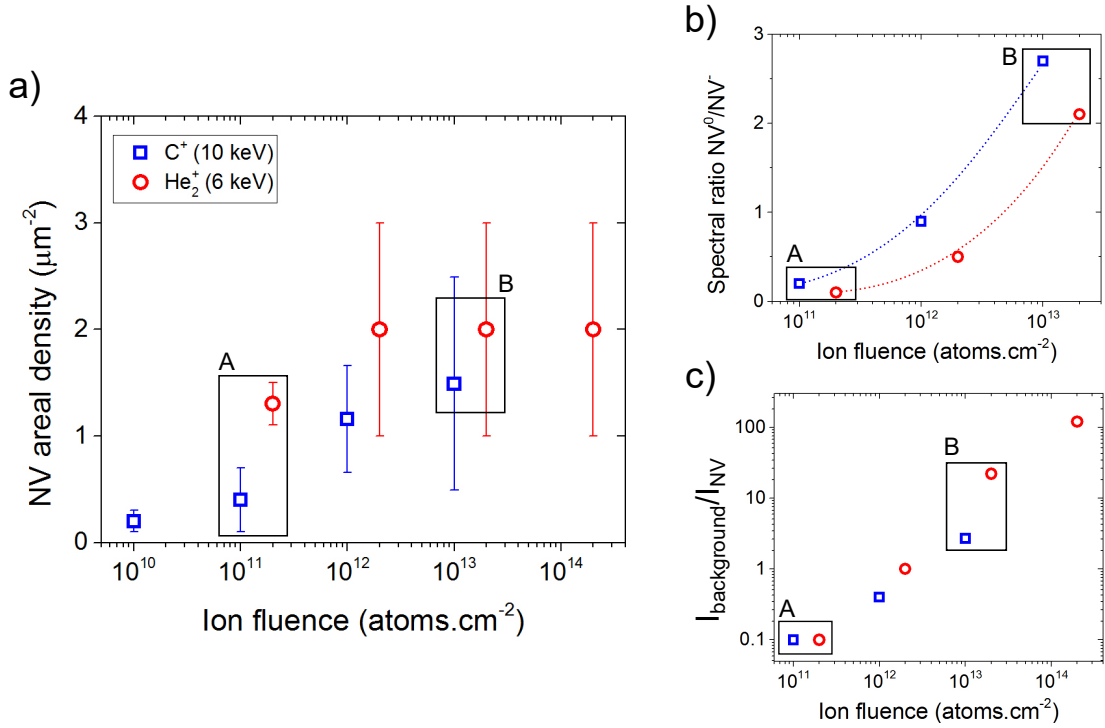
[4]In the presented experiments, molecular helium ions are implanted due to technical limitations of the experimental setup, namely a limited mass selection range by the utilized Wien mass filter (see Appendix A.2). It is however assumed that molecular ion implantation with an energy E is equivalent to single ion implantation with energy $E/2$ of the same atomic species.

Figure 2.5.: Confocal microscopy surface images of helium- and carbon-irradiated regions. Confocal microscopy surface images of individual regions irradiated with molecular helium (He_2^+) and carbon (C^+) ions with 6.0 and 10.0 keV of energy, respectively, are shown. The ion fluences are indicated on the top of the figure. The measurements were performed after thermal annealing and WCO. The scale bars represents 5 µm.

In order to quantify the amount of created NV centers by each implantation event, confocal microscopy surface images are acquired, as illustrated in figure 2.5. For both helium and carbon irradiation events, single NV centers are well-resolved for ion fluences below 10^{12} atoms.cm^{-2}. This allows the direct determination of the areal density of NV centers by counting the number of single emitters within a 20×20 µm^2 surface area. For higher ion fluences, a calibrated laser excitation intensity is utilized as reference, for which the fluorescence of a single NV center is known. The presence of the fluorescence background from parasitic lattice defects originated from the irradiation processes are also taken into account, as explored below.
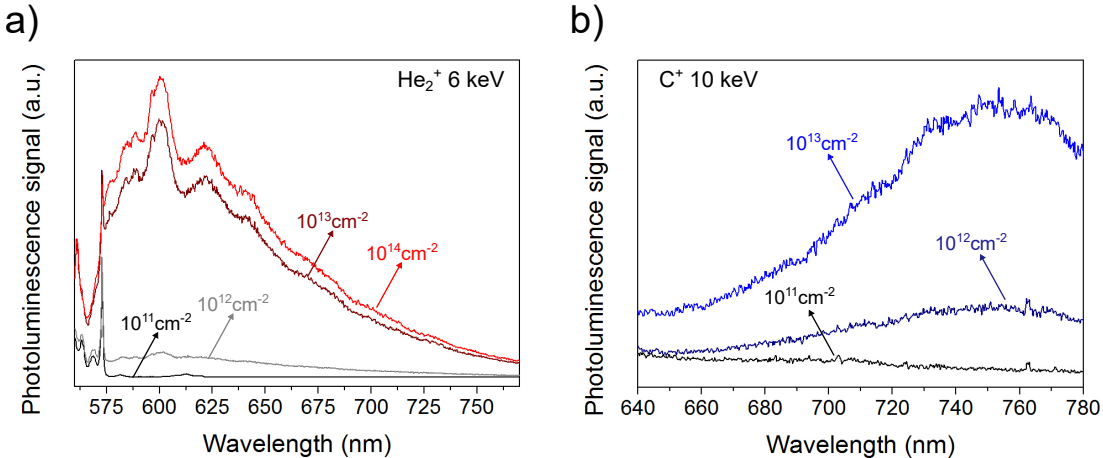
The calculated areal densities of NV centers by both molecular helium and carbon irradiation are shown versus the ion fluence in figure 2.6 a). Although the exact depth distribution of the created NV centers is unknown, the high density of NV centers (~ 2.0 cm^{-2}) achieved in an ultra-pure substrate indicates a relatively high conversion efficiency from nitrogen impurities to NV centers. The number of created vacancies is expected to increase monotonically with the number of irradiated atoms. In contrast to this, the observed areal density of NV centers shows a saturation effect for ion fluences $> 10^{12}$ atoms.cm^{-2} (figure 2.6 a). At the same time, the contribution of the neutral NV center (NV^0) photoluminescence signal also increases with the ion fluence for both helium and carbon irradiation cases, as seen in figure 2.6 b). These values are obtained by fitting reference NV^0 and NV$^-$ spectra to the measured photoluminescence signals by spectroscopy technique (see

Figure 2.6.: Resulting NV centers by helium and carbon irradiation of an ultra-pure type IIa diamond. a) The areal densities of NV centers resulting from molecular helium (He_2^+, red circles) and carbon (C^+, blue squares) irradiation with 6.0 and 10.0 keV of energy, respectively, are shown versus the ion fluence. Vertical error bars represent the standard deviation of the calculated areal density values. Regions marked as A and B represent regimes where the areal density of NV centers increases linearly and is saturated versus the ion fluence value, respectively. **b)** The obtained ratio NV^0/NV^- by photoluminescence spectroscopy technique is shown versus the ion fluence. **c)** The corresponding helium- and carbon-related photoluminescence background intensity normalized by the intensity of a single NV center is shown versus the ion fluence.

Appendix A.1 for technical information). This feature is attributed to the formation of irradiation-induced lattice damages that induce electronic states in the band gap of diamond in the vicinity of NV centers.

The presented confocal microscopy surface images in figure 2.5 also reveal the appearance of a photoluminescence background related to the helium and carbon irradiation with ion fluences $> 10^{12}$ atoms.cm^{-2}. The intensity of the helium- and carbon-related background signals relative to the photoluminescence of a single NV center is shown for different ion fluences in figure 2.6 c). As seen, the helium- and carbon-related background signal increases rapidly with the used ion fluence, setting a practical limit of $\sim 10^{13}$ atoms.cm^{-2} for resolving single NV centers by
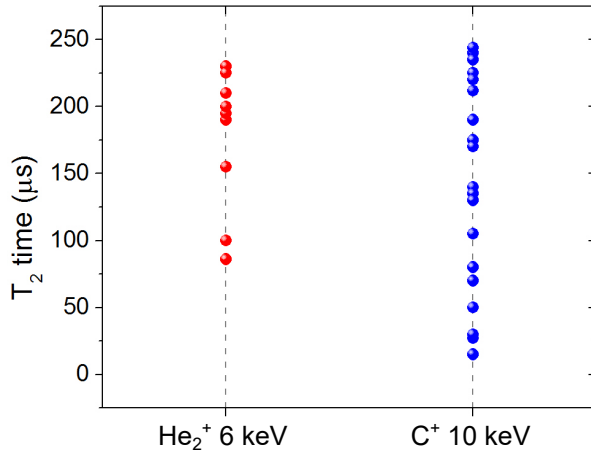
Figure 2.7.: Helium- and carbon-related photoluminescence spectra for different ion fluences. Measured photoluminescence background spectra resulting from helium (**a**) and carbon (**b**) irradiation with 6.0 and 10.0 keV of energy, respectively, are shown for different ion fluences. The real signal intensities are shown in figure 2.6 c).

confocal microscopy technique.

Moreover, photoluminescence spectroscopy technique gives further insights on the parasitic background signals. Figures 2.7 a) and b) show the measured spectra of the helium- and carbon-related backgrounds, respectively, for a wide range of ion fluences. In the case of helium, the spectra show a broad emission centered at approximately 600 nm, with a sharp line at ≈ 560 nm. The intensity of the helium-related background reaches up to hundred times the signal from a single NV center (figure 2.6 c) within the used ion fluence range. This signal is attributed to the formation of helium-vacancy defects in the diamond lattice [79, 151]. It is important to highlight that such helium-related background is only observed after the thermal annealing treatment. Such a behavior is typical for a number of irradiation-induced defects in diamond, which suggests a complex structure of these helium-related lattice defects as well.

In the case of carbon, the spectra show a broad emission centered at approximately 760 nm. The intensity of the carbon-related background only reaches up to three times the signal from a single NV center (figure 2.6 c) within the used ion fluence range due to an inefficient excitation of defects at 532 nm. This signal is typically observed in diamond substrates with a high concentration of vacancy-related defects such as small vacancy chains [79].

As previously mentioned, carbon ions are expected to produce more vacancies

Figure 2.8.: Spin coherence times of created NV centers by molecular helium and carbon irradiation. The histogram presents the measured T_2 times of several created NV centers by helium (red dots) and carbon (blue dots) irradiation with 6.0 and 10.0 keV of energy, respectively. The helium and carbon ion fluences are 10^{11} atoms.cm^{-2}. A magnetic field of 11 mT is aligned along the NV center axis. Error bars are omitted for clarity.

than helium ions for the given energies. However, such a difference is not observed in the corresponding number of created NV centers. In fact, both ion species generate similar densities of NV centers for increasing ion fluence up to the saturation regime, as seen in figure 2.5 and quantitatively analyzed in figure 2.6 a). By having a higher mass, individual carbon ions locally create a higher concentration of vacancies along the implanted ion track. This, in turn, increases the formation probability of vacancy-related defects. Therefore, the activation of alternative paths of vacancy recombination in diamond limits the formation efficiency of NV centers by ion irradiation.
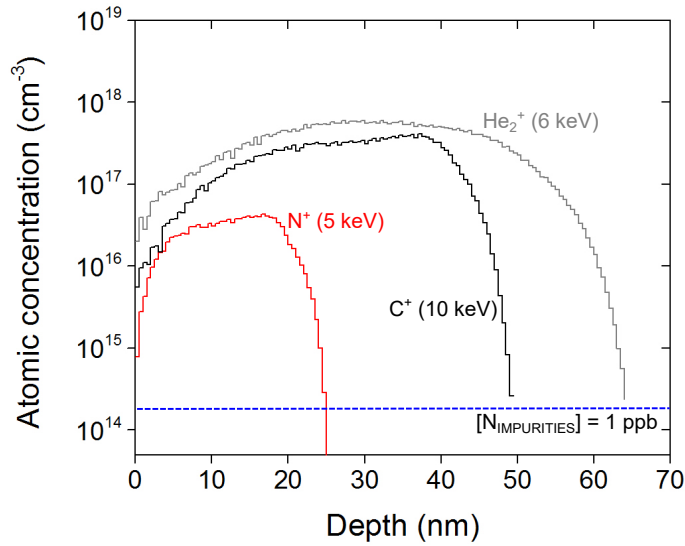
Such a balance in the formation of diverse lattice defects along implanted ion tracks is shown not to be positively affected (towards higher conversion efficiency of NV centers) with thermal annealing at a higher temperature. After submitting the diamond to a further treatment at a temperature of 1100°C under vacuum condition ($< 10^{-6}$ mbar) for two hours, no noticeable change is seen in the density of created NV centers by helium and carbon irradiation. Instead, such thermal treatment leads to a two-fold increase in the measured intensities of the helium- and carbon-related photoluminescence background signals. This suggest an enhanced formation of different vacancy complexes in the diamond lattice concurrent to the creation of NV centers, setting thereby an experimental limitation to the low-energy ion irradiation parameters.

The spin properties of NV centers by both molecular helium and carbon irradiation are also investigated. Figure 2.8 shows the statistic evaluation of T_2 times of several single created NV centers by helium (red dots) and carbon (blue dots) irradiation with 6.0 and 10.0 keV of energy, respectively. Irradiated regions with an ion fluence of 10^{11} atoms.cm^{-2} (for both helium and carbon) are chosen to avoid the helium- and carbon-related photoluminescence background. An external magnetic field of 11 mT is applied along one of the possible orientations of NV centers. As seen, spin coherence times of up to $\sim 250\,\mu s$ are measured for both analyzed ion irradiation cases. Regardless the limitations related to the formation of vacancy complexes along implanted ion tracks, the measured values indicate that NV centers are formed in a relatively defect-free environment. The ion irradiation technique will be revisited and further explored in Chapter 5.

2.3. Effects of ion co-implantation in diamond

The ion irradiation technique has been demonstrated to be suitable for the creation of near-surface NV centers with augmented properties. Since this method relies on the vacancy diffusion process, the resulting positioning accuracy is still insufficient for a scalable architecture of NV centers for magnetometry applications. In this sense, improvements of the nitrogen implantation technique are still of great interest. One alternative is to combine the excellent spatial control of nitrogen implantation to the potentially higher conversion efficiency and augmented properties of NV centers by ion irradiation technique - a technique known as *ion co-implantation* [152, 153].
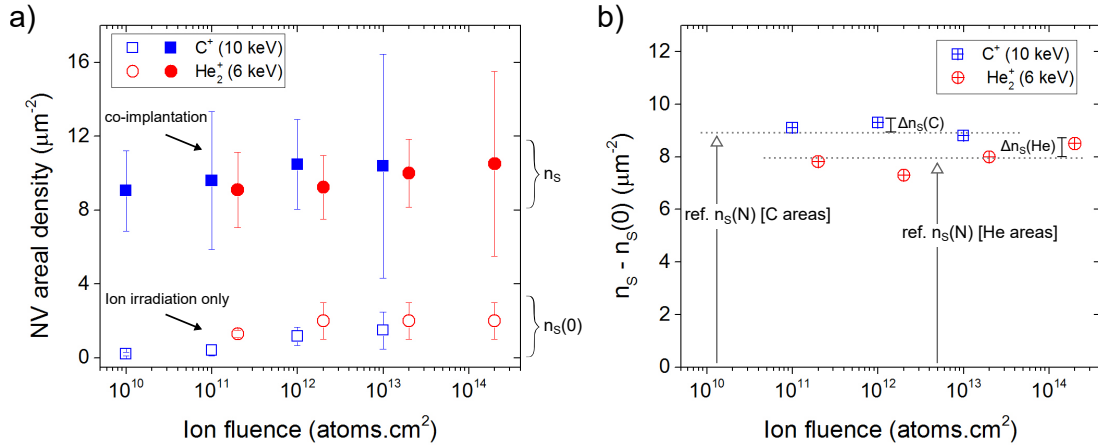
To investigate this method, a single-crystal [100]-oriented electronic-grade diamond synthesized by Element Six is used as substrate. This diamond substrate has similar characteristics as the one described in the last section. For a better accuracy in the combined ion implantation events and after-tracking of targeted regions, plateaus (squares with dimensions of $170 \times 170\,\mu m^2$) are fabricated on the diamond surface. The original diamond surface is covered by lithographically-patterned AZ 5214E photoresist (MicroChemicals, thickness of $\sim 1.2\,\mu m$). The sample is then exposed to Ar/O_2 capacitive RIE plasma using the following parameters: 37.5 mTorr of constant chamber pressure (base pressure of $< 10^{-6}$ mTorr), 100 and 11 sccm of Ar and O_2 gas flow, respectively, 70 W of capacitive RIE power, and 20°C of plate temperature. The exposure time is 18 min, resulting in an etching depth of approximately 200 nm (measured by AFM). The resulting structures can be easily identified in optical and confocal microscopy measurements.

Figure 2.9.: Atomic profiles of nitrogen, helium and carbon atoms by CTRIM for the co-implantation investigation. The depth distributions of nitrogen (red line), helium (gray line) and carbon (black line) atoms are shown for the implantation energies of 5.0 keV, 6.0 keV and 10.0 keV, respectively. The nitrogen, helium and carbon ion fluences are 7×10^{10} atoms.cm^{-2}, 2×10^{12} atoms.cm^{-2} and 10^{12} atoms.cm^{-2}, respectively. The atomic distributions are simulated using the CTRIM software for a [100]-oriented diamond surface and a 3°-off implantation angle. The blue-dashed line corresponds to the intrinsic concentration of nitrogen impurities in the used diamond (~ 1 ppb).

To evaluate the effect of ion co-implantation, individual regions of the diamond surface are first implanted with nitrogen ions with 5.0 keV of energy and fluence of 7×10^{10} atoms.cm^{-2}. Such a fluence has been chosen in order to create mainly individually-resolvable NV centers in confocal microscopy images. Afterwards, specific regions are co-implanted with either helium molecular ions (energy of 6.0 keV and ion fluences in the range of $10^{11} - 10^{14}$ atoms.cm^{-2}) or carbon ions (energy of 10.0 keV and ion fluences in the range of $10^{10} - 10^{13}$ atoms.cm^{-2}). The energies of the co-implanted species are chosen in order to create an overlap between the corresponding additional vacancy distribution profiles and the atomic distribution of the previously-implanted nitrogen atoms, as seen in figure 2.9. The ion fluence ranges are chosen in order to create enough extra vacancies, whereas the damage threshold for diamond amorphization is not reached [149, 150]. The diamond is then annealed at a temperature of 950°C under vacuum condition ($< 10^{-6}$ mbar) for two hours. The substrate is cleaned and oxygen-terminated by WCO treatment.

The resulting densities of NV centers are evaluated by confocal microscopy tech-

Figure 2.10.: Areal density of NV centers for different ion implantation combinations. a) The areal densities of created NV centers by either helium- or carbon-only irradiation ($n_S(0)$ - empty circles and squares, respectively) are compared to the densities in co-implanted areas (n_S - solid circles and squares). **b)** The efficiency of ion co-implantation technique is estimated by subtracting the areal densities of created NV centers by helium- or carbon-only irradiation from the measured values in co-implanted areas. This value is then compared to the areal density of created NV centers by nitrogen implantation (horizontal-dotted lines).

nique, similarly as described in the previous section. Here, the shape of the ion beam must be considered (see also Appendix A.2). For each implantation event, the ion beam (diameter of $\sim 100\,\mu m$) is aligned to the center of a fabricated plateau. The position of the sample with respect to the ion beam can be adjusted with micrometer-precision using motorized stages. However, the relative position of the focus (maximum) from each ion beam of different species varies slightly ($\sim 20\,\mu m$).

To avoid any data misinterpretation, this is considered in the presented experiment by first finding the maximum of the co-implantation beams with respect to the plateaus edges (alignment markers). The initial areal density of created NV centers by nitrogen implantation only ($n_S(N)$) is then corrected taking the corresponding value at the maximum position of the co-implantation beam. This method allows the correct derivation of the local areal density of NV centers in all co-implanted regions.

The corresponding results of this analysis are shown in figure 2.10. In addition, the measured areal densities of NV centers for each implantation event are summarized in table 2.1. The real effects of ion co-implantation with helium and carbon ions are depicted in figure 2.10 b) as $\Delta n_S(He)$ and $\Delta n_S(C)$, respectively. These values are estimated by first subtracting the density of NV centers related to

Table 2.1.: Summary of the areal density of NV centers for different events of ion implantation.

Density of NV centers (μm^{-2})				
Co-implantation ion species	co-implantation ion fluence (cm^{-2})	Nitrogen implantation only	Helium/Carbon only	Co-implantation
He_2^+ 6 keV	10^{11}	8 ± 2	1.3 ± 0.2	9.1 ± 2.0
	10^{12}	8 ± 2	2.0 ± 1.0	9.2 ± 1.7
	10^{13}	8 ± 2	2.0 ± 1.5	10.5 ± 1.8
C^+ 10 keV	10^{11}	9.1 ± 2.1	0.4 ± 0.2	9.6 ± 3.7
	10^{12}	9.1 ± 2.1	1.2 ± 0.5	10.5 ± 2.4
	10^{13}	9.1 ± 2.1	1.5 ± 1.0	10.4 ± 6.0

helium- and carbon-only irradiation events ($n_S(0)$ in figure 2.10 a) from the measured values in co-implanted regions (n_S in figure 2.10 a). Then, the subtracted values are compared to the density of created NV centers by nitrogen implantation with the applied beam-focus correction, as previously described ($n_S(N)$ values in figure 2.10 b).

Despite the uncertainties in the measured densities of NV centers, it is clear that the additional number of NV centers created by co-implantation remains minimal. The co-implantation-induced densities of NV centers show values of up to $\sim 0.4\,\mu m^{-2}$ and are relatively independent on the used co-implanted ion species. In the case of helium and carbon co-implantation events with ion fluences $> 10^{12}$ atoms.cm^{-2}, an increasing photoluminescence background signal is again observed in confocal microscopy images, similarly as discussed in figure 2.7. Since these background signals have been attributed to the formation of vacancy complexes, the low co-implantation-induced density of NV centers cannot be traced to a possible lack of vacancies in the diamond lattice.

According to the presented nitrogen atomic profile in figure 2.9, the concentration of implanted nitrogen atoms in the diamond lattice is above $10^{16}\,cm^{-3}$, being distributed within depths of up to $\sim 20\,nm$. The values of $\Delta n_S(He) \approx \Delta n_S(C) \approx 0.4\,\mu m^{-2}$ translates into a concentration of implanted nitrogen atoms of approximately $5 \times 10^{13}\,cm^{-3}$ that would be still available to create co-implantation-induced NV centers. Such a value is only $\sim 0.1\%$ of the initial concentration of implanted nitrogen atoms, being even far below the formation yield of the nitrogen implantation technique ($\sim 1\%$, see figure 2.4 c). The ion co-implantation technique is hence a direct summation of two different effects: created NV center by nitrogen implantation and conversion of nitrogen impurities to NV centers by ion irradiation. The presented results indicate that the majority of nitrogen atoms in the lattice are consumed by the formation of vacancy-related and other nitrogen-multi-vacancy defects (NV_N). This means that, even in the case of co-implantation, the

accumulation of lattice defects consume most of the created vacancies by the ion impacts.

2.4. Nitrogen δ-doping

An emerging technique utilized to create near-surface NV centers is known as *nitrogen δ-doping* [64–68]. This method is based on the introduction of nitrogen gas to the reactant plasma during the CVD diamond growth process. The controlled admixture of nitrogen and optimized growth conditions result in nanometer-thin (δ) nitrogen-doped diamond films with excellent crystal quality. Typical growth rates of $< 1\,\mathrm{nm.min^{-1}}$ are utilized, resulting in a nanometer-control of the nitrogen-doped film thickness [64].

In this method, NV centers are stochastically formed at incorporated nitrogen atom sites in the growing diamond lattice. Moreover, nitrogen-doped films can be post-irradiated with electrons and inert ions to create lattice vacancies [64, 154]. By exposing the irradiated film to a subsequent thermal annealing process, vacancies become mobile and create eventually further NV centers from ingrown nitrogen impurities. Recent investigations based on this method have demonstrated NV centers with T_2 times ranging up to $100\,\mathrm{\mu s}$ for depths of less than $5\,\mathrm{nm}$ [64]. Unfortunately, this method also induces the creation of NV centers outside of the nitrogen-doped film area. In general, this induces a strong background concentration of NV centers in confocal microscopy measurements due to the the much larger depth resolution ($\sim \mathrm{\mu m}$) in comparison to the thickness of the δ-doped diamond film..

Alternative methods for the creation of vacancies with enhanced spatial localization have been proposed recently. For instance, the exposure to a low-energy ($\sim 200\,\mathrm{keV}$) focused electron beam of a transmission electron microscope (TEM) results in a relatively-good positioning control and excellent spin properties of created NV centers [155]. Still, optimized conditions for an efficient NV center-based architecture for quantum sensing, namely, a nanometer-thin diamond film containing NV centers suitable for detecting external spins, are experimentally challenging. To this aim, the nitrogen δ-doping technique is revisited and further explored in Chapter 5.

2.5. Summary and Outlook

In summary, this chapter has presented the main methods to create NV centers in ultra-pure diamond crystals. The techniques have been evaluated based on the essential characteristics demanded for particular NV center-based quantum applications. Among all presented methods, the formation of vacancy-related lattice defects in diamond has been underlined as the limiting factor of both the conversion efficiency and the properties of created NV centers. Unfortunately, such paths of vacancy recombination are so far an intrinsic physical limitation of the creation methods of NV centers.

The following chapters are aspired to change this concept and address fundamental aspects related to the dynamics of NV centers and other lattice defects in diamond. The established concepts in this Chapter will be further utilized for the forefront development of creation techniques of NV centers with augmented properties for quantum technologies. The gained insights will pave the way for improved engineering of not only diamond, but also other solid-state quantum systems that rely on the targeted creation of spin impurities.

3. Diamond surface modification

As presented in the last Chapters, near-surface NV centers are outstanding sensors of magnetic fields [116, 129, 156, 157], capable of detecting a small number of external nuclear or electron spins located on the diamond surface. Due to their atomic-size and high-fidelity spin state manipulation/readout, NV centers behave like isolated atomic sensors (such as in ion traps and atomic vapor cells) [17], demonstrating high magnetic field sensitivity and nanometer spatial resolution. They hold the promise to revolutionize the field of spectroscopy in NMR and MRI [17, 27–31] as alternative magnetometer sensors to detect spin labels and enable biological imaging with unprecedented spatial resolution and sensitivity. As discussed in Chapter 2, however, device implementation of near-surface single or ensembles of NV centers still remains a challenge due to physical limitations related to the methods used for their engineering.

One possibility to increase the performance of NV centers-based sensing devices is to post-treat the diamond in order to bring NV centers closer to its surface [158], thus increasing the corresponding magnetic coupling strength. The basic requirements for such a treatment would be (i.) nanometer control of the etching rate (removal of material), (ii.) high reproducibility and, of great importance, (iii.) preservation of the optical and spin properties of nearby NV centers. As it will be briefly described in this Chapter, despite several methods have been proposed towards this effort, none of them fulfill all the above-mentioned requirements.

This Chapter starts by first introducing the theoretical concepts of plasma-matter interactions and plasma etching. Together with this, different methods used to etch semiconductor materials are described and the relevant advantages/ disadvantages are discussed. Second, the chemical composition of the diamond surface terminated by oxygen atoms is investigated. Using this as reference, the changes on the surface composition and morphology due to the diamond exposure to capacitively coupled plasmas are examined. At the end, a novel plasma process named "oxygen soft plasma" used to etch the diamond surface while fulfilling the three mentioned requirements is presented and the experimental results are discussed. In particular, the analysis of the plasma-treated diamond material by

different techniques shows no traces of plasma-induced damage while NV centers within the first nanometers below the etched surface still show high photo-stability and relatively good spin properties.

The main results presented in this Chapter are published in F. Fávaro de Oliveira *et al.*, Applied Physics Letters **107**, 073107 (2015).

3.1. Basic radio-frequency plasma concepts

3.1.1. Plasma: technological applications

The word "plasma" has been used since the 19$^{\text{th}}$ century in the field of physiology to define the liquid medium of blood (protein-salt solution) that suspends cells and platelets. In physics, as pointed out by H. M. Mott-Smith in his letter "*History of Plasmas*" [159], the same word was first used in the beginning of the 20$^{\text{th}}$ century by Irving Langmuir in his study of electric discharges in gas tubes. As described there, the discharge region in equilibrium would act as a medium carrying particles such as high-velocity free electrons and ions and would be thus similar to the blood plasma. Although this word has been widely adopted by physicists and engineers, it is known nowadays that there is in fact no medium carrying the involved particles. Plasma is considered a new (the fourth) state of matter.

One can distinguish a neutral gas from a plasma by means of the higher energy involved in the latter, i.e. higher temperatures of species, which results in the dissociation of atoms and molecules into charged ions and free electrons. Plasmas are consequently highly electric conductive. Importantly, the definition "free" means that the kinetic energy associated with electrons in plasma is much higher than the electric potential energy due to neighbor ions, so they are no longer considered bound. The velocity of free electrons in plasma follows the Maxwell-Boltzmann distribution, corresponding to temperatures between 5000 and 70000K [160]. One important parameter to be considered is the degree of plasma ionization, $\chi = \eta_{\text{ionized}}/(\eta_{\text{ionized}} + \eta_{\text{neutral}})$, representing the fraction of species (η) that are ionized. High temperature plasmas can be found in nature (e.g. in stars) as well as produced artificially (e.g. in controlled nuclear reactions in fusion research). These are characterized by a very high degree of ionization ($\chi \approx 1$), meaning that atoms and molecules are fully ionized. Plasmas with a small degree of ionization ($\chi \ll 1$), on the other hand, are used e.g for material processing. They consist mostly of neutral atoms or molecules and a small fraction of charged ions and free electrons

that are responsible for the plasma-material interactions.

A particular feature of plasmas is the condition of quasi-neutrality [160]. In a macroscopic view, plasmas are charge neutral, meaning that the number of electrons and charged ions must be equal under equilibrium. In a microscopic view, however, charged regions may be formed due to the simultaneous electrostatic attraction/repulsion between charged species and therefore induce local fluctuating electromagnetic fields. Perturbations due to thermal motion are random and cause local instantaneous spatial variations in the plasma electrostatic potential. The corresponding fields interact with nearby moving charged species and alter their motion. In this sense, describing plasma particles individually becomes extremely difficult, since such mutual local interactions gives rise to a collective behavior of the plasma particles. The condition of quasi-neutrality and related features will be further explored in the section 3.1.3.

Since the late 1970's, plasma physics has become again a subject of intense research. In particular, material processing for the fabrication of modern integrated electronics based mainly on silicon devices have stimulated the field of plasma-assisted processes, strongly influenced by their economical importance. These include surface modification, material deposition, development of new materials (i.e. amorphous silicon and silicon dioxide), material doping and etching [2, 161–163], features that are hardly achieved by other methods such as wet chemical treatments. Plasma treatments offers the advantage of anisotropic and fast material removal, enabling the creation of vertical sidewalls and through-wafer etched structures with sub-micrometer inter-spacing for the large scale fabrication of electronic components and Micro-Electro-Mechanical Systems (MEMS) devices in wafer-like scale [2, 164]. In modern industry, microfabrication of integrated circuits is a complex process that involves several fabrication steps, all of which approximately 30% are plasma-based [2, 165].

The technological triumph of silicon-based devices has served as an excellent platform for the development of plasma processes for diamond in many different application fields [54–57, 166]. One of the interests of this work is the development of plasma processes aiming not only at the fabrication, but also at the optimization of hybrid structures based on diamond and color centers. On one side, monolithic diamond structures such as tapered nano-pillars can be fabricated on a diamond substrate by plasma etching [55]. On the other side, the use of plasma processes for the direct modification and nanometer etching of the diamond surface is an excellent tool towards NV-based devices with enhanced optical and spin properties for quantum sensing. Hereinafter, the developed concepts will be mostly focused on plasmas with small degrees of ionization and low-pressure ($1 - 10^2$ mTorr),

parameters typically used for material processing.

3.1.2. Inter-particle interactions

The physics governing plasmas is complex due to the fact that charged ions and free electrons behave collectively and become a many-body problem that cannot be modeled by the usual kinetic collision theory. In contrast to solids, liquids and gases, humans do not have an intuition of how plasmas behave since they are not part of usual daily situations. The following sections aim to develop this basic intuition by the definition of relevant physical concepts, which will be extremely helpful when describing the plasma effects on diamond. By their nature, plasmas are remarkably adaptable and scalable, meaning that the physical concepts developed for plasmas created in a controlled laboratory environment are easily expanded to plasmas several orders of magnitude larger such as the ones found in nature.

In a first look, the dynamics of the plasma particles can be evaluated considering the inter-particle and particle-external forces interactions (i.e. due to electromagnetic fields). While the interaction between ions and free electrons is mainly of electrostatic nature [167], electromagnetic fields generated locally by random thermal motion of charged species in plasma must be evaluated using the Maxwell's equations. Moving charges are constantly trying to compensate these fields in order to maintain the equilibrium condition and the macroscopic charge neutrality. By knowing the position of every particle i with trajectory $\mathbf{x}_i(t)$ and velocity $\mathbf{v}_i(t)$, local fluctuations of electromagnetic fields are evaluated using the Maxwell's equations. Then, the knowledge of these fields can be used to update $\mathbf{x}_i(t)$ and $\mathbf{v}_i(t)$ by means of the Lorentz and Coulomb forces in a self-interactive way. Although easy to comprehend, such a direct evaluation is unfeasible due to the complexity and stochastic nature of the particle interactions and the involved electromagnetic fields.

Several theories have been proposed in order to simplify the modeled dynamics of plasma particles in certain regimes. For instance, the Vlasov theory [168] is based on the fact that binary collisions are insufficient to describe the interaction between plasma particles. For a given particle density and velocity distribution, the average distance traveled by a particle without suffering any scattering of its momentum due to collision events is defined by the mean free path. This is given by $\lambda_{\mathrm{mfp}} = \bar{v}_p/v_p$, with $\bar{v}_p$ and v_p being the average velocity and collision rate of plasma particles, respectively. The problematic lays on the long-range forces

created by local charge imbalances that influence the motion of particles with a radius of action well above λ_{mfp}.

The Vlasov theory averages the collective particle dynamics considering all particles of a certain type (i.e. free electrons). One can describe the instantaneous density of particles in the x, v (space, velocity) phase-space by defining a distribution function $f(\mathbf{x}, \mathbf{v}, t)$. The expression $f(\mathbf{x}, \mathbf{v}, t)\, d\mathbf{x} d\mathbf{v}$ is thus the number of particles that have positions between $\mathbf{x}$ and $\mathbf{x} + d\mathbf{x}$ and velocities between $\mathbf{v}$ and $\mathbf{v} + d\mathbf{v}$ at a given time t. The Vlasov equation (including binary particle collisions, with q and m being the charge and mass of the considered particle class, respectively) [168]:

$$\frac{\partial f}{\partial t} + \mathbf{v} \cdot \nabla f + \frac{q}{m}\left[\mathbf{E} + (\mathbf{v} \times \mathbf{B})\right] \cdot \frac{\partial f}{\partial \mathbf{v}} = \left(\frac{\partial f}{\partial t}\right)_{\mathrm{collision}}, \qquad (3.1)$$

makes use of a distribution function to describe the temporal evolution of groups of particles with the same $\mathbf{x}$ and $\mathbf{v}$ at a certain time t. The electromagnetic fields $\mathbf{E}$ and $\mathbf{B}$ given by the Maxwell's equations together with equation 3.1 form a complete set of self-consistent equations describing the particle dynamics of a plasma in equilibrium. Such a theory is suitable to describe the microscopic characteristics of a plasma. A more detailed description of the involved equations is given in Refs. [168, 169].

Alternatively, magnetohydrodynamics (MHD) [170] is a widely-adopted theory to accurately describe the plasma macroscopically by subdividing it into ideal fluid-like elements. Similar to the Vlasov theory, it also makes the use of distribution functions in the v, P (velocity, pressure) phase-space to describe each subdivision of the plasma. The corresponding behavior of each subdivision is an average over the properties exhibited by the collective of particles within each single fluid element. For example, instead of directly counting the number of free electrons in the plasma at each time t, one can average the total number density of electrons ($N_{i,\mathrm{elec}}$, number of particles per unit volume) within different elements at positions $\mathbf{x_i}(\mathrm{r})$ in the space and write it as:

$$N_{i,\mathrm{elec}} = \int_V f_{\mathrm{elec}} d\mathbf{v} = \frac{n_{\mathrm{total,elec}}}{V_{\mathrm{total}}}. \qquad (3.2)$$

This is known as the *zeroth order velocity moment* [171]. The direct counting of particles in the volume V_{total} on the right hand side of the above equation is substituted by the integration of a smooth and well-described distribution function

(f_{elec}) over the particle velocities **v**. The same approach can be used to define the velocity, momentum and other useful quantities [170]. For a very large number of particles, this kind of formulation becomes very powerful to describe the plasma properties macroscopically. A complete description of this theory is given in Refs. [170, 171].

The theories briefly explained above complement each other in order to build a solid description of the macroscopic and microscopic plasma dynamics. Relevant concepts common to these theories will be discussed in detail in the coming sections, aiming the main focus of this Chapter: the plasma processing of diamond materials.

3.1.3. The condition of quasi-neutrality and Debye shielding

To define the density of charges ρ and current density **J** , one has to consider a plasma in equilibrium, e.g. a plasma with a finite temperature and homogeneous ion and electron densities. One can write these quantities as functions of the number of ions (n_i, including higher Z > 1 charge states), the number of free electrons (n_e) and the corresponding average velocities (v_i and v_e, respectively) as:

$$
\begin{aligned}
\rho &= \sum_n q_n n_n = e \left(\mathrm{Z} n_i - n_e \right), \\
J &= \sum_n q_n n_n v_n = e \left(\mathrm{Z} n_i v_i - n_e v_e \right).
\end{aligned}
\tag{3.3}
$$

It is interesting to note that the applied power to heat a weakly-ionized plasma is efficiently transferred to free electrons due to their lower mass, whereas heavy ions exchange energy mainly by elastic collisions. This means that the temperatures of free electrons (T_{elec}) and ions (T_{ions}) can be different, even for a plasma in equilibrium. In fact, weakly-ionized plasmas are characterized by the adiabatic approximation, showing $\mathrm{T}_{\text{elec}} \gg \mathrm{T}_{\text{ions}}$. The condition of quasi-neutrality establishes that the electric potential in a plasma in equilibrium must be zero (or constant relative to a referential) and thus the number of positive and negative charges must be the same:

$$
\mathrm{Z} n_i = n_e \equiv n_0.
\tag{3.4}
$$

Consequently, ρ in equation 3.3 must be zero. The plasma quasi-neutrality holds under specific conditions, which will be investigated in the following. For instance, since plasma particles are in constant movement, one has to investigate the dynamics related to the local density of particles. Therefore, as discussed in section 3.1.2 in the MHD theory, one can subdivide a plasma in equilibrium into fluid-like elements. In this case, the plasma pressure due to n_m particles can be written as [169]:

$$\mathrm{P}_m = n_m k_\mathrm{B} T_m, \tag{3.5}$$

where k_B is the Boltzmann constant and T_m is the mth fluid element mean temperature with a corresponding mean velocity of $\mathbf{v}_m$. The thermal motion of charged species entering and leaving an individual fluid-like element results in the equation of motion in the form [169]:

$$m_m n_m \frac{d\mathbf{v}_m}{dt} = q n_m \mathbf{E} - \nabla \mathrm{P}_m, \tag{3.6}$$

with m_m being the mass of particles and $\mathbf{E} = -\nabla\phi$ being the electric field (written as the negative gradient of the electric potential). If the plasma pressure is sufficiently low, e.g. the collision rate is negligible ($\upsilon_p \approx 0$), the change in velocity due to binary collisions (left-most time derivative in equation 3.6) can be neglected. This approximation can be used for e.g. low-pressure plasmas, where λ_mfp is sufficiently large. Consequently, the equations 3.5 and 3.6 are reduced to:

$$q n_m \nabla\phi + k_\mathrm{B} T_m \nabla n_m = 0. \tag{3.7}$$

The expression above can be interpreted as the dynamic balance between the electrostatic force and the force generated by thermal perturbations in the density of particles represented by ∇n_m. By integrating this equation, the resulting solution is:

$$n_m = n_{m,0} \exp\left(-\frac{q\phi}{k_\mathrm{B} T_m}\right), \tag{3.8}$$

where $n_{m,0}$ is a constant representing the initial density of particles within the mth fluid element. This equation is known as the *Boltzmann density relation*. It is

important to reenforce that the density of particles can only be described by this relation if the thermal perturbations are slow e.g. the adiabatic approximation holds. In highly-ionized plasmas, inertial effects due to a high rate of energy transfer from electrons to ions equilibrate their corresponding temperatures and the adiabatic approximation is not valid anymore. Since these types of plasma are beyond the scope of the presented experiments in this thesis, the Boltzmann density relation is assumed to fully describe the density of free electrons and ions in a plasma in equilibrium.

Let us now consider a positive test charge $(+q)$ that is slowly inserted into a plasma initially in equilibrium. The presence of such test particle will disturb the local density of charges in such a way that free electrons are attracted and ions are repelled by it. These displacements result into a local finite electric potential, which is the superposition of the potentials of the test charge and the dislocated plasma species. For an observer located far enough, the electric potential of the test charge is shielded, i.e. partially canceled by the negative electron cloud induced in its vicinity. This phenomenon is known as *screening* of the electric potential of the test charge and was first discussed by P. Debye in case of electrolyte solutions [172]. If we assume the origin of coordinates as the position of the test particle, the screened electric potential at a position r_i can be calculated using the Poisson's equation:

$$
\begin{aligned}
\nabla^2 \phi &= -\frac{\rho}{\varepsilon_0} \\
&= -\frac{1}{\varepsilon_0} \left[q\delta(r_i) + \sum_n q_n n_n(r_i) \right],
\end{aligned}
\tag{3.9}
$$

where $q\delta(r_i)$ represents the test charge located at the origin of the coordinates and $\sum_n q_n n_n(r_i)$ represents the density of charges in plasma that participate in the screening of the potential, in a similar form as in equation 3.3. Using equation 3.8, one can thus rewrite the Poisson's equation as:

$$
\begin{aligned}
\nabla^2 \phi &= -\frac{1}{\varepsilon_0} \left[q\delta(r_i) + \sum_n q_n n_{m,0} \exp\left(-\frac{q\phi}{k_{\mathrm{B}} T_m}\right) \right] \\
&= -\frac{1}{\varepsilon_0} \left[q\delta(r_i) - e n_{m,0,\mathrm{elec}} \exp\left(-\frac{q\phi}{k_{\mathrm{B}} T_{m,\mathrm{elec}}}\right) + Z e n_{m,0,\mathrm{ions}} \exp\left(-\frac{q\phi}{k_{\mathrm{B}} T_{m,\mathrm{ions}}}\right) \right].
\end{aligned}
$$

Since the potential perturbation due to the insertion of a single charged particle

in a initially neutral plasma can be assumed as infinitesimal, e.g. $q\phi \ll k_{\mathrm{B}}T_{m,\mathrm{elec}}$, the terms $\exp\left(-\frac{q\phi}{k_{\mathrm{B}}T_m}\right)$ can be expanded using the Taylor series. Finally, by defining the *effective* temperature $1/T_{\mathrm{eff}} = 1/T_{m,\mathrm{elec}} + 1/T_{m,\mathrm{ions}}$, the Poisson's equation takes the form of:

$$\nabla^2\phi = \frac{1}{\varepsilon_0}\left[q\delta(r_i) - \frac{2n_{m,0}e^2\phi}{k_{\mathrm{B}}T_{\mathrm{eff}}}\right].$$

If we define the plasma *Debye lenth* as:

$$\lambda_{\mathrm{D}} = \sqrt{\frac{\varepsilon_0 k_{\mathrm{B}}T_{\mathrm{eff}}}{n_{m,0}e^2}}, \tag{3.10}$$

the solution for the electric potential in equation 3.1.3 is finally given by:

$$\phi(r_i) = \frac{e}{4\pi\varepsilon_0 r_i}\,\exp\left(-\frac{\sqrt{2}r_i}{\lambda_{\mathrm{D}}}\right). \tag{3.11}$$

The electric potential given above is relevant in different aspects related to the plasma particles. Any charged particle in the plasma can be assumed as the "test charge", as defined in the beginning of this investigation. Therefore, the effective potential of *any* charged particle can be described by equation 3.11. The electric potential screening of the test charge given by the exponential decay in equation 3.11 defines roughly the dimension for which the condition of quasi-neutrality holds and all particles are confined within a shielded plasma with overall constant potential. Furthermore, this shielding is effective within a distance in the order of the Debye length and is therefore known as *Debye shielding*.

3.1.4. Plasma sheath

The analysis above assumed a large homogeneous plasma (size much larger than λ_{D}). However, an interesting phenomenon occurs when a plasma is confined into a chamber. The potential in bulk plasma is constant, meaning that electrons and ions are isotropically free to move. When moving close to a boundary, electrons and ions will consequently exit the plasma region and hit e.g. the chamber walls or the surface of a material being processed. As previously discussed, free electrons

have a much higher temperature and consequently higher average velocity than ions. As a consequence, initially, the collision rate of electrons at the boundaries is much greater than the rate of ions.
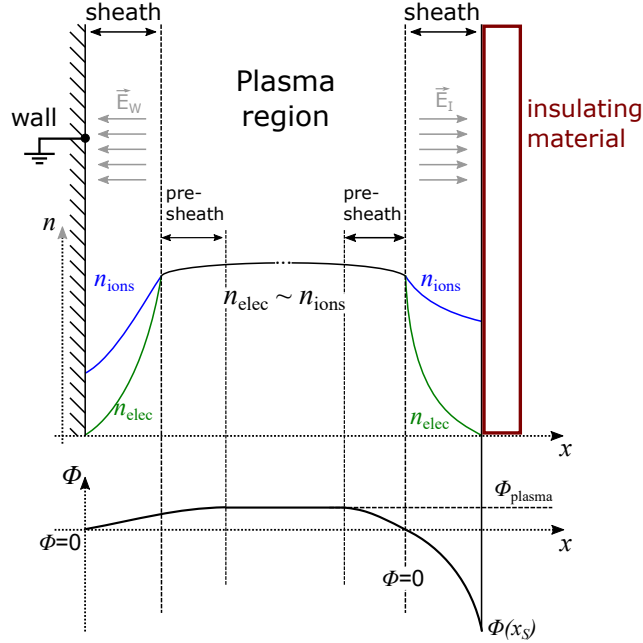
This situation changes rapidly after the initial ionization process of plasma particles. The local electron density at the boundaries shields the electric potential of plasma, thus confining further electrons within the plasma volume. In the equilibrium, the electron density at the boundaries is given by the Boltzmann relation (equation 3.8), being approximately zero within a Debye length. A schematic representation of this condition can be seen in figure 3.1. The non-neutral region between the plasma and a boundary is known as the *plasma sheath*. Hereinafter, the discussion will focus on the plasma-insulator type of boundary, which is specifically named as *floating sheath*. For plasmas with a relatively low concentration of free electrons ($\sim 10^{11}\,\text{cm}^{-3}$), the sheath length is usually in the order of $10^{-4}\,\text{m}$ [169].

The potential difference induced by the shielding effect in the sheath is known as the *self-bias voltage* ($\phi\left(x_S\right)$ in figure 3.1) . Consequently, an electric field pointing towards the sample surface is established (see the upper part of figure 3.1) and positively-charged ions are highly accelerated towards the insulator surface. On one side, the directionality of the energetic ion bombardment on the material is the essence of the anisotropic plasma etching mechanism, where the etching direction is defined by the direction of the electric field in the sheath region. On the other side, such an ion bombardment can heavily damage the material surface exposed to plasma, resulting in undesired changes in its properties. This feature will be further explored for the particular case of diamond in section 3.3.3.

The electric potential in the plasma sheath defines the ion bombardment energy and therefore must be carefully analyzed. For simplicity, ions are assumed to enter the sheath area in a plane $x = 0$ with a velocity $v_{i,0}$ (pre-sheath/sheath boundary, figure 3.1). Ions are accelerated by the self-bias voltage and reach the sample surface (x_S) with an average velocity v_i. For the case of a negligible collision rate within the sheath region, the conservation of energy gives:

$$\frac{1}{2}m_i v_i^2 = \frac{1}{2}m_i v_{i,0}^2 - q\left|\phi\left(x_S\right)\right|.$$

The charge continuity equation (3.3) in the case of a negligible ionization rate in the sheath results in the relation $n_{i,0}v_{i,0} = \left.\left(n_i v_i\right)\right|_{x_S}$. The combination of these two equations results in the expression for the number of ions in the sheath region:

Figure 3.1.: Sketch of the Debye shielding at the plasma boundaries representing two different cases: a grounded wall (left) and an insulating material (right). In the upper figure, the charge density n is schematically represented versus the position x. In bulk plasma, the condition of quasi-neutrality holds. In regions close to the grounded chamber wall and an insulating material, a charge imbalance is generated due to the different electron and ion thermal velocities. As a consequence, an electric field pointing towards the boundaries is established in the sheath region. The lower figure schematically presents the resulting electric potential. Figure adapted from Ref. [165].

$$n_i\left(x_S\right) = n_{i,0}\left[1 - \left(\frac{2q\left|\phi\left(x_S\right)\right|}{m_i v_{i,0}^2}\right)\right]^{-\frac{1}{2}}. \tag{3.12}$$

The Poisson's equation for the electric potential anywhere in the sheath can be written by combining equations 3.4, 3.8, 3.9 and 3.12 as:

$$\nabla^2\phi\left(x_i\right) = \frac{en_0}{\varepsilon_0}\left\{\exp\left(-\frac{q\phi\left(x_i\right)}{k_\mathrm{B}T_\mathrm{elec}}\right) - \left[1 - \left(\frac{2q\phi\left(x_i\right)}{m_i v_{i,0}^2}\right)\right]^{-\frac{1}{2}}\right\}. \tag{3.13}$$

The non-linear equation above governs the behavior of the electric potential and the density of charged particles within the floating sheath region. Since the average ion temperature is much lower than the electron temperature, the average

ion velocity in the bulk plasma is negligible. As the ions move closer to the plasma boundary with an insulating material, they sense a small electric field generated by the screening of the charges at the boundary. This region is called *pre-sheath* and is typically much wider than the sheath itself (see figure 3.1). The electric potential in the pre-sheath region is equal to the lifted plasma potential (ϕ_{plasma}). Ions accelerated by this potential towards the sheath have therefore a non-zero average velocity.

This implies that the function describing the electric potential must be zero at the pre-sheath/sheath boundary and its absolute value must increase with larger values of x until its maximum absolute value $|\phi(x_S)|$ (see figure 3.1; the signal of this potential will be examined further in this section). This translates into the relation:

$$\exp\left(-\frac{q\phi(x_i)}{k_B T_{\text{elec}}}\right) < \left[1 - \left(\frac{2q\phi(x_i)}{m_i v_{i,0}^2}\right)\right]^{-\frac{1}{2}}.$$

In the case of RIE processes, $q\phi(x_i) \ll k_B T_{\text{elec}}$, and one can thus expand both potential-dependent terms using Taylor series, leading to a velocity condition in the pre-sheath/sheath boundary:

$$v_{i,0} > \sqrt{\frac{k_B T_{\text{elec}}}{m_i}}. \tag{3.14}$$

This is known as the *Bohm sheath criterion*, which defines the minimum velocity (the *Bohm velocity*) that an ion must have to reach the material surface:

$$v_B = \sqrt{\frac{k_B T_{\text{elec}}}{m_i}}. \tag{3.15}$$

Moreover, this criterion provides the lifted plasma potential:

$$\phi_{plasma} = \frac{k_B T_{\text{elec}}}{2e}. \tag{3.16}$$

The above-presented description of the plasma sheath assumed a constant ion and zero electron currents from the plasma bulk to the boundaries. In a floating sheath, the initial ionization of plasma particles charges the material negatively,

as previously explained. However, the equilibrium condition changes as the ion current slowly charges the insulating material positively. Being an insulator means that the material is incapable of eliminating the excess of charges. Hence, a DC plasma discharge cannot be stable if the plasma boundaries are insulating materials. To overcome this problem, plasma processes utilized for material processing must operate with a time-varying voltage.

Differently than in DC discharges, time-varying voltages generate plasma discharges that are sustained by the corresponding oscillation of the electrons (i.e. electron cloud) as a response to the time-varying electric field in the sheath. In this sense, the applied voltage frequency must be such that electrons respond instantaneously to any changes in the sheath potential, whereas ions respond only to a time-averaged electric potential in the sheath. For plasma used in the material processing, voltage frequencies are typically in the radio frequency (RF) range (between $1 - 100\,\text{MHz}$) [165]. An RF frequency of $f_{\text{RF}} = 13.56\,\text{MHz}$ is used as a compromise between plasma stability and hardware complexity. In this case, the time-averaged floating sheath potential is given by [165]:

$$\bar{\phi}_{\text{FS}} = \frac{3}{4}\frac{J_0^2}{e\varepsilon_0 n_e \omega^2},\tag{3.17}$$

where J_0 is the displacement electron current density and $\omega = 2\pi f_{\text{RF}}$ is the applied RF-frequency. The electric potential derived above is equivalent to the previously-defined self-bias voltage. This parameter can be tuned accordingly to the utilized RF-power and frequency. A higher power translates into a higher ionization rate and thus higher values of J_0. Importantly, a negligible electron-ion recombination rate is assumed for the case of low-pressure plasmas for material processing. In this simplified case, the energy of ion bombardment on the material surface is given by $E_{\text{bomb}} = Ze\left[\bar{\phi}_{\text{FS}} + \phi_{plasma}\right]$, reaching values of several hundred Volts.

3.1.5. RF-plasma etching mechanism of diamond

Diamond is known for its chemical inertness and extremely strong carbon bonds, which makes the material structuring (removal) by wet chemical treatments notoriously challenging. In this sense, plasma material processing (also known as *dry etching*) has been demonstrated as a powerful tool towards patterning of diamond substrates, leading to a controlled and uniform material removal with high final lattice structural quality and surface smoothness. The first reports on diamond dry etching date over two decades [173] and since then this technique has become

widely adopted and has been highly refined in the fields of diamond fabrication and surface modification.

Among several different reactant gases (fluorine [56, 174], chlorine [57, 175] and hydrogen [176]), oxygen-based plasma processes [55, 173, 176–179] are the most common for the dry etching of carbon-like materials such as diamond and graphite. In this particular case, the energy transferred to the plasma reactant gas supplies free electrons, atomic and molecular oxygen ions, and reacting oxygen free radicals ($O^\star$; atomic oxygen with unpaired electrons). The removal of material is a complex combination of physical and chemical processes, where plasma ions and radicals interact differently with surface carbon atoms. This method of material processing is known as *reactive ion etching* (RIE).

As investigated in the last section, the energetic steady ion bombardment physically sputters the diamond surface during the RIE process with enough energy to break carbon bonds. The highly reactive radicals come to play in different functions. First, they react chemically with the sputtered carbon atoms and form volatile products such as $CO_{(g)}$ and $CO_{2,(g)}$ [174] faster than the time that carbon bonds need to be reestablished. Second, they modify/break the carbon bonds on the diamond surface layer, thus etching the material by direct chemical reactions.

At the end of the plasma process, oxygen atoms bind to the diamond surface at carbon dangling bond sites, e.g. carbon atoms trapped in the diamond lattice that have unpaired valence electrons. This constitutes a non-diamond surface layer of hydrocarbons and oxygen-bonded atoms known as the diamond *surface termination* [177]. This non-diamond surface layer is also observed on diamonds exposed to hydrogen- and fluorine-based plasmas [66, 132, 134], resulting in the possibility of diamond to have different surface terminations.

The addition of other gases in oxygen-based plasmas results in interesting effects. For instance, the introduction of argon (Ar/O_2 plasma) significantly increases the number of ions in plasma, thus intensifying the sputtering of the diamond surface. This results in a higher density of active sites on the diamond surface, through which more oxygen-carbon chemical reactions are possible. If the density of oxygen radicals in plasma is sufficiently high, the final result is a higher etching rate and strong anisotropy [176, 179]. This kind of etching process is known as *ion-enhanced etching*. The argon ion bombardment also transfer enough energy to the diamond sub-surface layers such that the carbon covalent bonds rearrange from sp^3 (diamond) to sp^2 (graphite) hybridized configurations [179].

The introduction of fluorine (CF_4/O_2, for example) changes the degree of dis-

sociation of oxygen molecules, which leads to a higher density of oxygen ions and reactive radicals in plasma [180]. Physical sputtering and carbon-oxygen chemical reactions are thereby intensified and the diamond surface dangling bonds created by the ion bombardment are more efficiently covered. Moreover, fluorine is more reactive than oxygen, meaning that the formation of fluorine-carbon volatile products take place and contribute to the ion-enhanced etching of diamond. Fluorine radicals also break the carbon bonds more easily, resulting in an increased density of active sites on the diamond surface. Such plasma processes result not only in higher etching rates, but also in a smoother surface morphology and a higher purity of the diamond phase in the surface top-layers [56].

The use of oxygen-based RIE processes to etch diamond limits the choice of masks that can be used to pattern-transfer with sub-micrometer dimensional control. Organic photo-resists are very susceptible to oxygen ion-enhanced etching, which makes them unfeasible for processes where high selectivity is required. Commonly, resists such as polymethyl methacrylate (PMMA, electron-beam sensitive resist) have an etching selectivity in oxygen plasma of less than $1 : 1$ with respect to diamond, which limits the diamond etching depth significantly (up to a few hundreds of nanometers, depending on the thickness of the used resist). Furthermore, poor etching selectivity reduces the edge sharpness of the pattern transferred to the substrate due to the faster etching at the mask edges [55].

Masks can be fabricated using different metals [179, 181, 182] such as nickel, titanium, chromium, gold and platinum, or materials that are resistant against oxygen ion-enhanced etching such as silicon dioxide (SiO_2) and silicon nitride (Si_3N_4) [178, 183]. The patterning of these materials is easily achieved by combining typical lithography with deposition techniques such as thermal evaporation [184]. The mask pattern lateral resolution is ultimately limited by the lithography process utilized. By using these types of mask, much higher mask-to-diamond etching selectivities can be achieved [182, 183], thus allowing the removal of several micrometers in depth while still delivering extremely sharp edges transferred to the substrate with very high aspect-ratios.
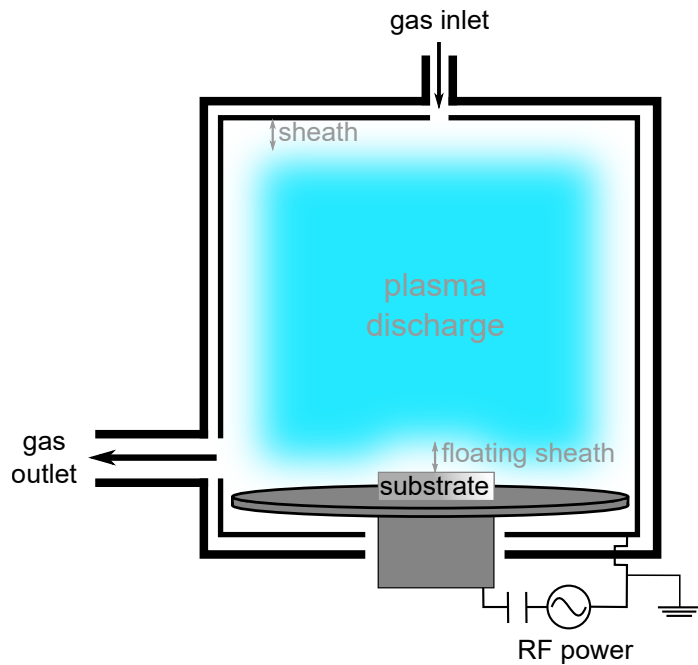
3.2. Sources of plasma

The choice of the mechanism used to transfer energy to the plasma species leading to their dissociation is of great importance. It determines the resulting density of species (i.e. ions, free electrons and radicals), the sheath potential and thus the etching mechanism that prevails. In the following sections, two main types of

plasma sources will be discussed in details together with the relevant advantages and disadvantages of each system for their application in material processing.

3.2.1. Capacitively coupled reactive ion etching plasma

Figure 3.2 presents schematically the most common type of plasma utilized for dry etching: the capacitively coupled RIE. In this case, the energy needed to sustain the discharge is applied by an electrode immersed directly in the plasma. The resulting capacitive floating sheath is a high-voltage region between the plasma and the electrode. For this reason, the material to be processed is usually placed on the power electrode immersed in the plasma region, which leads to a high-rate and energetic physical sputtering by plasma ions. The ion-enhanced plasma etching in such a device is therefore highly anisotropic [55, 56, 181].

Figure 3.2.: Schematic representation of a capacitive RIE chamber. In the plasma bulk, the condition of quasi-neutrality holds. At the plasma boundaries with the grounded walls and the substrate, the plasma sheath is formed. The capacitively coupled system transfers energy to the gas molecules constantly introduced through the gas inlet by the application of an RF high voltage. In order to maintain a constant pressure and remove the etching residuals, the chamber is evacuated with a controlled flow through the gas outlet.
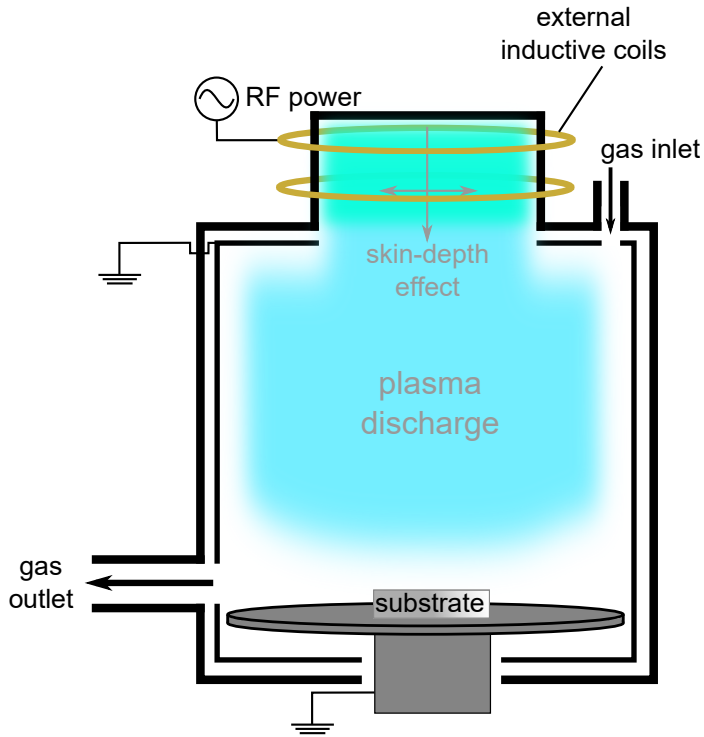
The main drawback of such capacitive processes on the processed material is also related to the sputtering of the diamond surface. Due to the presence of high-voltage sheaths, the ion bombardment produces a highly-damaged diamond top-layers that contain vacancies, implanted ions and non-diamond carbon phases such as graphite [50]. This damaged region extents itself to a few nanometers below the diamond surface and has a major impact on the quality of nearby color centers (see section 3.3.3).

Moreover, the power transfer to plasma species using low-pressure capacitive systems is rather inefficient. Even at large RF powers, most of the energy is consumed in the acceleration of ions and electrons as the sheath changes its shape and position at each part of the power cycle (displacement current flow). Only a small fraction of the energy is available to sustain the plasma via ionizing electron-molecule collisions. Typically, the rate between ionized particles and neutral species is $\sim 10^{-4}$ for low-pressure RF capacitive plasmas. Additionally, no independent control of the ion current and energy versus the density of radicals is available, since both depend directly on the ionization process induced by the RF cycle of the electrode.

3.2.2. Inductively-coupled plasma

The above-mentioned limitations of capacitively coupled discharges have brought the need of alternative methods to achieve an efficient power transfer to plasma species, leading to low-pressure, high-density plasmas. First reports on the inductive power transfer to discharges in gas tubes date way back to the 19$^{\text{th}}$ century [185], making the inductively-coupled plasma (ICP) one of the most implemented and well-studied alternatives to capacitive systems. Nowadays, the hardware complexity is relatively low; inductive external coils are used to efficiently couple the RF field to the plasma species via Joule heating (electron-molecule collisions) across a dielectric wall. A schematic representation of the chamber configuration used in ICP processes can be seen in figure 3.3.

As a current circulates through the induction coils, a magnetic field perpendicular to its direction is induced inside the plasma chamber. Consequently, an in-plane electric field with the opposite direction of the coil current is established in the plasma region, obeying Maxwell's equations. An schematic representation of the generated fields can be seen in figure 3.4. As the ionization process occurs, the plasma charged species shield this induced electric field, as previously described. This induces an electric current in the plasma region that is characterized by larger

Figure 3.3.: Schematic representation of an inductively-coupled plasma chamber.
The alternating power applied to the coils that surround the chamber dielectric
walls is inductively transferred to the plasma species. The shielding of the produced
electric fields is known as the skin-depth effect, and gives roughly the region where
electrons can gain kinetic energy and return to the plasma bulk region without
suffering collisions. These electrons sustain the plasma discharge by ionizing gas
molecules. The substrate to be processed is located remotely from the plasma
region and the etching occurs by chemical reactions between radicals and surface
atoms.
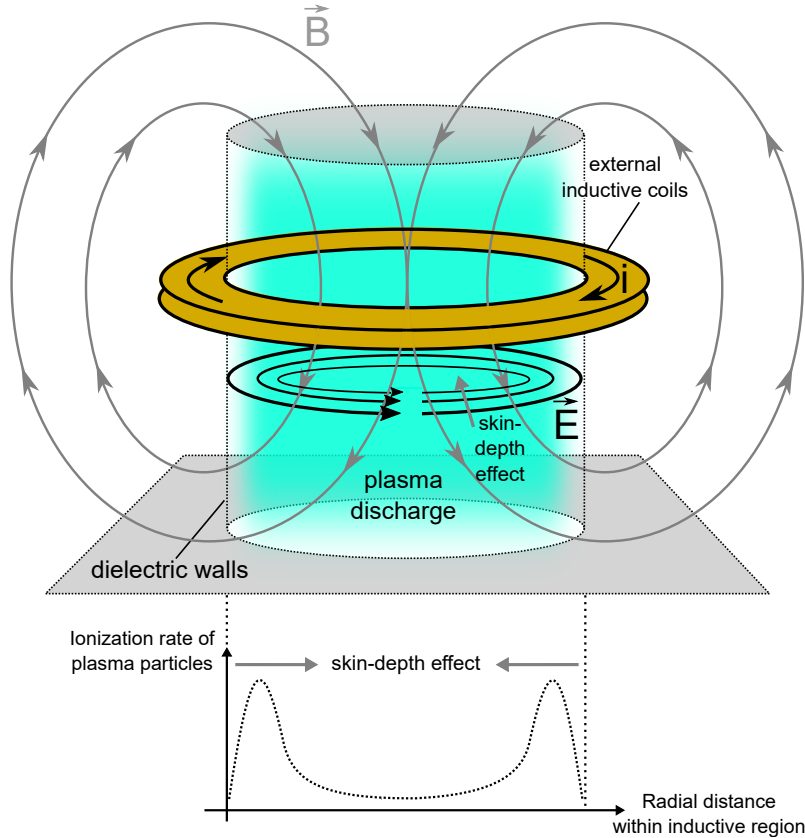
values closer to the dielectric walls (where the electric field amplitude is higher).
Such a region is called plasma *skin-depth* (δ_{skin}) and the corresponding shielding of
the electric field by an electron current flowing in this region is known as *skin-depth
effect*.

The skin-depth in a collision-free ICP is given by [165]:

$$\delta_{\text{skin}} = \sqrt{\frac{2}{\mu_0 \sigma_{\text{p}} \omega}}, \tag{3.18}$$

where ω is the RF induction frequency, μ_0 is the magnetic constant and σ_{p} is the
plasma electrical conductivity. Similarly as in the case of capacitive systems, an RF

Figure 3.4.: Magnetic and electric fields induced by the electric currents in the coils of the ICP system. Schematic representation of the magnetic and electric fields generated by induction coils, where a current i flows. According to Faraday's law, the magnetic field is perpendicular to the current direction, whereas the electric field is in-plane with the coil and has opposite direction of the electron current. The lower graph represents schematically the skin-depth region, where the generation rate of ionized particles decays towards the center of the inductive region due to shielding effects. Figure partially adapted from Ref. [165].

frequency of 13.56 MHz is usually used for hardware simplification. If the plasma pressure is sufficiently low, e.g. the mean-free path of electrons is much larger than δ_{skin}, electrons that penetrate the skin-depth region gain kinetic energy and return to the bulk plasma region without suffering collisions. These electrons are thus responsible for sustaining the plasma discharge. In the case of ICP plasmas for material processing, δ_{skin} is on the order of centimeters [186]. This means the plasma ionization is only effective within this characteristic space length away from the position of the induction coils. In reality, collisions must be taken into account, as they increase the skin-depth. The plasma bulk expands itself and is stable in the processing chamber for space regions with a distance roughly given

by δ_{skin} (see figure 3.3).
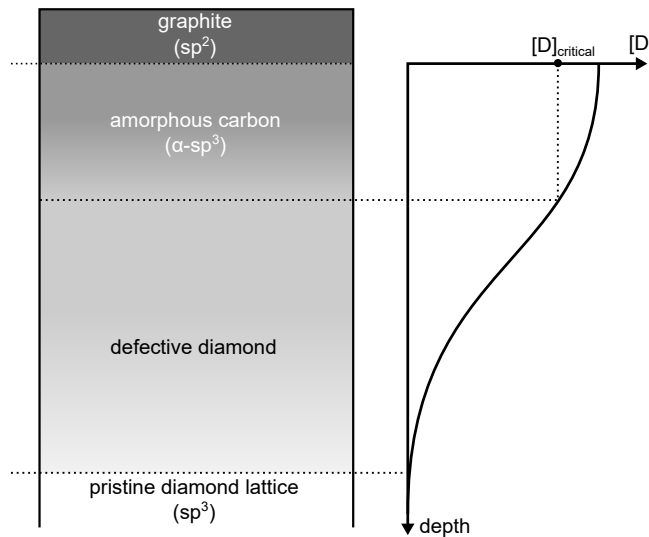
This feature allows an independent control of the ion current and energy, and radical density at the material location, e.g the material to be processed can be located remotely from the plasma discharge. The density of radicals would depend directly on the plasma density (and thus on the inductive power) at the position of the material in relation to the induction region, whereas the ion current and energy can be externally driven by an extra capacitive system to induce an external bias voltage (this type of system is a hybrid capacitive RIE/ICP plasma). This independent control of the properties of ions still retains the advantages of using the directionality of ion bombardment in ion-enhanced etching (as described in the previous section), while higher densities of radicals are possible for augmented chemical reactivity in low-pressure plasmas. ICP processes alone are therefore highly isotropic [187, 188].

In low-pressure ICPs, the electron-ion recombination occurs much faster than the corresponding radical recombination rate. At regions located farther than δ_{skin} from the induction region, the density of ions decreases faster than the density of radicals. If a substrate is located at this physical position, the material removal occurs mainly through chemical reactions at its surface rather than by ion-enhanced etching. In this case, the sheath is nonexistent at the material position and there is no ion bombardment of the material. The main advantages of using ICP over capacitive RIE processes are, first, the higher plasma density that can be achieved, and, second, the smooth material removal through chemical reactions. The plasma-induced damages are thus expected to be much reduced by using ICP-based processes. This is the key roadblock to the novel plasma process presented in section 3.4.

3.3. Typical treatments and the diamond surface composition

3.3.1. High-temperature annealing

A common feature to the techniques used to artificially create NV centers in diamond such as implantation and irradiation of species is the subsequent thermal annealing treatment. This is an important step related to the vacancy mobility in diamond, as previously discussed in section 2.1.1. The diamond exposure to high temperatures is also necessary to reconstitute the diamond lattice that has been

Figure 3.5.: Schematic representation of the diamond surface composition after thermal annealing. Schematic representation of the surface composition of a the diamond top-layers after thermal annealing (surface termination not shown for clarity). The top-layers are converted to graphite, whereas the sub-surface region presents a smooth phase transition including the amorphous carbon. The curve on the right represents the concentration of lattice defects ([D]) versus the depth. A highly defective region leads to the amorphisation of diamond. Figure adapted from Ref. [53].

damaged by the ion/electron impact [78]. A drawback is related to the fact that diamond is a meta-stable phase of carbon. High temperature annealing under an atmosphere with even a minimum oxygen concentration [49] leads to lattice re-constitution with additional phase transitions (sp^3 - sp^2) in the top-layers of the diamond substrate [189–191].

The phase composition of diamond after thermal annealing is schematically presented in figure 3.5. The top-layers of the substrate are completely graphitized and, at thermodynamic equilibrium, the transition from the bulk sp^2 to the pristine sp^3 carbon phases is accompanied by an in-between region of disordered lattice known as *amorphous carbon* (α-sp^3) [53]. The thickness of this disordered lattice depends on the annealing temperature, as well as on the initial crystal quality of the diamond substrate. The phase transition profile at the substrate surface corresponds directly to a profile of defects, as schematically represented at the right hand side of figure 3.5.

Although graphite can be easily removed by wet chemical processes, amorphous carbon is chemically inert. Moreover, the disordered lattice of amorphous carbon

is known to induce electronic states in the band gap of diamond, e.g. unpaired electrons from the defective lattice [53]. This is a potential reasons of the strongly degraded spin and optical properties of NV centers in the near-surface region after thermal annealing. Moreover, energetic plasma ion bombardment is expect to increase the thickness of the defective diamond layers [53].
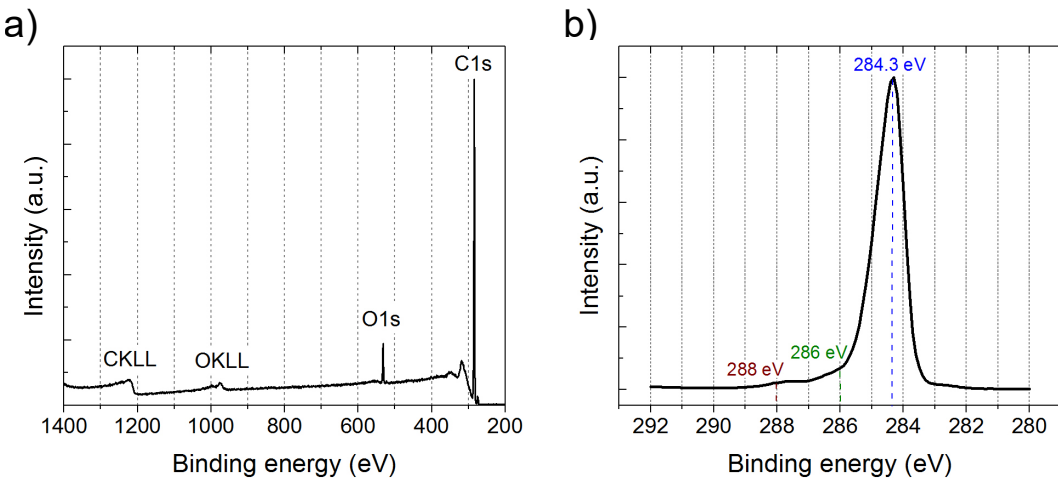
3.3.2. Wet chemical oxidation

The discussion presented in section 1.4 revealed that the presence of hydrocarbons and oxygen atoms at the diamond surface (an oxygen-terminated surface) favors the negative charge stability of NV centers by avoiding the surface band bending. One of the simplest techniques for such chemical surface modification is exposing the diamond to a highly-oxidizing chemical solution [192].

Such a method can be employed to remove graphitized layers (induced by thermal annealing) and convert the diamond surface termination from hydrogen to oxygen with an efficient coverage. This is important not only for the charge state of near-surface NV centers, but also for the semiconducting properties of the diamond surface [101, 102, 134]. The chemical composition of the diamond surface after such oxidizing chemical treatment is the object of study of this section.

To investigate this, a single-crystal [100]-oriented electronic grade type IIa diamond with a polished surface synthesized by Element Six is utilized. In order to gain both quantitative and qualitative insights into the chemical composition of the diamond surface after each treatment, the substrate is analyzed by X-ray photoelectron spectroscopy (XPS), as described in Appendix A.3. Since energy transfer of the primary X-ray beam can ionize atoms located at the top-surface layers and reduce the measurement sensitivity, charge-accumulation at the excited region of the insulating substrate is avoided by previously overgrowing a thick highly boron-doped conductive diamond layer on the substrate surface by CVD technique. Further details on the growth process can be also found in Appendix D.

The diamond surface oxidation is performed by WCO treatment, as previously described in section 2.1. The wide-energy XPS spectrum measured normal to the diamond surface is shown in figure 3.6 a). The carbon C1s and oxygen O1s core level signals are clearly visible. The later is located at the expected binding energy of 532 eV [66, 193] and represents a mixture of singly- and doubly-bound oxygen atoms at the diamond surface.

a)

b)

Figure 3.6.: XPS spectra of diamond after wet chemical oxidation. a) Wide-energy XPS signal of the C1s and O1s core levels acquired normal to the diamond surface. The oxygen surface coverage is estimated by using the C1s and O1s peak areas (see text). The Auger peaks corresponding to the KLL carbon and oxygen electron emissions are also observed at ~ 1220 and ~ 980 eV, respectively. **b)** High resolution XPS signal of the C1s core level acquired normal to the diamond surface. The peak at 284.3 eV of binding energy corresponds to the signal from carbon-carbon sp^3 bonds. The peaks at 286 and 288 eV of binding energies correspond to oxygen functional groups at the surface. The signal intensities are normalized by the respective peak value at 284.3 eV of binding energy.

The relative peak intensity determines the percentage of oxygen coverage of the diamond surface. Other factors such as different X-ray ionization cross-sections for different species and detector efficiency can make a qualitative evaluation challenging, but the calculated oxygen-to-carbon ratio in figure 3.6 a) of approximately 0.13 indicates a high surface coverage by oxygen atoms [194]. Although an unambiguous evaluation of the O1s peak is not possible due to the low energy resolution at the O1s peak, the absence of signal related to other elements in the spectrum indicates the dominance of oxygen groups at the surface.

Further insights on the surface termination and the carbon hybridization are provided by the C1s core high-resolution XPS spectrum acquired normal to the diamond surface shown in figure 3.6 b). The dominant peak at the 284.3 eV of binding energy is associated to carbon-carbon bonds characteristic of the diamond phase in a sp^3 hybridized configuration [195, 196]. The asymmetry observed in the peak towards higher binding energies is associated to carbon-oxygen surface functional groups such as carbonyl (C=O, ~ 288 eV) and ether (C-O-C, ~ 286 eV) [192, 194]. Importantly, no traces of graphite can be observed in figure 3.6 b), indicating its complete removal after the WCO treatment. Furthermore, signal from

amorphous carbon at the diamond surface could not be unambiguously identified (i.e. intensity below the detection limit), which means this defective layer has indeed a thickness of even less than a few atomic layers. This chemical composition of the oxygen-terminated surface will be used as the reference in the analysis of surface modification by different plasma treatments.
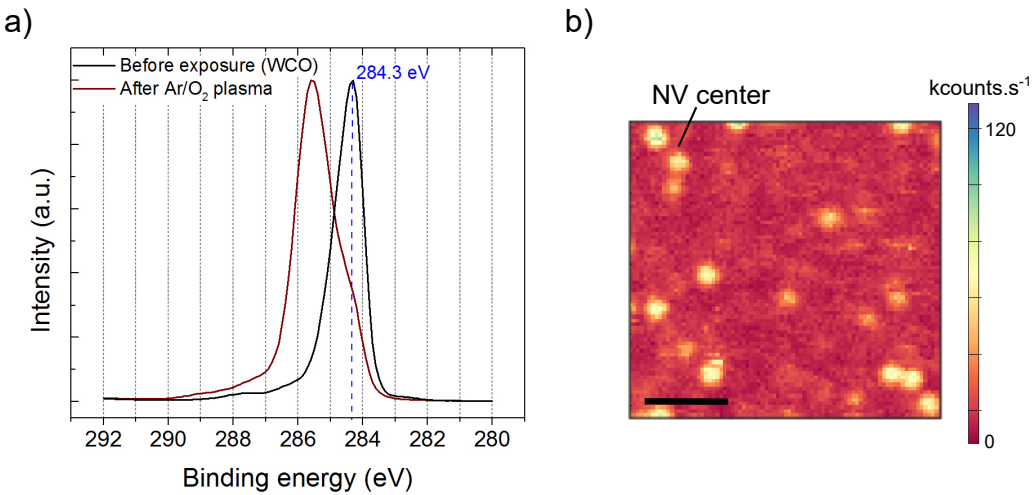
3.3.3. Surface damage by capacitively-coupled RIE plasma

The changes on the properties of the diamond surface after the exposure to a capacitively coupled RIE plasma process are experimentally investigated utilizing the same substrate as described for the WCO treatment (see section 3.3.2). Part of the diamond surface after the WCO treatment is masked by lithographically-patterned AZ5214E photoresist (MicroChemicals, thickness of $\sim 1.2\,\mu m$). The sample is afterwards exposed to Ar/O_2 capacitive RIE plasma using the following parameters: 37.5 mTorr of constant chamber pressure (base pressure of $< 10^{-6}$ mTorr), 100 and 11 sccm of Ar and O_2 gas flow, respectively, 70 W of capacitive RIE power, and 20°C of plate temperature. The exposure time is 16 min, where the resulting etching rate was measured by AFM to be approximately $11\,nm.min^{-1}$.

Such a plasma process delivers a strong ion bombardment on the diamond surface by the auxiliary Ar ions, which results in detectable damages to the diamond top-layers, as preliminarily investigated in Ref. [53]. At first, the chemical composition of the surface after the described plasma exposure is analyzed by XPS. Figure 3.7 a) shows the high-resolution XPS spectra of the C1s core level acquired normal to the diamond surface. The black line represents the reference chemical composition resulting from the WCO treatment, as previously explained (see figure 3.6 b). This confirms that the used mask efficiently protected the diamond surface from the plasma attack.

The dark-red line represents the chemical composition of the diamond surface after the Ar/O_2 capacitive RIE plasma process. The spectrum shows a broadband peak with a reduced intensity at the carbon-carbon sp^3 hybridized bonds at 284.3 eV of binding energy. A strong component shifted by $+1.2$ eV from the sp^3 bulk component is observed as the dominant signal. This is associated to a surface layer of amorphous phase of carbon (α-sp^3) with a few nanometers in thickness [50, 53]. Such phase transition induced by the energy transfer from the ion bombardment to carbon atoms is the signature of plasma-induced lattice damages.

Another aspect related to the ion bombardment of diamond is the possible creation of vacancies at the sub-surface region. This is particularly important in

Figure 3.7.: **Investigation of the diamond surface before and after the exposure to Ar/O$_2$ capacitive RIE plasma. a)** High resolution XPS signal of the C1s core level acquired normal to the diamond surface before (black line) and after (dark-red line) the diamond exposure to Ar/O$_2$ capacitive RIE plasma. The peaks at 284.3 eV of binding energy corresponds to the signal from carbon-carbon sp^3 bonds. A strong shift of approximately +1.2 eV in the binding energy is observed in the peak after the plasma exposure. The signal intensity is normalized by the peak value at 284.3 eV of binding energy. **b)** Confocal microscopy image of the diamond surface exposed to the Ar/O$_2$ capacitive RIE plasma process and subsequently annealed at a temperature of 950°C for two hours. The scale bar represents 2 μm.

applications using artificially-created NV centers, since these vacancies would migrate during thermal annealing and induce a background concentration of color centers from ingrown nitrogen atoms [51]. Figure 3.7 b) presents the confocal microscopy image (see Appendix A.1) of the surface of a ultra-pure diamond substrate annealed at a temperature of 950°C for two hours after the substrate exposure to the Ar/O$_2$ capacitive RIE plasma for 15 min. As indicated by the image, single NV centers are observed over the whole area exposed to the plasma treatment. The majority of these NV centers presents a reduced photon-emission rate, no magnetic response and a blinking behavior under 532 nm laser excitation. This indicates the presence of lattice defects in their vicinity, which leads to a depletion of their negative charged state (i.e. dominance of NV^0). Regions that are not exposed to the Ar/O$_2$ capacitive RIE plasma process prior to thermal annealing present a small background density of NV centers of less than 10% from the corresponding density in figure 3.7 b).

3.4. Low-damage oxygen plasma process
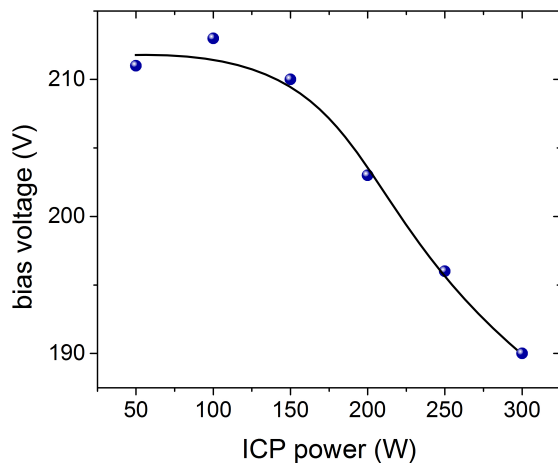
As investigated in the last sections, the plasma processing of diamond materials is a well-established technique in terms of a smoothness, uniformity and high versatility in the controlled removal of material. Highly sensitive quantum sensing using the electron spin of NV centers via dipole-dipole magnetic coupling would be highly benefited from the centers being as close as possible to the targeted sensing species, i.e. closer to the diamond surface. The nanometer control resulting from the plasma etching of diamond is therefore a potential technique to post-treat diamond materials, thus bringing NV centers closer to the surface.

The drawbacks related to the plasma-induced lattice damage have so far limited the compatibility of plasma processes with NV centers. Recent reports [51, 52] have investigated the use of different types of systems to generate plasma (i.e. capacitive RIE, barrel and downstream reactors) related to the quality of the etched material and the properties of NV centers located in the nanometer vicinity of the etched surface. Although remarkable results have been achieved, a nanometer-precise, uniform, and high-selective etching process, by which the damages to the etched diamond surface are avoided, is yet to be demonstrated.

3.4.1. Process parameters

The oxygen soft plasma process has been developed using a plasma machine with separated capacitively coupled RIE and ICP sources (see Appendix B for technical details). The oxygen plasma recipe consists of two steps. At first, the capacitively coupled radio frequency (RF) source with 30 W of power is used to ignite the RIE plasma for a few seconds. Afterwards, the capacitive RF source is switched off, and the plasma is sustained only by the ICP source with a power of 180 W (this can be varied upon application, see below). The constant parameters through the two steps are 10 mTorr of chamber pressure (base pressure of $< 10^{-6}$ mTorr), 30 sccm of O_2 gas flow and 20°C temperature of the substrate holder. This process is hereinafter referred to as *oxygen soft plasma.*

The chamber design is the key feature related to the oxygen soft plasma process: the ICP source used to performed the treatment is located remotely in the chamber, e.g. the relative position between the ICP source and the diamond substrate to be processed is larger than the skin-depth of the produced plasma (see section 3.2.2 and figure 3.4). This is further evidenced by using both capacitively coupled RF and ICP sources simultaneously. Figure 3.8 presents the change of bias voltage for

Figure 3.8.: Bias-voltage dependency on the ICP power for an RIE/ICP oxygen plasma process. The corresponding change in bias voltage using increasing ICP power is shown for the use of both capacitively coupled RF and ICP sources together. A decrease in the bias voltage indicates a higher recombination rate of ions in the plasma bulk and sheath. The line is a guide to the eye.

increasing ICP power while the capacitive RF power is kept constant at 30 W. As seen, no significant change in the self-bias voltage was observed while varying the ICP power up to 200 W.

For higher powers, a stronger decrease in the bias voltage indicates the transition where ions generated in the ICP inductive region begin to penetrate the floating sheath induced at the sample surface by the use of the capacitive RF power. In this case, the higher ion recombination rate due to a higher density translates into weaker ion currents during each RF cycle. Therefore, the ICP power for the novel oxygen plasma process presented in the following sections is limited to 200 W. In this way we assure that the diamond surface is mainly exposed to neutral chemical oxygen radicals during the oxygen soft plasma (ICP power only), thus avoiding the drawbacks related to the ion bombardment of the material.

3.4.2. Surface analysis by XPS technique

To investigate the material properties of the diamond surface after its exposure to the oxygen soft plasma, a single-crystal [100]-oriented electronic grade type IIa diamond with a polished surface synthesized by Element Six is utilized. A thick boron-doped diamond layer is overgrown on the diamond surface to avoid charge accumulation during XPS measurements, as previously discussed. The initial root
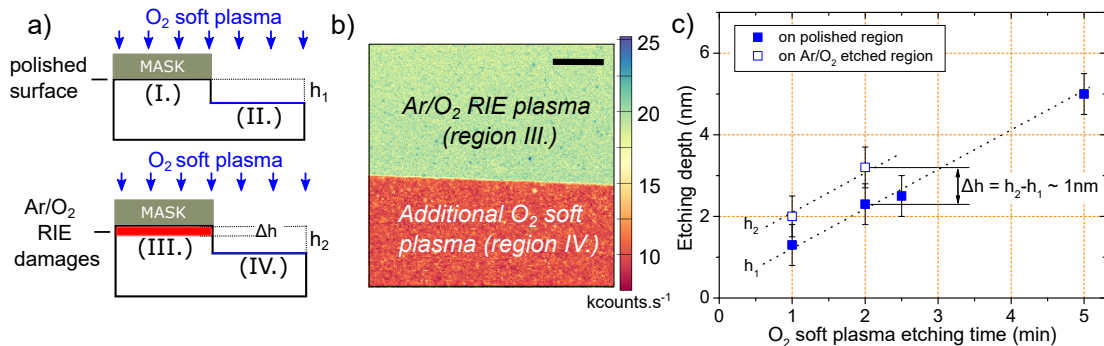
mean square (RMS) surface roughness is measured by AFM to be in the range of 1 nm, which allows a precise analysis of the surface morphology.

The experiment is schematically represented in figure 3.9 a). First, roughly half of the polished diamond surface is covered by lithography-patterned AZ5214E photoresist (thickness of $\sim 1.2\,\mu$m). Subsequently, the sample is exposed to Ar/O_2 capacitive RIE plasma for 16 min using the parameters described in section 3.3.3, which results in the removal of material to a depth of ~ 180 nm. Next, another mask using the same type of photo-resist is patterned both on the polished and the Ar/O_2-etched regions, leaving small stripes ($\sim\mu$m wide) open to the following exposure to the oxygen soft plasma. The last step can be repeated several times on the same substrate to investigate different exposure times and ICP powers.

As seen in figure 3.9 a), this sequence of steps results in four different surface areas on the same diamond substrate, namely (I.) polished, (II.) polished processed with oxygen soft plasma, (III.) Ar/O_2 capacitive RIE as-etched, and (IV.) Ar/O_2 etched processed with oxygen soft plasma. To assure an oxygen-terminated surface and to remove any traces of graphite, the substrate is cleaned after each plasma process using the WCO treatment (see section 3.3.2).

The effects of the oxygen soft plasma on the morphology from each of the described areas of the substrate surface are analyzed by confocal microscopy and AFM (technical details can be found in Appendix A.1). Figure 3.9 b) shows the confocal microscopy image of the diamond surface at the interface between regions corresponding to the Ar/O_2 as-etched (III., upper part of the image) and Ar/O_2 etched after the additional oxygen soft plasma exposure (IV., lower part of the image). As seen in the figure, the Ar/O_2 plasma-induced lattice damages (investigated in section 3.3.3) are revealed as a slightly increased luminescence background in the confocal image. The lower part of the image corresponds to the additional oxygen soft plasma exposure with an ICP power of 180 W for 1 min. As seen, such a treatment is enough to eliminate the photoluminescence background related to the plasma-induced lattice damages.
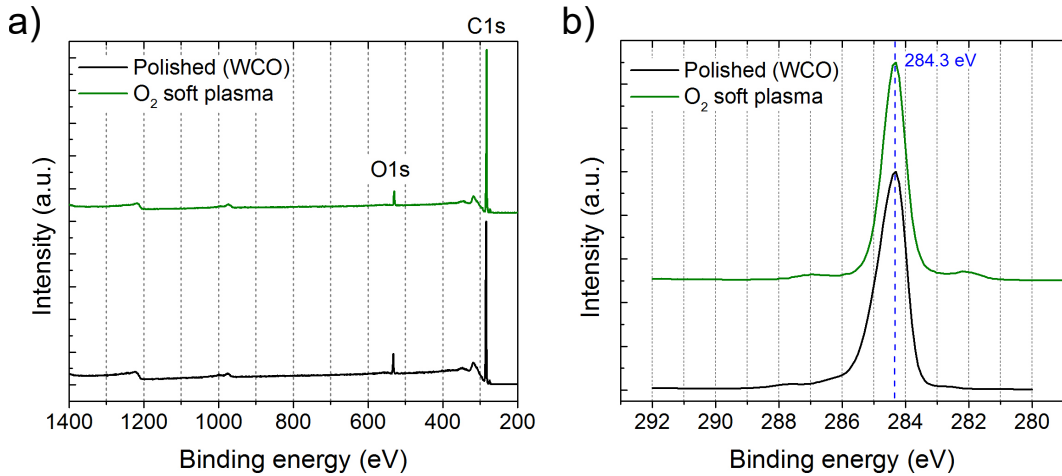
Supporting AFM measurements are shown in figure 3.9 c). There, individual areas of the initially polished (I.) and Ar/O_2 etched (III.) substrate surface are exposed to the oxygen soft plasma with 180 W of power for different etching times. For each time, the etching depth at both regions is measured by AFM, being represented by h_1 and h_2 in figures 3.9 a) and c). The uncertainty in the etching depth is connected directly to the surface roughness of ~ 1 nm (RMS). The exposure of both areas to the oxygen soft plasma for 1 min reveals an additional etching depth of approximately $1-2$ nm at the originally Ar/O_2 etched region in

Figure 3.9.: Investigation of the diamond surface morphology and the effects of the soft oxygen plasma. a) Schematic representation of the performed etching experiment to evaluate different surface morphologies and chemical compositions (see text). **b)** Confocal microscopy image of the diamond surface previously treated with Ar/O_2 capacitive RIE plasma (see section 3.3.3) and afterwards partially treated with the oxygen soft plasma; the photo-luminescence contrast between the damaged surface by the Ar/O_2 ion bombardment and the post-treated region is clearly seen. The scale bar represents $20\,\mu m$. **c)** AFM etching depth measurements from two regions of the diamond substrate treated using the oxygen soft plasma (initially polished (I.) and previously etched by Ar/O_2 capacitive RIE plasma for $\sim 180\,nm$ (III.)). The difference in the etching rate is represented by Δh, which is attributed to the initial faster removal of Ar/O_2 plasma-induced damaged layers (schematically indicated in a as the red area).

comparison to the initially polished (represented by Δh in figure 3.9 c). Longer exposure times do not result in any significant variation in Δh. This difference is therefore attributed to the faster initial removal of the amorphous carbon phase in the damaged top-layers of the substrate previously exposed to the capacitively coupled RIE plasma. Moreover, the etching rate of diamond by the oxygen soft plasma with $180\,W$ of ICP power is thereby calibrated to be $\sim 1.5\pm 1.0\,nm.min^{-1}$. This is reproducibly observed using several substrates.

Figure 3.10 b) shows high-resolution XPS measurements of the C1s core level related to the regions originally polished after WCO (I., black line) and Ar/O_2 etched after an additional treatment of oxygen soft plasma with $180\,W$ of ICP power for $1\,min$ (IV., dark-green line). As apparent from the figure, both spectra are very similar, showing the dominance of the signal from the sp^3 hybridized carbon-carbon bonds together with small components shifted towards higher binding energies representing carbon-oxygen functional groups at the diamond surface. Importantly, the XPS signature of plasma-induced lattice damages (see figure 3.7) is absent from the XPS spectrum after the oxygen soft plasma treatment. Moreover, both oxygen soft plasma and WCO treatments result in similar intensities of the O1s core level, as shown in the corresponding wide-energy XPS spectra

Figure 3.10.: XPS measurements comparing the WCO and oxygen soft plasma treatments. a) Wide-energy XPS signals of the C1s and O1s core levels and **b)** high resolution XPS signals of the C1s core level. Both were acquired normal to the diamond surface in two different regions of the substrate, namely polished after WCO (black lines) and Ar/O_2 etched after an additional treatment of oxygen soft plasma for 1 min (dark-green lines). The signal intensities are normalized by the peak value at 284.3 eV of binding energy and are vertically shifted for clarity.

in figure 3.10 a). This indicates a similar high oxygen coverage of the diamond surface.

As investigated in section 3.3.3, new NV centers can be formed after annealing plasma-damaged diamond surfaces at high temperatures. In contrast to what is shown in figure 3.7, no new NV centers are observed in confocal microscopy surface images of regions additionally treated with the oxygen soft plasma and subsequently annealed at high temperature. This further supports the previous assumptions and confirms the complete removal of the damaged top-layers that would host plasma-induced vacancies.

3.4.3. Depth profiling of NV centers by step-etching

Near-surface NV centers are exquisite tools that can be used to detect plasma-induced lattice damages, since their properties are extremely sensitive to surface modifications and electronic states induced in the lattice energy band gap [51, 52, 197]. To further validate the compatibility of the oxygen soft plasma process with nearby spin defects, the depth distribution of NV centers created in the nanometer vicinity of the diamond surface is analyzed. To this aim, a single-

crystal [100]-oriented electronic grade type IIa diamond with a polished surface synthesized by Element Six is utilized. NV centers are created by implanting nitrogen ions with $5.0\,\mathrm{keV}$ of energy and an ion fluence of $4 \times 10^{10}\,\mathrm{cm}^{-2}$. The substrate is subsequently annealed at a temperature of $\sim 950°\mathrm{C}$ under vacuum condition ($< 10^{-6}\,\mathrm{mbar}$) for two hours. An oxygen-terminated surface is obtained by using the WCO treatment.
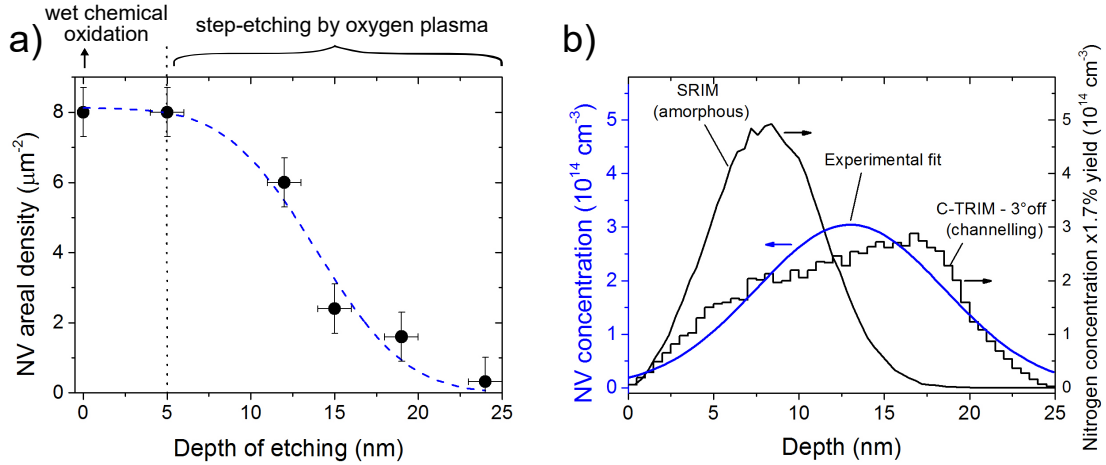
The evaluation consists of sequential etching steps using the oxygen soft plasma followed by confocal microscopy measurements to evaluate the remaining areal density of NV centers. Each etching step comprised the removal of $4\,\mathrm{nm}$ from the diamond surface by capacitively coupled RIE oxygen plasma ($10\,\mathrm{mTorr}$, $30\,\mathrm{W}$ RF power and $1\,\mathrm{min}$ exposure time), followed by $1\,\mathrm{min}$ of exposure to the oxygen soft plasma ($180\,\mathrm{W}$ of ICP power). The last treatment aims the removal of any residual plasma-induced damages, as confirmed in the previous section.

The experimental areal density of NV centers versus the etching depth is shown in figure 3.11 a). For simplicity, the experimental data are fitted using a Gaussian complementary error function, which represents the antiderivative of a Gaussian distribution function (see Appendix E). It should be highlighted that the experimental point related to the first etching step at $5\,\mathrm{nm}$ (vertical-dotted line in figure 3.11 a) does not show any abrupt reduction in the density of NV centers in comparison to the initial values for the oxygen-terminated surface by WCO treatment. This is in contrast to other plasma processes reported in literature [51, 52]. The developed plasma process can thereby be ascertained to preserve the optical properties of nearby NV centers.

The fitted volumetric concentration distribution of implanted nitrogen atoms is shown in figure 3.11 b) (blue line). Together with this, atomic nitrogen distribution profiles simulated using SRIM and CTRIM are shown according to the experimental ion fluence. As seen, the experimental distribution is in good agreement with the CTRIM simulated profile for a [100]-oriented diamond surface. The implantation angle gives the relative contribution of ion stopping/channeling and the used value of $3°$ is in the frame of the accuracy specified for the surface polishing and accuracy of the implantor setup (see appendix A.2).

These results show that the step-etching technique by the oxygen soft plasma is sensitive enough to resolve the ion channeling effect even for a very narrow distribution of NV centers close to the diamond surface (i.e. for a low implantation energy). Moreover, the presence of ion channeling in the presented experimental results supports previous theoretical investigations of ion implantation in diamond [147]. By comparing the distributions in figure 3.11 b), a formation yield of NV
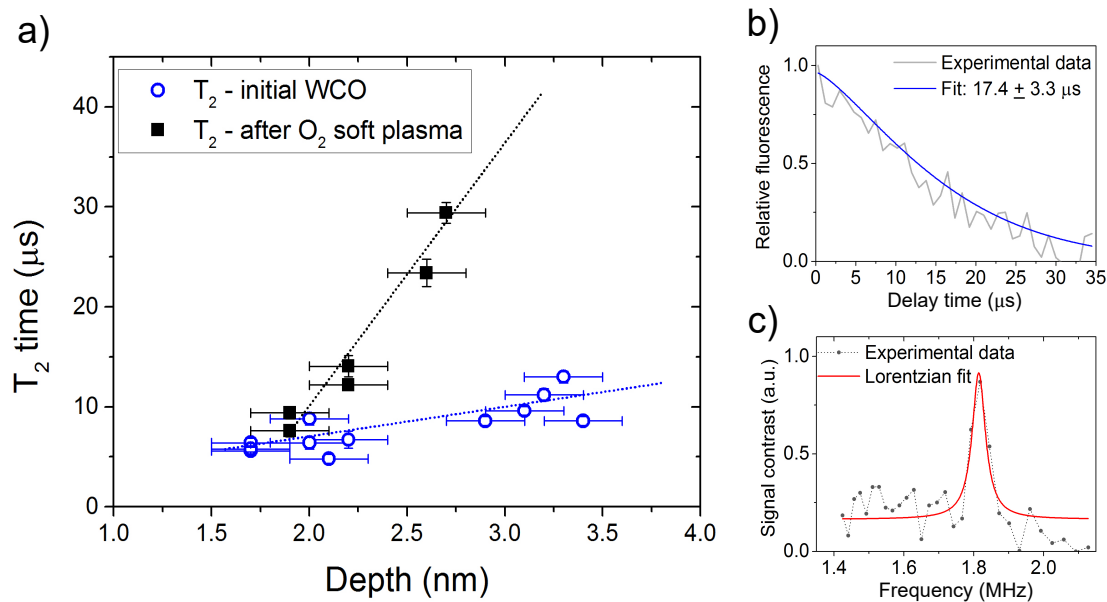
Figure 3.11.: Depth distribution of near-surface NV centers by step-etching technique. a) Experimental values of the areal density of NV centers by 5.0 keV of energy vs. the etching depth. The fit corresponds to a Gaussian complementary error function (dashed line). **b)** The depth profile of NV centers using the corresponding Gaussian distribution function is shown (blue line) together with corresponding atomic nitrogen distribution profiles simulated using SRIM and CTRIM.

centers from implanted atoms of $1.7 \pm 0.3\%$ is obtained, which is a typical value for the used implantation energy (see section 2.2.2).

3.4.4. Spin benchmark measurements

The influence of the oxygen soft plasma on the spin characteristics of near-surface NV centers are of great interest considering their use in quantum sensing applications. The figure of merit utilized to evaluate the spin characteristics of NV centers before and after the surface exposure to the oxygen soft plasma is the corresponding T_2 times. To avoid any undesired decoherence effects due to e.g. polishing-induced defects and the ^{13}C nuclear spin bath [88], this experiment is conducted on an initially as-grown surface of a ^{12}C isotopically purified (99.999%) diamond CVD layer with more than 50 μm of thickness, overgrown on a ultra-pure single-crystal [100]-oriented electronic grade CVD diamond substrate (Element Six). The substrate is implanted with nitrogen ions with 2.5 keV of energy and an ion fluence of 7×10^9 cm^{-2} and subsequently annealed at a temperature of 950°C under vacuum condition ($< 10^{-6}$ mbar) for two hours. The mean depth of NV centers is expected to be ~ 5 nm [145, 146]. An oxygen-terminated surface is achieved by WCO treatment.

Figure 3.12.: Effect of the oxygen soft plasma on the spin properties of near-surface NV centers. a) Spin coherence times (T_2, Hahn echo sequence) vs. depth of single NV centers evaluated by the NMR signal from protons on the diamond surface. **b)** An example of the decoherence decay used to extract the T_2 time of an NV center is shown; no traces of the electron spin echo envelope modulation (ESEEM) originated from nearby ^{13}C nuclear spins can be observed, confirming the isotopic purification of the diamond film. **c)** An example of the observed contrast in the decoherence decay of an NV center is shown when the precession frequency of external proton nuclei is locked-in by the used detection scheme (see text).

Single NV centers are addressed by confocal microscopy technique and T_2 times are measured using a Hahn-echo microwave sequence (see Appendix A.1 and section 1.3, respectively). A magnetic field of approximately 42 mT is applied parallel to one of the possible orientations of NV centers. Further on, NMR signal from proton nuclear spins located on the diamond surface (from the immersion oil) is acquired using a XY8-16 microwave pulse sequence and used to calibrate the depth of NV centers (see Appendix G for further details). The results are summarized in figure 3.12.

The substrate surface hosting NV centers is exposed to the oxygen soft plasma with 200 W of ICP power for 2 min, corresponding to an etching depth of approximately 3 nm (measured by AFM). As seen in figure 3.12 a), NV centers located a few nanometers (< 4 nm) below the diamond surface with stable photoluminescence are still observed after the plasma exposure. This further supports the assumption of the preservation of the optical properties of near-surface NV centers

by the developed plasma process. Likewise, the T_2 times of NV centers below the etched surface show even an improvement of up to 3 times in comparison to values measured for the bare WCO-treated surface. A high NMR signal amplitude ranging up to $B_{\mathrm{RMS}} = 3.1\,\mu\mathrm{T}$ is estimated from the sensing of protons on the diamond surface, being especially enhanced for NV centers located very shallowly ($< 2.5\,\mathrm{nm}$).

Although the preservation of values alone would already represent a remarkable result, the reason for the enhanced values measured after the substrate exposure to the oxygen soft plasma is not clear. One possibility is the modification of the electronic configuration of the diamond surface and the reduction in the density of active sites (e.g. dangling bonds), which would negatively affect the optical and spin properties of nearby NV centers. Indeed, fluctuations of surface charges are believed to be a significant source of decoherence due to e.g. electric field fluctuations [37], meaning the developed plasma process may increase the surface charge stability. The sources of spin decoherence for NV centers created by nitrogen implantation near the diamond surface will be further investigated in Chapter 4.

3.5. Summary and outlook

In this Chapter, an alternative method for etching diamond was presented. The development of such smooth plasma process is one of the key techniques utilized in this work for material modification and structuring. Throughout the next Chapters, methods to engineer near-surface NV centers with augmented properties using different diamond structures will be demonstrated. The capabilities of controlled material removal with high selectivity and reproducibility, while preserving the optical and spin properties of nearby NV centers will be in the heart of all fabricated structures.

4. Tailoring spin defects in diamond by lattice charging effects

The technique of nitrogen implantation followed by thermal annealing was introduced in Chapter 2. Despite its excellent spatial positioning accuracy, the main drawback of this method is the concomitant low efficiency in the conversion from implanted nitrogen atoms to NV centers (yield), while the resulting NV centers suffer from degraded spin and optical properties. This has been attributed mainly to residual implantation damages in the surrounding region of the path of implanted ions in the lattice (and consequently around NV centers) that are not fully eliminated by the thermal annealing treatment.

Despite the remarkable achievements reported using implanted NV centers, degraded spin properties limit their interaction time with target spin systems [27, 198], which is the key roadblock to NV centers-based quantum applications. Understand the formation dynamics of implanted NV centers and the development of methods to overcome the mentioned issues are therefore of extreme importance. This would have an impact not only on diamond-based devices, but also a broader implication for other solid-state defect-host materials.

In this Chapter, the nitrogen implantation technique is further explored. First, numerical simulations are used to analyze the formation of NV centers and different lattice defects at the nano-scale and their correlation to the observed degraded spin performance of implanted NV centers. According to these results, a novel method to tailor the formation of implantation lattice defects is presented. The technique is based on implanting nitrogen atoms into the space-charge layer of injected free carriers (holes) in a ultra-pure diamond substrate, generated by a nanometer-thin heavily boron-doped diamond surface film. The concomitant effects of the induced excess of free charge carriers on the diffusion and recombination of implantation defects (including NV centers) are analyzed. At the end, noise spectroscopy technique is utilized to gain further insights into the noise environment of NV centers created near to the diamond surface utilizing both the developed method and the conventional nitrogen implantation technique.

The main results presented in this Chapter are published in F. Fávaro de Oliveira *et al.*, Nature Communications **8**, 15409 (2017).

4.1. Numerical simulations: formation of NV centers and lattice defects

4.1.1. Implantation process: Molecular Dynamics simulation
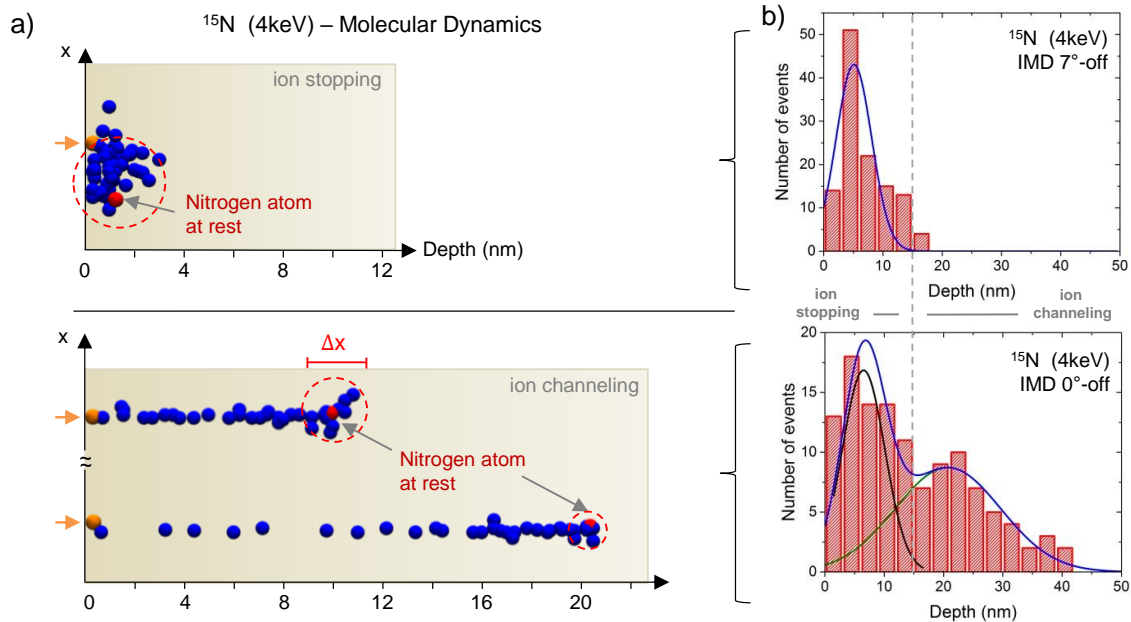
The basic concepts of the kinetics of ion implantation have been discussed in section 2.2. In this section, the distribution of vacancies at individual nitrogen implantation sites in diamond is investigated by Molecular Dynamics (MD) simulations[1], similarly to Ref. [147]. The ITAP MD (IMD) program package [199, 200] is used to simulate individual nitrogen implantation events for a kinetic energy of 4.0 keV in a [100]-oriented diamond cell with $5.5 \times 5.5 \times 52\,\text{nm}^3$ of volume. The interatomic interactions are generally represented by a bond-ordered Tersoff potential [201–205], with the interaction parameters as given in Refs. [205, 206]. For interatomic separations smaller than 0.3 Å, the Tersoff potential is smoothly switched to a two-body Ziegler-Biersack-Littmark (ZBL) potential [207, 208].

In a first step, the simulated diamond cell is brought into thermodynamic equilibrium (at room temperature). This is achieved by five NPT (constant number of particles, pressure and temperature) and one final NVE (constant number of particles, volume and pressure) simulation steps [147]. The initial four steps are employed to simulate the heat of the structure up to 1000 K, allowing it to relax at this temperature, cool down to room temperature (RT) and finally relaxing it at RT using periodic boundaries in all directions. The last NPT step has the periodic boundary conditions in the z-direction (implantation direction) removed. Finally, the NVE step balances the system with the ground layers of the diamond cell fixed in the z-direction. The entire NPT ensemble simulations are performed with a time step of 0.1 fs and the NVE equilibrium step with 0.01 fs.

Afterwards, the nitrogen atom (to be implanted) is placed on the top of the diamond surface at a distance of $d = 2.51$ Å, assuring that its initial location is beyond the action range of the Tersoff potential. The nitrogen atom is then implanted in the diamond cell by the attribution of the mentioned kinetic energy in a direction normal to the diamond surface. The final condition of the diamond

---
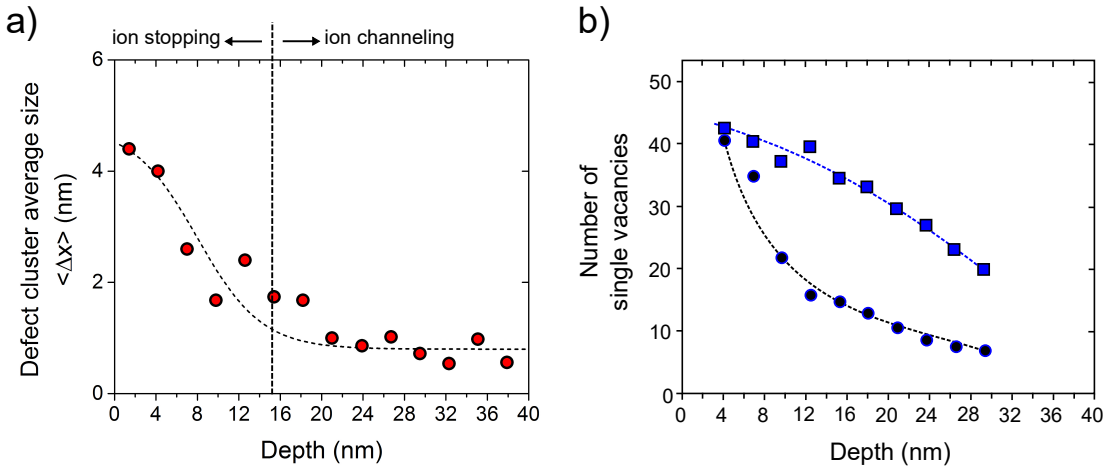
[1]Simulations performed in collaboration with Denis Antonov.

Figure 4.1.: Molecular dynamics simulation of nitrogen ion tracks in the diamond lattice. a) Individual simulated nitrogen implantation sites (indicated by orange arrows) by Molecular Dynamics with 4.0 keV kinetic energy are shown. The upper and lower figures represent the cases of absent and pronounced ion channeling, respectively. Blue dots depict implantation-induced vacancies, whereas red dots depict the implanted nitrogen atoms at the rest position (orange dots represent the ion penetration position). The size (Δx) of the volume containing the cluster of single vacancies that surrounds each implanted nitrogen atom at rest is highlighted by the red-dashed circles. **b)** Simulated atomic distributions of nitrogen atoms by Molecular Dynamics are shown. The two different implantation off-angles (7° and 0°) represent the cases of absent and pronounced ion channeling, respectively. The solid lines are Gaussian distribution fitting functions (see equation 2.1).

cell is analyzed by comparing the lattice condition before and after the nitrogen implantation event. A shell with a radius of 1.54 Å is placed around each lattice atom, in which the number of atoms allows a direct analysis of the concentration of lattice defects generated by the implantation event.

The IMD simulation is repeated 120 times to provide enough statistical information. In each repetition, the starting position of the nitrogen atom on the xy-plane is randomly varied. In this way, the ion channeling effect on the stopping depth of implanted atoms can be analyzed. Implantation trajectories of nitrogen ions in diamond simulated with identical kinetic energies, but resulting in different ion implantation depths are shown in figure 4.1 a). The upper and lower simulation projections on the xz-plane represent cases of absence and pronounced ion

Figure 4.2.: Molecular dynamics simulation: defect-clusters of implantation defects.
a) The size of simulated defect-clusters by Molecular Dynamics are shown as a function of the nitrogen penetration depth. The vertical-dashed line represents the separation between the ion stopping and channeling ranges, as depicted in figure 4.1 b). **b)** The depth-dependencies of single vacancies counted at individual implantation sites (squares) and confined within defect-clusters of nanometer radius (see figure 4.1) around implanted nitrogen atoms at rest (circles) are shown. In both figures, dashed lines are guides to the eye.

channeling, respectively. As seen, the spatial distribution of as-implanted vacancies is strongly influenced by the ion channeling effect. The corresponding depth distributions of implanted nitrogen atoms are shown in figure 4.1 b). The two different implantation off-angles (7° and 0°) represent the cases of absence and pronounced ion channeling, respectively. The observed distributions clearly identify the expected differences in the rest-position of implanted nitrogen atoms when ion channeling is dominant.

The disordered region along individual implanted ion tracks in the diamond lattice is defined as a *defect-cluster*. These highly-disordered regions are highlighted by the red-dashed circles in figure 4.1 a). The corresponding simulated depth-dependency of the average size of defect clusters (Δx) is shown in figure 4.2 a). The value of Δx decreases rapidly with increasing implantation depth and reaches a constant value for nitrogen atoms at the ion channeling tail of the depth distribution.

As shown in figure 4.2 b), the number of vacancies created per implanted nitrogen ion (squares) shows similar values when integrated over the whole implantation path. This is a signature of the predominant nuclear energy loss mechanism as the implanted atom penetrates the crystal lattice. Nonetheless, a smaller number

of vacancies is observed in the immediate vicinity of nitrogen atoms that rest at larger depths (ion channeling range). This is evidenced in figure 4.2 b) (circles), where the number of vacancies within defect clusters is shown as a function of the implantation depth. As illustrated by the correlation of figures 4.2 a) and b), as-implanted nitrogen atoms that rest closer to the diamond surface are surrounded by a higher concentration of single vacancies.

The presented simulations show that, regardless the penetration depth of nitrogen, typical distances between single vacancies are below 1 nm around implanted nitrogen atoms with low energy. This corresponds to extremely high local densities of vacancies in the close vicinity of the implanted atom, reaching values of up to $\sim 10^{21}\,\mathrm{cm^{-3}}$. In contrast, ultra-pure diamond substrates with $\sim 10^{14}\,\mathrm{cm^{-3}}$ concentration of nitrogen impurities [89] result in concentrations of free electrons of approximately $10^{13}\,\mathrm{cm^{-3}}$ due to the activation of nitrogen donors at high temperatures. Under these conditions, single vacancies are mainly in the neutral charge state, such that vacancy recombination results in the formation of vacancy-related defects with higher probability than the formation of a single NV center within individual defect-clusters [209].

4.1.2. Annealing process: kinetic Monte Carlo simulation

In this section, the vacancy dynamics is further investigated by kinetic Monte Carlo (KMC) simulations[2]. The defect-clusters simulated by IMD are used as input for the spatial distribution of vacancies, carbon interstitial and implanted nitrogen atoms. Simulations are performed based on the simple model of hopping frequency of vacancies [78] given by:
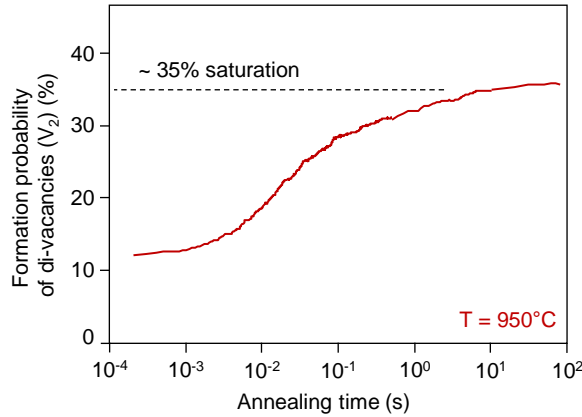
$$\Gamma = \omega_{\mathrm{a}}\exp\left(-\frac{E_{\mathrm{a}}}{k_{\mathrm{B}}T}\right), \qquad (4.1)$$

at an annealing temperature of $T = 950°\mathrm{C}$. Here, $\omega_{\mathrm{a}} = 10^{13}\,\mathrm{s^{-1}}$ [78, 138] denotes the frequency at which vacancies attempt to overcome the energy barrier E_{a} (e.g. activation energy). The values of E_{a} are 2.3 eV for vacancies [138], 1.7 eV for nitrogen interstitial atoms [210] and 1.5 eV for carbon interstitial atoms [211].

The Monte Carlo scheme models the thermal diffusion of vacancies, allowing to investigate its influence on the conversion from implanted nitrogen atoms to NV

---

[2]Simulations performed in collaboration with Denis Antonov and Timo Häußermann.

Figure 4.3.: Kinetic Monte Carlo simulation of the formation of di-vacancies in diamond. The simulated formation probability of di-vacancies during thermal annealing at 950°C is shown as a function of the annealing time. The simulation presents a rapid increase in the formation probability of di-vacancies within the first second of annealing time, followed by a saturation at a value of 35% for longer times.

centers (formation yield). The analysis considers the most predominant mechanisms of vacancy losses such as migration and recombination at the surface, recombination with interstitial carbon atoms and the formation of vacancy-related complexes. In contrast to substitutional nitrogen atoms (P1 centers) which hardly move at $T = 950$°C, interstitial nitrogen atoms are highly mobile during thermal annealing [212, 213]. In order to get enough statistics, 100 simulation runs are performed with different starting configurations of the defect-clusters by IMD.

At first, the simulation shows that the recombination of vacancies with interstitial carbon atoms occurs within the first second of thermal annealing at the mentioned temperature. After this initial rapid phenomenon of vacancy disappearance, less than 50% of the initial number of vacancies suggested by the IMD simulations are available to possibly form NV centers. The simulated vacancy diffusion process reaches a steady-state (e.g. no significant changes on the formation of defects) for simulation times longer than 2 hours. In average, more than 90% of the implantation-induced vacancies are consumed at the end of each of the simulation rounds.

As highlighted in Chapter 2, the formation of di-vacancies and small vacancy chains limits the formation efficiency and degrades the properties of created NV

centers by ion implantation. The di-vacancy (V_2) in diamond [78, 138, 214] is a paramagnetic vacancy-related defect in diamond of particular interest for the presented work. These vacancy complexes are known to be thermally-stable within the used annealing temperature range in our experiments [89]. Furthermore, such spin defects can be sources of magnetic noise and therefore a possible source of spin decoherence of nearby NV centers created by nitrogen implantation.

The simulated average formation probability of di-vacancy complexes in diamond versus the annealing time is show in figure 4.3 ($T = 950°$C). As seen, approximately 35% of all implantation-induced vacancies within defect-clusters are expected to recombine and form di-vacancies in the implanted diamond lattice. Moreover, the rapid increase in the formation probability of di-vacancy complexes within the first second of annealing represents the completeness of the initial fast recombination of carbon interstitial atoms and vacancies, as previously described. In the case of low-energy nitrogen implantation, a nanometer-volume surrounding individual implanted nitrogen atoms (e.g. and potential NV centers) is calculated to host in average $4 - 6$ di-vacancies for depths of < 5 nm below the diamond surface. The exact configuration of di-vacancies depends however on the stopping depth of the implanted nitrogen, e.g. on the depth of the created NV center (see figure 4.1 a).

4.1.3. Spin decoherence: numerical estimations
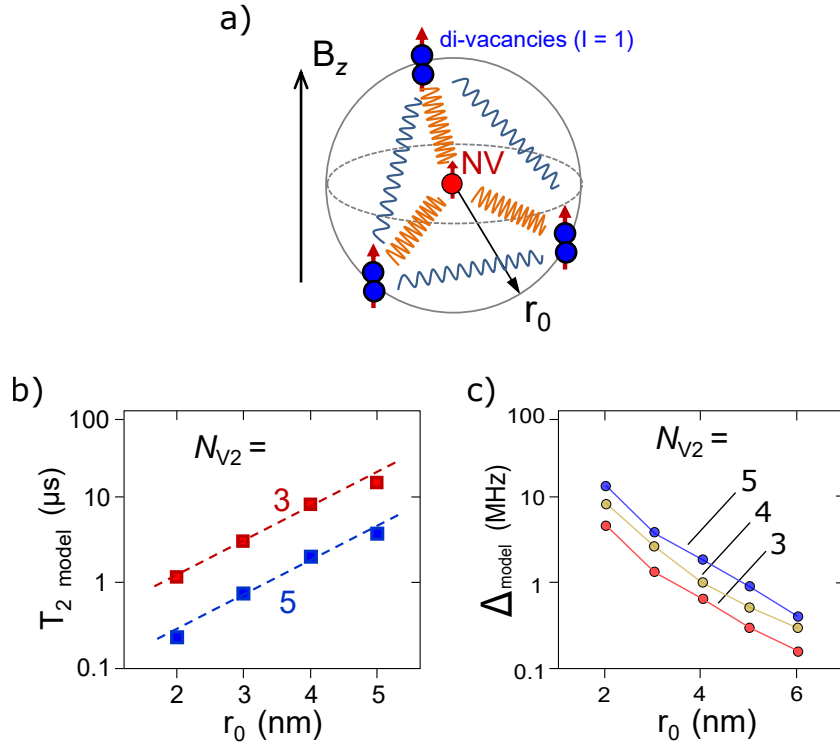
To gain further insights into the effects of V_2 spins on nearby NV centers, numerical calculations[3] are used to estimate the resulting spin properties and magnetic noise characteristics of an implanted NV center. For simplicity, the V_2 spins are equally distributed on the surface of a sphere of radius r_0 centered on the probed NV center, as sketched in figure 4.4 a). This allows the reduction of variables involved in the calculations to r_0 and the number of di-vacancies (N_{V2}) only.

The electron spins of individual V_2 complexes (spin $I = 1$ systems) are assumed in the calculation to be mutually coupled to each other and to the central NV center electron spin (S) via magnetic dipole interactions. In the presence of an external magnetic field of 33 mT aligned to the NV center axis (chosen as z-axis), the system Hamiltonian can be written as:

$$H = H_{\mathrm{NV}} + H_{\mathrm{int}} + H_{V2}, \tag{4.2}$$

---

[3]Numerical calculations performed in collaboration with Dr. Ya Wang.

Figure 4.4.: Numerical estimation of the V_2-NV center interactions. a) A schematic representation of the 3D model used to represent the presence of N_{V2} di-vacancy spins equally distributed on the surface of a sphere of radius r_0 centered on the NV center is shown. **b)** Calculated T_2 times of the NV center coupled to different numbers of V_2 spins are shown as a function of the radius r_0. **c)** Calculated coupling strength related to the magnetic noise generated by N_{V2} di-vacancies at the NV center position is shown as a function of the radius r_0. These values correspond to the calculated noise spectra sensed by the NV center using a CPMG-32 dynamical decoupling microwave sequence (see text and Appendix F).

where each term correspond respectively to the intrinsic components of the NV center, NV center and V_2 hyperfine interactions and intrinsic V_2 spins. These terms can be written individually as:

$$H_{\mathrm{NV}} = D_{\mathrm{NV}} S_{\mathrm{z}}^2 + \gamma_{\mathrm{e}} B S_{\mathrm{z}}, \tag{4.3}$$

$$H_{\mathrm{int}} = S_{\mathrm{z}} \sum_j \mathbf{A}_{j,\mathrm{z}}.\mathbf{I}^j, \tag{4.4}$$

$$H_{\mathrm{V2}} = D_{\mathrm{V2}} \sum_j \left(I_{\mathrm{z}}^j \right)^2 + \gamma_{\mathrm{e}} B \sum_j I_{\mathrm{z}}^j + \sum_{i,j} \mathbf{I}^i.\mathbf{D}_{ij}.\mathbf{I}^j. \tag{4.5}$$

The values of the zero-field splitting of the NV center and V_2 spins are largely

different, being $D_{\mathrm{NV}} = 2.870\,\mathrm{GHz}$ and $D_{\mathrm{V2}} = -0.31\,\mathrm{GHz}$, respectively [214]. The hyperfine tensor $\mathbf{A}_{j,z}$ and the dipolar interaction tensor $\mathbf{D}_{i,j}$ depend directly on the spatial configuration of the NV center relative to the V$_2$ spins.

In a rotating frame defined by the NV center, the Hamiltonian can be rewritten using the density matrix notation (similarly as in Ref. [215]):

$$H = |0\rangle\langle 0| \otimes H_0 + |{+}1\rangle\langle{+}1| \otimes H_{+1} + |{-}1\rangle\langle{-}1| \otimes H_{-1}, \qquad (4.6)$$

where $H_0 = H_{\mathrm{V2}}$ and $H_{\pm 1} = \pm \sum_j \boldsymbol{A}_{j,z} \cdot \mathbf{I}^j + H_{\mathrm{V2}}$. Considering the transition between the $|\mathrm{gs}\rangle$ spin sublevels $m_{\mathrm{s}} = 0 \to m_{\mathrm{s}} = -1$, the coherence decay of the NV center electron spin due to the coupling with V$_2$ spins is obtained by calculating [215]:

$$T_{\mathrm{cpmg}2N+1} = Tr(U_0'(\tau)\, \underbrace{U_0'(2\tau')U_{-1}'(2\tau')}_{N}\, U_0'(\tau')U_{-1}(\tau')\, \underbrace{U_0(2\tau')U_{-1}(2\tau')}_{N}\, U_0(\tau')),$$

$$(4.7)$$

$$T_{\mathrm{cpmg}2N+2} = Tr(U_{-1}'(\tau')\, \underbrace{U_0'(2\tau')U_{-1}'(2\tau')}_{N}\, U_0'(2\tau')U_{-1}'(\tau')$$

$$U_0(\tau')U_{-1}(2\tau')\, \underbrace{U_0(2\tau')U_{-1}(2\tau')}_{N}\, U_0(\tau')),$$

$$(4.8)$$

where $2N + 1$ and $2N + 2$ are the total number of microwave π-pulses (for the odd and even cases, respectively) in the utilized spin modulation sequence. In the presented results, $N = 0$ represents the Hahn-echo scheme and $N > 1$ represents the Carr-Purcell-Meiboom-Gill (CPMG) dynamical decoupling sequence (see Appendix F). The evolution operators $U_0(\tau) = e^{-iH_0\tau}$ and $U_{-1}(\tau) = e^{-iH_{-1}\tau}$ represent the NV center spin state conditional to the evolution of the surrounding V$_2$ spins. For convenience, the time interval between the microwave $\pi/2$-pulse and the subsequent π-pulse of the CPMG sequence is represented in the simulations by $\tau' = \frac{\tau}{2N}$ (see also Appendix F).

For $N_{\mathrm{V2}} < 7$, the evolution of the spin state of the central NV center can be calculated exactly using the above-described equations. As mentioned, only configurations where V$_2$ spins are equidistantly distributed on a sphere of radius r_0 are considered in the calculations. For $N_{\mathrm{V2}} = 3$ and 4, it is straightforward to see

that the equidistant configurations are an equilateral triangle and a tetrahedron, respectively. For $N_{V2} = 5$, there is no evident equidistant solution. Here, the configuration where two points sit at opposite poles and the other three points form an equilateral triangle in the equatorial plane is utilized. Moreover, since a simple geometrical rotation of the modeled sphere (figure 4.4 a) corresponds to a new configuration of spin interactions due to the symmetry-breaker orientation of the NV center, calculations are averaged over several possible spatial configurations.

Figure 4.4 b) presents the average calculated T_2 time (Hahn-echo scheme) of the NV center as a function of the modeled sphere radius r_0 for two different numbers of di-vacancies ($N_{V2} = 3, 5$). As seen, the presence of even a small number of di-vacancies in the nanometer vicinity of an NV center deplete the corresponding T_2 time to a few µs. In addition, figure 4.4 c) shows the average calculated values of the magnetic noise coupling strength between the NV center and N_{V2} nearby di-vacancies as a function of r_0. These values are extracted for the calculated coherence decays of the NV center modulated by a CPMG dynamical decoupling sequence with 32 microwave π-pulses (similar parameters will be used in the described experiments).

The presented results indicate that vacancy complexes are a major source of spin decoherence of created NV centers by low-energy nitrogen implantation, even in the close vicinity of the diamond surface. Up to date, there is no available experimental technique that can be employed to suppress the formation of these lattice defects during thermal annealing.

4.2. The p^+-i diamond junction

One possible way to suppress the vacancy recombination is to charge single vacancies within defect-clusters during the thermal annealing treatment, e.g. when vacancies are mobile in the diamond lattice. In this case[4], Coulomb repulsion between near-neighbor charged-vacancies is on the order of $\sim$ eV. The addition of such barrier in the corresponding activation energy of vacancy complexes hence greatly reduces the formation probability of V_2 and higher-order vacancy complexes in implanted diamond substrates. To implement this concept, a novel concept of a planar all-diamond doped-junction is proposed.

---

[4]Private discussions with Prof. Dr. P. Deák.

4.2.1. Basic concepts

The design foundation of the investigated structure is the theory of p^+-n^- junctions in semiconductor physics [216]. Such structure is characterized by an abrupt change in the doping profiles of acceptor (N_A, p^+-region) and donor (N_D, n^--region) impurities within spatially-separated layers of the semiconductor material. For the purpose of this work, the thermal equilibrium condition will be considered, e.g. no applied external voltage is considered. This scenario is schematically represented in figure 4.5 a).

Under equilibrium, the electric field in the regions far from the junction area must be zero at both sides. Consequently, no charge transfer (electrons and holes) occurs between the doped regions, which results in the invariance of the Fermi level across the junction area (E_F, figure 4.5 b). This scenario defines the space-charge neutrality condition, e.g. the number of positive and negative charges within each individual doped-regions must be the same:

$$n + N_A^- = p + N_D^+. \tag{4.9}$$
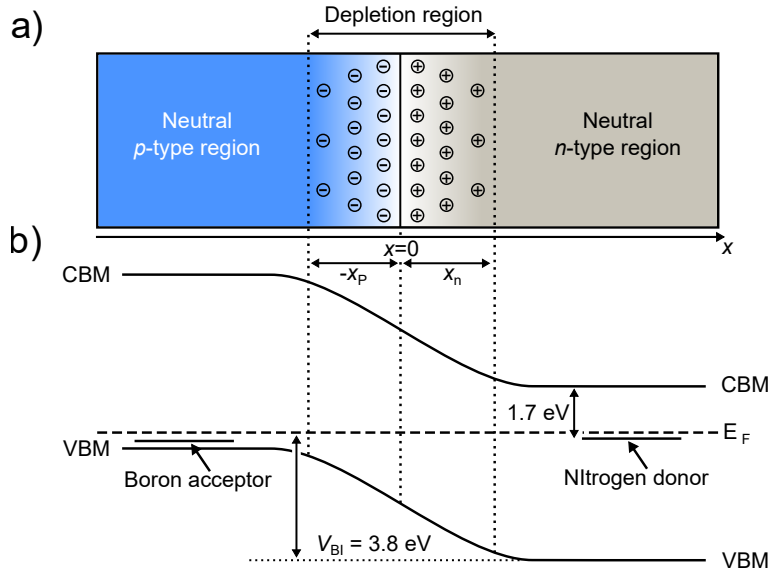
Here, n and p represent the number of free electrons and holes, respectively, and N_A^- and N_D^+ represent the number of ionized acceptor and donor impurities, respectively. In the n- and p-type neutral regions of the semiconductor, $n = N_D$ and $p = N_A$, respectively.

At the junction area, there are two competitive processes that must be considered. First, the different impurity doping profiles induce the diffusion of holes from the p-type side and electrons from the n-type side across the junction. In this case, electrons and holes recombine, forming a charge depletion region at the junction area, as sketched in figure 4.5 a). Second, the non-zero net charge in the depletion region induces an electric field across the junction that counterbalances the previously-mentioned transfer of free carriers from both sides. In equilibrium, the space-charge in the depletion region is equal to:

$$\rho^-(x) = -q\left[N_A^- - p\right], \tag{4.10}$$

in the p-type side and:

$$\rho^+(x) = q\left[N_D^+ - n\right], \tag{4.11}$$

Figure 4.5.: Schematic representation of a p^+-n^- junction structure. a) A schematic representation of a p^+-n^- junction structure in thermal equilibrium is shown. The neutral p-type region has equal concentrations of ionized acceptors and electrons, whereas the neutral n-type region has equal concentrations of ionized donors and holes. The depletion regions and the corresponding depletion width at the p-type (x_P) and n-type (x_n) areas are also shown. The circles with negative (positive) signs represent the excess of electrons (holes) within the depletion region. **b)** Schematic representation of the energy band diagram across a p^+-n^- junction structure in the case of diamond. The p-type area is doped with boron acceptors (shallow energy level close to the VBM) and the n-type area is doped with nitrogen donors (energy level of 1.7 eV below the CBM). The built-in potential ($V_{BI} = 3.8$ eV) [90] of diamond is also shown. Figure partially adapted from Ref. [216].

in the n-type side. For junctions with p- and n-type sides doped with comparable concentrations of acceptor and donor impurities ($N_A \approx N_D$), the depletion approximation can be used to simplify the analysis [80]. In this case, $n(x) = p(x) = 0$ within the depletion region and the space-charge at the junction area is defined by the majority carrier-doping concentration at each side. From equations 4.10 and 4.11, this translates into $\rho^-(x) = -qN_A^-$ and $\rho^+(x) = qN_D^+$ in the p- and n-type sides, respectively.

Since the total charge of the semiconductor must be zero (equation 4.9), the negative and positive net charge per unit of area in the p- and n-type sides of the depletion region, respectively, must be equal. This results in the condition of:

$$N_A x_P = N_D x_n, \tag{4.12}$$

where x_{P} and x_{n} are the corresponding depletion widths in the *p*- and *n*-type regions, respectively. Poisson's equation provides the electric potential behavior in the depletion region, given by [216]:
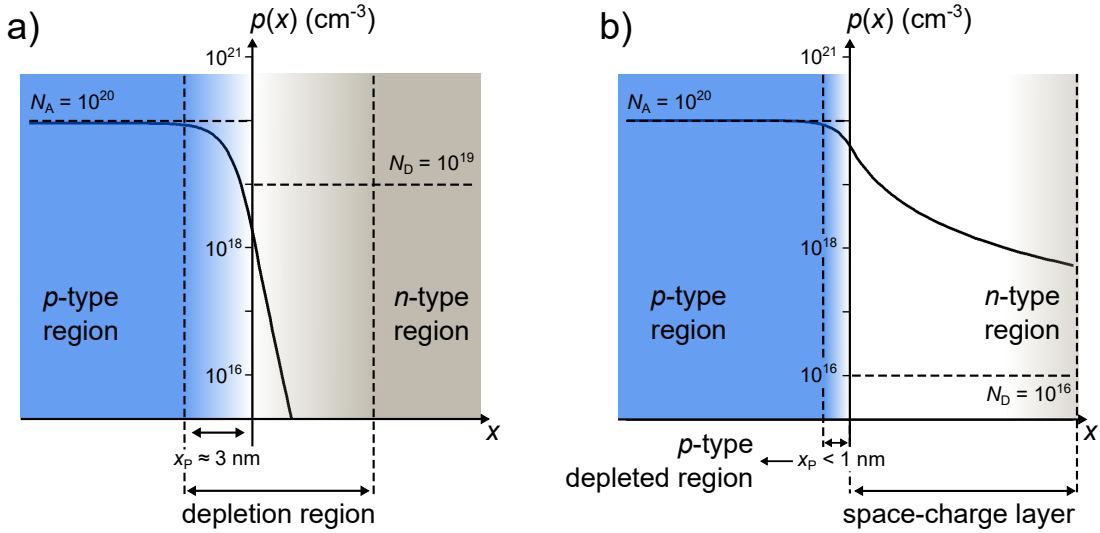
$$-\frac{d^2\phi}{dx^2} = \frac{dE}{dx} = \frac{\rho(x)}{\varepsilon},$$ (4.13)

where x is the defined axis shown in figure 4.5 a), E is the electric field across the depletion region and ε is the material permittivity. The spatial integration of this equation along the x-axis at each side of the p^+-n^- junction provides the space-charges (equations 4.10 and 4.11) and corresponding depletion widths (equation 4.12) for a given junction configuration. For complex structures, the exact numerical solution of this set of equations can be obtained by finite elements modeling, e.g. computational tools such as the SILVACO software [217].

In the case of diamond, a p^+-n^- junction can be engineered using the interface between boron- and nitrogen-doped films [90]. As previously mentioned, these two dopant atoms have similar atomic radii to carbon atoms, meaning that they assume substitutional diamond lattice positions without inducing significant lattice strain and growth defects. In heavily boron-doped diamond (*p*-type layer, $N_{\mathrm{A}} > 10^{20}\,\mathrm{cm}^{-3}$), boron impurities behave as shallow acceptors, with a zero activation energy at room temperature (energy level close to the valence band maximum (VBM), figure 4.5 b) [80]. In nitrogen-doped diamond (*n*-type layer), nitrogen impurities are deep donors, with an energy level located at $1.7\,\mathrm{eV}$ below the conduction band minimum (CBM, figure 4.5 b) [218, 219].

The SILVACO software is utilized to simulate the distribution profile of free holes in a classical diamond p^+-n^- junction with $N_{\mathrm{A}} = 10^{20}\,\mathrm{cm}^{-3}$ (boron acceptors) and $N_{\mathrm{D}} = 10^{19}\,\mathrm{cm}^{-3}$ (nitrogen donors). The equilibrium condition of the structure is simulated using typical parameters for the activation energies of boron acceptors and nitrogen donors in diamond with the given concentrations. Moreover, the simulation mesh set in the SILVACO software is optimized, taking into account the relevant length scales, e.g. using a mesh grid smaller than the expected value of the depletion widths at both sides of the junction. The simulation result is shown in figure 4.6 a).

At the interface, a concentration of free holes of $\sim 10^{18}\,\mathrm{cm}^{-3}$ is present. This value is smaller than the donor impurity concentration in the *n*-type region ($N_{\mathrm{D}} = 10^{19}\,\mathrm{cm}^{-3}$, see figure 4.6 a). Therefore, the space-charges at both sides of the junction ($\rho^-(x)$ and $\rho^+(x)$ in equations 4.10 and 4.11) are characterized by the corresponding majority carrier-doping concentration and are reasonably described

Figure 4.6.: Concentration of free positive charge carriers in diamond p^+-n^- and abrupt p^+-n junctions. a) The simulated concentration profile of free holes by SILVACO software is shown for the case of a classical diamond p^+-n^- junction. In this case, the concentration of acceptor impurities in the p-type side is set to $N_A = 10^{20}$ cm^{-3} and the concentration of donor impurities in the n-type side is set to $N_D = 10^{19}$ cm^{-3}. The corresponding depletion width in the p-type side is $x_P \approx 3$ nm. **b)** The simulated concentration profile of free holes by SILVACO software is shown for the case of an abrupt diamond p^+-n junction. In this case, the concentration of acceptor impurities in the p-type side is set to $N_A = 10^{20}$ cm^{-3} and the concentration of donor impurities in the n-type side is set to $N_D = 10^{16}$ cm^{-3} (the term "abrupt" refers to $N_A \gg N_D$). The corresponding depletion width in the p-type side is $x_P < 1$ nm. Consequently, holes are injected into the n-type region for spatial lengths much larger than x_P, forming a space-charge layer (see text). In both cases, the thermodynamic equilibrium condition of the simulated structure is shown for a temperature of 950°C.

by the depletion approximation. A depletion width of a few nanometers is observed at the p-type side, with a corresponding depletion layer width of a few tenths of nanometers.

The case of a one-side diamond abrupt p^+-n junction is analyzed in figure 4.6 b). The SILVACO software is utilized to simulate the distribution profile of free holes across the junction, with the set concentration of boron acceptors in the p-type side ($N_A = 10^{20}$ cm^{-3}) being much higher than the concentration of nitrogen donors in the n-type side ($N_D = 10^{16}$ cm^{-3}). As seen in figure 4.6 b), the p-type region injects a concentration of free holes $p \sim 10^{19}$ cm^{-3} in the n-type layer that is much larger than the corresponding donor impurity concentration (N_D). Hence, this type of junction, e.g. with a large ratio between acceptor/donor impurity concentrations at the junction interface, deviates from the expected behavior given

by the depletion approximation.
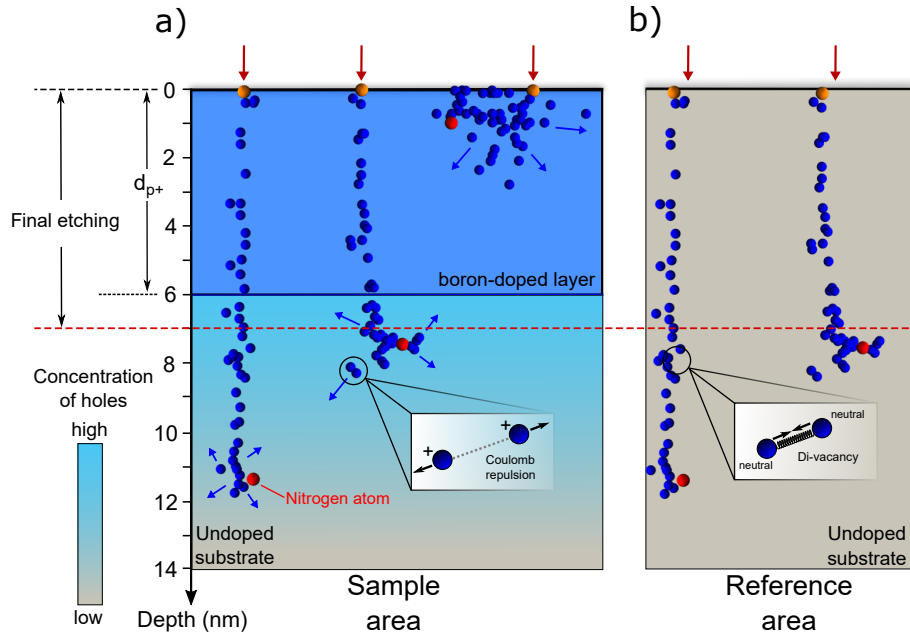
In this respect, free charge carriers must be taken into account for the numerical evaluation of the space-charges at each side of the junction, e.g. considering the full set of parameters in equations 4.10 and 4.11. The simulation shows that the depletion width in the p-type region of the abrupt junction is very small ($x_P < 1$ nm) for the given doping parameters. Moreover, the space-charge in the n-type region is dominated by free holes for distances larger than 100 nm from the junction area (see equation 4.12 and figure 4.6 b).

The n-type substrate region is thus positively-charged by the injected holes from the p-type region. Accordingly, the Fermi level in this region is pinned towards the VBM. Such a feature is known as the space-charge effect and the region where $\rho^+(x)$ is dominated by free holes is known as the space-charge layer [216] (in the n-type region, figure 4.6 b). Due to the value of $N_A \gg N_D$, the investigated structure behaves similarly as in the case of a p^+-doped/insulator/n^--doped junction [76]. Accordingly, the discussed abrupt diamond junction is hereinafter referred to as p^+-i junction. The presented simulation results in this section will be utilized to design the junction structure for the charging of implantation-induced defects in an implanted diamond lattice, as discussed in the following sections.

4.2.2. Structure layout

To experimentally implement this concept, a single-crystal [100]-oriented electronic grade type IIa diamond synthesized by Element Six is used as substrate. The homogeneous doping concentration of nitrogen impurities incorporated during the growth process (low-ppb range, $N_D \approx 10^{14}$ cm^{-3} [89, 139]) serve as the n-type region of the fabricated junction. For the p-type region, a heavily boron-doped diamond film is overgrown on the surface of the diamond substrate by CVD technique (technical details can be found in Appendix D). The fine-polished substrate surface has prior to growth an initial roughness of ~ 1 nm (RMS, measured on several areas by AFM).

The diamond boron-doping is realized by introducing a solid boron rod directly in the plasma region of the CVD chamber. Such a solid-state doping method enables the growth of diamond films with a sharp doping cut-off at the junction interface (approaching $\frac{dN_A}{dx} \sim 10^{20}$ cm^{-3}.nm^{-1} (see Appendix D). The set parameters result in the growth of metal-like diamond films, with boron impurity concentrations of $N_A \sim 10^{20}$ cm^{-3}, as previously investigated in Ref. [90].
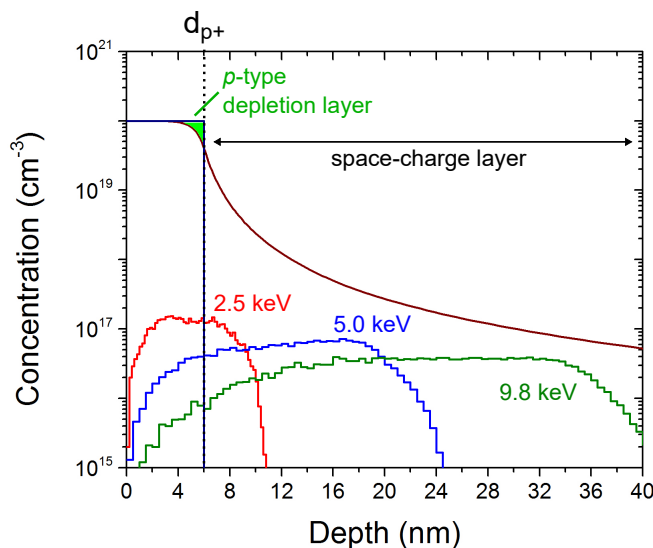
Figure 4.7.: Simulated implantation defects in diamond and the proposed p^+-i junction structure. a) A schematic representation of the novel method of nitrogen implantation across a planar p^+-i diamond junction is shown with the corresponding experimental steps: overgrowth of a heavily boron-doped surface layer (thickness of 6 nm), nitrogen implantation followed by thermal annealing and the final plasma etching step to remove the boron-doped layer (7 nm) - the final fabricated region is named as "sample area" throughout the text. The concentration of injected free charge carriers (holes) in the substrate region is schematically represented by the blue-gray color scale. **b)** A schematic representation of the fabricated reference area is shown. Here, NV centers are created by conventional nitrogen implantation and thermal annealing. Importantly, the same etching step of (7 nm) is performed in this region to allow a direct comparison of created NV centers by both methods. In both figures, the red arrows represent individual implantation sites simulated by Molecular Dynamics with 4.0 keV nitrogen kinetic energy, as previously described. Blue dots represent implantation-induced vacancies, whereas red dots represent the rest position of implanted nitrogen atoms. These results have been previously discussed in section 4.1.1.

Accordingly, the interface between the boron-doped film and the substrate of the fabricated junction presents a step-like change in the concentration of acceptor impurities, with a N_A/N_D ratio above 10^6. As discussed in the last section, the depletion width in the p-type region is hence sub-nanometer and, consequently, the n-type region (ultra-pure substrate) is positively-charged by injected holes. The thickness of the overgrown boron-doped layer of the fabricated junction can be hence very small, and is chosen to be ~ 6 nm in the presented junction. Figure 4.7 a) shows a schematic representation of the proposed p^+-i diamond junction

layout.

In figure 4.8, the simulated profile of free holes by SILVACO software is shown considering the previously-described p^+-i diamond junction characteristics. The nanometer depletion width in the p-type layer is highlighted by the green-marked area. As seen, the space-charge layer is extended to depths of above 100 nm in the ultra-pure substrate, even for the small thickness of the boron-doped layer of ~ 6 nm. This assures the charging of the substrate area by injected holes.

The next fabrication step is the creation of NV centers in the diamond substrate. To this aim, nitrogen implantation events are performed with 2.5, 5.0 and 9.8 keV of energy and ion fluences ranging from 10^{10} cm^{-2} up to 5×10^{12} cm^{-2}. Afterwards, the diamond substrate is annealed at a temperature of 950°C under high vacuum condition ($< 10^{-6}$ mbar) for two hours. Importantly, the absence of boron impurity diffusion in the diamond lattice assures the stability of the p^+-i diamond junction

Figure 4.8.: Simulated concentration of free charge carriers and donor impurities in a p$^+$-i diamond junction by SILVACO and CTRIM. The simulated concentration profile of free holes by SILVACO software is shown for the described p^+-i diamond junction (dark-red line). In this case, the concentration of acceptor impurities in the p-type side is $N_A \sim 10^{20}$ cm^{-3} (dark-blue line) within a ~ 6 nm-thick boron-doped film. The thermodynamic equilibrium condition of the simulated structure is shown for a temperature of 950°C. Simulated distribution profiles of implanted nitrogen atoms by CTRIM are shown for three different implantation energies (2.5, 5.0 and 9.8 keV) and a fixed ion fluence of 10^{11} cm^{-2}. These simulation are performed for a [100]-oriented diamond lattice and a 3°-off implantation angle, as previously discussed in Chapter 3.

under the used annealing conditions [220].
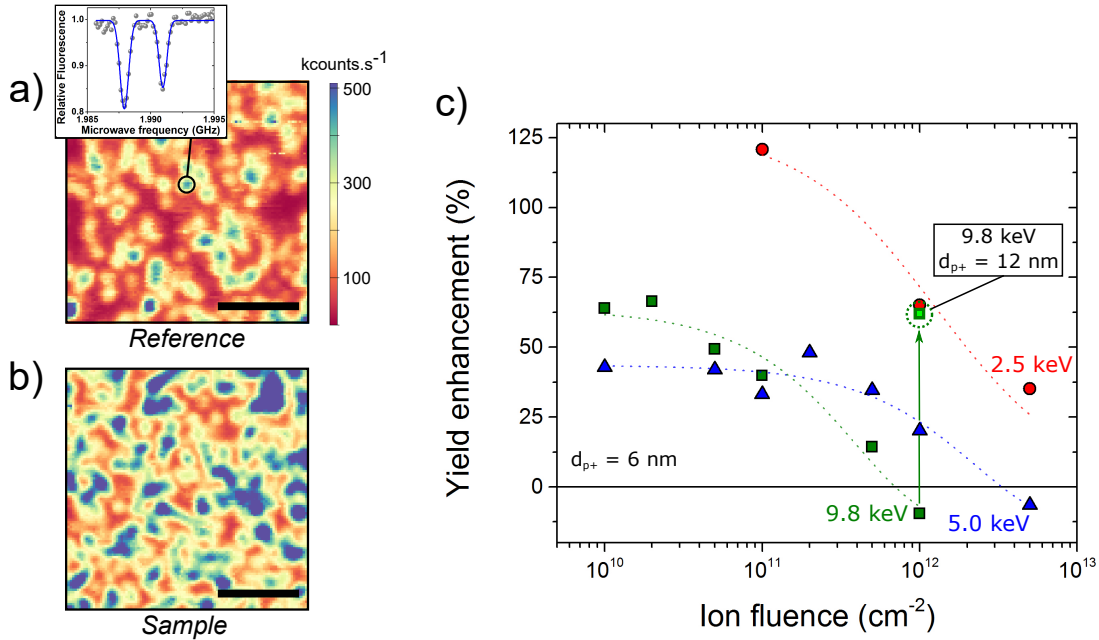
As schematically-represented in figure 4.7 a) (nitrogen ion tracks by IMD simulations), induced lattice defects by the nitrogen implantation process can be localized within the space-charge layer (in the ultra-pure substrate region) by choosing a suitable implantation energy. This is further supported by the corresponding simulated atomic distribution profiles of nitrogen atoms by CTRIM for the cases of nitrogen implantation with 2.5, 5.0 and 9.8 keV of energy, shown in figure 4.8. Due to a high concentration of injected holes in the ultra-pure substrate region ($> 10^{19}$cm^{-3}, figure 4.8), implantation-induced single vacancies localized within defect-clusters are expected to be in the 2^+ charge state during the thermal annealing process [221]. As previously mentioned, this induces an additional energy barrier to the formation of vacancy-related defects in the diamond lattice and reduces their corresponding formation probability.

After nitrogen implantation and thermal annealing, the surface of the p^+-i diamond junction is etched for 7 nm utilizing the low-damage oxygen plasma process described in Chapter 3. This step is crucial in order to precisely remove the boron-doped diamond layer and leave a pristine oxygen-terminated diamond surface. Such fabricated area of the diamond substrate will be referred to as "sample area" in the presented results. For comparison, a "reference area", e.g. NV centers created by conventional nitrogen implantation and thermal annealing (no boron-doped layer, see figure 4.7 b), is also fabricated on the same diamond substrate. This excludes any substrate-related effects such as variation in the intrinsic concentration of nitrogen impurities in the presented experiments. At the end, created NV centers are addressed by confocal microscopy technique, as described in Appendix A.1.

4.3. Augmented properties of NV centers by charging of vacancies

4.3.1. Formation yield

The resulting areal density of created NV centers by nitrogen implantation with the three mentioned energies are estimated from confocal microscopy surface images of the sample and reference areas. It should be emphasized that hereinafter all presented measurements correspond to the fabricated diamond substrate after the final plasma etching step performed on both regions. At first, the formation yield

Figure 4.9.: Improved formation yield of NV centers by nitrogen implantation across a p^+-i diamond junction. a) and **b)** present confocal microscopy surface images of the reference and sample areas, respectively, after nitrogen implantation (5.0 keV $^{15}N^+$, 10^{10} cm^{-2} fluence), thermal annealing and final etching step (7 nm). The inset shows a typical ODMR spectrum of an implantation-induced NV center (^{15}N hyperfine splitting of ≈ 3 MHz). Scale bars show $2\,\mu$m. **c)** Enhancement in the formation yield of NV centers as a function of nitrogen ion fluence for three different implantation energies (2.5, 5.0 and 9.8 keV). The thickness of the boron-doped layer (d_{p+}) is 6 nm. The highlighted point corresponds to the yield enhancement for nitrogen implantation with 9.8 keV of energy in a second fabricated diamond substrate with a thicker ($d_{p+} = 12$ nm) boron-doped layer (see text). The dashed-lines are guides to the eye. Horizontal error bars are negligible, whereas vertical error bars are in the range $< \pm 10\%$, representing the standard deviation of the measured values (not shown for clarity).

of NV centers at the reference area is estimated to be approximately 0.3, 0.6 and 1.0 percent for the implantation energies of 2.5, 5.0 and 9.8 keV, respectively. These values are in good agreement with previously-reported experiments under similar conditions [35], which assures the crystal quality of the fabricated diamond substrate.

Figures 4.9 a) and b) show examples of confocal microscopy surface images, acquired from the reference and sample areas, respectively, both implanted with 5.0 keV of energy and 10^{10} cm^{-2} of ion fluence. As seen, the sample area (e.g. nitrogen implantation across the p^+-i junction) results in higher formation yield values in comparison to the reference area. Indeed, an approximately two-fold

enhancement is observed for all three investigated implantation energies, as shown by the relative formation yield values in figure 4.9 c). Accordingly, together with an enhanced self-diffusion at elevated temperatures [221], the charging effect of lattice defects leads to an increased number of single vacancies available for the formation of NV centers.

Similar effects can also be responsible for the yield enhancement observed by the additional low-energy, post-implantation electron irradiation technique, performed before the thermal annealing treatment, as investigated in Ref. [222]. The reported enhancement factor of ~ 1.8 is similar to the values obtained in our experiments using the p^+-i junction technique. Charging of implantation defects may be hence an universal technique to tailor the evolution of implantation damages in the lattice of spin host materials.

The presented results in figure 4.9 further suggests a preferential path for the formation of NV centers: the implanted nitrogen atom would be located in a split-interstitial site surrounded by single vacancies that occupy the nearest neighbor sites [222, 223]. IMD simulations presented in section 4.1.1 further reveal that as-implanted nitrogen atoms occupy interstitial rather than substitutional positions in the diamond lattice (60% and 40% calculated probabilities, respectively) [147]. Moreover, the results indicate that the recombination rate of a single vacancy and an interstitial nitrogen atom, followed by trapping a second vacancy located in the second-neighbor lattice position to form a stable NV center is enhanced by vacancies being positively charged. Electrostatic repulsion between vacancies should thus not only prevent the formation of vacancy complexes, but also facilitate the interstitial nitrogen atom (not charged) to occupy the nearest vacancy position.

4.3.2. Space-charge compensation by lattice defects

Figure 4.9 c) also reveals that the yield enhancement smoothly decreases with increasing nitrogen ion fluence for all implantation energies. This is a result of the charge compensation of holes in the space-charge layer of the substrate by implantation-induced lattice defects (e.g. vacancies and interstitial atoms) and implanted nitrogen donors. In most cases, lattice defects are known to introduce additional electronic levels within the diamond bandgap that can trap charge carriers at their positions [76].

As seen in figure 4.9 c), the ion fluence at which the yield enhancement is reduced to zero (referred to as critical ion fluence) shifts towards lower values for higher implantation energies. Since higher energies lead to a shift in the distri-

bution profile of implantation-induced defects towards the substrate region - as evidenced in figure 4.8 - the charge compensation must occur at the space-charge layer induced in the substrate area of the fabricated p^+-i junction.
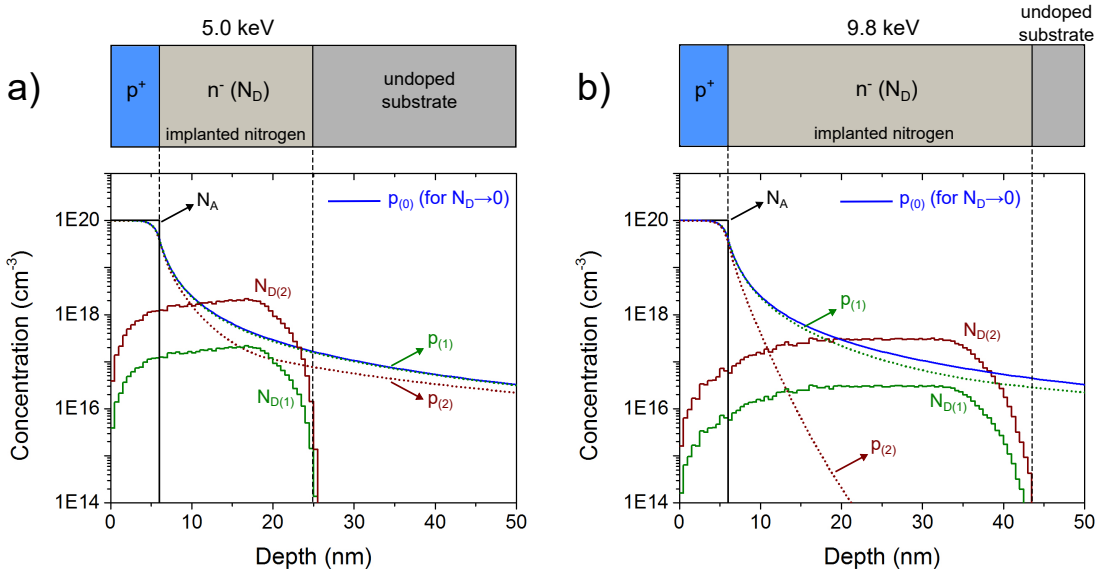
This is further supported by numerical simulations of the p$^+$-i structure in the presence of compensating donors with different doping profiles. Figure 4.10 shows the resulting space-charge layers induced in the ultra-pure diamond substrate, simulated by SILVACO software. The simulated distribution profiles of nitrogen atoms by CTRIM are shown for the cases of implantation events with 5.0 keV (a) and 9.8 keV (b) of energy. The ion fluences below the critical value are taken from the results in figure 4.9 c), e.g. 3×10^{11} cm^{-2} ($N_{D(1)} \approx 10^{17}$ cm^{-3}) and 8×10^{10} cm^{-2} ($N_{D(1)} \approx 10^{16}$ cm^{-3}) for 5.0 keV and 9.8 keV of implantation energy, respectively. In these cases, the induced space-charge layer in the substrate area remains unaffected by the additional induced concentration of donors by the nitrogen implantation (see $p_{(1)}$ in figures 4.10 a and b). Within these ion fluence ranges (for the given implantation energies), the Fermi level in the substrate region is efficiently pinned towards the VBM by injected holes and, hence, vacancies are still positively-charged during thermal annealing.

The scenario changes for ion fluences above the critical value. From figure 4.9 c), this value is estimated to be $\approx 8 \times 10^{11}$ cm^{-2} ($N_{D(2)} \approx 10^{17}$ cm^{-3}) for the case of 9.8 keV of implantation energy. In this case, the induced space-charge layer is strongly compensated by implantation-induced donors in the substrate area (see $p_{(2)}$ in figure 4.10 b). The nitrogen implantation with the given parameters induces an n-type region in the substrate, with a concentration of donors comparable to the concentration of free injected holes at the junction interface. The fabricated structure behaves thereafter as a classical p^+-n^- junction, as previously discussed. Consequently, implantation-induced defects are not efficiently charged during thermal annealing - a similar scenario as in the conventional nitrogen implantation technique.

In contrast to this, implantation with 5.0 keV of energy with a similarly-scaled ion fluence ($\approx 3 \times 10^{12}$ cm^{-2}, corresponding to $N_{D(2)} \approx 10^{18}$ cm^{-3}) results only in a slight reduction in the concentration of free holes in the substrate area (see $p_{(2)}$ in figure 4.10 a). Hence, the simulation results reaffirms that the charge compensation effect occurs in the substrate region of the p^+-i junction. Moreover, in the case of the presented experiments, charge compensation of acceptor impurities directly in the boron-doped diamond film (as discussed in Ref. [224]) would result in the opposite behavior of the critical ion fluence versus implantation energy.

Additionally, the enhanced formation yield is still observed for the nitrogen

Figure 4.10.: Space-charge layer compensation by implantation-induced defects. The upper pictures in **a)** and **b)** show schematic cross-sections of the resulting diamond junctions. The p-type layers are the boron-doped films, whereas implanted nitrogen atoms induce n-type layers in each diamond junction region. **a)** The simulated space-charge layers by SILVACO software are shown for the cases of nitrogen implantation with $5.0\,\mathrm{keV}$ of energy and $3 \times 10^{11}\,\mathrm{cm}^{-2}$ ($p_{(1)}$ and $N_{\mathrm{D}(1)}$) and $3 \times 10^{12}\,\mathrm{cm}^{-2}$ ($p_{(2)}$ and $N_{\mathrm{D}(2)}$) ion fluences. **b)** Similarly, the simulated space-charge layers by SILVACO software are shown for the cases of nitrogen implantation with $9.8\,\mathrm{keV}$ of energy and $8 \times 10^{10}\,\mathrm{cm}^{-2}$ ($p_{(1)}$ and $N_{\mathrm{D}(1)}$) and $8 \times 10^{11}\,\mathrm{cm}^{-2}$ ($p_{(2)}$ and $N_{\mathrm{D}(2)}$) ion fluences.

ion implantation with $9.8\,\mathrm{keV}$ of energy and $10^{12}\,\mathrm{cm}^{-2}$ ion fluence in the case of a second diamond substrate fabricated with a thicker ($12\,\mathrm{nm}$) boron-doped film (similar fabrication steps as previously described with a final etching step of $17\,\mathrm{nm}$; see the highlighted square in figure 4.9 c). Further information about the second diamond substrate can be found in Appendix H. As a result of the thicker boron-doped layer, nitrogen implantation with the same energies (2.5, 5.0 and $9.8\,\mathrm{keV}$) results in lower concentrations of implantation-induced defects (charge traps in the lattice) and nitrogen donors in the substrate area. This leads to a shift in the critical ion fluence towards higher values. Importantly, the results obtained from the two fabricated diamond substrates confirm indirectly the presence of free injected holes in the substrate area of the p^+-i junction during thermal annealing.

4.3.3. Spin measurements

To address the impacts of the surrounding implantation-induced lattice defects, NV centers themselves are utilized as sensors to probe the local noise environment. A comparison between the sample and reference areas provides the opportunity to estimate directly the resulting effect of the p^+-i junction (e.g. charging of lattice defects during thermal annealing) on the spin properties of implanted NV centers. The experiments are carried out on created NV centers by $5.0\,\mathrm{keV}$ of implantation energy and $10^{10}\,\mathrm{cm}^{-2}$ ion fluence, owing to the possibility to sample implantation sites with different contributions of ion channeling.
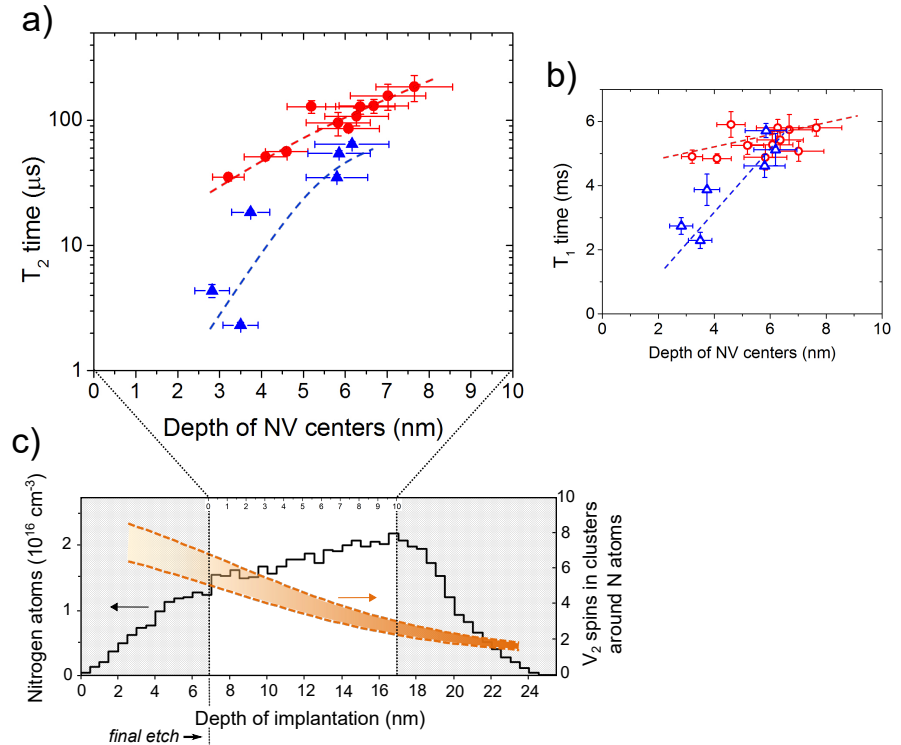
The T_2 (Hahn-echo scheme) and T_1 times of several NV centers are measured at both regions of the fabricated diamond substrate and are shown in figures 4.11 a) and b), respectively. The depth of each NV center is measured independently by spin relaxometry technique, as explored in Appendix G.2. As seen in figure 4.11 a), T_2 times ranging up to $\sim 180\,\mathrm{\mu s}$ are observed for NV centers confined within $2-8\,\mathrm{nm}$ of depth at the sample area.

Comparing NV centers with similar depths at both areas reveal a tenfold-improvement in T_2 times for depths $< 5\,\mathrm{nm}$ at the sample area. This remarkable difference in T_2 times is also observed in the statistics of a larger number of NV centers at both areas (see figure A.12 in Appendix I). Moreover, the enhancement in T_2 times is reproducibly observed for NV centers created using different configurations of the p$^+$-i junction structure, e.g. diamonds fabricated with different thicknesses of the boron-doped layer and different nitrogen implantation energies. Further information can be found in Appendix I. Noticeably, measured T_2 times of NV centers at the reference area approach the values of those from the sample area with increasing depth (see figure 4.11 a). This behavior is attributed to the depth distribution of di-vacancies electron spins at the reference area, as it will be explained below.

The simulated atomic distribution profile by CTRIM in figure 4.11 c) represents the expected distribution of nitrogen atoms implanted with $5.0\,\mathrm{keV}$ of energy. In addition, the number of V_2 spins surrounding created NV centers within individual defect-clusters is expected to be in the range given by the orange-dashed lines in figure 4.11 c). These values are obtained by kinetic Monte Carlo simulations using the simulated IMD defect-clusters as input, as previously discussed in section 4.1.2. As apparent from the figure, the number of V_2 spins per defect-cluster is three-fold reduced within the first $10\,\mathrm{nm}$ of depth of NV centers (see upper scale limited by black-dashed vertical lines in figure 4.11 c). The results indicate that the number of V_2 spins in close vicinity of the NV centers becomes negligible for depths $> 5\,\mathrm{nm}$.

Therefore, the observed decoherence rate of NV centers within this depth range is dominated by the generated magnetic noise by surface spins [36]. Since the surface conditions are the same at both sample and reference areas, similar T_2 times are expected, as indeed seen in our experiments (figure 4.11 a).

In contrast to this, NV centers located at depths of $< 5\,\text{nm}$ are surrounded by a small number of V_2 electron spins (figure 4.11 c). A comparison between the observed depth-dependencies in figures 4.11 a) and c) indicates that the additional

Figure 4.11.: **Augmented spin properties of created NV centers by the p^+-i junction technique. a)** and **b)** T_2 (Hahn-echo) and T_1 times, respectively, of individual NV centers as a function of depth at the sample (circles) and reference (triangles) areas (external magnetic field of $\sim 33\,\text{mT}$ aligned to the measured NV center axis). The depth of each NV center is measured independently by spin relaxation technique. Dashed-lines are guides to the eye. The error bars correspond to the standard deviation of the data fit. **c)** Simulated distribution profile of nitrogen atoms by CTRIM for $5.0\,\text{keV}$ of implantation energy ($10^{10}\,\text{cm}^{-2}$ ion fluence) in a [100]-oriented diamond lattice and an incident angle of $3°$. The two vertical dashed lines align the projected depth of the implanted nitrogen atoms to the experimental depth range of NV centers measured by spin relaxation technique, after the final etching of $7\,\text{nm}$. The orange lines delimit the simulated distribution profile of di-vacancies (see text).
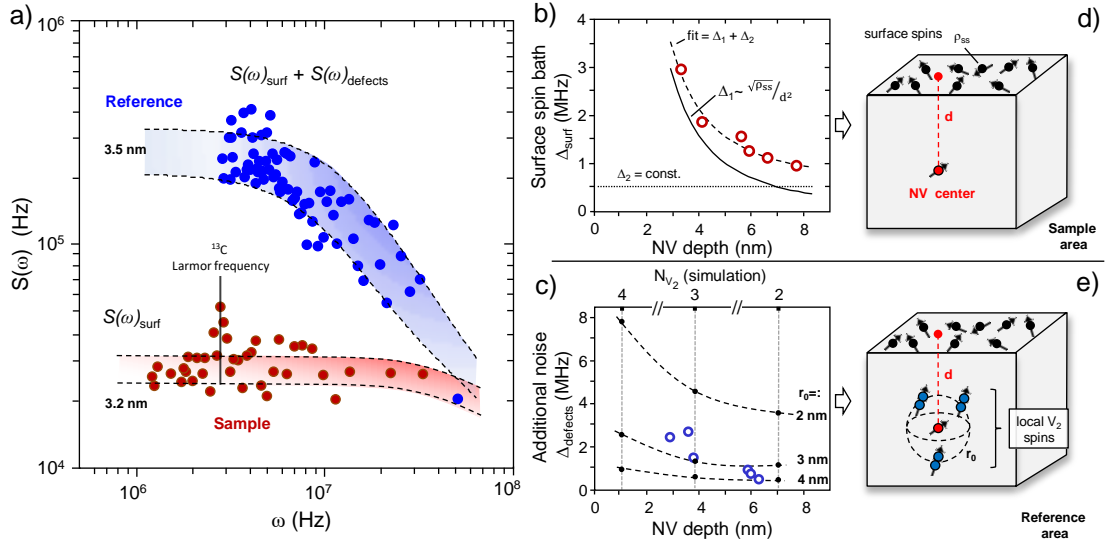
sensed spin noise by NV centers at the reference area arises mainly from the larger number of created V_2 spins in the local defect-cluster region. Furthermore, a similar behavior is observed in the measured T_1 times, as seen in figure 4.11 b). The achieved values of $5-6\,$ms are significantly longer than those typically observed from near-surface NV centers[65, 124, 125], thus assuring the pristine quality of the processed diamond substrate. Both measured T_1 and T_2 times of NV centers and their corresponding depth-dependencies further support the assumption that our method suppresses the formation of vacancy complexes within individual defect-clusters.

4.4. Suppressed spin magnetic noise

To further analyze the magnetic noise environment affecting the created NV centers at both sample and reference areas, noise spectroscopy technique is utilized (see Appendix F). Dynamical decoupling microwave sequences with associated spectral filter functions can be utilized to sample the magnetic noise sensed by NV centers within different frequency ranges. The investigated NV centers are the same as from the figure 4.11. In the presented case, the CPMG pulse sequence is utilized to measure the coherence decays of individual NV centers, with different numbers (N) of microwave π-pulses. As described in details in Appendix F, spectral decomposition technique is employed to extract the corresponding noise power spectral density ($S(\omega)$) of the coupling of the NV center to the magnetic environment.

Figure 4.12 a) presents the resulting power spectral densities of two sampled NV centers with similar depths ($\sim 3\,$nm), where blue and red dots correspond to NV centers located at the reference and sample areas, respectively. These curves are extracted from CPMG-32 coherence decays, as previously explained. Single Lorentzian functions are utilized to fit the experimentally-extracted noise power spectral densities of NV centers an the sample area (see Appendix F).

Figure 4.12 b) shows the corresponding noise coupling strength values as a function of the depth of NV centers at the sample area (red circles). The used model (dashed line) to fit the experimental values comprises two coupling strength contributions, e.g. Δ_1 and Δ_2. The first component corresponds to the surface spin bath of electron spins ($S = 1/2$), with a $1/d^2$ depth dependency, as previously investigated in Ref. [124]. The second component has a constant amplitude (with values well-below the amplitude related to surface spins), representing the coupling of the NV center to residual paramagnetic spins in the diamond lattice such as P1

Figure 4.12.: Suppressed magnetic noise of NV centers at the sample area. a) The experimentally-extracted noise power spectral densities of NV centers at the sample (red dots) and reference (blue dots) areas at similar depths ($\sim 3\,\mathrm{nm}$) are shown. These curves are derived from coherence decays (CPMG pulse sequence, $N = 32$ π-pulses) by means of spectral decomposition technique. The dashed curves and shadowed areas establish margins for fitting the spectra by Lorentzian functions. **b)** Extracted coupling strength as a function of depth for NV centers at the sample area. The dashed curve is a two-component fit comprising the model of surface spin bath [124] (solid curve (1)) and a constant noise contribution (dotted curve (2)). **c)** The analysis of the experimentally-extracted additional noise component (from residual lattice defects) from sampled NV centers at the reference area (blue dots) is shown. The black dots connected by the dashed curves represent the margins of the noise coupling strength calculated for different numbers of di-vacancy electron spins surrounding the sampled NV center. These margins are calculated assuming the simplified modeled NV-V_2 configuration depicted in e), which represents residual defects after conventional nitrogen implantation and thermal annealing (see text). **d)** and **e)** schematic representations of the resulting spin systems around a single implantation-induced NV center at the sample and reference areas, respectively.

centers and ^{13}C nuclear spins [36].

Using this approach, a density of surface electron spins of $\rho_{ss} \approx 10^{13}\,\mathrm{spins.cm}^{-2}$ is estimated, which is in good agreement with previous experiments [124]. The derived value of ρ_{ss} is precisely in the range of the spatial density of electronic states for oxygen-terminated diamond surfaces [133]. Such states are responsible for the band bending at the bare diamond surface, as previously explored in section 1.4.

Furthermore, fitting the extracted noise spectral densities of NV centers at the sample area yield typical values of correlation times (τ) in the range of $\sim 10\,\mathrm{ns}$. The details of an analytical estimation of surface spins can be found in Appendix J. For the mentioned spin density ρ_{ss}, the average distance of near-neighbor surface spins is approximately $1.3\,\mathrm{nm}$, corresponding to a mutual coupling of $\sim 50\,\mathrm{MHz}$. Hence, stochastic flip-flops among near-neighbor surface spins result in a fluctuating magnetic noise at the NV center location, with corresponding calculated correlation times in the range of $\sim 10-50\,\mathrm{ns}$. Therefore, the experimentally-derived values of noise correlation times can be attributed mostly to dipolar spin-spin interactions of the near-surface NV center and the surrounding surface spin bath.

As previously mentioned, the fabrication process (e.g. the employed plasma etching process) results in identical surface surface spin bath characteristics at both the sample and reference areas. For this reason, a double-Lorentzian component is utilized to fit the experimental noise power spectral density of NV centers at the reference area. This double-component noise comprises the described fixed $S(\omega)_{\mathrm{surf}}$ and an additional $S(\omega)_{\mathrm{defects}}$ noise contributions, as depicted in figure 4.12 a). For each estimated depth of NV centers, the parameters of $S(\omega)_{\mathrm{surf}}$ are set fixed according to the experimental curve in figure 4.12 b). In this way, the noise coupling strength and correlation time of the additional noise source (e.g. $S(\omega)_{\mathrm{defects}}$) can be extracted independently. This additional noise component is responsible for the faster coherence decay of created NV centers in the reference area, as seen in figure 4.11 a).

For this noise component, the extracted correlation times are in the range of $70-100\,\mathrm{ns}$. Figure 4.12 c) shows the noise coupling strength values as a function of the depth of created NV centers at the reference area (blues circles). The same figure also shows margins for the calculated coupling strength for a modeled structure, comprising a single NV center surrounded by N_{V2} di-vacancy electron spins, as previously described in section 4.1.3 (see also figure 4.12 e). Within the given margins in figure 4.12 c), the calculated results are reasonably confined to the range obtained in the presented experiments for the additional magnetic noise component of probed NV centers at the reference area. Importantly, estimated values of r_0 (e.g. radial distance between the NV center and surrounding V_2 spins) and the corresponding number of di-vacancies at different depths correlate well to the previously-presented results of the IMD, KMC and CTRIM simulations. This allows the attribution of such noise to the residual implantation-induced lattice defects that are not fully eliminated by the thermal annealing at the reference area (e.g. by conventional nitrogen implantation). Importantly, this magnetic noise signature is only present for sampled NV centers at the reference area.

4.5. Summary and outlook
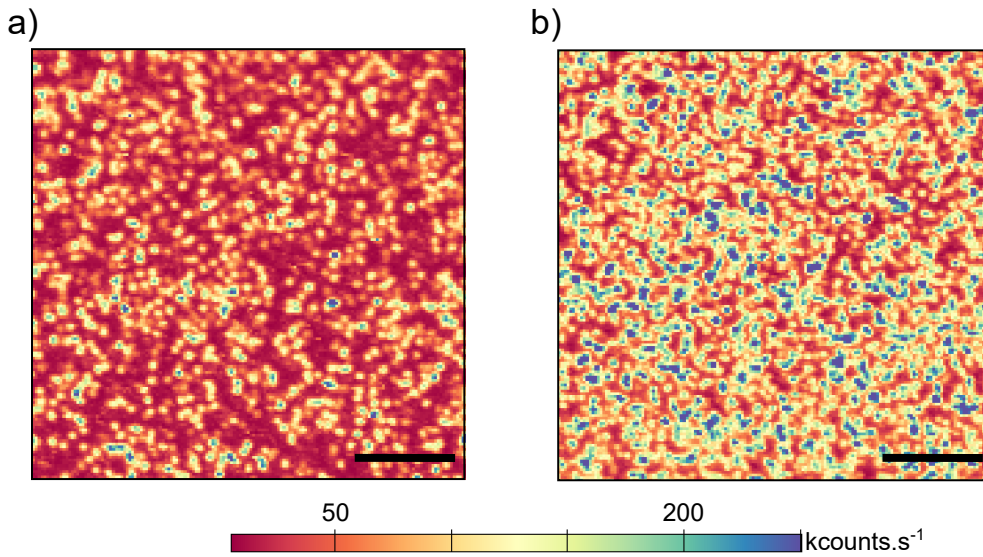
The presented experimental and numerical modeling results draw a consistent picture of the formation dynamics of NV centers in diamond by low-energy nitrogen implantation and thermal annealing. Charging of single vacancies within defect-clusters has been shown as an efficient method to suppress the formation of implantation-induced paramagnetic defects that can degrade the quantum performance of near-surface NV centers. This aspect is of particular interest, since it can be extended to the broader research field of ion implantation in semiconductor materials.

In the case of diamond, the formation of di-vacancy and small vacancy chains is identified as a potential source of spin decoherence, whereas for other semiconductor materials different structural defects may account for degraded spin performance. In all cases, there is a critical threshold for the size of implantation-induced defect-clusters which may not be fully eliminated by thermal annealing. As a result, charging of implantation-induced lattice damages may be a universal tool towards better quantum properties of implanted spin defects in solid-state hosts. Importantly, extending the coherence times of near-surface spin systems and increasing the corresponding formation yield are decisive steps towards more sensitive nano-scale quantum sensors and coupling of single spin impurities to e.g. superconducting resonators [225].

In the future, the concept of defect charging may be implemented into various methods beyond the suggested p^+-i junction structure and also combined with different post-implantation techniques. As follows, the developed technique is foreseen to be employed in two research areas.

Ion co-implantation. The presented results in section 2.3 have pointed to a negligible improvement of ion co-implantation technique, e.g. a negligible amount of implanted nitrogen atoms can be further converted into NV centers by the additional co-implantation-induced concentration of lattice vacancies. As discussed, this is limited by additional paths of vacancy recombination that are activated during thermal annealing and consume most of the co-implantation-induced vacancies in the formation of vacancy-related defects.

The gained enhancements by utilizing the p^+-i junction structure presented in this Chapter would have a significant impact when combined to the ion co-implantation technique. In principle, vacancy recombination would be strongly suppressed during thermal annealing, which would lead to a higher number of vacancies for the formation of NV centers. A preliminary analysis of this hypothesis

a) b)

Figure 4.13.: Confocal microscopy images of the sample and reference areas implanted with CN⁻ molecular ions. The confocal surface images of the diamond surface after the implantation with CN^- molecular ions are presented for the reference (**a**) and sample (**b**) areas, respectively. The calculated areal densities of NV centers are $2.73\,\mathrm{cm}^{-2}$ and $5.97\,\mathrm{cm}^{-2}$ at the reference and sample areas, respectively. All images are acquired after thermal annealing and final plasma etching step of $7\,\mathrm{nm}$. The scale bars represent $5\,\mu\mathrm{m}$.

is briefly investigated here by implanting CN^- molecules into a diamond substrate. In this way, nitrogen atoms are provided simultaneously with an increased concentration of lattice vacancies due to the carbon ion impact [226].

In the presented results, CN^- molecular ions are implanted with $10.0\,\mathrm{keV}$ of energy and $10^{11}\,\mathrm{cm}^{-2}$ fluence[5]. Two implantation events are performed at individual regions of a diamond substrate, one being the p^+-i junction structure and another being the bare ultra-pure substrate (reference area). The utilized diamond substrate is fabricated with similar parameters as previously described in section 4.2.2 ($6\,\mathrm{nm}$-thick boron-doped film). After thermal annealing and the final plasma etching step of $7\,\mathrm{nm}$, confocal microscopy technique is used to estimate the corresponding areal density of created NV centers at both areas of the fabricated diamond substrate. These results are shown in figure 4.13.

For the reference area, no significant difference is observed in the formation yield of NV centers if compared to conventional nitrogen implantation at similar depths. However, the formation yield of NV centers at the sample area is enhanced
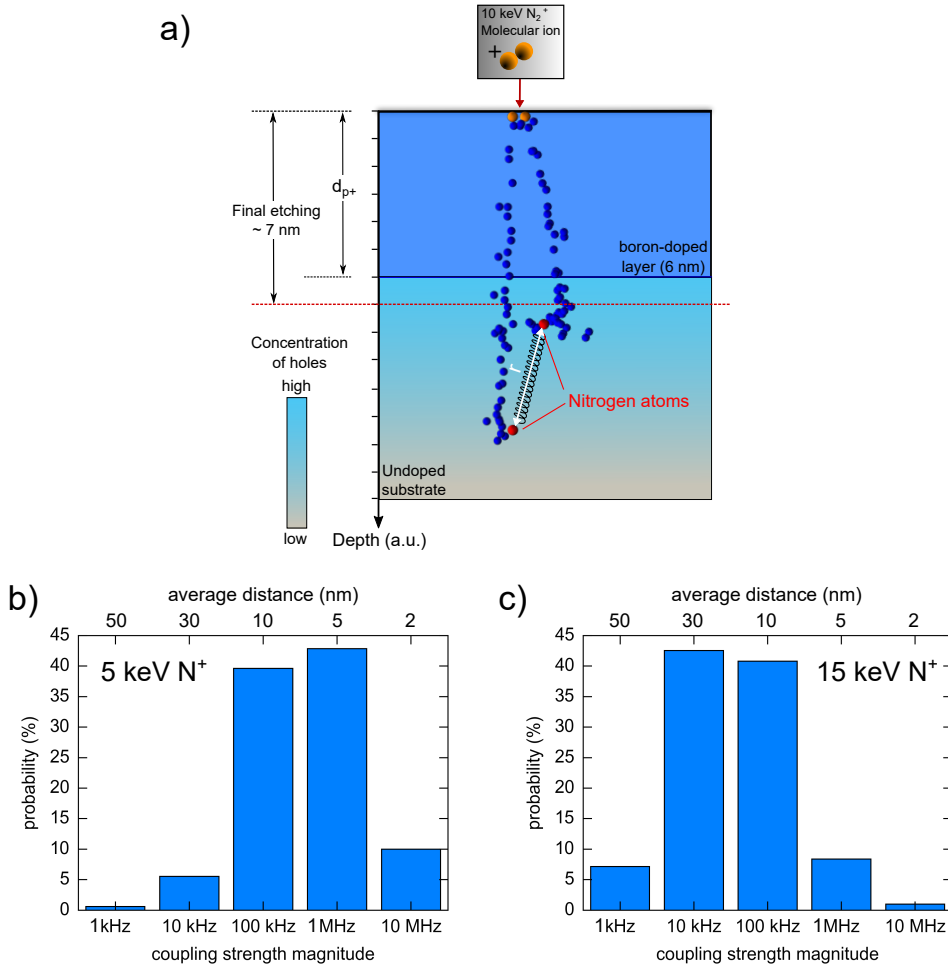
[5]Collaboration with Prof. Dr. Jan Meijer, Felix-Bloch-Institut für Festkörperphysik in Leipzig.

by $\approx 120\%$ in comparison to the reference area, as shown in figure 4.13. This observed enhancement in the formation yield at the sample area is a factor of two higher than the one reported in section 4.3, e.g. for nitrogen-only implantation across the p^+-i junction with similar energy. This confirms the initial assumption that vacancy recombination paths limit the formation yield of NV centers and, hence, charging of implantation defects is a useful tool towards the creation of NV centers with higher efficiency. This is an important step towards the deterministic creation of NV centers for e.g. the engineering of spin arrays in diamond devices [58, 226].

Creation of entangled pairs of NV centers. The precise engineering of coherently-coupled spin systems in solid-state hosts hold the promise to revolutionize the field of quantum information processing. To this aim, the creation of coupled pairs of NV centers in diamond have been previously demonstrated [227, 228]. In these reports, NV centers are created by methods based on the nitrogen implantation technique, wherewith the spatial localization of NV centers and the engineering of e.g. spin arrays are improved by implantation through auxiliary masks such as nano-channels in mica [229] and lithographically-fabricated nano-apertures on metals [230]. As discussed in Chapter 2 (see figure 2.3), the positioning accuracy of implanted atoms is ultimately limited by the ion straggling, which is reduced to tenths of nanometers for low-energy nitrogen implantation.

Despite the remarkable achievements reported in literature, so far advances are limited by the probabilistic nature of the creation of NV centers in diamond. Since the formation yield of NV centers by nitrogen implantation technique is extremely low (especially for energies $< 10\,\mathrm{keV}$ - as discussed in Chapter 2), a large number of nitrogen atoms must be implanted within a nanometer-region of the diamond lattice. This results in residual implantation-induced lattice defects that lead to concomitant degraded NV center spin performance as a trade-of for the needed spatial positioning accuracy. In this case, the formation probability of strongly-coupled pairs of NV centers, e.g. with coupling strength stronger than the corresponding decoherence rate ($\upsilon_\mathrm{d} > \frac{1}{T_2}$), is much less than 1% [231].

Recently, optimum conditions for the nitrogen implantation process aiming the creation of coupled pairs of NV centers have been investigated in Ref. [231]. As highlighted, higher formation yield and improved spin performance of created NV centers would be necessary for an efficient device architecture based on pairs of NV centers for e.g. quantum information processing and nano-scale magnetic field sensing. To this aim, the implantation of nitrogen ions in the p^+-i junction may be an invaluable technique. For instance, the presented enhancements in section 4.3 regarding the formation yield and spin coherence times of NV centers would

Figure 4.14.: Creation of coupled pairs of NV centers utilizing the p^+-i junction technique. a) Schematic representation of the creation of pairs of NV centers by implanting nitrogen molecular ions across a p^+-i diamond junction. The distance between the rest-position of the two implanted nitrogen atoms is represented by r. Assuming the conversion of both implanted nitrogen atoms, **b)** and **c)** represent the corresponding occurrence of the coupling strength between NV centers within certain frequency ranges for the cases of $5.0\,\mathrm{keV}$ and $15\,\mathrm{keV}$ of energy per implanted atom, respectively (courtesy of Ingmar Jakobi).

result in roughly an order of magnitude improvement in the formation probability of coupled pairs of NV centers for the case of nitrogen implantation with $5.0\,\mathrm{keV}$ of energy through mask nano-apertures [231].

The implementation of the p^+-i junction technique in the creation of coupled pairs of NV center is briefly investigated below. As sketched in figure 4.14 a), molecular nitrogen ions (N_2^+) are implanted across the boron-doped layer into
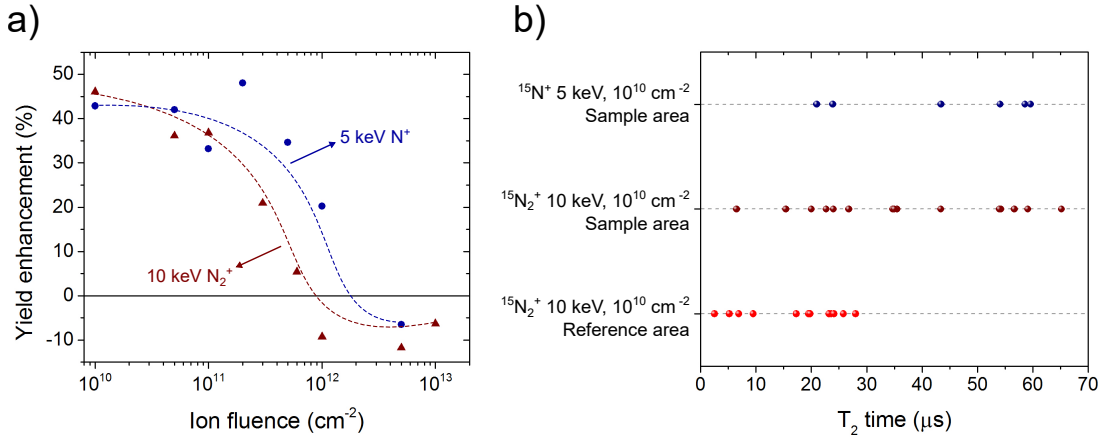
the ultra-pure substrate. In this case, nitrogen atoms are dissociated by the ion impact at the diamond surface, after which each nitrogen atom travels within the diamond lattice with initially approximately half of the ion implantation energy [35]. As discussed, the distance between nitrogen atoms at rest will be limited by the ion straggling, thus increasing the formation probability of pairs of NV centers in comparison to N^+ (single atoms) implantation.

Here, the case of N_2^+ implantation with $10\,keV$ of energy (per ion) is briefly investigated. The trade-off between ion straggling (e.g. implantation energy) and formation probability of strongly-coupled pairs of NV centers becomes clear in the comparison of figures 4.14 b) and c). In these figures, SRIM simulations are utilized to estimate the average distance between implanted atoms at rest with the given energies, where b) and c) represent the cases of $5.0\,keV$ and $15\,keV$ of energy per implanted atom, respectively. From these values, assuming that both nitrogen atoms are converted to NV centers, the average coupling strength (υ_d) can be estimated using [231]:

$$\upsilon_d = \frac{\mu_0 \hbar \gamma^2}{2r^3} \left(\cos(\theta_{AB}) - 3\cos(\theta_{Ar})\cos(\theta_{Br}) \right), \qquad (4.14)$$

where γ is the NV center electron spin gyromagnetic ratio, θ_{AB} is the angle between the two quantization axis of the NV centers, and θ_{Ar}, θ_{Br} are the angles between each NV center quantization axis and the vector connecting them. As seen from figures 4.14 b) and c), the formation probability of strongly-coupled pairs of NV center with $\upsilon_d \sim MHz$ is much higher for the case of implantation with $5.0\,keV$ of energy per nitrogen atom (under the probabilistic condition of both nitrogen atoms being converted to NV centers).

Further fabrication steps of the diamond substrate after the molecular nitrogen implantation are similar to those described in section 4.2.2 ($6\,nm$-thick boron-doped film, $7\,nm$ final plasma etching depth). For comparison, a reference area is also fabricated on the investigated diamond substrate. The created NV centers are afterwards addressed by confocal microscopy technique. The corresponding areal density of NV centers is shown in figure 4.15 a) as a function of the ion fluence. The resulting density of NV centers by molecular nitrogen implantation with $10.0\,keV$ of energy (red dots) is compared to the previously-investigated results in figure 4.9 c) (blue dots, nitrogen implantation with $5.0\,keV$ of energy). Importantly, the enhancement in the formation yield of NV centers is reproducibly observed. Moreover, measured T_2 times of NV centers at both sample and reference areas of the fabricated diamond substrate show again a substantial increase in the average
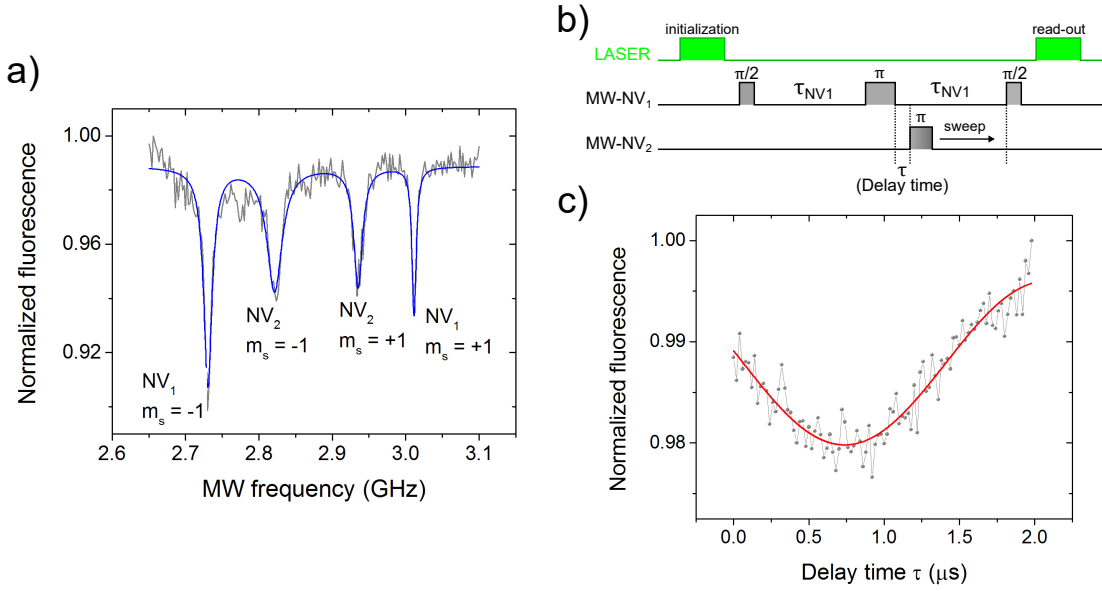
Figure 4.15.: Enhanced properties of NV centers by molecular nitrogen implantation in a p^+-i diamond junction. a) Enhancement in the formation yield of NV centers as a function of nitrogen ion fluence for two different fabricated diamond substrates. The blue dots represent the implantation of nitrogen ions with 5.0 keV of energy (previously presented in figure 4.9 c), whereas dark-red triangles represent the implantation of molecular nitrogen ions with 10.0 keV of energy. The thickness of the boron-doped layer is 6 nm and the final etching depth is 7 nm for both cases. The dashed-lines are guides to the eye. Horizontal error bars are negligible, whereas vertical error bars are in the range $< \pm 10\%$, representing the standard deviation of the measured values (not shown for clarity). **b)** Statistics on the T_2 times of NV centers at the sample (dark-red dots) and reference areas (red dots) of individual regions implanted with N_2^+ 10.0 keV of energy and fluence of 10^{10} atoms.cm^{-2} is shown. For comparison, dark-blue dots show the T_2 times of a few NV centers at the sample area of a region implanted with N^+ 5.0 keV of energy and fluence of 10^{10} cm^{-2}.

value corresponding to the sample area, as shown in figure 4.15 b).

For the investigation of pairs of NV centers, the number of NV centers within observed bright spots in confocal microscopy images is investigated either by photoluminescence intensity or second-order auto-correlation measurements ($g^2(\tau)$). Spots that potentially host two NV centers are further investigated for the dipolar coupling, utilizing the double electron-electron resonance (DEER) protocol described in Ref. [231] (see also figure 4.16 b).

Preliminary, the investigation of 100 random spots in confocal microscopy images reveals one pair of NV centers with $T_2 \approx 10\,\mu$s and $\upsilon_d = 370\,$kHz, as shown in figure 4.16 c). It should be highlighted that no pairs of NV centers could be found at the reference area of the fabricated substrate after the investigation of more than 300 spots (e.g. potentially hosting two NV centers, as previously described). However, a more precise statistics is further limited by the high concentration of created NV

Figure 4.16.: **DEER measurement of a coupled pair of NV centers. a)** The acquired ODMR signal of the sampled pair of NV centers (each one along a different crystallographic directions) is shown. The four observed lines correspond to the $m_s = 0 \rightarrow \pm 1$ spin transitions of the two NV centers (magnetic field aligned to NV_1). **b)** A diagram of the used DEER sequence is shown. Laser pulses are used to initialize and read-out the spin state of the NV centers in the confocal spot. A Hahn-echo microwave sequence is applied to the NV centers sensor (with a fixed inter-pulse delay), whereas an applied π-pulse resonant to the target (e.g. coupled) NV centers is swept with a variable delay time τ. **c)** The resulting oscillation in the spin population of the sensor NV centers due to the dipolar coupling to NV_2 is shown. The solid line correspond to a fit to a cosine function with a frequency of $\upsilon_d = 370\,\text{kHz}$.

centers at the sample area due to the maskless ion implantation. Implantation through nano-apertures fabricated in e.g. a PMMA mask [231] must be utilized to reduce the areal density of NV centers and to confine the sampled NV centers within a smaller region of the diamond substrate.

5. Towards optimized nanometer-thin doped diamond films with embedded NV centers

The nitrogen δ-doping technique has been briefly introduced in section 2.4. The challenges of this technique are mainly related to the diamond growth mechanism itself. First of all, although the depth confinement can be controlled with nanometer precision (i.e. the growth rate is well-controlled), the xy-spatial positioning of these NV centers is completely random. Furthermore, the density of NV centers resulting from ingrown nitrogen impurities is extremely low and hardly controllable [64]. These features have limited the integration of such technique with e.g. diamond photonic cavities [232].

Alternatively, the nitrogen-doped layers can be post-irradiated by electrons, inert ions and protons/neutrons to create additional vacancies [61, 62, 154, 233]. Since this method relies on the separation between nitrogen atoms (ingrown) and vacancies (lattice damages by irradiation), the formation of NV centers still occurs in a relatively defect-free environment. The use of such combined methods is therefore one of the most promising techniques so far for device implementation of NV centers with improved optical and spin properties.

To this aim, some constrains still need to be addressed. Among others, the activation of NV centers beyond the nitrogen-doped targeted surface layer is unavoidable when its thickness (in the order of a few nanometers) is much smaller than the projected range of irradiation-induced vacancies into the substrate [64]. Furthermore, reported values on the conversion efficiency from ingrown nitrogen atoms to NV centers after irradiation and thermal annealing indicate a rapid decrease with increasing separation between the targeted nitrogen-doped layer and the irradiated regions. For instance, in a structure where vacancies are created in a buffer cap layer located approximately 50 nm away from the nitrogen-doped region, the conversion efficiency was shown to be less than 1% [154]. In contrast to this, vacancies created directly within a nitrogen-doped bulk diamond have

demonstrated a conversion efficiency of $\sim 10\%$ [62]. This suggests that the vacancy diffusion during thermal annealing is the key parameter to be understood for further optimization.

The presented results in this Chapter address these issues. At first, the vacancy diffusion process related to the efficient creation of NV centers is investigated utilizing the depth distribution of NV centers created by low-energy helium irradiation followed by thermal annealing. Associated limitations of this technique give further insights into the vacancy diffusion and recombination behavior in diamond. Based on experimental results, an empirical analysis of vacancy diffusion is presented. These features are the roadblock to understand the vacancy diffusion connected to the formation of NV centers in nitrogen-doped diamond. At the end, the δ-doping technique and relevant aspects are discussed. An optimized architecture utilizing CVD overgrowth, irradiation and etching techniques is presented, aiming the quantum sensing of external spins at the diamond surface.
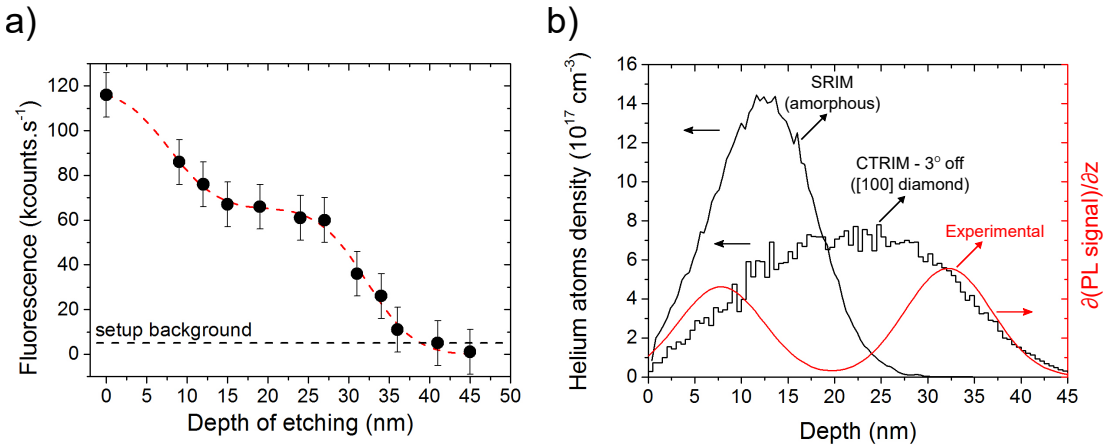
The main results presented in this Chapter are published in F. Fávaro de Oliveira *et al.*, Nano Letters **16**, $2228 - 2233$ (2016).

5.1. Helium irradiation of homogeneously-doped diamond substrates

5.1.1. Spatial distribution of defects revealed by step-etching

The helium irradiation of ultra-pura diamond substrates shows a particular feature. As explained in section 2.2.3, irradiation with low ion fluences followed by thermal annealing converts ingrown nitrogen impurities to single NV centers, whereas irradiation with high fluences ($> 10^{12}$ atoms.cm^{-2}) results in the additional appearance of a photoluminescence background signal in confocal microscopy images (see figure 2.7 a). This background was attributed to helium-vacancy defects created within the atomic profile of irradiated atoms in diamond.

The observation of both NV centers and helium-related defects provides the unique opportunity to simultaneously extract the depth distributions of irradiated atoms and resulting NV centers. This knowledge will provide further insights on the formation of NV centers based purely on the thermal diffusion of vacancies. This investigation is conducted on a single-crystal [100]-oriented electronic grade type IIa diamond synthesized by Element Six. This substrate has a homogeneous

a)

b)

Figure 5.1.: Depth distribution of helium-related defects by step-etching. a) The helium-related background intensity measured by confocal microscopy is shown versus the etching depth. The ion fluence is 2×10^{12} atoms.cm^{-2}. The dashed line is the fit corresponding to two Gaussian complementary error functions. Vertical error bars correspond to the standard deviation of the measured photoluminescence intensity. Horizontal error bars correspond to the uncertainty in the AFM depth measurements, being in the range of 1 nm (not shown for clarity). **b)** Experimentally-extracted depth distribution of helium atoms (red line, the partial derivative of the photoluminescence signal) is compared to simulated atomic distributions (black lines). The SRIM and CTRIM simulations consider the ion implantation in an amorphous and a [100]-oriented crystal, respectively.

doping concentration of nitrogen impurities incorporated during the growth process in the low-ppb range. The fine-polished surface has an initial roughness of ~ 1 nm (RMS), measured on several areas by AFM.

Vacancies are created in the near-surface region of the substrate by molecular helium ion irradiation (He$_2^+$) with 4.0 keV of energy (see Appendix A.2 for technical details). Different regions of the substrate are irradiated with fluences ranging from 10^{10} atoms.cm^{-2} up to 10^{14} atoms.cm^{-2}. Afterwards, the diamond is annealed at a temperature of 950°C under vacuum condition ($< 10^{-6}$ mbar) for two hours. It should be highlighted that longer annealing times do not result in any significant difference in the resulting density of NV centers. This indicates that the concentration of available vacancies for the formation of NV centers has been fully depleted after two hours of treatment [78, 89]. Afterward, irradiated regions of interest were sequentially etched using the oxygen soft plasma to a specific depth. Etching steps correspond to the removal of material for $1 - 5$ nm of depth. At each etching step, the helium-related background intensity and the areal density of NV centers are measured by confocal microscopy technique.
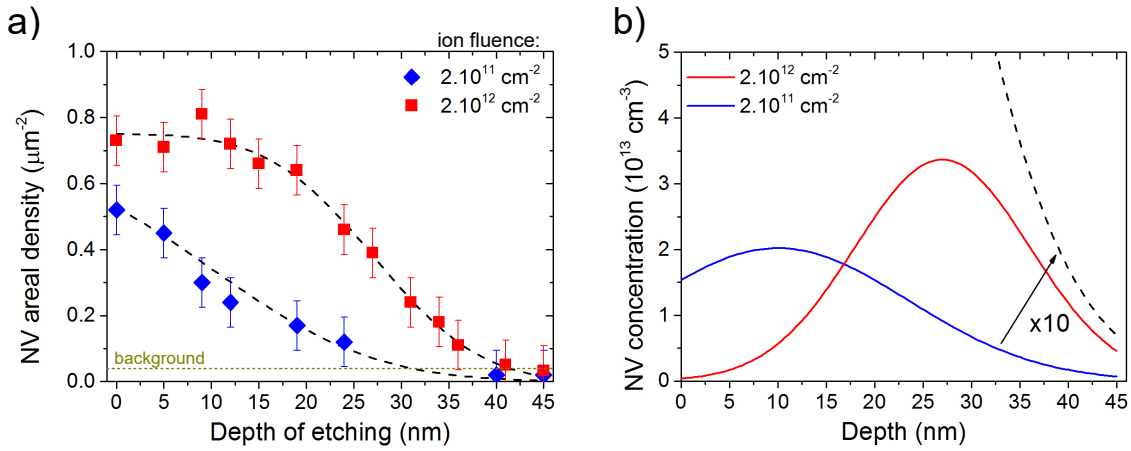
Figure 5.1 a) shows the measured intensity of the helium-related photoluminescence background (black dots) for a fluence of 2×10^{12} atoms.cm^{-2} versus the etching depth. The ion fluence has been chosen as a compromise between the helium-related background intensity and the capability to still identify single NV centers in confocal microscopy images, as discussed in section 2.2.3. The dashed-line in the figure represents a fit function, which comprises two Gaussian complementary error functions (see Appendix E).

The resulting experimental depth distribution of helium atoms is presented in figure 5.1 b) by the red line. This corresponds to the two Gaussian distribution functions, e.g the derivative of the photoluminescence background versus the depth. For comparison, simulated helium atomic profiles are shown (black lines). The SRIM program simulates the ion implantation process in an amorphous material, whereas the CTRIM program considers its crystallographic structure. In the presented case, a [100]-oriented diamond and a 3°-off implantation angle are set as initial simulation conditions, as similarly discussed in section 3.4.3. As seen, the experimental profile correlates with the CTRIM simulated depth distribution of helium atoms. The ion channeling tail of the helium atomic profile must be therefore taken into account to further evaluate the depth distribution of vacancies.

Figure 5.2 a) shows the measured areal densities of NV centers versus the etching depth. The two curves represent individual regions irradiated with fluences of 2×10^{11} atoms.cm^{-2} (blue diamonds) and 2×10^{12} atoms.cm^{-2} (red squares). The dashed-lines correspond to individual fits using Gaussian complementary error functions, as previously explained. The experimentally-extracted depth distributions of NV centers for both ion fluences are shown in figure 5.2 b).

For the ion fluence of 2×10^{12} atoms.cm^{-2}, comparing the depth distributions in figures 5.1 b) and 5.2 b) shows that NV centers are created efficiently (i.e. with higher probability) only within the penetration range of the irradiated helium atoms. In fact, the creation of the majority of the observed NV centers is limited to distances of approximately $10 - 20$ nm (in radius) from the as-implanted helium ion tracks. We define thereby an *effective radius (volume) of NV center formation.* This represents the distance from the initial position of vacancies, for which the probability of an NV center to be formed by vacancy-capture is maximized. This is in contrast to what has been usually considered for techniques that rely on the thermal diffusion of vacancies to create color centers.

The range related to the formation of NV centers by ion irradiation is believed to be comparable to the diffusion length (λ_{diff}) of vacancies in diamond at high temperatures [64, 154]. The later extends to several hundreds of nanometers under
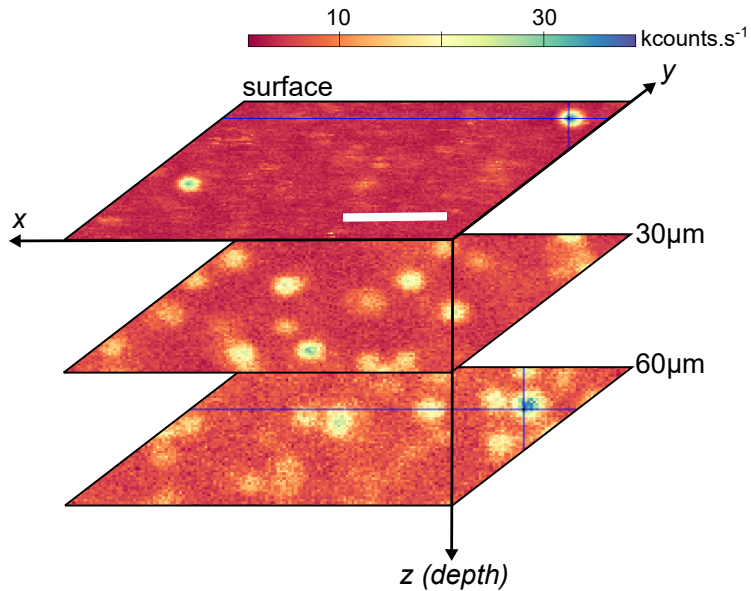
Figure 5.2.: Depth distribution of NV centers after helium irradiation and thermal annealing. a) The areal density of NV centers measured by confocal microscopy is shown versus the etching depth. Single NV centers are created by helium irradiation on individual regions with ion fluences of 2×10^{11} (blue diamonds) and 2×10^{12} atoms.cm^{-2} (red squares). The dashed lines are individual fits corresponding to Gaussian complementary error functions. Vertical error bars correspond to the standard deviation of the measured areal density of NV centers (see Appendix E). Horizontal error bars correspond to the uncertainty in the AFM depth measurements, being in the range of $1\,$nm (not shown for clarity). **b)** Experimentally-extracted depth distributions of NV centers for the two mentioned ion fluences. The black-dashed line corresponds to a linear extrapolation ($\times 10$) of the distribution for the 2×10^{11} atoms.cm^{-2} ion fluence (blue line).

the annealing conditions used in this experiment [78, 154]. This contradiction can be explained by considering each individual helium ion tracks to behave as point-like sources of vacancies, as explored in details by the numerical calculations presented in section 5.2.

5.1.2. Estimation of the conversion efficiency by helium irradiation

A critical aspect related to the conversion efficiency of nitrogen impurities to NV centers by ion irradiation is an accurate estimation of the initial concentration of nitrogen in the utilized diamond substrate in our experiments. As specified, the concentration of ingrown nitrogen impurities incorporated during the CVD growth process should be less than $5\,$ppb [139]. Such a high degree of purity makes it difficult, to measure the nitrogen impurity concentration by means of standard techniques. For instance, ensemble electron paramagnetic resonance

Figure 5.3.: Confocal microscopy images of an ultra-pure diamond substrate at different depths. Confocal microscopy images acquired from an ultra-pure type IIa diamond substrate (see text) after thermal annealing at 950°C for two hours. The top-to-bottom images represent the areal densities of NV centers for the surface and at depths of approximately 30 μm and 60 μm, respectively. The scale bar represents 5 μm.

(EPR) technique would require the use of well-calibrated, high-resolution spectra and specially-designed microwave cavities to provide enough sensitivity for the detection of nitrogen with concentrations in the low-ppb range in diamond [89].

As investigated in details in Ref. [234], the ratio between incorporated nitrogen atoms during the crystal growth and formed NV centers is approximately 300 : 1. This provides an indirect method to estimate the concentration of nitrogen impurities in the diamond lattice by measuring the as-grown density of NV centers. Figure 5.3 shows confocal microscopy images acquired from the non-irradiated regions of the same diamond substrate described in the previous section (after thermal annealing and WCO treatments). The top-to-bottom images represent the areal densities of NV centers for the surface and at depths of approximately 30 μm and 60 μm, respectively.

As apparent from figure 5.3, the surface image shows a reduced density of NV centers in comparison to the deeper images. This can be attributed to the presence of polishing-induced defects at the sub-surface layers that extend to a thickness of up to $1 - 2$ μm. This behavior is observed in several diamond substrates and is
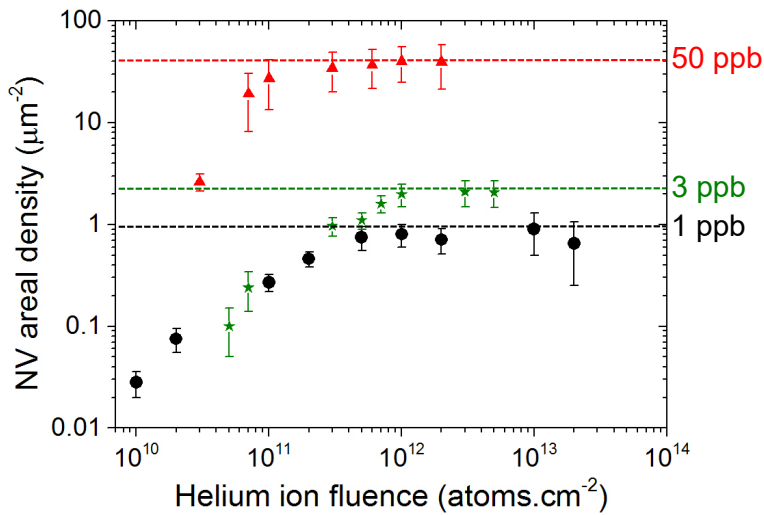
investigated in details in Appendix C. By the given axial resolution of the confocal microscope [235], the observed NV centers are thus assumed to be confined within a volume of approximately $20 \times 20 \times 1\,\mu m^3$. By counting the number of single NV centers in several confocal images at depths of $30\,\mu m$ and $60\,\mu m$, we obtain a concentration of $0.8 \pm 0.2\,ppb$ of ingrown nitrogen impurities. This value is in good agreement with the measurements reported in Ref. [89] on similar type IIa diamond substrates.

As discussed in section 2.2.3 (figure 2.6 a), the areal density of NV centers presents a saturation behavior for ion fluences $> 10^{12}\,atoms.cm^{-2}$. Consequently, the depth distribution of NV centers shown in figure 5.2 b) for an ion fluence of $2 \times 10^{12}\,atoms.cm^{-2}$ (red line) represents the maximum achievable concentration of NV centers by the helium irradiation technique. The conversion efficiency of this technique can be directly estimated by the ratio between the maximum concentration of NV centers in this figure and the concentration of nitrogen impurities in the imaged volume by confocal microscopy. A conversion efficiency of approximately 15% is estimated for the helium irradiation in the near surface region. This value is in agreement with previous reports on the irradiation of diamond using a helium microscope [62] and represents a noticeable improvement (an order of magnitude) in comparison to standard nitrogen implantation at comparable depths [35]. This further highlights the potential application of this technique in quantum sensing applications.

5.1.3. Estimation of the nitrogen impurity concentration in ultra-pure diamond substrates

The knowledge of the conversion efficiency by helium irradiation and thermal annealing is itself a road to estimate the concentration of ingrown nitrogen impurities in diamond. The figure-of-merit value used for such estimation is the areal density of NV centers at saturation, e.g. after helium irradiation with high ion fluences ($> 10^{12}\,atoms.cm^{-2}$). It is assumed that the conversion efficiency scales linearly with the nitrogen doping level for values smaller than $\sim 100\,ppb$, for which the distance between nitrogen atoms is larger than the effective radius of NV center formation.

Figure 5.4 shows the areal density of NV centers versus the helium ion fluence for three different diamond substrates. The first diamond (black dots) is the type IIa ultra-pure substrate described in the last sections. The saturation in the areal density of NV centers at approximately $1\,NV.\mu m^{-2}$ represents the conversion of

Figure 5.4.: Areal density of NV centers vs. helium fluence for three diamonds with different nitrogen impurity concentrations. The areal density of NV centers measured by confocal microscopy technique is shown versus the helium ion fluence. The different doping levels of 1 (black dots), 3 (green stars) and 50 ppb (red triangles) are extracted from three diamond substrates (see text). Error bars correspond to the standard deviation of the measured areal densities of NV centers.

the estimated ~ 0.8 ppb of nitrogen doping to NV centers after thermal annealing. The two other substrates are single-crystal [100]-oriented electronic grade type IIa diamond substrates grown by HPHT method[1]. The final nitrogen concentration in these diamonds is proportional to the level of nitrogen impurities in the catalysts used for the HPHT growth. On both substrates the intrinsic boron concentration at the regions irradiated by helium is in the low-ppb range (roughly estimated by UV absorption and ensemble EPR techniques [89]). The diamond surfaces are mechanically fine-polished to a roughness of ~ 1 nm (RMS, measured by AFM).

According to the helium irradiation technique, the first HPHT substrate shows a saturation density of NV centers that corresponds to a nitrogen impurity concentration of approximately 3 ppb (green stars in figure 5.4). It should be highlighted that this substrate is a single and very homogeneous [100] sector laser-cut from a much larger diamond. This diamond has been also analyzed by rapid-passage ensemble EPR (similarly as in Ref. [89]), which resulted in an excellent agreement with the estimated value of nitrogen impurity concentration by helium irradiation technique.

The second HPHT substrate shows a much higher saturation concentration of

---

[1]Collaboration with Prof. Dr. Junichi Isoya, University of Tsukuba, Japan.

NV centers corresponding to the nitrogen doping level of approximately 50 ppb (red triangles in figure 5.4). It should be highlighted that this substrate presents a very inhomogeneous distribution of nitrogen and boron impurities (roughly estimated by UV absorption). The analysis by rapid-passage ensemble EPR revealed an average nitrogen impurity concentration of approximately 20 ppb. The deviation between the measured values by EPR and helium irradiation techniques is not completely clear, but it is mainly attributed to the inhomogeneity in the distribution of impurities and errors in the estimation of the areal density of NV centers by confocal microscopy technique (see Appendix E).
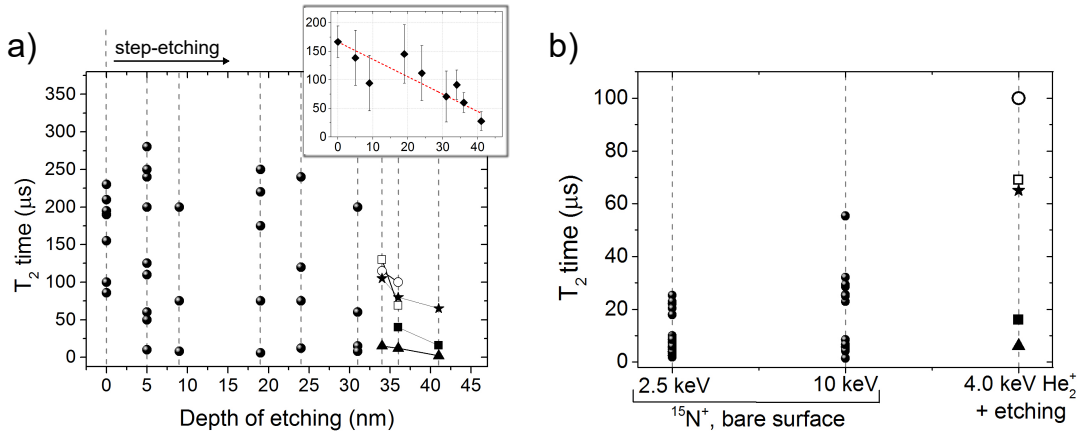
The helium irradiation technique is demonstrated as a very sensitive tool to measure the nitrogen impurity concentration in diamond for the low-ppb range. Results from different samples indicate that the sensitivity of this technique is mostly limited by the homogeneity of the impurities in the analyzed crystal and is ultimately limited by the resolution of the confocal microscope. Due to the high conversion efficiency of the helium irradiation technique, we estimate a minimum detectable nitrogen impurity concentration of less than 0.1 ppb.

5.1.4. Spin measurements

The spin properties of NV centers through the step-etching calibration process of the helium-irradiated diamond substrate is analyzed. The evaluation of the T_2 times as the NV centers are brought closer to the diamond surface gives a rough estimation of the quality of the etched surface and the diamond crystal. Moreover, this analysis also provides T_2 times that can be potentially achieved by utilizing an optimized δ-doped structure.

To this aim, several spatially-isolated NV centers are addressed by confocal microscopy after each etching step and T_2 times are measured, as described in section 1.3. The used substrate in this analysis is the same as described in section 5.1.1. A magnetic field of approximately 15 mT is aligned to one of the possible orientations of NV centers in the [100] crystal. The T_2 times versus the corresponding etching depth are shown in figure 5.5 a).

At first, NV centers under the bare surface show relatively long T_2 times, with values reaching up to 240 µs (for depths < 50 nm). This further supports the initial assumption that the NV centers are formed in a relatively defect-free environment, where the vacancies are created remotely from the position of ingrown nitrogen impurities. As evidenced by the inset of figure 5.5 a), a decrease in the average value of T_2 times is observed for increasing etching depth. This is attributed to a

Figure 5.5.: Spin-spin relaxation times of NV centers through the calibration etching steps. a) T_2 times of single NV centers are shown versus the etching depth through the etching calibration steps used to produce the depth distributions in figure 5.2 b). Two regions were traced corresponding to ion fluences of 2×10^{11} and 2×10^{12} atoms.cm^{-2} (no discrimination in the figure). At the final etching steps, individual NV centers were traced and are individually represented in the figure by the empty squares (NV1), empty circles (NV2), stars (NV3), filled squares (NV4) and triangles (NV5). The inset shows the average T_2 value vs. the etching depth, with the error bars representing the standard deviation of the measurement statistics. **b)** The T_2 times of the individually-traced NV centers (NV1 $-$ 5) by helium irradiation are compared to values from NV centers created by conventional nitrogen implantation with energies of 2.5 and 10 keV with ion fluences of 10^{10} cm^{-2} at the bare diamond surface.

higher probability of NV centers to be located closer to the diamond surface, where magnetic noise from the surface spin bath induces a stronger spin decoherence.

At the final etching steps, the remained NV centers are expected to be hosted within $5 - 10$ nm of depth, according to the depth distributions in figure 5.2 b). Thereafter, five individual NV centers were traced through the etching steps and are individually identified in figure 5.5 a). If a traced NV center disappears from the confocal microscopy image after the etching step, it is assumed to have a depth equal to the step-etched depth.

Figure 5.5 b) shows the T_2 times of the five traced NV centers at the final etching step before disappearance. As seen, T_2 times up to 100 µs are demonstrated for an expected depth of less than 10 nm. The same figure shows also T_2 times from NV centers created by standard nitrogen implantation with energies of 2.5 and 10 keV (ion fluences of 10^{10} cm^{-2}, values measured under the bare diamond surface). These two implantation energies would correspond to NV centers with average depths of 5 nm and 15 nm, respectively. The gained improvements by

irradiating doped crystal for the creation of NV centers with augmented properties
are further emphasized by comparing T_2 times from created NV centers by helium
irradiation to reference values by nitrogen implantation.

5.1.5. Limits of the helium irradiation technique

Another interesting aspect can be observed in figure 5.2 b). There, the black-
dashed line represents the linearly-extrapolated depth distribution of NV centers.
This is obtained by simply multiplying the distribution of the 2×10^{11} atoms.cm^{-2}
ion fluence by a factor of ten. This represents the expected depth distribution of
NV centers for the 2×10^{12} atoms.cm^{-2} ion fluence. As seen from the figure, the
experimental depth distribution of NV centers (red line) deviates from the extrap-
olated distribution (black-dashed line). In fact, the experimental distribution for
this ion fluence shows a strong suppression in the formation of NV centers in the
sub-surface region with depths of less than 30 nm.

Simulations using the SRIM program result in vacancy concentrations from
10^{18} cm^{-3} up to 10^{20} cm^{-3} within the used ion fluence range in this experiment.
This is approximately two orders of magnitude lower than the damage threshold
for diamond amorphization [149, 150] and therefore cannot explain this feature.
Similar effects have been observed for helium irradiadion of ultra-pure diamonds
with 30 keV of energy [62], meaning the sub-surface suppression in the formation of
NV centers observed in our experiments is not induced by vacancy losses through
surface recombination.

Both sub-surface suppression in the formation of NV centers (figure 5.2 b) and
the saturation effect in the areal density of NV centers (figures 2.6 a and 5.4) can
be attributed to the activation of additional paths of vacancy recombination during
thermal annealing. For such a low helium-irradiation energy, the sub-surface region
is expected to host most of the created vacancies [145]. At depths of $20 - 30$ nm,
the onset of the suppression effect in figure 5.2 b), the average distance between
helium atoms in the diamond lattice is in the range of 10 nm for the given ion
fluence $(2 \times 10^{12}$ atoms.cm$^{-2})$. This distance is actually less than the expected
lateral struggling for irradiation of molecular helium ions with 4.0 keV of energy
(approximately 15 nm, as given by SRIM simulations).

Since the effective radius of NV center formation was estimated to be approxi-
mately $10-20$ nm, the irradiation with ion fluences $> 10^{12}$ atoms.cm^{-2} leads to the
overlap of near neighbor ion tracks. Such an overlap increases the formation prob-
ability of vacancy-related defects such as di-vacancies and small vacancy chains.

This, in turn, results in a reduced number of vacancies available for the formation of NV centers. The calculated conversion efficiency of the helium irradiation technique is thus limited by this vacancy recombination phenomenon. Furthermore, the observed increase in the helium-related photoluminescence background with increasing ion fluence (see figure 2.7 a) reinforces the assumption of activation of alternative paths of vacancy recombination other than the creation of NV centers.

5.2. Analytical estimation of the vacancy diffusion in diamond
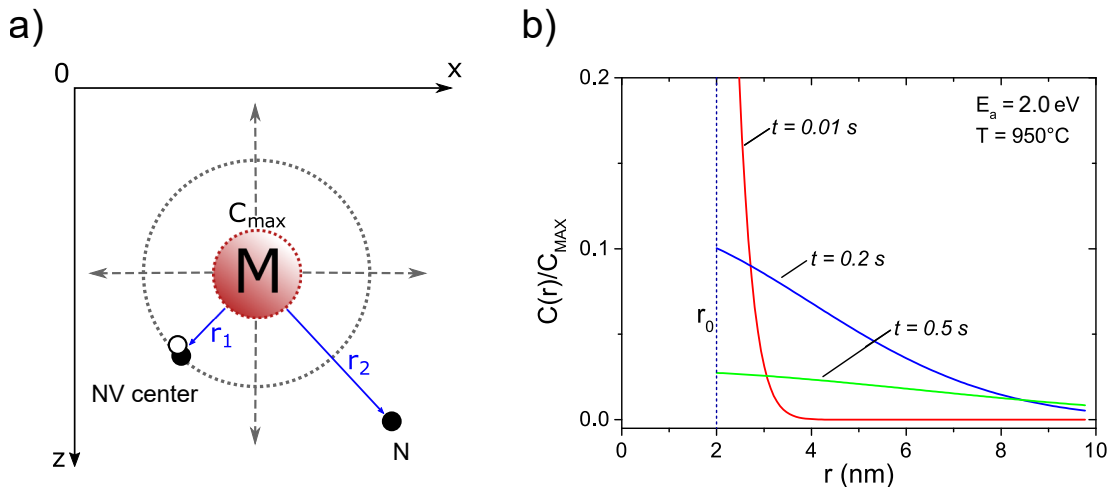
In this section, analytical estimations of the vacancy diffusion in diamond during the thermal annealing are presented to provide further insights into the limits of helium irradiation technique. We start by recalling the definition of defect clusters made in section 4.1.1. The following evaluation considers the experimental results from the diamond substrate described in section 5.1.1 (~ 0.8 ppb of nitrogen impurity concentration).

5.2.1. Defect clusters: the vacancy diffusion from point-like sources

In the case of linear relation between the resulting areal density of NV centers and the ion fluence range ($< 10^{12}$ atoms.cm^{-2}, see figure 5.4), the average distance between defect clusters is much larger than their average size. This allows the assumption that defect clusters are distributed in the diamond lattice as point-like defects. Moreover, vacancy recombination processes that occur within the defect-clusters are neglected for simplicity. The vacancy diffusion during thermal annealing can be estimated using a simple analytical description considering the release of vacancies from point-like sources in a quasi-3D space (including the diamond surface). This is schematically shown in figure 5.6 a).

For an isotropic diffusion in the diamond lattice at a given annealing temperature T, the radial distribution of vacancies at a exposure time t ($C(\mathbf{r}, t)$) can be expressed as:

$$C(\mathbf{r}, t) = \frac{M}{(4\pi Dt)^{3/2}} \exp\left(-\frac{|\mathbf{r}|^2}{4Dt}\right), \tag{5.1}$$

a)

b)
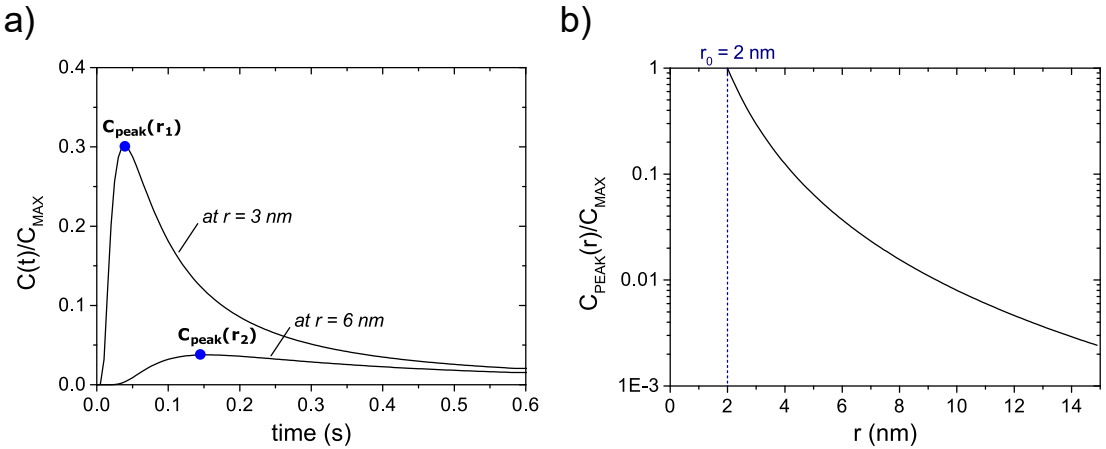
Figure 5.6.: Diffusion of vacancies in diamond from point-like sources. a) Schematic representation of the vacancy diffusion from a defect cluster with a radius of r_0 with M single vacancies (red circle). **b)** Radial dependency of the concentration of vacancies at a temperature of 950°C. Red, blue and green lines correspond to the annealing exposure times of 0.01, 0.2 and 0.5 s, respectively. The maximum values are normalized to the initial concentration of vacancies within the defect cluster (C_{MAX}).

where $\mathbf{r}$ is the radial distance from the point-like source, M in the number of vacancies within the defect cluster and D is the vacancy diffusion coefficient given by [221, 236]:

$$D = D_0 \, \exp\left(-\frac{E_{\mathrm{a}}}{k_{\mathrm{B}}T}\right). \tag{5.2}$$

This coefficient depends on the activation energy of vacancy diffusion $E_{\mathrm{a}} \sim 2.0\,\mathrm{eV}$ [78, 138] and on an experimental pre-factor $D_0 = 3.6 \times 10^{-6}\,\mathrm{cm^2.s^{-1}}$ [236]. At this point, it would be useful to evaluate the spatial and temporal evolutions of the vacancy concentration at random positions $\mathbf{r}_i$ (see figure 5.6 a). These positions would represent the location of ingrown nitrogen impurities relative to the defect cluster.

Figure 5.6 b) shows the radial distribution of vacancies from a defect cluster with a size of $r_0 = 2\,\mathrm{nm}$ containing $M = 5$ single vacancies, calculated for different annealing exposure times according to equations 5.1 and 5.2. The temperature is 950°C, the same used in our experiments. The average size of the defect clusters is estimated by SRIM simulations and the similar study on nitrogen implantation in diamond presented in section 4.1.1. They correspond to a region with the

a)

b)

Figure 5.7.: **Numerical evaluation of the concentration of vacancies in diamond in a nanometer volume around defect clusters. a)** Temporal dependency of the concentration of vacancies at a temperature of 950°C for fixed positions in the diamond lattice (r) around a defect cluster. **b)** Radial dependency of the peak concentration of vacancies ($C_{\mathrm{PEAK}}(\mathbf{r}_i)$). All values are normalized to the initial concentration of vacancies within the defect cluster (C_{MAX}).

highest disorder, i.e. a region that contains most of vacancies created by the ion impact. The number of vacancies within the defect cluster is the average number of vacancies per implanted helium ion according to SRIM simulations. The vacancy concentration values in figure 5.6 b) are normalized to the concentration in a defect cluster with the mentioned radius and number of single vacancies.

The temporal evolution of the vacancy concentration for two radial positions ($r = 3\,\mathrm{nm}$ and $6\,\mathrm{nm}$) is shown in figure 5.7 a). As seen, vacancies diffusing from the defect cluster reach positions $\mathbf{r}_i$ similarly as waves, with a peak concentration given by $C_{\mathrm{PEAK}}(\mathbf{r}_i)$. As shown in figure 5.7 b), this maximum value decreases strongly with increasing distance from the defect cluster. According to the presented analysis, the maximum concentration of vacancies reaching a position $\mathbf{r}_i$ from the defect cluster is reduced by more than two orders of magnitude for distances above 10 nm. It should be highlighted that the spatial dependency in figure 5.7 b) is independent of the values of E_{a} and T. These parameters only affect the evolutions shown in figures 5.6 b) and 5.7 a).

At the atomic scale, $C_{\mathrm{PEAK}}(\mathbf{r}_i)$ is related to the maximum density of stochastic jumps of vacancies (similarly as in a random walk problem) as a function of the radial distance from the defect cluster. At each distance $\mathbf{r}_i$, the occurrence of these random jumps defines the probability for a vacancy to be localized in the atomic vicinity of a nitrogen impurity in the diamond lattice. In this scenario, the

probability of this vacancy to be either trapped by the nitrogen atoms or diffuse away from it must be considered. An exact solution for this problem is challenging, but one can conclude from figure 5.7 b) that the probability of trapping diffusing vacancies at a position $\mathbf{r}_i$ is strongly limited to a few nanometers of distance from the defect cluster.

On the other hand, the volumetric probability ($P(\mathbf{r}_i)$) of the lattice to have a vacancy-trapping site, e.g. a nitrogen impurity in the volume surrounding the defect cluster, increases proportionally to $\mathbf{r}_i^3$. The probability of an NV center to be formed within such a volume is ultimately proportional to the product $C_{\text{PEAK}}(\mathbf{r}_i) \cdot P(\mathbf{r}_i)$. Consequently, the formation probability of an NV center is confined to a nanometer-volume around the initial helium ion tracks in the diamond lattice. Furthermore, the above-presented analysis does not consider additional paths of vacancy losses such as recombination with interstitial carbon atoms and aggregation into vacancy complexes [138]. In this case, the spatial dependency shown in figure 5.7 b) would have a non-monotonic behavior and a much steeper decay with increasing distance from the defect cluster.

The estimates made up to now are in agreement with the experimental results presented in the last sections. Indeed, the depth distribution of NV centers in the presented experiments indicates that the vacancy diffusion in diamond related to the efficient conversion of nitrogen impurities to NV centers is a nanometer-localized phenomenon. The consideration of individual defect clusters as point-like sources of vacancies clearly disassociates the concepts of effective radius (volume) of NV center formation and the vacancy diffusion length in diamond.

5.2.2. Numerical estimations of the effective radius of NV center formation

The definition of the explored defect clusters above can be further employed to numerically estimate the formation efficiency of NV centers and its dependency on the helium ion fluence, as previously discussed experimentally. Therefore, the concept of effective volume of creation of NV centers must be further explored. This volume (hereinafter referred to as V_{eff}) is associated to a range of distances from a defect cluster that confines the non-zero formation probability of an NV center at vacancy-trapping sites. The formation probability is considered to be negligible outside of this volume.

The size of an individual defect cluster increases with the number of single

vacancies within its volume. For simplicity, it is assumed that:

$$V_{\text{eff},M>1} = M V_{\text{eff},M=1} = M \left(\frac{4}{3} \pi r_{\text{eff}}^3 \right), \qquad (5.3)$$

where $V_{\text{eff},M=1}$ is the reference volume of a defect cluster containing a single vacancy. This is directly connected to a corresponding effective radius of NV center formation (r_{eff}). The total density of NV centers ([NV]) can be expressed as a function of the depth distribution of helium atoms ($He(z)$) for a given ion fluence as:

$$[\text{NV}] = \int_0^\infty \text{NV}(z)dz = \frac{4}{3} \pi r_{\text{eff}}^3 [\text{N}] \int_0^\infty M(z) He(z) dz. \qquad (5.4)$$

Here, $\text{NV}(z)$ represents the depth distribution of NV centers and $[\text{N}]$ the concentration of nitrogen impurities in the diamond (constant for the homogeneously-doped substrate). The pre-factor of the right hand side integral is thus the formation probability of an NV center at vacancy-trapping sites. Moreover, the right hand side integral itself represents the total number of vacancies in the diamond lattice produced by the helium irradiation. Consequently, the function $M(z)He(z)$ represents the depth distribution of vacancies in the diamond lattice.
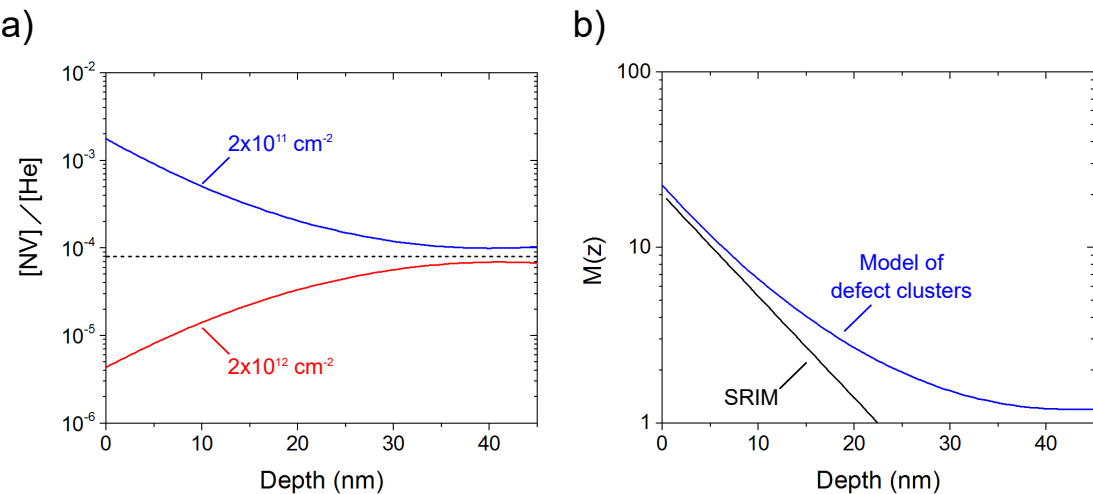
A corresponding SRIM simulation gives an average of 5 vacancies created per implanted molecular helium atom with $4.0\,\text{keV}$ of energy. For an ion fluence of $2 \times 10^{11}\,\text{atoms.cm}^{-2}$ and a concentration of nitrogen impurities of $\sim 0.8\,\text{ppb}$ ($\sim 1.44 \times 10^{14}\,\text{cm}^{-3}$), equation 5.4 yields $r_{\text{eff}} \approx 10\,\text{nm}$. This value is in agreement with the effective radius of NV center formation estimated in section 5.1.1 of $10-20\,\text{nm}$.

Moreover, knowledge about r_{eff} allows the estimation of the vacancy capture cross-section at trapping sites (λ_{CS}). This is given by the ratio between r_{eff} and the experimentally-extracted probability of a vacancy to be at the position of a nitrogen atom (located at the surface of the sphere defined by r_{eff}). Thereby, a value of $\sim 1.8\,\text{Å}$ is obtained, which is comparable to the inter-atomic lattice spacing in diamond. Thus, vacancies can be only trapped when located directly at the adjacent lattice position of a nitrogen impurity.

5.2.3. An analytical approach to the depth distribution of NV centers

As previously described, the density of NV centers by helium irradiation saturates for ion fluences $> 10^{12}$ atoms.cm^{-2}. Linked to this, the corresponding depth distribution of NV centers presents a sub-surface suppression. These phenomena are incorporated in the presented numerical calculation by introducing a suppression factor ($\beta(z)$) in equation 5.4. This function incorporates important features related to the vacancy diffusion from defect clusters into the model, as explored below.

At first, increasing ion fluences translates into decreasing average distances between defect clusters in the diamond lattice. At some limit, this distance becomes comparable to the defect cluster size, setting a threshold for the overlap of near-neighbor clusters. In the case of molecular helium irradiation with 4.0 keV of energy, an ion fluence of approximately 10^{12} atoms.cm^{-2} reaches this threshold of approximately 10 nm. Furthermore, the overlap of adjacent defect clusters also
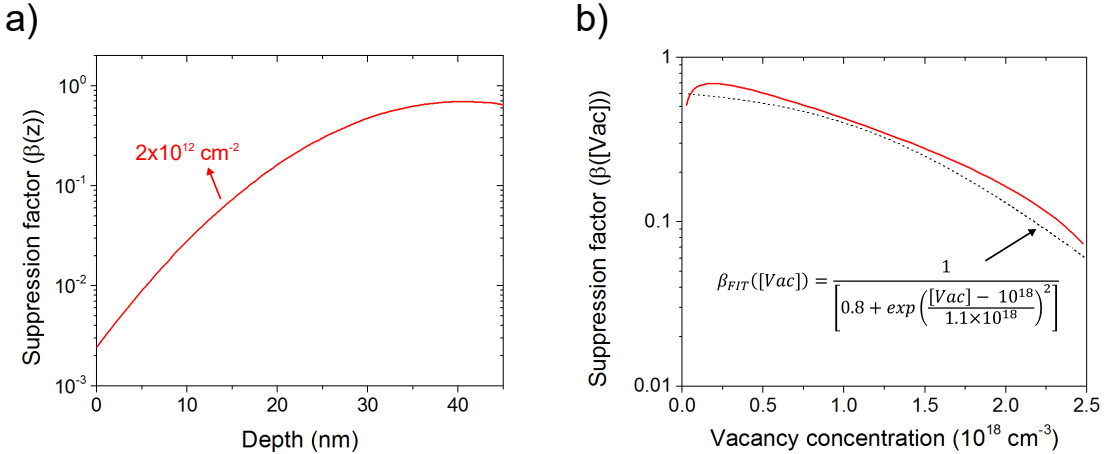
Figure 5.8.: Numerical evaluation of the distribution of vacancies for different ion fluences. a) The ratio between the density of NV centers (experimental) and implanted helium atoms (CTRIM) is shown for two different ion fluences: 2×10^{11} atoms.cm^{-2} (blue line) and 2×10^{12} atoms.cm^{-2} (red line). The dashed line represents the mentioned ratio at the ion channeling tail of the distribution. **b)** Depth distribution of vacancies ($M(z)$) from the proposed model (blue line) and from SRIM simulations (black line) are shown. The modeled $M(z)$ has been obtained simply by dividing the [NV]/[He] ratio for the ion fluence of 2×10^{11} atoms.cm^{-2} (blue line in a) by the average value given by the dashed-line in a).

leads to the activation of alternative paths of vacancy recombination. This, in turn, reduces the number of vacancies available for the formation of NV centers. In the model, the formation probability of a single NV centers is assumed negligible within the defect cluster volume.

The ratio between the experimentally-extracted concentration of NV centers and the corresponding distribution of implanted helium atoms ([NV]/[He]) at each depth is shown in figure 5.8 a) for the helium ion fluences of 2×10^{11} atoms.cm^{-2} (blue line) and 2×10^{12} atoms.cm^{-2} (red line). The atomic helium distribution is taken from CTRIM simulations for a [100]-oriented diamond crystal and a 3°-off implantation angle. These parameters reasonably reproduce the depth distributions of implanted species in the low-keV range of energies, as discussed in Chapter 3. The dashed line in figure 5.8 a) represents the [NV]/[He] ratio value obtained at the ion channeling tail (for depths > 30 nm). In this case, the average number of vacancies per defect cluster is expected to be strongly reduced, close to unitary.

This is further evidenced in figure 5.8 b), where the depth distribution of vacancies ($M(z)$) from the presented analysis is shown. Indeed, individual defect cluster are expected to host approximately one vacancy for depths > 30 nm. Moreover,

Figure 5.9.: Empirical suppression factor on the number of vacancies available for the formation of NV centers. a) The suppression factor $\beta(z)$ used to represent the reduction in the number of vacancies available for the formation of NV centers due to the overlap of adjacent defect clusters is shown for the case of helium irradiation with ion fluence of 2×10^{12} atoms.cm^{-2}. **b)** The suppression factor for the case of helium irradiation with ion fluence of 2×10^{12} atoms.cm^{-2} (red line) is shown vs. the corresponding vacancy concentration (extracted from figure 5.8 b). The black-dashed line corresponds to a generic fit (shown in the inset equation) that gives the suppression factor for the case of irradiation with any given helium ion fluence.

the model is further supported by the agreement seen between the modeled $M(z)$ and the simulated by SRIM (black line in figure 5.8 b) at the ion stopping range (depths of $< 20\,\mathrm{nm}$). Importantly, since this analysis is based on experimental results, vacancy losses through recombination with carbon interstitials and at the diamond surface are included per definition.
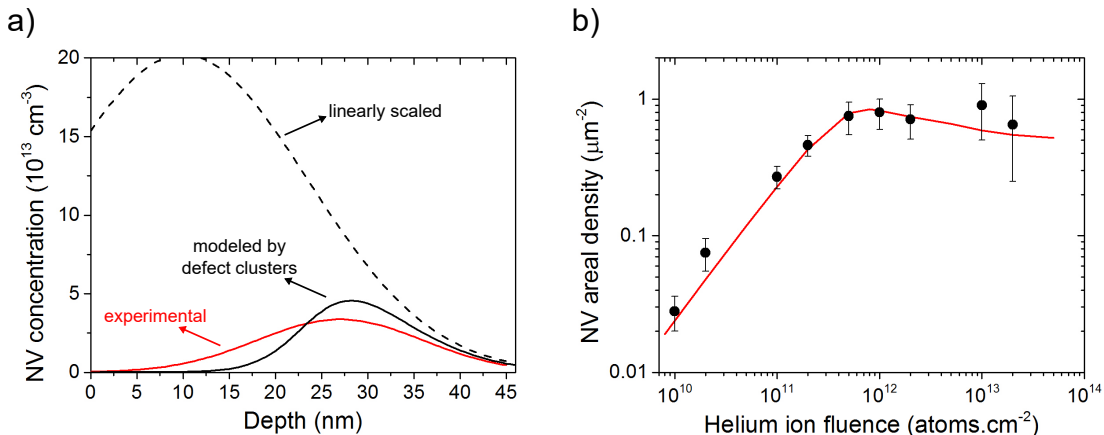
The suppression factor used in the presented analysis is calculated from figure 5.8 a): at each depth z_i, the value $\beta(z_i)$ is given by dividing the [NV]/[He] for the ion fluences of 2×10^{12} and $2 \times 10^{11}\,\mathrm{atoms.cm^{-2}}$ (division between the red and blue functions in figure 5.8 a). The resulting function is shown in figure 5.9 a). Furthermore, the corresponding dependency of the suppression factor on the vacancy concentration ($\beta([Vac])$) is shown in figure 5.9 b). The generic form of $\beta([Vac])$ is thus given by the fitting function shown in the inset. Importantly, this function describes $\beta(z)$ for the case of irradiation with any given ion fluence.

5.2.4. Model verification: the limits of helium irradiation

The function $\beta(z)$ is thus integrated in equation 5.4 as a factor in the right hand side integral. It represents an ion fluence-dependent correction factor for the depth distribution of created vacancies by helium irradiation that are available for the formation of NV centers. By using the developed concepts in the last sections, equation 5.4 can be finally used to model the depth distributions of created NV centers by ion irradiation (see figure 5.2 b).

The modeled depth distribution of NV centers is shown in figure 5.10 a) (black-solid line) for the ion fluence of $2 \times 10^{12}\,\mathrm{atoms.cm^{-2}}$. The corresponding experimental distribution is also shown (red line), originally presented in figure 5.2 b). As seen, the modeled distribution can reasonably reproduce the sub-surface suppression in the formation of NV centers for depths $< 30\,\mathrm{nm}$ and the maximum concentration of NV centers. In addition, equation 5.4 can be used to integrate the modeled depth distribution of NV centers for varying ion fluences. The resulting modeled behavior of the density of NV centers for different ion fluences is shown in figure 5.10 b) (red line). Black dots are the experimental results of the areal density of NV centers for different ion fluences. The model of defect clusters successfully reproduces the saturation on the areal density of NV centers for helium ion fluences $> 10^{12}\,\mathrm{atoms.cm^{-2}}$.

Both modeled results confirm the initial assumptions that alternative paths of vacancy recombination are indeed responsible for the limitation in the spatial distribution of NV centers by helium irradiation. Ultimately, this model can be

a)

b)

Figure 5.10.: Model verification: limits of the helium irradiation technique. a) The modeled depth distribution of NV centers using equation 5.4 with the integrated suppression factor ($\beta(z)$) is compared to the experimental one (see figure 5.2 b). The helium ion fluence is 2×10^{12} atoms.cm^{-2}. The dashed line represents the linearly-scaled ($\times 10$) experimental distribution from the ion fluence of 2×10^{11} atoms.cm^{-2}. **b)** The areal density of NV centers is shown versus the helium ion fluence. The black dots are experimental values, whereas the red line represents the defect-cluster model.
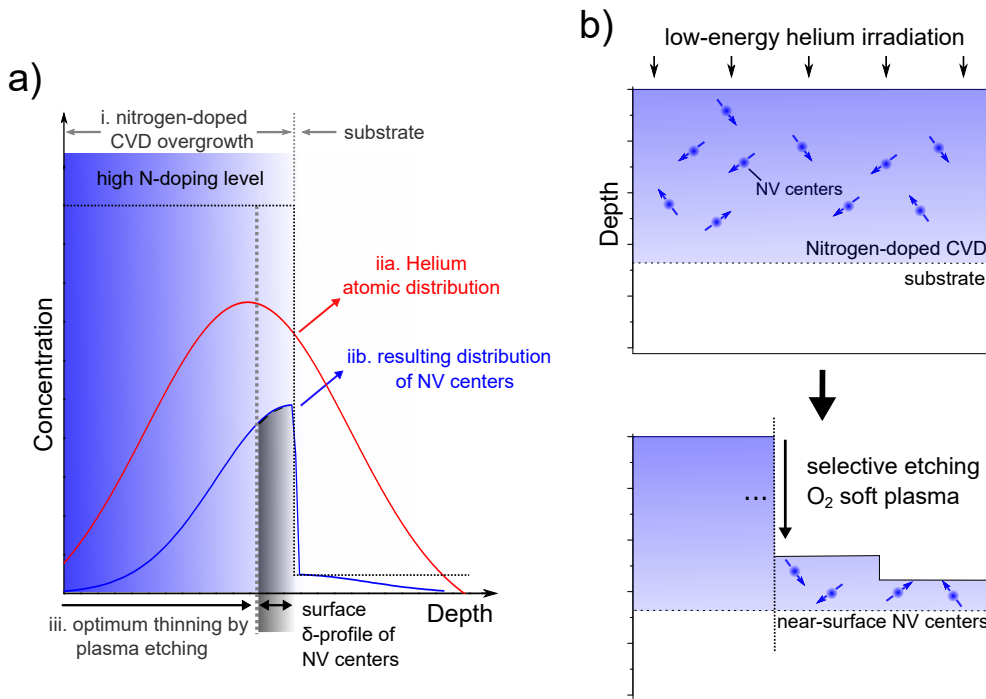
further used to estimate the depth distribution and corresponding areal density of NV centers for irradiated diamond substrates with different nitrogen doping profiles. This ability is a powerful tool in order to optimize the diamond doped-structure for quantum sensing applications, as will be explored in the next section. Moreover, the gained insights on the vacancy diffusion and recombination behavior during thermal annealing are extremely important to understand the formation mechanism of spin-defects in solid-state host materials.

5.3. Optimized nitrogen δ-doped diamond structure

The experimental and modeled results obtained in the last sections have provided so far crucial information towards optimized conditions for nitrogen δ-doping technique. In this section, an optimized δ-doped structure architecture is proposed and experimentally verified towards quantum sensing applications.

5.3.1. Structure architecture

To further explore the advantages of combining ion irradiation and nitrogen δ-doping techniques, an optimized structure architecture is proposed. Figure 5.11 shows a schematic representation of such a structure (a) and the related fabrication steps (b). First, a thin diamond film with controlled nitrogen doping is overgrown on the surface of a ultra-pure diamond substrate. Second, a profile of vacancies is created in the structure by low-energy helium irradiation. The following thermal annealing treatment converts ingrown nitrogen impurities into NV centers, as discussed in the last sections. As a consequence of the nitrogen-doped growth, a sharp doping profile is created at the interface between the substrate and overgrown film. This leads eventually to a sharp cut-off in the corresponding depth distribution of NV centers (see figure 5.11 a).

Figure 5.11.: **Proposed architecture of the nitrogen δ-doped diamond structure for quantum sensing. a)** Schematic representation of the structure architecture for the engineering of a thin (δ) profile of NV centers at the diamond surface for quantum sensing applications. The fabrications steps of nitrogen-doped CVD growth, helium irradiation and plasma etching are optimized to confine the maximum of the depth distribution of NV centers directly at the structured diamond surface. **b)** The corresponding experimental method is presented. At the end, NV centers are expected to be hosted within $\sim 10\,\text{nm}$ of depth.
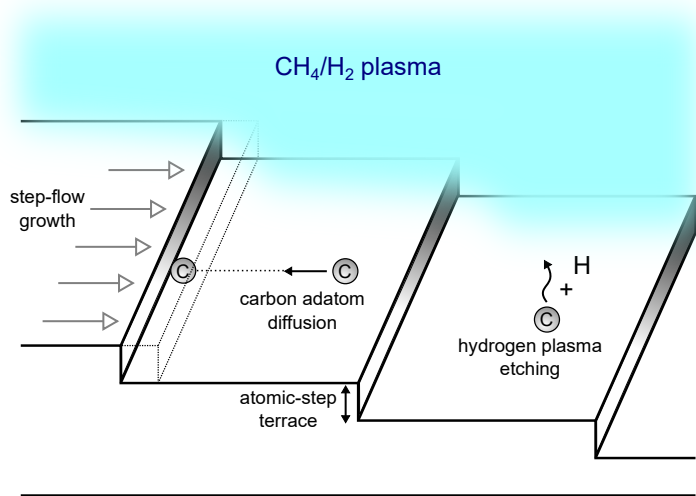
The third and final fabrication step is the use of plasma etching to remove part of the overgrown diamond film. An important aspect related to the fabrication process is the initial thickness of the nitrogen-doped diamond film. This parameter should correspond to the maximum in the expected depth distribution of NV centers (see figure 5.11 a). In this way, the density of NV centers at the final surface (after etching) can be maximized while avoiding the activation of NV centers in the substrate region. Importantly, the ion straggle in the *z*-direction and consequently the depth uncertainty of NV centers are taken into account by fabricating the structure based on the presented results in the last sections. Moreover, the oxygen soft plasma process is a key process used to etch the proposed structure, thus assuring a pristine final diamond surface.

5.3.2. Nitrogen incorporation during CVD diamond growth

For the presented optimized structure in this Chapter, the ability to grow diamond films with nanometer precision in its thickness and consistent control of the nitrogen doping level are of essential importance. The CVD growth of diamond films for the present experiments has been performed in a reactor designed specifically for the homoepitaxial growth of high-quality diamond layers with atomically flat surface. Technical information can be found in Appendix D.

The deposition of high-quality diamond layers by CVD occurs in a mode known as *step-flow growth* [237] (schematically represented in figure 5.12). The film deposition is a competition between the incorporation of carbon adatoms (single carbon atoms generated in plasma that reach the diamond surface) at the terrace edges and the removal of non-diamond carbon phases by the hydrogen plasma. The latter process is extremely important for the stabilization of the diamond surface during growth and the deposition of high-quality diamond layers. Carbon adatoms that do not reach the terrace edges would eventually serve as additional growth sites on the terrace surface, which results in non-epitaxial film growth and produces lattice defects such as dislocations and pyramidal hillocks [238].

The successful growth of atomically-flat diamond films depends basically on two parameters. First, the deposition rate of carbon adatoms controls the amount of carbon radicals that reach the diamond surface and therefore the film growth rate. An increasing rate results in a faster growth, but also leads to a higher concentration of lattice defects since many carbon adatoms would not have enough time to reach the terrace edges [238]. Therefore, step-flow growth is usually performed using a plasma gas mixture with low CH_4/H_2 ratio (usually less than 1%) [239].

Figure 5.12.: Schematic representation of the step-flow growth of high-quality diamond by CVD. The growth mechanism of CVD diamond films known as step-flow is schematically shown. The film growth is a compromise between the diffusion of carbon adatoms towards the terrace edges and the removal of non-diamond carbon phases by the hydrogen plasma. Figure partially adapted from Ref. [71].

Second, the substrate temperature regulates the diffusivity of carbon adatoms at the terrace surface and the carbon-hydrogen reactivity. Higher temperatures lead to an increased velocity of carbon adatoms towards the terrace edges (higher diffusivity), but also result into a stronger hydrogen plasma etching of the substrate. CVD processes conducted under high substrate temperatures result, in general, into increased surface roughness and degraded crystal quality. Therefore, typical substrate temperatures in the range of $\sim 800°C$ are utilized [239].

The effect of introducing nitrogen into the plasma gas mixture of the CVD process has been both theoretically [240, 241] and experimentally [242, 243] investigated. Although the higher growth rate of nitrogen-doped diamond is well understood, nitrogen incorporation in diamond during the CVD process is still a point of controversy. Experimentally, it is impossible to verify if nitrogen is incorporated through N-related species (catalyst effect) or through substitutional nitrogen atoms (direct growth) that diffuse towards the terrace edges. In essence, the addition of nitrogen in the plasma gas mixture is believed to increase the hydrogen surface abstraction, thus increasing the concentration of reactive carbon surface sites.

In the present experiment, the nitrogen incorporation in diamond during CVD
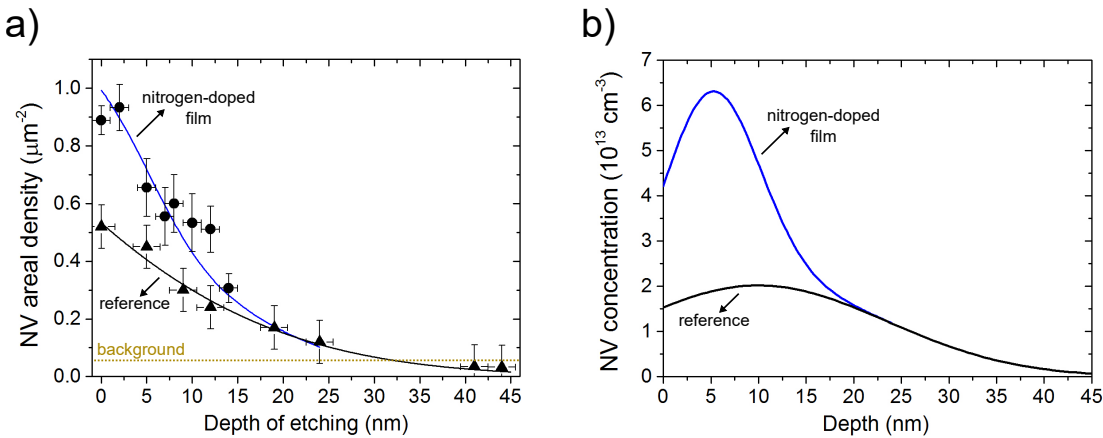
growth is demonstrated to be challenging. Two approaches are followed in order to experimentally address this feature in the CVD growth of diamond films ([100] crystal direction). First, several diamond films are grown with increasing CH_4/H_2 ratio at each experiment, while the nitrogen concentration in gas is kept constant. This translates essentially into a faster film growth rate.

Second, several diamond films are grown with constant and low CH_4/H_2 ratio ($< 0.5\%$), while the nitrogen concentration in gas is increased at each experiment. In this way, the growth rate is kept relatively constant while the concentration of nitrogen in plasma is increased. In all processes, the growth time is such that the final film thickness varies from 5 nm to 30 nm (depending on the specific experiment). The substrate temperature is set to 750°C in all experiments. The final nitrogen concentration in the grown films is evaluated by helium irradiation technique, as described in section 5.1.3.

No clear tendency is identified from all performed growth experiments. The first approach shows no significant change in the nitrogen concentration in the grown films by increasing the CH_4/H_2 gas ratio. The measured nitrogen concentrations are still in the low-ppb range. The second approach, however, shows a slight increase in the nitrogen concentration in the grown film for $N_2/(CH_4 + H_2)$ ratios higher than $\sim 1\%$. The observed subtle differences are attributed to a chamber-related feature. Due to the large chamber volume and relatively slow nitrogen gas flow, the growth time was not sufficient for the saturation condition of nitrogen species in the plasma. This means the $N_2/(CH_4 + H_2)$ ratio in plasma would be still increasing, and would be far from the desired value before the growth process stopped. Nonetheless, the sample with the higher nitrogen concentration and good film quality is utilized to experimentally realize the optimized δ-doped structure proposed in the previous section.

5.3.3. Experimental realization

The nitrogen-doped diamond film is grown on the surface of a single-crystal [100]-oriented electronic grade type IIa diamond synthesized by Element Six. The surface was previously mechanically fine-polished to a roughness of ~ 1 nm (RMS, measured by AFM). The base parameters for the CVD process are described in Appendix D. In this experiment, the following specific parameters are used: 26 mbar of chamber pressure (base pressure $< 10^{-6}$ mbar) and 300, 0.4, 40 sccm of H_2, CH_4 (gas with natural abundance of ^{13}C, 1.1%) and N_2 gas flow, respectively. The growth rate is previously calibrated on other diamond substrates by weight differ-

a) b)
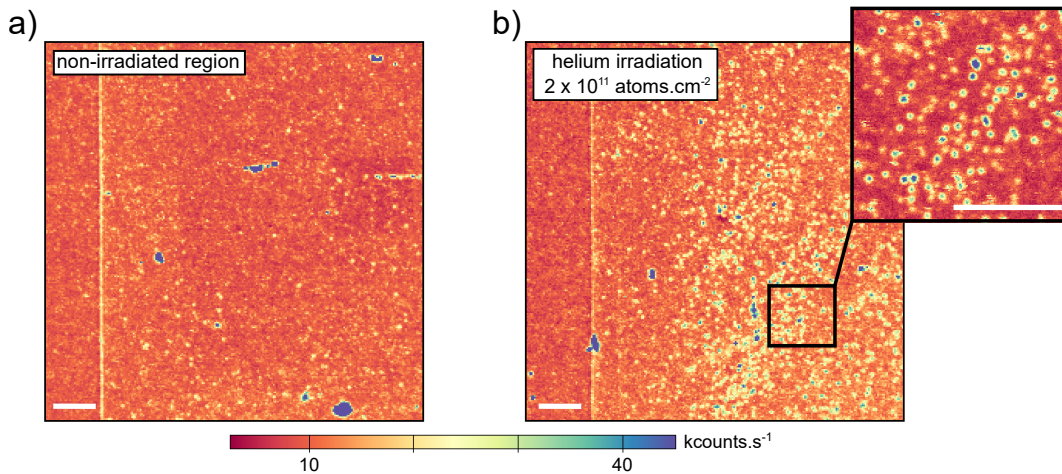
Figure 5.13.: Step-etching calibration of the nitrogen-doped diamond film. a) The areal density of NV centers measured by confocal microscopy is shown versus the etching depth. Single NV centers are created by helium irradiation on individual regions with ion fluences of 2×10^{11} atoms.cm^{-2}. The dots and triangles correspond to the step-etching calibration of the nitrogen-doped film and the reference diamond substrate with ~ 0.8 ppb of nitrogen impurities, respectively. The solid lines are individual fits corresponding to Gaussian complementary error functions. Vertical error bars correspond to the standard deviation of the measured areal density of NV centers (see Appendix E). Horizontal error bars correspond to the uncertainty in the AFM depth measurements. **b)** Experimentally-extracted depth distributions of NV centers for the nitrogen-doped film (blue line) and the reference diamond substrate (black line). The peak in the concentration of NV centers seen in the blue line identifies the higher nitrogen doping level in the grown film.

ence before and after the growth process. The growth time is 4 min and is set to be conforming to the desired film thickness, as discussed in section 5.3.1.

Vacancies are created in the near-surface region of the substrate by molecular helium ion irradiation (He$_2^+$) with 4.0 keV of energy. Different regions of the substrate are irradiated with fluences of either 2×10^{11} atoms.cm^{-2} or 2×10^{12} atoms.cm^{-2}. Afterwards, the diamond is annealed at a temperature of 950°C under vacuum condition ($< 10^{-6}$ mbar) for two hours. The surface is cleaned and oxidized by WCO treatment. According to the previous section, the concentration of nitrogen impurities in the grown film was not a priori calibrated. For this reason, step-etching technique is used to extract the depth distribution of NV centers at regions irradiated with a helium fluence of 2×10^{11} atoms.cm^{-2} (absence of helium-related background in confocal microscopy images, see section 2.2.3).

Figure 5.13 a) shows the areal density of NV centers versus the etching depth. The values corresponding to the nitrogen-doped grown film (black dots) are com-

Figure 5.14.: Confocal microscopy images of the nitrogen-doped grown film surface.
The images of the diamond surface after the nitrogen-doped CVD growth are
presented for a non-irradiated region (**a**) and a region irradiated with helium
at a fluence of 2×10^{11} atoms.cm^{-2} (**b**). All images are acquired after thermal
annealing and WCO treatment. The non-homogeneous incorporation of nitrogen
in micro-regions of the grown film is imprinted on the areal density of NV centers
resulting from the helium irradiation. The vertical line observed at the left hand
side of both images refers to an alignment marker (etched plateau) for confocal
microscopy images. The scale bars represent $10\,\mu$m.

pared to reference values from a ultra-pure diamond substrate with $\sim 0.8\,$ppb of
nitrogen impurities under the same irradiation/annealing conditions (previously
presented in figure 5.2 a). The blue-solid line corresponds to a fit using two Gaus-
sian complementary error functions, one representing the nitrogen-doped film and
another the reference diamond substrate. The corresponding depth distribution of
NV centers is shown in figure 5.13 b). A peak in the concentration of NV centers
clearly identifies the higher level of nitrogen doping in the grown film. There, the
concentration of nitrogen impurities is estimated to be approximately $10\,$ppb with
a corresponding film thickness of $15 - 20\,$nm.

The uncertainty in the experimental data can be related to the non-homogeneous
incorporation of nitrogen in the grown film at different micro-regions of the dia-
mond. This is further supported by the confocal microscopy surface images of the
nitrogen-doped grown film presented in figure 5.14. Therewith, the areal density of
NV centers can be estimated for non-irradiated regions (a) and helium-irradiated
with and ion fluence of 2×10^{11} atoms.cm^{-2} (b) (images acquired after thermal
annealing and WCO treatments). As seen, the non-homogeneous incorporation
of nitrogen in diamond is imprinted on the areal density of NV centers in the
helium-irradiated area. Micro-features are observed in the confocal image with

varying densities of NV centers (see also the inset in figure 5.14 b). These features are attributed to a preferential nitrogen incorporation at polishing grooves and regions with a higher miss-oriented crystal angle [244].
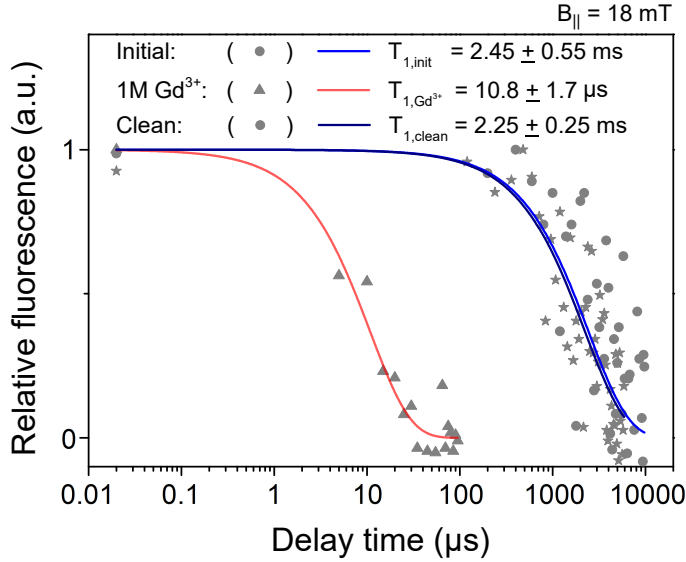
Eventually, the final fabrication step is performed on a particular region of the diamond surface irradiated with helium at a fluence of 2×10^{11} atoms.cm^{-2}. The oxygen soft plasma is used to remove approximately $10 \, \text{nm}$ of the original film in order to bring the calibrated peak in the concentration of NV centers (figure 5.13 b) directly to the structure surface. The spin properties of the remaining NV centers are the object of study of the next section.

5.3.4. Quantum sensing benchmark measurements: spin relaxometry technique

After the described plasma etching process, the remaining NV centers are expected to be distributed within a depth of $5 - 10 \, \text{nm}$. As previously explored in Chapter 1, the electron spin of the NV center is sensitive to magnetic noise induced by spins located on the diamond surface. In the present experiment, NV centers hosted in the fabricated structure are utilized as sensors to detect Gd^{3+} electron spins intentionally placed on the diamond surface. The thin film containing Gd^{3+} ions is created on the diamond surface as described in Appendix G.2. The T_1 times of individual NV centers in the optimized δ-doped structure are measured in the presence and absence of such layer with an aligned external magnetic field of $\sim 18 \, \text{mT}$.

It should be highlighted that some NV centers presented a blinking photoluminescence in the presence of the Gd^{3+}-containing layer. This can indicate transitions from the negative to the neutral charge state due to i.e. surface charge instability [37]. Therefore, the diamond surface is terminated with fluorine, utilizing the process described in Appendix B.1. After this process, the majority of NV centers showed a stable photoluminescence through all the performed measurements. Importantly, measured T_1 and T_2 times showed no significant changes with the modification of the diamond surface termination from oxygen to fluorine.

Figure 5.15 shows a typical T_1 time measurement in the presence and absence (initial and cleaned surface conditions) of the film containing Gd^{3+} ions. It should be emphasized that measurements of the T_1 time of all addressed NV centers present consistent values throughout the measurement steps of the depth calibration process. Importantly, the extracted Gd^{3+}-induced spin relaxation rate allows
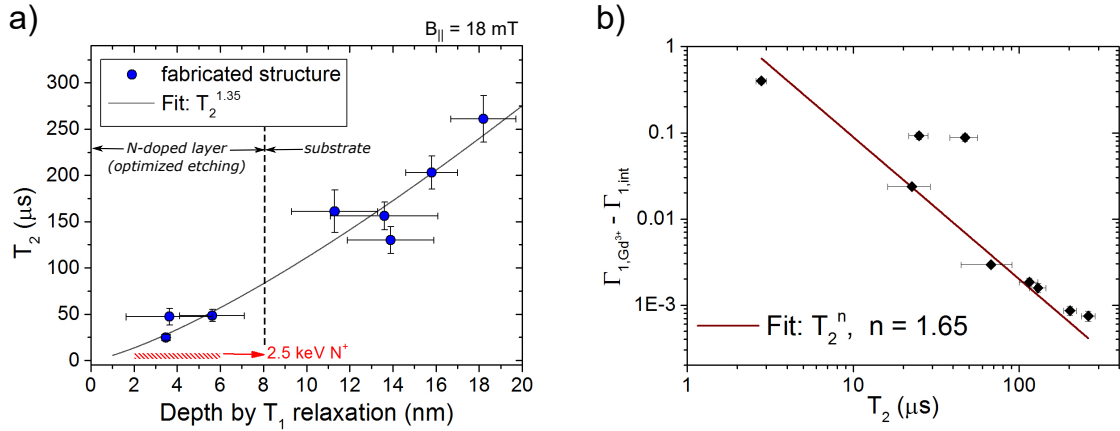
Figure 5.15.: Detection of Gd^{3+} ions by spin relaxometry technique. A typical result of a T_1 spin relaxometry measurement is presented. From the measured T_1 times, the Gd^{3+}-induced spin relaxation can be extracted and hence be used to estimate the depth of individual NV centers.

the direct evaluation of the depth of individual NV centers, as discussed in Appendix G.2.

During the spin relaxometry measurements, T_2 times are also measured and are shown in figure 5.16 a). As seen, the results show a decrease in T_2 times for decreasing depth, which is attributed to stronger interactions with the surface spin bath [36]. Figure 5.16 b) shows the decay rate of the longitudinal magnetization induced by Gd^{3+} ($\Gamma_{1,\text{total}}$ in equation A.13) versus the measured T_2 times of individual NV centers. Importantly, the combined T_2^n fits in figures 5.16 a) and b) correlate well to the expected behavior given by the model (see Appendix G.2). This confirms the consistency of the spin relaxation model to estimate the depth of NV centers in this experiment.

Moreover, NV centers located in the optimized δ-doped structure for depths of < 5 nm show T_2 times of up to 50 µs. This represents a five-fold improvement in comparison to T_2 times of NV centers created by conventional nitrogen implantation at comparable depths (red-marked region in figure 5.16). It should be highlighted that the nitrogen-doped grown film contains the natural abundance of ^{13}C atoms. In addition, the comparison between T_2 times of NV centers in the optimized δ-doped structure and in the ultra-pure substrate (figure 5.16 a) assures the crystal quality of the grown nitrogen-doped diamond film.

Figure 5.16.: Spin coherence times of NV centers in the optimized δ-doped structure. a) Spin coherence times of individual NV centers are shown as a function of the depth (estimated by spin relaxometry). The vertical-dashed line separates T_2 times from NV centers located at the optimized δ-doped structure (left side) and in the diamond substrate (right side). The highlighted region in red represents typical T_2 times of NV centers created by conventional nitrogen implantation with 2.5 keV of energy. Vertical error bars correspond to the uncertainty in the data fitting. Horizontal error bars correspond to the depth uncertainty due to the used model. **b)** The decay rate of the longitudinal magnetization induced by Gd^{3+} is shown versus the T_2 time of individual NV centers. Both T_2^n fits in a) and b) assure the consistency of the used model to estimate the depth of NV centers.

As a figure-of-merit for the potential application of the presented structure in quantum sensing applications, one can estimate the minimum detectable AC magnetic field. This would be roughly given by [129] $B_{\min} \sim (1.7837 \times 10^{-10})(1/\sqrt{TT_2})$, where T represents the signal acquisition time. Assuming $T_2 = 50\,\mu s$ and a typical value of $T = 60\,s$, the minimum detectable ac magnetic field is estimated to be approximately 3.3 nT. This means the presented δ-doped method delivers NV centers with sufficient magnetic sensitivity to detect the signal of a single proton spin on the diamond surface under optimum experimental conditions [65].

5.4. Summary and outlook

This Chapter has presented a detailed analysis on the generation of NV centers by low-energy helium irradiation in diamond. The presented results revealed key information regarding the vacancy diffusion at the nanoscale. The creation of NV centers by ion irradiation was demonstrated to be localized within the atomic

profile of irradiated atoms with a high conversion efficiency of $\sim 15\%$. Furthermore, in comparison to conventional nitrogen implantation, an order of magnitude enhanced T_2 times were observed for NV centers by helium irradiation with less than 10 nm of depth. The helium irradiation technique has also been proved to be an efficient method to determine the concentration of nitrogen impurities in ultra-pure diamond substrates.

Analytical estimates of vacancy diffusion have been verified using the presented experimental results. Importantly, the model assuming individual ion tracks as defect clusters could successfully reproduce and explain the limits in the depth distribution and conversion efficiency of NV centers by helium irradiation. As shown, the overlap between neighbor defect clusters for ion fluences $> 10^{12}$ atoms.cm^{-2} has pointed toward alternative paths of vacancy recombination such as the formation of vacancy chains. This, in turn, would suppress the formation efficiency of NV centers at the sub-surface regions of the irradiated diamond and limit the nitrogen-to-NV center conversion efficiency.

At the end, the gained insights on the activation of NV centers in homogeneously-doped diamond substrates have been used to optimize the fabrication architecture of a δ-doped diamond structure for quantum sensing. The experimental realization of such structure has been presented, whereby the spin measurements indicated that the NV centers located within such optimized structure would yield in a magnetic sensitivity enough to detect a single nuclear spin on the diamond surface. This highlights the potential capabilities of such structure to host NV centers with augmented properties for quantum sensing applications.

The presented results also reveal aspects that can be further improved in order to fully develop the sensing capabilities of such NV center-based devices. These features will be briefly explored below.

Control in the nitrogen-doped CVD growth. The growth of epitaxial nitrogen-doped CVD diamond films with high doping level and sharp interfaces is a rather difficult experimental task. The creation of sharp nitrogen doping profiles relies mostly on the needed time for the growth chamber to be saturated with the added N_2 gas to the plasma. In the presented case, the nitrogen gas flow was set to the maximum allowed by the used hardware (40 sccm, as mentioned), but the concentration of the ingrown nitrogen impurities in the film was still rather low (~ 10 ppb).

Recent reports indicate some approaches that can be used to overcome this issue. The most straightforward would be the implementation of a rapid gas switching

mechanism and an in situ residual gas composition analysis (mass spectrometer at the outlet of the chamber). The first would allow a much faster introduction of nitrogen in the gas mixture, thus leading to a nanometer-sharp interface between the δ-doped film and the ultra-pure substrate [67]. The latter would provide further information about the gas saturation behavior. Combined to depth profile analysis such as the helium irradiation technique and secondary ion mass spectroscopy (SIMS), this would allow a precise estimation of the ratio between the nitrogen content in the gas mixture and nitrogen atoms incorporated into the grown film.

Alternatively, as discussed in Ref. [245], the CVD growth of diamond films on a nitrogen-terminated surface leads to a very high incorporation of nitrogen impurities ($\sim 10^{20}$ cm^{-3}) and nanometer-sharp interfaces. The control on the doping level is achieved by changing the density of nitrogen atoms at the diamond surface, e.g. by controlling the nitration process of the utilized substrate [246]. This technique would be very useful for applications based on high-density ensembles of NV centers such as wide-field imaging [141].

Integration in photonic structures. The estimated magnetic sensitivity of near-surface NV centers hosted in the optimized δ-doped structure is extremely limited by the poor collection efficiency of emitted photons [55, 247]. The use of tapered diamond nano-pillars hosting near-surface NV centers provides an order of magnitude improved photon collection efficiency, which translates into a three-fold enhanced magnetic sensitivity. When combined to the relatively-long T_2 times of near-surface NV centers by helium irradiation, such enhancement would facilitate a wide range of NV center-based magnetometry applications. The integration into such structures would require homogeneous density of NV centers and consequently nitrogen incorporation in the CVD diamond film over a large area. As discussed in this Chapter, this can only be achieved if the initial surface morphology is extremely smooth, e.g the miss-orientation angle and grooves due to polishing and growth defects are minimized.

Appendices
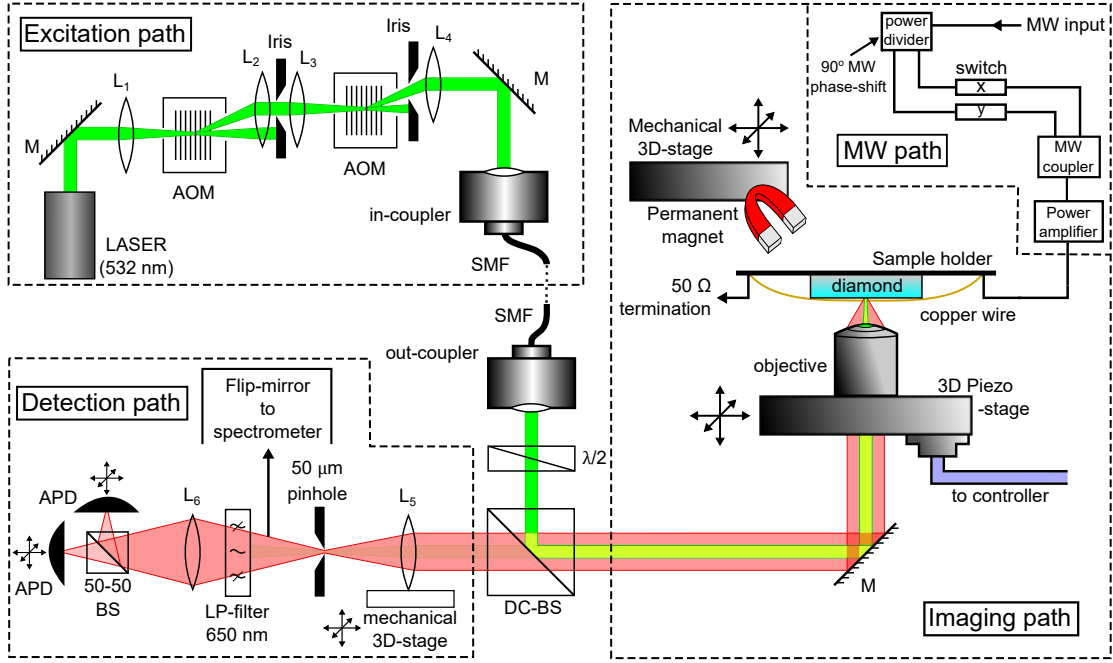
A. Description of the utilized equipments

A.1. Scanning confocal microscope

In this section, the utilized experimental setup to optically characterize as well as to perform coherent manipulation of the corresponding electron spin of NV centers in diamond is described. All presented measurements in this Thesis have been performed at room-temperature. A schematic representation of the experimental setup is presented in figure A.1. At first, the excitation path of the home-built confocal microscope [248] consists of a transverse CW collimated green LASER ($\lambda = 532\,\text{nm}$, GEM 532). To perform optical pulses, the beam is focused into acousto-optic modulators (AOMs) by the lenses L_1 and L_3 in figure A.1. A double-AOM configuration is adopted for an optimized bright/dark rate of optical pulses. This is of particular importance to enhance the signal-to-noise ratio (SNR) in measurements with long phase accumulation times such as T_1 times ($\sim\text{ms}$ dark time versus $\sim\text{µs}$ bright time).

Afterwards, the collimated beam is focused into a single-mode optical fiber (SMF) by the fiber in-coupler and transmitted to the imaging path. This assures a Gaussian profile of the beam, resulting in a diffraction-limited confocal point spread function (PSF) at the end [248]. The collimated beam propagates further from the fiber out-coupler, reaching a half-wave plate to adjust the desired linear polarization of the excitation light. A dichroic beam splitter (DC-BS in figure A.1, $\approx 90\%$ reflectance of $532\,\text{nm}$ excitation light and $\approx 90\%$ transmission of $> 570\,\text{nm}$ emitted light) is utilized to steer the excitation beam towards the microscope objective lens.

For the presented measurements, two objective lenses were utilized. An oil objective (Zeiss West, Plan-Neofluar Magnification of 100x) with a high numerical aperture (NA = 1.30) was used for most of the presented confocal microscopy images and spin measurements due to the a higher number of acquired photons

Figure A.1.: Schematic representation of the utilized setup for the characterization of NV centers. Experimental setup utilized for optical characterization and coherent spin manipulation of NV centers, comprising of a home-built confocal microscope, a scanning-stage for the imaging of diamond, and external magnet and microwave apparatus. The excitation wavelength is 532 nm. In the figure, mirrors are represented by M, lenses by L_i, single-mode optical fiber by SMF, beam-splitters by BS, and avalanche photo-diodes by APD.

and, consequently, an enhanced SNR. For performed spin relaxometry measurements with deposited Gd^{3+}-containing films (see Appendix G.2), an air objective (Olympus, MplanApo Magnification of 50x and NA = 0.95) was utilized to avoid the potential dissolution of the deposited film into the immersion oil. As depicted in figure A.1, the microscope objective lens is mounted on a 3D piezo-stage with sub-nanometer precision and a closed-loop control system for optimum stability. By scanning the objective, the LASER beam enters the objective back-plan at different angles, thus allowing the scanning of the confocal PSF on the diamond substrate.

The imaged diamond substrate is hold fixed by the sample holder, where a 20 μm copper wire is placed in the close vicinity of the substrate surface to deliver the microwave field for coherent spin manipulation of NV centers. The sample holder is specially designed for impedance-matching to the microwave path (50 Ω) in order to avoid power losses and reflection within the microwave transmission line. Microwave pulses are generated by field-programmable gate arrays (FPGAs),

where two microwave channels (with 90° relative phase shift) can be controlled independently by two high frequency switches. For the measurements of pairs of NV centers, an additional microwave path is added to the setup (not shown in the figure for clarity). Above the substrate, a permanent magnet is mounted on a manual 3D stage for the alignment of the external magnetic field to a specific orientation of NV centers in the diamond substrate.
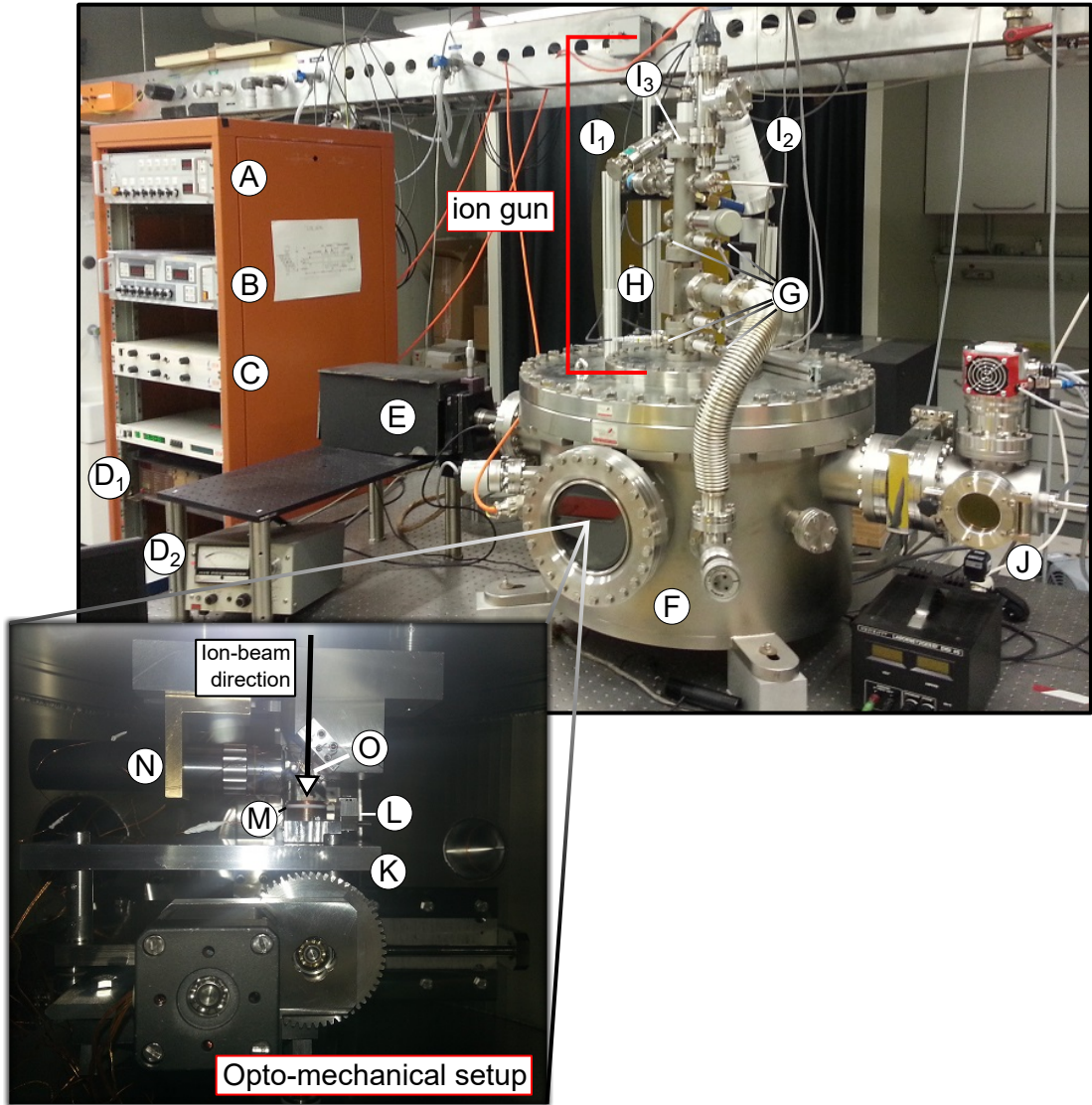
The photoluminescence of the illuminated region of the diamond substrate is collected by the same objective lens and transmitted by the dichroic beam splitter to the detection path of the setup. To spatially-filter the photoluminescence signal, the emitted light is focused on a pinhole. In this way, an image of the confocal PSF can be obtained (this is the signature of the confocal microscopy technique). The size of the pinhole is previously optimized by projecting the free-image (e.g. no spatial filter) of individually-resolvable NV centers onto the chip of a cooled-CCD camera (Cascade 512B) - see Ref. [55] for further details. The observed full width at half maximum (FWHM) of the imaged Airy disk [249] covered approximately two pixels of the camera chip (each pixel is $\approx 16\,\mu m$ in size). Therefore, a $50\,\mu m$ pinhole is chosen in order to efficiently collect most of the emitted photons of NV centers, while spatially-filtering the photoluminescence background.

A long-pass filter ($650\,nm$ LP) is utilized to further block the remaining excitation light and transmit only the wavelengths in the range of the photo-emission of negatively-charged NV centers. At the end, the pinhole is imaged onto the chips of avalanche photo-diodes (APDs) in a so-called Hanbury-Brown and Twiss configuration [250]. This allows the recording of the second-order auto-correlation function ($g^2(\tau)$), and therefore to address the number of NV centers within a confocal spot [55, 251].

For further characterization of the emitted photoluminescence signal, a flip-mirror is positioned at the detection path (see figure A.1) and the collected light is focused into a multi-mode optical fiber by a fiber in-coupler (elements not shown in figure A.1 for clarity). The photoluminescence spectra are then acquired using a SP2300 spectrograph (Princeton Instruments) coupled to a multi-mode fiber, where a $575\,nm$ long-pass filter is used to block the excitation laser.

A.2. Implantation setup

The utilized setup for ion implantation with energies below $10\,keV$ is described in this section. Figure A.2 presents an image of the experimental apparatus. It consists of an extractor-type, differentially-pumped focused ion gun (gas-source

Figure A.2.: Home-built ion implantation setup and relevant features. An image of
the utilized setup for the ion implantation of diamond with energies below 10 keV
is shown. The inset presents the opto-mechanical apparatus for the target ion
implantation on specific areas of the diamond substrates and the in-situ calibration
of the ion beam (see the text).

IQE 12/38, Specs), modified for an ion extraction energy of up to 10 keV (high-
voltage power supply represented by A in the figure). The ion gun is installed at
the top of a vacuum chamber (F), with two optical ports (E and F) and several
electric ports. A quick load-lock system (J) is utilized, such that the main chamber
remains always under high vacuum ($< 10^{-8}$ mbar) condition.

A variety of positively-charged ion species can be implanted by connecting the desired gas sources to the ports, represented by I_1 and I_2. In the presented experiments, isotopically-purified nitrogen (^{15}N), electronic grade helium (He) and carbon dioxide (CO_2) gases are used for the described implantation events throughout the Chapters. The ion source operates with a hot filament that ionizes the gas via electron bombardment (region I_3 in figure A.2). The ionized particles are then accelerated by an extraction voltage towards the main chamber with the targeted kinetic (implantation) energy. The focusing of the ion beam can be adjusted down to $\sim 100\,\mu$m in diameter by electric lenses (G).

A Wien mass filter ($\mathbf{E} \times \mathbf{B}$) is utilized to select the desired ion species to be implanted, avoiding the introduction of unknown impurities in the substrate (B - power supply and H - Wien filter position). The ion fluence is controlled by switching the Wien filter voltage (i.e. controlling the passage of the ion current) for a specific time period. By this method, the rise and cut-off times of the ion current are previously calibrated to be $\approx 40\,$ms and $< 1\,$ms, respectively. These values are taken into account for the calculations of the ion fluence in all presented experiments.

The inset of figure A.2 presents the opto-mechanical system localized inside the main vacuum chamber. It consists of three motorized stages (3D degree of freedom in the positioning of the substrate relative to the ion beam) with sub-µm step resolution (C are the corresponding controllers). On the top of these stages, a plate (K) hosts the lock system for the sample holder (L) and a Faraday cup (M). The later is designed with a metallic cap with several apertures of different diameters (ranging from $\approx 100\,\mu$m up to $\approx 1\,$mm), with which the ion beam current and hence the ion fluence can be calibrated (the picoammeters for the independent current reading at the bottom and cap regions of the Faraday cup are represented by D_1 and D_2, respectively). To avoid any heating-related effects such as thermally-induced diamond graphitization, relatively low ion current densities ($< 3\,$A.m^{-2}) are utilized.

A custom-built optical microscope is also designed for the in-situ imaging of the targeted regions of the substrate to be implanted. The ion beam direction is roughly represented by the arrow in the inset of figure A.2. A mirror with a fabricated hole in its center is placed at the top of the target region, $45°$ in comparison to the ion beam direction (O). An objective lens (N in figure A.2, Mitutoyo, Magnification of $10\times$ and NA $= 0.28$ - large field of view of $\approx 2.4\,$mm) is used to project the image of the target region onto an external CCD camera through the optical port E.

For all used gas sources, the resulting ion beam shows a Gaussian spatial distribution profile. The described ion fluence values in this Thesis are therefore corrected for the mean-value of the ion current over the area corresponding to the FWHM of the Gaussian ion beam shape, times the set implantation time.

A.3. X-ray photoelectron spectroscopy
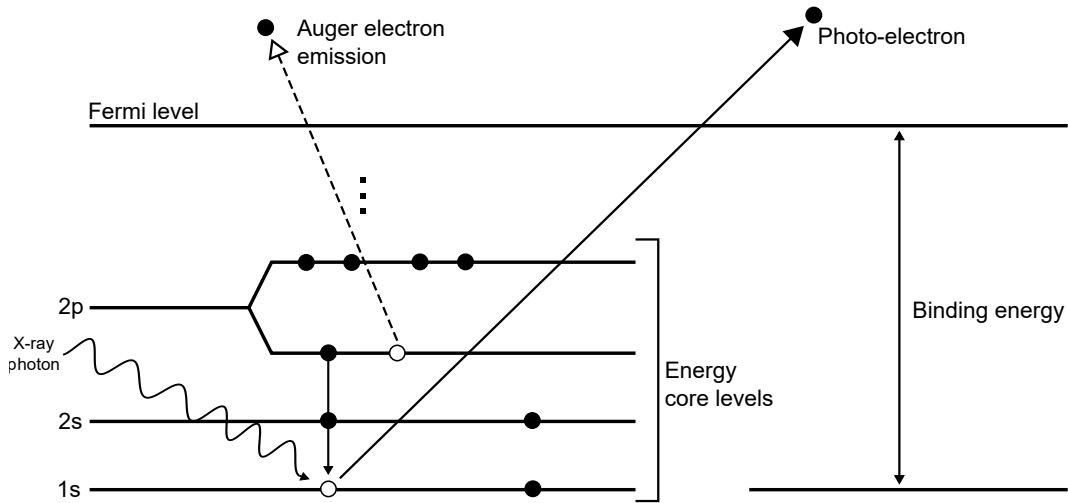
The characterization of the physical and chemical composition of the diamond surface is of primordial importance due to their decisive influence on the surface energy band bending and hence, on the properties of near-surface NV centers (see Chapter 1, section 1.4). To this aim, a widely-adopted technique is the X-ray photoelectron spectroscopy (XPS) [252]. X-ray photons ($E_{\text{x-ray}} = h\nu$) ionize atoms of the target material, from which electrons are ejected from different electronic shells as a result of the photoelectric effect (e.g. absorption of an X-ray photon with sufficient energy to overcome the electron binding energy). Importantly, $E_{\text{x-ray}}$ must be sufficiently high in order to efficiently ionize atoms from the majority of the elements of the periodic table. A schematic representation of this process is shown in figure A.3 for the case of electron photo-emission from the 1s electronic shell.

In XPS, the experimentally-measured quantity is the kinetic energy (E_{k}) of the ejected core electrons. This value depends directly on $E_{\text{x-ray}}$ and therefore is not an intrinsic property of the analyzed material. Hence, the electron binding energy (E_{bi}) is the parameter of interest that defines unambiguously the chemical environment of atoms in the target material. These quantities are related by [252]:

$$E_{\text{bi}} = h\nu - E_{\text{k}} - W_{\text{f}}, \tag{A.1}$$

where W_{f} is the spectrometer (e.g. detector) work function. This quantity must be determined by calibrating the XPS experimental apparatus using reference target materials. In this way, acquired XPS spectra in different setups using i.e. different X-ray sources can be directly compared. Each chemical element possesses a characteristic electronic structure (also depending on the chemical environment), which translates into unique XPS spectra.

The relevant physical and chemical composition properties of the target material can be deduced from the observed core-level and Auger electron emission peaks in XPS spectra. The later are the result of the electron recombination within

Figure A.3.: **Schematic representation of the XPS photo-electron emission process.**
A schematic representation of the absorption of an X-ray photon by an electron
at the 1s shell, followed by its ejection (ionization process) is shown. The ionized
atom returns to its ground-state when the core hole left in the e.g. 1s shell is
subsequently filled by an electron initially at a higher-energy shell. During this
process, an Auger electron can be emitted depending upon the electron shell
configuration after the filling of the core hole. Figure adapted from Ref. [252].

electronic shells of individual ionized atoms, such that their return to their ground-
state energy level (equilibrium configuration) either by ejecting further electrons
from outer levels (Auger electrons) [253] or emitting X-ray photons (see figure
A.3).

The XPS technique classifies the observed peaks according to the spectroscopy
notation. At first, the principal quantum number ($n = 1, 2, ...$) is shown, followed
by the angular momentum (l) indicated by letters (core levels s, p, d, ...) and
finally the total angular momentum quantum number (j) as a suffix [252]. This
notation is utilized throughout the presented XPS results in this Thesis. It should
be also noted that XPS peaks corresponding to different core levels/different chem-
ical components usually present different relative intensities and line widths (that
is, the FWHM of the measured peak). The ionization efficiency of specific elec-
tronic shells governs the relative peak intensity, whereas the linewidth is a result
of contributions from the natural width of the core level and from the resolution
of the used equipment for the detection of ejected photo-electrons.

The depth of analysis in the target material depends on the energy and incident
angle of the X-ray beam. This depends on the characteristic inelastic mean free
path (IMFP, λ), which defines the average distance traveled by a photo-electron

ejected within the excited region of the material before losing kinetic energy due to collision events with other atoms. Generally, photo-electrons that reach the detector are emitted within the top $1 - 10$ atomic layers of the material, corresponding to a depth of analysis of up to $\sim 3\lambda$, depending on the incident angle of the X-ray beam. In the case of diamond, this value is approximately $2.2\,\text{nm}$ [254] for the used $E_{\text{x-ray}}$ range (see below).

In the presented experiments[1], XPS spectra are acquired using an AXIS ULTRA (Kratos Analytical) spectrometer, equipped with a monochromatic Al Kα X-ray source ($E_{\text{x-ray}} = 1486.6\,\text{eV}$, line width of $\approx 0.85\,\text{eV}$). The binding energy scale (e.g. the spectrometer work function) is previously calibrated by means of silver and gold reference samples. All presented XPS spectra are acquired at room-temperature. The observed peaks in the XPS spectra are fitted using pseudo-Voigt functions [255]. A quantitative analysis of the chemical composition of the top-layers of diamond is performed by integrating the peak area of a specific chemical element (i), providing the corresponding intensity of the photo-electron peak (I_i). The relative atomic concentration of the analyzed chemical element is thus given by [252]:

$$N_i = \frac{I_i}{\sigma_i \lambda K}, \tag{A.2}$$

where σ_i is the cross-section for photo-electron emission (characteristic of the analyzed chemical element) and K represents a scaling parameter due to experimental factors [252].

B. Plasma processes

All reported plasma processes in this Thesis are performed using an Oxford PlasmaPro NGP80 capacitively-coupled plasma unit, equipped with an additional ICP source (Oxford Plasma Technologies).

---

[1]Collaboration with Dr. Mitsuharu Konuma, Max Planck Institute for Solid State Research in Stuttgart.

B.1. Fluorine-terminated diamond surface
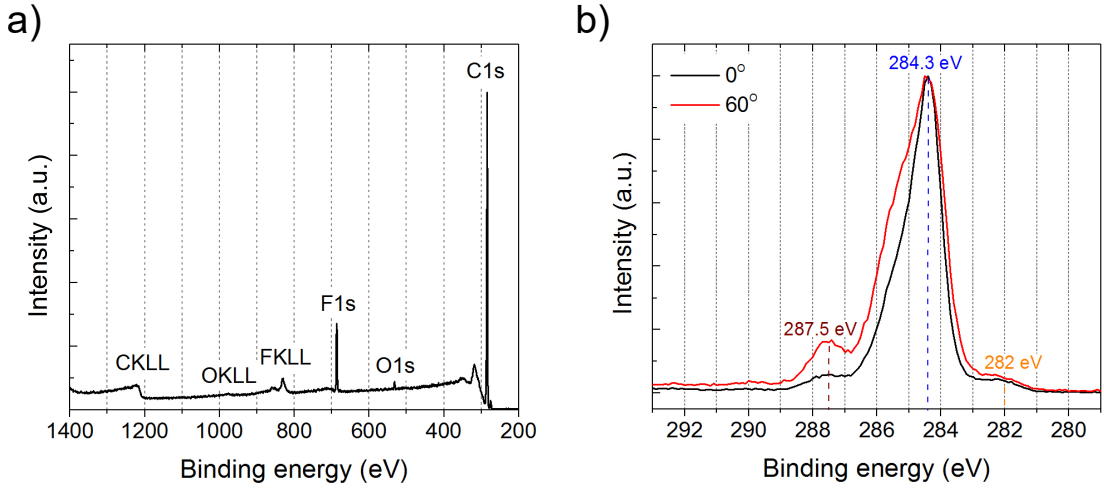
The diamond exposure to fluorine-based plasmas is of interest in two different areas related to the material modification, namely material etching and change of the surface chemical composition. In the first case, ion-enhanced etching by fluorine plasma processes yields a relatively high etching rate and smooth surface morphology. As an example, the fabrication of thin diamond membranes using Ar/SF_6 plasma have been reported [56]. Even though the diamond film was etched for a depth of $> 25\,\mu m$ with an etching rate of $170\,nm.min^{-1}$, the final surface roughness was shown to be less than a nanometer.

In the second case, fluorine-terminated diamond surfaces are achieved using either CF_4 [132, 256] or SF_6 [66, 257] ICP processes. Fluorine has a higher electronegativity in comparison to carbon, which means the C-F surface dipole points towards the fluorine atom. This gives the fluorine-terminated diamond surface a high positive electron affinity [258]. The drawback of the diamond exposure to a CF_4 plasma is the formation of a polymer layer with a few nanometers of thickness, which leads to an inefficient surface coverage by fluorine atoms [132].

To briefly investigate the chemical composition of fluorine-terminated diamond surfaces exposed to SF_6 ICP plasma process, a single-crystal [100]-oriented type IIa diamond (Element Six) is utilized as substrate. A thick boron-doped diamond film is overgrown on the surface of the diamond substrate to avoid the charge accumulation during the chemical analysis by XPS technique. Previous to the plasma exposure, the diamond is treated by WCO, resulting in an initial oxygen-terminated surface. The substrate is then exposed to the SF_6 ICP process, similarly as in Ref. [66].

The recipe is divided into two parts. At first, the capacitively-coupled radio frequency source with 50 W of power is used to ignite the plasma for a few seconds. Afterwards, the capacitive RF source is switched off, and the plasma is sustained only by the ICP source with a power of 500 W for 4 min. The constant parameters throughout the two steps are 20 mTorr of chamber pressure (base pressure of $< 10^{-6}$ mTorr), 100 sccm of SF_6 gas flow and 20°C of substrate holder temperature. Importantly, no apparent etching and no increase in surface roughness are observed, even for longer exposure times (surface morphology measured by AFM).

Figure A.4 a) shows the wide-energy XPS spectrum measured normal to the diamond surface. Apart from the pronounced C1s peak (carbon-carbon sp^3 hybridized bonds), the F1s signal at 686 eV of binding energy is observed, confirming the presence of fluorine atoms at the diamond surface [66, 257]. The gas dissoci-

Figure A.4.: XPS spectra of diamond after the exposure to SF$_6$ ICP process. a) Wide-energy XPS spectrum of the C1s and F1s core levels acquired normal to the diamond surface. The O1s peak is still observed, indicating the presence of residual oxygen on the diamond surface. The Auger peaks corresponding to the KLL carbon, oxygen and fluorine electron emissions are also observed at ~ 1220, ~ 980 and ~ 830 eV, respectively. **b)** High resolution XPS spectra of the C1s core level. The black- and red-solid lines represent the acquired spectra normal and at an angle of 60° to the diamond surface, respectively. The dominating peak at ~ 284.3 eV of binding energy corresponds to the signal from carbon-carbon sp^3 hybridized bonds. In both spectra, th signal intensities are normalized by the peak value at 284.3 eV of binding energy.

ation in the SF$_6$ plasma is expected to produce fluorine radicals, which strongly interact chemically with the initial oxygen termination. The replacement of the oxygen atoms from the original surface termination will result in the production of volatile sulfur oxyfluorides (i.e. SOF$_4$), which leaves active surface sites available for carbon-fluorine bonds to be formed [257]. The oxygen coverage of the diamond surface is hence expected to be drastically reduced after such a process. This is indeed observed in the presented experiments, as confirmed by the strong reduction of the O1s XPS peak intensity (at 532 eV of binding energy) after the SF$_6$ plasma exposure as compared to the peak intensity after the WCO treatment (e.g. comparing figure A.4 a to figure 3.6 a).

The fluorine-to-carbon ratio in figure A.4 a) is approximately 0.26. Since the ionization efficiency of fluorine by X-ray photons is much higher than of carbon [66], a quantitative analysis of the fluorine surface coverage is unfeasible from only the acquired spectrum normal to the surface. Moreover, the O1s peak is still observed in the wide-energy XPS spectrum, even after the plasma exposure. This can be explained by two different features. One possibility is the less-efficient

surface coverage by fluorine atoms after the SF_6 plasma exposure, attributed to the different initial surface termination, e.g. oxygen in the presented experiment versus hydrogen in Ref. [66]. Another possibility is the sample surface contamination by water molecules prior to measurements [258]. Since the measurements are performed at room temperature, even weakly-bonded oxygen atoms would still be detected.

The C1s core high-resolution XPS spectrum of the diamond surface after the exposure to the SF_6 plasma is shown in figure A.4 b) for two detection angles with respect to the diamond surface (0° and 60°). First and foremost, no traces of covalent oxygen-carbon bonds can be identified in both spectra. This reinforces the attribution of the observed O1s signal in figure A.4 a) to the surface contamination by water molecules. The peak at 284.3 eV of binding energy associated to sp^3 hybridized carbon-carbon bonds is clearly identified in both spectra. The surface composition is better accessed in the spectrum corresponding to the 60° detection angle due to a smaller depth of analysis (see the discussion in Appendix A.3). The peak asymmetry towards higher binding energies with a shift of approximately $+1.3$ eV is attributed to the induced chemical shift by carbon atoms bond to single fluorine atoms [258, 259]. The pronounced peak at 287.5 eV of binding energy is attributed to weakly-bonded carbon atoms to multiple fluorine atoms (e.g. CF_2 and CF_3 molecules [258, 259]). The weak peak at 282 eV of binding energy can be attributed either to sp^2 hybridized carbon-carbon bonds (graphitized top-layers) or π-bonded (C-C) carbon atoms at the diamond surface [258].

Several reports in literature indicate that the negative charge stability, the formation yield and the spin properties of near-surface NV centers are enhanced by terminating the diamond surface with fluorine atoms [66, 132, 256]. The reported results strongly indicate that NV centers in nitrogen delta-doped diamond films are more benefited by this change in surface termination than implanted ones. This can be due to the higher achieved crystal quality by the CVD growth process, making NV centers less susceptible to the effects of lattice defects. This is further confirmed by the results presented in Chapter 5.

C. On polishing-induced defects

Micro-polishing is the process of smoothing the morphology and planarization of a grown diamond crystal surface for a specific application. Since diamond is the hardest known bulk material, the mechanical polishing of its surface is a technical challenging problem. Different mechanical and chemical methods for polishing and

planarization can result in orders of magnitude reduction in the surface roughness and excellent alignment of the final surface and a specific crystallographic plane [77]. The traditional mechanical method is the use of a scaife plate (usually made of iron) that rotates at a relatively high speed, loaded with a fine-grain diamond powder. The diamond to be polished is pressed against the scaife plate and the removal of material occurs by micro-chipping along one crystallographic plane (depending upon the initial orientation of the diamond surface). The final surface roughness is ultimately limited by the grain size of the used diamond powder and can be in the order of a few nanometers using additional chemical methods (chemo-mechanical processes) [77].

Although the chemical composition of the crystal does not change significantly by the mechanical polishing, residual stress, non-uniform crystal orientation, phase transitions and sub-surface lattice displacements can drastically degrade the final quality of the polished material [77, 260]. These polishing-induced lattice defects have been reported to propagate a few micrometers below the diamond surface [260]. Near-surface NV centers can thus have their optical and spin properties degraded by electronic states induced in the band gap by polishing-induced lattice defects.
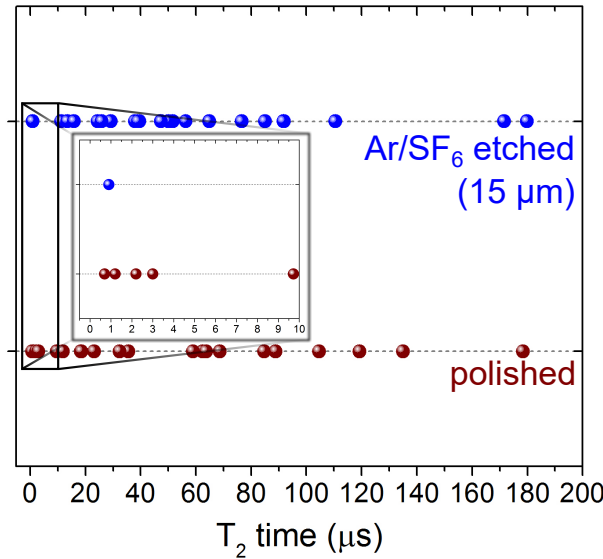
Here, this is briefly investigated using NV centers themselves as sensors. A high-purity single-crystal [100]-oriented electronic grade type IIa diamond (Element Six) is taken as substrate. The diamond surface is mechanically-polished to a final surface roughness of a few nanometers (measured by AFM) and a $< 3°$ non-uniformity in the crystal orientation (nominally along the [100] direction). Part of the substrate is then exposed to an RIE/ICP Ar/SF$_6$ plasma, using an auxiliary type Ib diamond as a mask to protect roughly half of the substrate polished surface. The plasma parameters are taken from Ref. [56]: 20 mTorr of constant chamber pressure (base pressure of $< 10^{-6}$ mTorr), 40 and 25 sccm of SF$_6$ and Ar gas flow, respectively, 100 W of capacitive RIE power, 600 W of ICP power, and 20°C of plate temperature. The resulting etching rate is ~ 200 nm.min^{-1}, as confirmed by AFM. The exposed part of the diamond substrate is etched to a depth of 15 µm, being sufficient to remove the damaged lattice sub-surface region due to the mechanical polishing process [260, 261]. The low damage oxygen plasma described in Chapter 3 is further utilized to remove a few nanometers of the etched surface, assuring the removal of any plasma-induced damages. Importantly, the used plasma process results in a pristine and smooth final diamond surface [56].

Afterwards, single NV centers are created by implanting nitrogen atoms with 5.0 keV of energy and ion fluence of 7×10^9 cm^{-2}, and subsequently annealing the diamond substrate under vacuum condition ($< 10^{-6}$ mbar) at a temperature of

$\sim 950°C$ for two hours. The mean depth of the created NV centers is expected to be $\sim 10\,nm$ [145, 146]. In this way, a single substrate would allow the direct comparison of the properties of NV centers under the etched and polished surface morphologies.

The T_2 times of single NV centers are used to probe the defect environment of the surrounding lattice. A magnetic field of approximately $30\,mT$ is aligned to one of the four possible axis of NV centers and the T_2 times are measured at each region as described in section 1.3. Figure A.5 shows the measured T_2 times of ~ 60 random NV centers at each mentioned area of the diamond substrate. The red and blue dots represent NV centers under the polished and etched surfaces, respectively. As observed, the values at both regions are very similar and spread over a large range, from 1 to $180\,\mu s$.

The inset in figure A.5 highlights the region of the histogram that corresponds to very short ($< 10\,\mu s$) T_2 times. As seen, the occurrence of such short values is slightly higher for NV centers under the polished surface in comparison to the etched surface. Nevertheless, this subtle difference indicates that the polishing-induced lattice defects have a minor influence on the resulting spin properties of implanted NV center at both regions. Hence, the magnetic noise of the surface spin bath and implantation-induced defects dominates the observed spin decoherence

Figure A.5.: Evaluation of polishing-induced defects using near-surface NV centers.
Statistics on the spin coherence times of NV centers localized under the polished (red dots) and etched with Ar/SF_6 plasma (blue dots) surface morphologies. The inset highlights the occurrence of short ($< 10\,\mu s$) T_2 times.

and is responsible for the wide spread in the measured values of T_2 times [36].

D. Diamond growth by microwave plasma-enhanced CVD

The epitaxial growth of high-quality diamond films are performed by microwave plasma-assisted CVD technique. Previous reports indicate that hydrogen atoms present in plasma are incorporated into the diamond films during growth [262, 263]. As investigated in Ref. [264], in this case, created NV centers would be passivated by hydrogen atoms, forming the optically inactive NVH defect during thermal annealing. In order to out-diffuse hydrogen atoms from the grown films before the creation of NV centers, the as-grown diamond substrates are annealed at a temperature of ≈ 900°C under vacuum condition ($< 10^{-6}$ mbar) for one hour [265].

D.1. Nitrogen-doped diamond films

The growth of thin nitrogen-doped diamond films (presented in Chapter 5) is performed in a home-built CVD reactor[2]. The base growth parameters are 1.2 kW of microwave power and 750°C of substrate temperature. The methane (CH_4, natural abundance of ^{13}C, 1.1 %), hydrogen (H_2) and nitrogen (N_2) gas flow and the growth time are varied according to specific requirements of the presented experiments in Chapter 5.

D.2. Boron-doped diamond films

The growth of heavily boron-doped diamond films is performed in an *ASTEX* 5000^{TM} reactor[3], similarly as described in Ref. [90]. The resulting growth rate of the boron-doped film is calibrated as schematically-presented in figure A.6 a). At first, specific regions of the grown film surface are covered by lithographically-patterned AZ 5214E photoresist (MicroChemicals, thickness of ~ 1.2 µm). Ohmic contacts are fabricated at the exposed regions of the film by thermal evaporation of

---
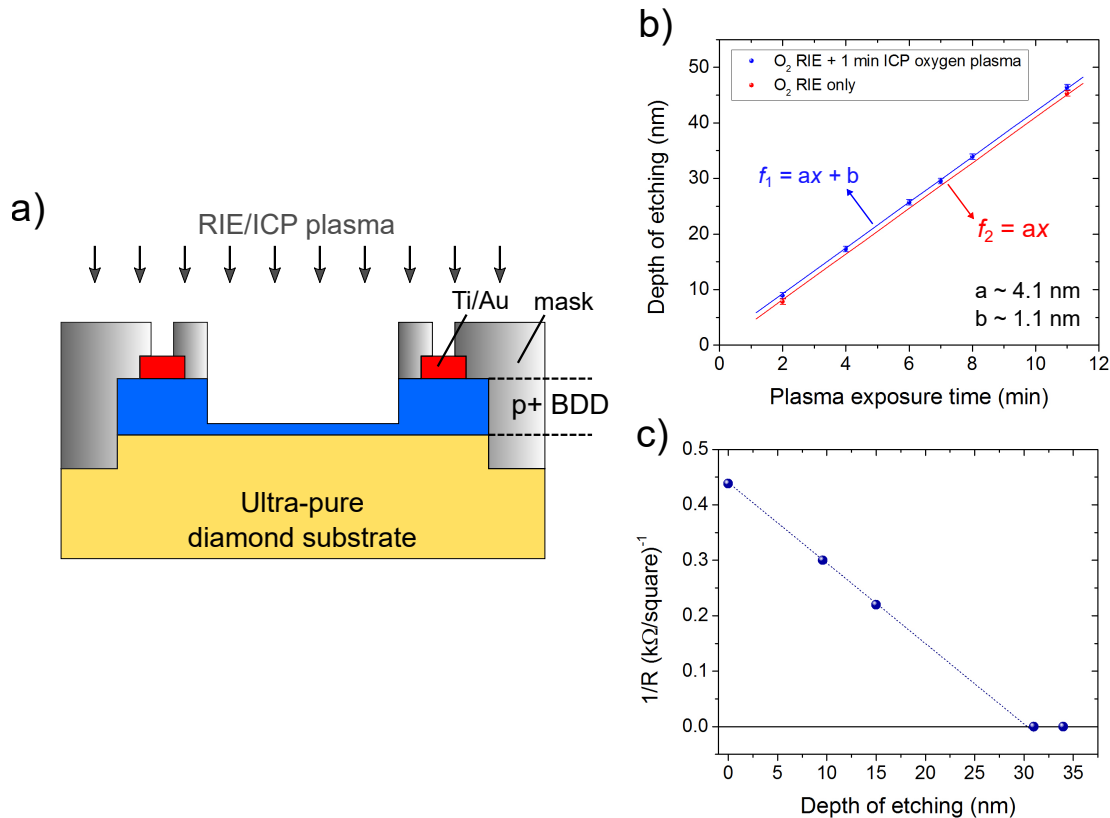
[2]Collaboration with Prof. Dr. Fedor Jelezko, Institute for Quantum Optics, University of Ulm.
[3]Collaboration with Dr. Alberto Pasquarelli, Institute of Electron Devices and Circuits, University of Ulm.

titanium (~ 20 nm thick) and gold (~ 100 nm thick) metals [266]. A second step of lithographically-patterned photoresist further exposes regions of the boron-doped diamond film to be etched between contacts (see figure A.6 a).

Etching steps are performed using the described oxygen plasma process in Chapter 3. At each step, the resulting etching depth and sheet resistance of the remain-

Figure A.6.: Growth rate calibration of the boron-doped diamond films. a) Schematic representation of the fabricated structure for the measurement of the sheet resistance of the grown boron-doped diamond film through plasma etching steps. Titanium-gold Ohmic contacts are fabricated on specific regions of the diamond substrate by combined photo-lithography and metal thermal evaporation techniques (see text). **b)** The resulting etching rate of the boron-doped diamond film (measured by AFM) is shown as a function of the plasma exposure time. Blue and red dots represent the experimentally-extracted etching depths at regions of the diamond substrate treated with only oxygen RIE plasma and with an additional treatment using the described ICP oxygen plasma process in Chapter 3 for one minute, respectively. The resulting etching rate (≈ 4 nm.min^{-1}) is very similar to the calibrated value using ultra-pure diamond substrates (see Chapter 3). **c)** Measured sheet resistance of the boron-doped diamond film is shown as a function of the etching depth. The dashed line is a linear fit.

ing diamond film are measured. Figure A.6 b) shows the experimentally-extracted etching rate of the boron-doped diamond film. The blue and red dots correspond to performed etching steps using the oxygen RIE plasma process only and with an additional treatment using the described ICP oxygen plasma process in Chapter 3 for one minute. The presented results in figure A.6 b) indicate that the etching rate of ultra-pure and heavily boron-doped diamond films are every similar for the utilized plasma processes.

Figure A.6 c) presents the measured sheet resistance of the boron-doped film as a function of the etching depth. The value of $\frac{1}{R} \rightarrow 0\,(\mathrm{k\Omega/square})^{-1}$ corresponds to the complete removal of the conducting boron-doped diamond film. Thereby, the boron-doped diamond film thickness and consequently the growth rate are extracted.

E. Density of NV centers by confocal microscopy

As previously mentioned in Appendix A.1, created NV centers are addressed by confocal microscopy technique in the presented experiments in this Thesis. Hence, the resulting areal density of NV centers is directly estimated from confocal microscopy surface images of diamond substrates. To this aim, two methods are utilized. The first method is rather simple: a calibrated photoluminescence intensity of single NV centers and second-order auto-correlation measurements ($g^2(\tau)$) are utilized for the direct counting of the number of NV centers within a high-resolution confocal microscopy image. This method is suitable to estimate low ($< 1\,\mathrm{\mu m}^{-2}$) areal densities of NV centers.

The second method is comprised of an image-analyzer algorithm written in Python language. The image of a single NV center (with set photoluminescence thresholds corresponding to the signal of the NV center (high value) and the background (low value)) is used as a reference for the integrated photoluminescence signal in the program. Then, the confocal microscopy image to be analyzed is sub-divided in the program into slices of the same size of the reference image, and the corresponding integrated signals per slice are compared to the reference. At the end, the calculated areal density of NV centers is the average value of the integrated signal over all sub-divisions of the original image. Both methods are in good agreement within a $\pm 10\%$ of error margin.

The depth distributions of NV centers and other optically-active defects in diamond have been investigated in Chapters 3 and 5. To this aim, the experimentally-

extracted areal density of NV centers (for example, see figure 3.11) as a function of the etching depth is utilized. For simplicity, the experimental data are fitted using Gaussian complementary error functions in the form of [267]:

$$[\mathrm{NV}] = A \left[1 + \mathrm{erf} \left(-\frac{d - \mu}{\sqrt{2}\sigma} \right) \right], \tag{A.3}$$

where [NV] is the areal density of NV centers, A is the function amplitude, d is the etching depth, and erf() is the corresponding Gaussian error function [267]. In such a case, the volumetric concentration distribution of NV centers in diamond is obtained by setting the mean (μ) and standard deviation (σ) values from the fit of equation A.3 in the corresponding Gaussian distribution function, as discussed in section 2.2 (for example, see figure 3.11). As seen throughout the presented experiments, extracted distribution profiles by this technique are in relatively good agreement with results of simulation methods such as CTRIM and IMD.

F. Noise spectral decomposition technique

The coherence decay of the NV center electron spin has the general form of $C(t) = \exp[-\chi(t)]$ due to the coupling to the magnetic environment, where the function $\chi(t)$ represents the time-dependency of the decoherence process. The NV center coherent spin manipulation using e.g. dynamical decoupling microwave sequences suppresses specific frequency components of the magnetic noise by the associated, characteristic spectral filter function ($F_t(\omega, t)$, in the frequency domain) of the applied sequence [268–270]. This filter provides information related to how the applied pulse sequence suppresses phase accumulation of the electron spin of the probed NV center as a function of noise frequency.

In the regime of weak coupling of the NV center to the environment (applicable to the presented results throughout this Thesis), the induced modulation of the NV center spin results in a coherence decay with a functional in the form of [268]:

$$\chi(t) = \frac{1}{\pi} \int_0^\infty S(\omega) \frac{F_t(\omega, t)}{\omega^2} d\omega, \tag{A.4}$$

where $S(\omega)$ is the power spectral density function that describes the coupling of the NV center spin to the environment. Hence, by measuring the NV center coherence

for different inter-pulse spacing and number of π-pulses, one can recover $S(\omega)$ through the deconvolution process in equation A.4. Such a technique is known as noise spectral decomposition [268–271].

The form of the NV center coherence decay depends specifically on the applied microwave pulse sequence, e.g. on the corresponding filter function, and on the noise characteristics of the environment. If an appropriate modulation is applied to the NV center electron spin, such that:

$$\frac{F_t(\omega, t)}{\omega^2 t} \approx \delta(\omega - \omega_0), \tag{A.5}$$

e.g. the filter function can be approximated to a Dirac δ-function centered at the target frequency ω_0, equation A.4 can be approximated to [271]:
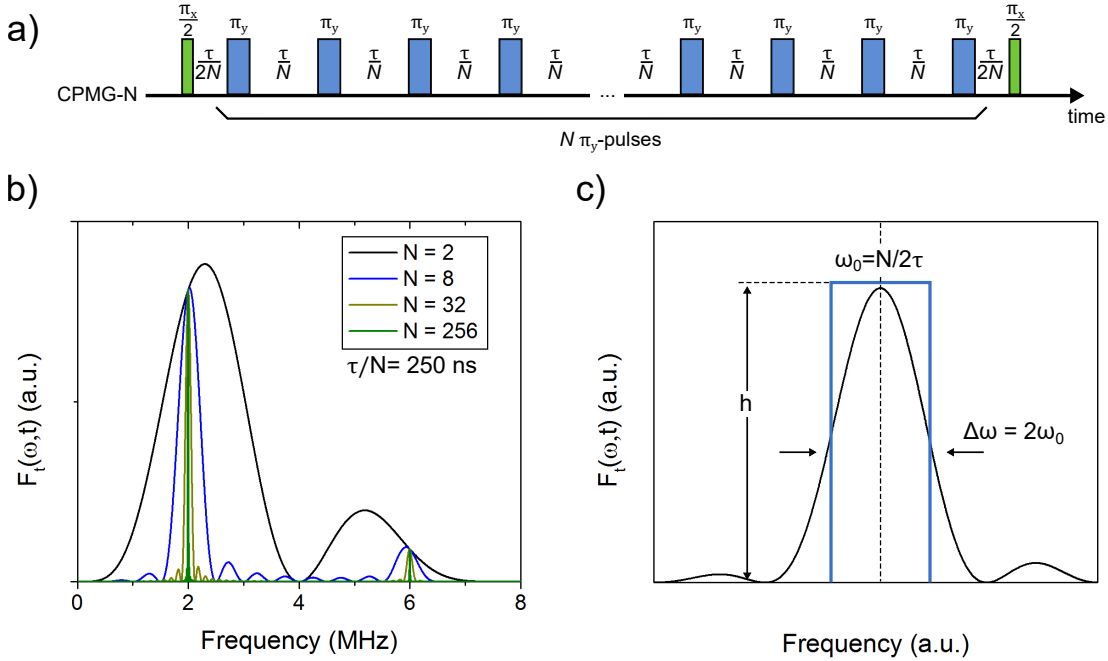
$$\chi(t) = \frac{t S(\omega_0)}{\pi}. \tag{A.6}$$

A reasonable approximation to such an ideal case (e.g. equation A.5) is the Carr-Purcell-Meiboom-Gill (CPMG) pulse sequence [272]. A schematic representation of the CPMG pulse sequence is shown in figure A.7 a). Similarly as in the Hahn-echo scheme, the first $\pi_x/2$ microwave pulse prepares the NV center spin into a superposition state, i.e. $\frac{(|0\rangle + |-1\rangle)}{\sqrt{2}}$. The subsequent train of N π_y-pulses (microwave phase shifted by 90°, see section 1.3) refocuses the accumulated phases that are not synchronized to the inter-pulse delay $\left(\frac{\tau}{N}\right)$ and protects the quantum coherence of the $|y\rangle$ spin state component (axis defined by the Bloch sphere, as discussed in section 1.3). Consequently, spin decoherence within the frequency range defined by $F_t(\omega, t)$ is attenuated and the measured NV center quantum coherence is ultimately prolonged (for a large number of applied π-pulses) to the spin-lattice relaxation time in the rotating frame ($T_{1\rho}$) [36, 124].

The corresponding filter function of the CPMG microwave sequence is given by [268]:

$$F_t(\omega, t) = 8 \sin^4\left(\frac{\omega t}{4N}\right) \left[\frac{\sin\left(\frac{\omega t}{2}\right)}{\cos\left(\frac{\omega t}{2N}\right)}\right]^2. \tag{A.7}$$
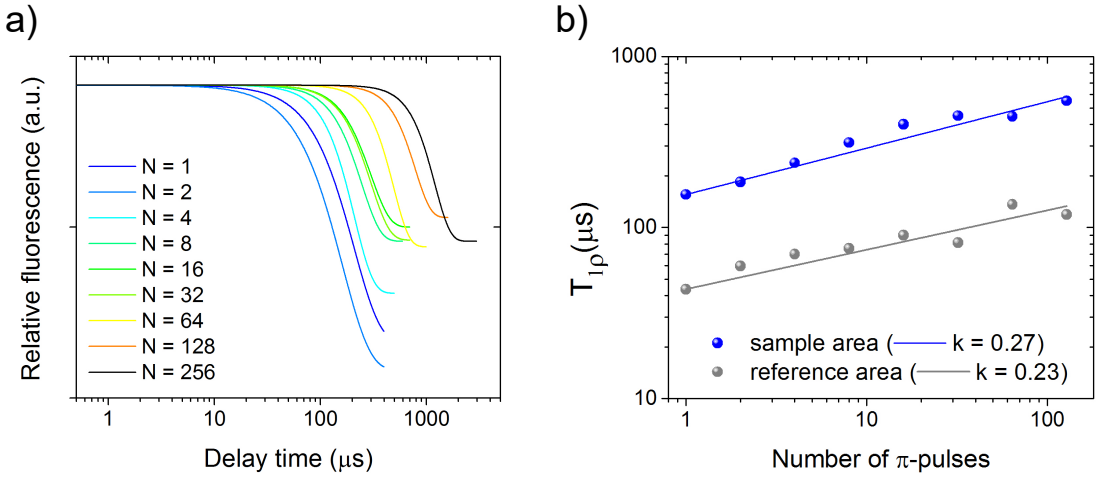
According to this equation, the shape of $F(\omega, t)$ is shown in figure A.7 b) for different numbers of π-pulses and a fixed inter-pulse delay of $\tau/N = 250$ ns. As can

Figure A.7.: **Noise spectral decomposition from CPMG coherence decay.** **a)** Schematic representation of the CPMG microwave pulse sequence. The green and blue pulses represent microwave phases shifted by 90°. The total evolution time is given by 2τ. **b)** Corresponding noise filter function of the CPMG microwave pulse sequence, as given by equation A.7. The three different colored lines represent the simulated shapes of $F_t(\omega, t)$ for different numbers of π-pulses. The inter-pulsing time is set to a value of 250 ns. **c)** For larger numbers of π-pulses, the spectral deconvolution is performed by approximating the filter function shape to a discrete box-shaped function at the target frequency ω_0. Figure partially adapted from Ref. [128].

be seen, the filter function of the CPMG sequence can be reasonably approximated to a Dirac δ-function for larger numbers of π-pulses. In this case, the spectral deconvolution (equation A.4) is performed similarly as described in Ref. [27]. The filter function centered at a noise locked-in frequency $\omega_0 = \frac{N}{2\tau}$ is approximated to a box-shaped discrete function with dimension $\Delta\omega = 2\omega_0$ (FWHM of the peak) and a height (h) depending on the experimental signal amplitude.

Similarly to previous reports [36, 136, 270, 271], the power spectral density is presumed to take the form of a $1/f$ noise source. This is mainly due to the stochastic nature of the flip-flops of nearby spins that are sensed by the probed NV center. In Chapter 4 (section 4.4), the noise environment of created NV centers by the p^+-i junction technique are compared to conventional nitrogen implantation. For a quantitative analysis, the experimentally-extracted power spectral densities

a)

b)

Figure A.8.: Measured coherence decays of NV centers utilizing the CPMG pulse sequence. a) The measured coherence decays (fitting functions are shown for clarity) from an individual NV center (depth of $\approx 7.8\,\text{nm}$ at the sample area - see Chapter 4) are shown as the colored lines, representing different number of π-pulses. The experimental delay time represents the total sequence time 2τ. For these measurements, an external magnetic field of $\sim 33\,\text{mT}$ is used, aligned to the NV center axis. **b)** Exemplification of the scaling of $T_{1\rho}$ time with the number of microwave π-pulses for two NV centers at the sample (blue dots) and reference (gray dots) areas (see text). The solid lines are fits according to equation A.9.

are fitted using Lorentzian functions in the form of [271]:

$$S\left(\omega\right) = \sum_i \frac{\Delta_i^{\,2}\tau_i}{\pi}\frac{1}{1+\left(\omega\tau_i\right)^2}, \tag{A.8}$$

where Δ is the noise coupling strength and τ is the correlation time of the coupling between the NV center and the noise environment. The indexes $i = 1, 2$ represent fitting to single- and double-Lorentzian functions, as discussed in Chapter 4.

Figure A.8 a) shows an example of the measured coherence decays using the CPMG pulse sequence (fitting functions are shown for clarity). The different colors represent individual measured coherence decays with different numbers of π-pulses of the CPMG sequence. The measured spin coherence by CPMG sequence (e.g. $T_{1\rho}$ time) are expected to scale with the number of π-pulses according to [136]:

$$T_{1\rho} = N^k T_2, \tag{A.9}$$

where T_2 is the measured spin coherence time using the Hahn-echo scheme and k is the scaling factor. Figure A.8 b) shows an exemplification of a typical scaling factor value observed in the presented results in Chapter 4. For all measured NV centers, scaling factors ranging from 0.23 to 0.44 are observed at both sample and reference areas of the described diamond substrate in section 4.3.3 (depths of less than 10 nm). These values are in agreement with previous reports of near-surface NV centers [136].
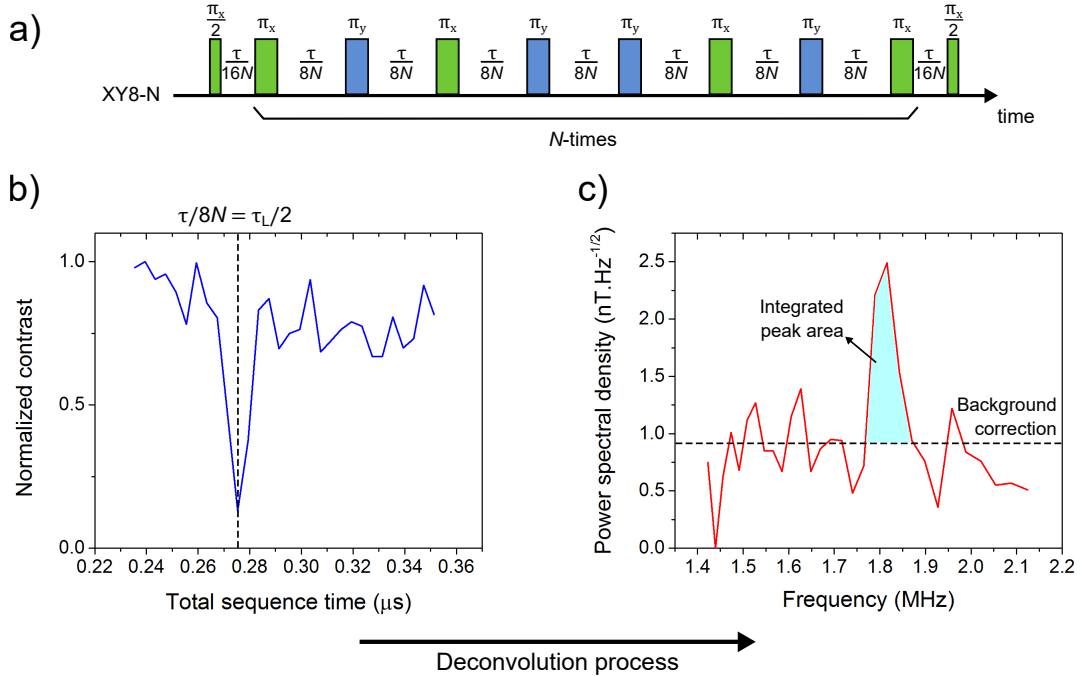
G. Depth-calibration measurements

G.1. NMR technique

In this section, relevant aspects of the depth calibration method based on the detection of external proton spins on the diamond surface are briefly explored. The detection scheme is based on the noise spectroscopy technique using the XY8-N dynamical decoupling microwave sequence, as described in Ref. [27]. A schematic representation of the XY8-N pulse sequence is shown in figure A.9 a). The reconstruction of the noise power spectral density follows the described analytical approach in Appendix F, e.g. the deconvolution of the measured coherence decay with a corresponding filter function. It should be noted that the filter function of the XY8-N sequence is also given by equation A.7.

The generated magnetic noise by protons located within a nanometer-volume in the vicinity of the diamond surface is dominated by statistical fluctuations in the corresponding spin polarization due to the incomplete cancellation of randomly-oriented spins. This, in turn, generates a fluctuating magnetic field at the position of near-surface NV centers ($B_{\mathrm{fluc,z}}(t)$). The corresponding oscillation frequency of this field is centered around the Larmor precession frequency (f_{L}) of proton spins, with deviations due to statistical spin polarization [27].

The spin modulation by the XY8-N microwave pulse sequence efficiently decouples the NV center electron spin from the noise environment for frequencies higher than $8N/\tau$ (e.g. higher than the inverse of the inter-pulse delay, see figure A.9 a). As an example, figure A.9 b) shows the measured coherence decay of an implanted NV center (parameters given in section 3.4.4), modulated by a XY8-10 microwave pulse sequence. When the inter-pulse spacing ($\frac{\tau}{8N}$) matches half of the value of the magnetic noise oscillation period ($\frac{\tau_{\mathrm{L}}}{2}$), the coherence is lost due to the non-cancellation of the phase accumulated by the NV center electron spin.

Figure A.9.: Detection of the magnetic noise of proton spins by a near-surface NV center sensor. a) Schematic representation of the XY8-N microwave pulse sequence. The green and blue pulses represent microwave phases shifted by 90°. The total sequence time is given by τ. **b)** The detection of the oscillating magnetic field of proton spins by the NV center electron spin under the manipulation with XY8-10 sequence is exemplified in the measured coherence decay. As seen, a drop in the fluorescence contrast is seen when the microwave inter-pulse spacing is equal to half of the value of the magnetic noise oscillation period ($\frac{\tau}{8N} = \frac{\tau_L}{2}$). For this measurement, an external magnetic field of $\sim 42\,\mathrm{mT}$ is applied along the axis of the NV center. **c)** The deconvolution of the measured coherence decay with the filter function results in the power spectral density.

The deconvolution using the corresponding filter function results in the power spectral density, as presented in figure A.9 c). The noise signal of detected proton spins is revealed as a peak in the power spectral density, centered at the proton Larmor precession frequency. As shown, the RMS magnetic field strength of the noise signal of protons at the position of the NV center sensor can be calculated by integrating the background-corrected area under the peak [27]. The depth of the NV center sensor (d_{NV}) is hence calculated using the analytical model given in Ref. [27]:

$$B_{\mathrm{RMS}} = \frac{\mu_0 \mu_{\mathrm{P}}}{2} \sqrt{\frac{\rho}{d_{\mathrm{NV}}^3}}, \tag{A.10}$$

where $\mu_P \approx 1.41 \times 10^{-33}\,\mathrm{J.T^{-1}}$ is the proton magnetic moment and $\rho = 5 \times 10^{28}\,\mathrm{m^{-3}}$ is the proton density e.g. in the immersion oil of the microscope objective.

G.2. Spin relaxometry technique
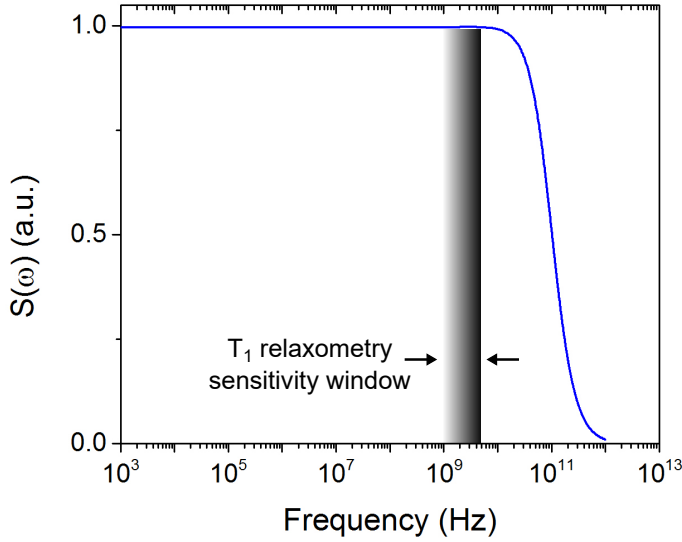
Gadolinium ions (Gd^{3+}) possess a high magnetic moment of $S = 7/2$ as a result of seven unpaired electrons in their 4f orbital. Due to the stochastic nature of the magnetic fluctuations, the mean amplitude of the magnetic field is zero ($\langle B \rangle = 0$). However, statistical spin polarization results in a non-zero root mean square (RMS) magnetic field ($B_{\mathrm{RMS}} = \sqrt{\langle B^2 \rangle}$), which can be detected by nearby NV centers. In the limit of a large number of Gd^{3+} ions, the corresponding noise spectral density can be written as [141]:

$$S_{\mathrm{Gd}}(\omega) = \sqrt{\frac{2}{\pi}}\,\frac{f_{\mathrm{t}}}{\left[(\omega - \omega_0)^2 + f_{\mathrm{t}}^2\right]}, \qquad (\mathrm{A.11})$$

where $\tau_{\mathrm{c}} = \omega_0^{-1}$ is the correlation time of the Gd^{3+} inter-spin interactions and f_{t} is the fluctuation rate of the RMS magnetic noise, in the order of several GHz [141]. The induced magnetic field by Gd^{3+} ions at the position of an NV center can be further separated into components ($\langle B_x^2 \rangle$, $\langle B_y^2 \rangle$, $\langle B_z^2 \rangle$), with the z-axis being defined as the axis of the NV center probe.

Magnetic field fluctuations transverse to the NV center axis (x and y directions) induce magnetic dipole transitions between the NV center spin sub-levels. This results into a significant decrease in the corresponding T_1 time of the NV center in the presence of Gd^{3+} ions. The detection scheme based on changes in the spin-lattice relaxation rate ($\Gamma_1 = 1/T_1$) of NV centers is known as *spin relaxometry* [141, 273, 274]. As evidenced in figure A.10, Gd^{3+} ions exhibit a broad noise power spectral density, with a significant intensity at the zero-field splitting frequency of the NV center ground state ($D = 2.870\,\mathrm{GHz}$ for the transition $m_{\mathrm{s}} = 0 \rightarrow m_{\mathrm{s}} = \pm 1$). Since electron spins have a much higher ($\sim 1000\times$) magnetic moment than nuclear spins, the spin relaxometry technique presents a much higher dynamic range than NMR-based methods.

The amplitude of the transverse magnetic field at the position of an NV center in the diamond lattice (depth of d_{NV}) generated by Gd^{3+} ions is given by [141]:

Figure A.10.: Noise spectral density of Gd^{3+} ions. Noise spectral density of fluctuating magnetic field due to Gd^{3+} ions is shown according to equation A.11. The black-shaded area represents the frequency range of the $m_s = 0 \rightarrow m_s = \pm 1$ electronic spin transitions of the NV center ground state.

$$\left\langle B_x^2 \right\rangle + \left\langle B_y^2 \right\rangle = \left\langle B^2 \right\rangle = \frac{2.1 \times 10^4 \pi N_A C_{Gd}}{16 d_{NV}^3} \left(\frac{\mu_0 \mu_B^2 g_{NV} g_{Gd}}{4\pi \hbar} \right)^2, \qquad (A.12)$$

where N_A is the Avogadro's number, μ_0 is the vacuum permeability, C_{Gd} is the volumetric concentration of Gd^{3+} ions, g_{NV} and g_{Gd} are the electron g-factors of NV centers and Gd^{3+} ions, respectively. For an NV center initialized in the $|gs\rangle$ $m_s = 0$ spin sublevel, the decay rate of the longitudinal magnetization ($\Gamma_{1,total}$) is finally written as [141]:

$$\Gamma_{1,total} = \frac{1}{T_{1,Gd^{3+}}} - \frac{1}{T_{1,int}} \approx \frac{2 f_t \langle B^2 \rangle}{f_t^2 + D^2}, \qquad (A.13)$$
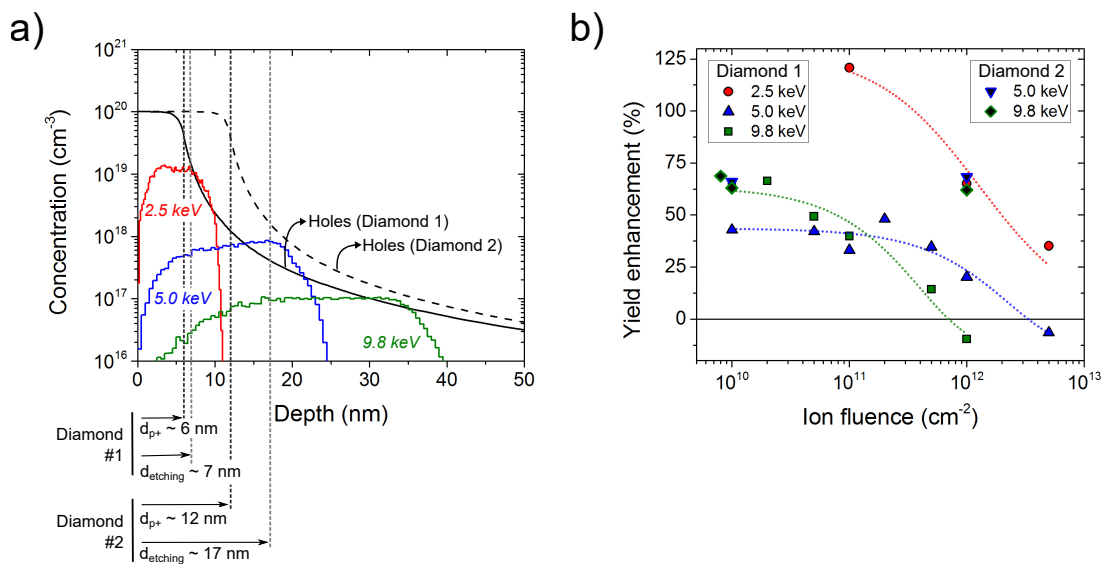
with $T_{1,Gd^{3+}}$ and $T_{1,int}$ being the spin relaxation times in the presence and absence of Gd^{3+} ions, respectively.

In the presented experiments, the thin film containing Gd^{3+} ions is created by spin-coating the diamond surface with a solution of Gadovist (Bayer Schering Pharma) with a nominal concentration of $1\,M$ and subsequent drying in air. This result in a $\sim 1\,\mu m$-thick transparent layer that covers the diamond surface homogeneously. In the presence of such a layer, the Gd^{3+}-induced spin relaxation of NV

centers is measured. Subsequently, the removal of the film containing Gd^{3+} ions is performed by washing the diamond with millipore water and WCO treatment.

H. Space-charge compensation in fabricated diamond substrates with different structure parameters

As described in Chapter 4, nitrogen implantation with different energies in the space-charge layer induced by the p^{+}-i junction structure has shown approximately

Figure A.11.: **Space-charge layer of the two fabricated diamond substrates and the charge compensation effect. a)** The simulated concentration profiles of free holes versus the depth by SILVACO software are shown for two fabricated p^{+}-i diamond junctions (black-solid line for $d_{p+} = 6\,\mathrm{nm}$ - Diamond 1 - and black-dashed line for $d_{p+} = 12\,\mathrm{nm}$ - Diamond 2). In both cases, the concentration of acceptor impurities in the p-type layer is $N_A \sim 10^{20}\,\mathrm{cm}^{-3}$. The thermodynamic equilibrium condition of the simulated structure is shown for a temperature of 950°C. Simulated profiles of implanted nitrogen atoms by CTRIM are shown for the critical ion fluences corresponding to Diamond 1 (see figure 4.9 c) - $3 \times 10^{13}\,\mathrm{cm}^{-2}$ for 2.5 keV, $3 \times 10^{12}\,\mathrm{cm}^{-2}$ for 5.0 keV and $8 \times 10^{11}\,\mathrm{cm}^{-2}$ for 9.8 keV. These simulation are performed for a [100]-oriented diamond lattice and a 3°-off implantation angle, as previously discussed in Chapter 3. **b)** Enhancement in the formation yield of NV centers versus the ion fluence for the three mentioned implantation energies and two fabricated diamond substrates.
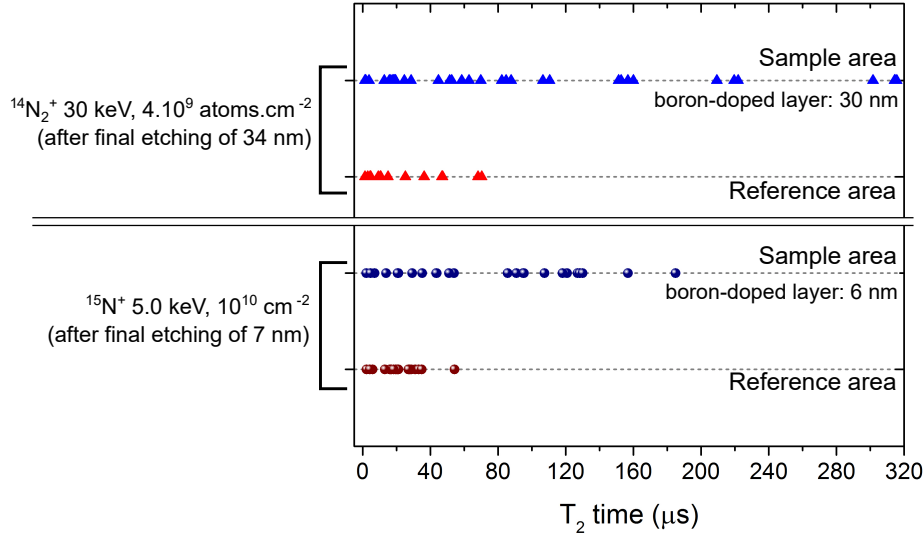
a twofold formation yield enhancement of NV centers. In this section, the behavior of the yield enhancement in two fabricated diamond substrates with different thicknesses of the boron-doped layer ($d_{\mathrm{p+}} = 6\,\mathrm{nm}$, etched for $7\,\mathrm{nm}$ - Diamond 1 and $d_{\mathrm{p+}} = 12\,\mathrm{nm}$, etched for $17\,\mathrm{nm}$ - Diamond 2) is investigated.

Figure A.11 a) shows the simulated concentration profiles of free holes as a function of the depth by SILVACO software (for both diamond substrates). In addition, simulated distribution profiles of implanted nitrogen atoms by CTRIM are shown for three different implantation energies (2.5, 5.0 and 9.8 keV) in a [100]-oriented diamond lattice (3°-off implantation angle). As depicted, the boron-doped layer of Diamond 1 ($d_{\mathrm{p+}} = 6\,\mathrm{nm}$) is transparent to the nitrogen implantation in all three cases, whereas the Diamond 2 ($d_{\mathrm{p+}} = 12\,\mathrm{nm}$) is transparent only in the 5.0 and 9.8 keV cases.

The corresponding enhancement in the formation yield of NV centers in both fabricated diamond substrates versus the ion fluence is shown in figure A.11 b). As seen, similar enhancement values are observed for created NV centers in both fabricated diamond substrates. As discussed in section 4.3.2, the formation yield enhancement is reduced with increasing ion fluence due to the charge compensation of free injected holes in the substrate area by implantation-induced defects. The presented results in figure A.11 b) reveal that no space-charge compensation occurs in Diamond 2 for the cases of $5.0\,\mathrm{keV}$ (ion fluence of up to $10^{12}\,\mathrm{cm}^{-2}$) and $9.8\,\mathrm{keV}$ (ion fluence of up to $10^{12}\,\mathrm{cm}^{-2}$). In these cases, the concentration of donor impurities and lattice defects in the substrate area is still much less than the concentration of injected holes, resulting in the efficient charging of implantation induced defects (and hence in the presented enhancements).

I. Supplementary spin measurements of created NV centers by the p^+-i junction technique

The histogram in figure A.12 presents the statistics on T_2 times of NV centers at both sample and reference areas of two different fabricated diamonds. For the first diamond, the lower case in figure A.12, T_2 times from NV centers created by nitrogen implantation with $5.0\,\mathrm{keV}$ of energy and an ion fluence of $10^{10}\,\mathrm{cm}^{-2}$ are shown (same diamond substrate used to produce the results in figure 4.11). For this fabricated diamond substrate, the thickness of the boron-doped layer is initially $6\,\mathrm{nm}$. These measurements are performed on the bare oxygen-terminated surface after the final plasma etching step of $7\,\mathrm{nm}$ (etching performed on both

Figure A.12.: **Statistics of the spin coherence times of NV centers located at the**
sample and reference areas of two fabricated diamond substrates. In
the lower part, T_2 times of ~ 30 NV centers at the sample (blue dots) and ref-
erence (red dots) areas of the first fabricated diamond substrate ($d_{\mathrm{p+}} = 6\,\mathrm{nm}$)
are shown (5.0 keV of energy with an ion fluence of $10^{10}\,\mathrm{cm}^{-2}$, see the discussion
of figure 4.11). The measurements are performed after the final etching step of
7 nm. In the upper part, T_2 times of ~ 35 NV centers at the sample (blue trian-
gles) and reference (red triangles) areas of another fabricated diamond substrate
($d_{\mathrm{p+}} = 30\,\mathrm{nm}$) are shown for the case of molecular nitrogen (N_2^+) implantation
with an incident angle of $7°$ and 30 keV of energy (ion fluence of 4×10^9 atoms
cm^{-2}). The measurements are performed after the final etching step of 34 nm.
For all presented measurements, an external magnetic field of approximately
33 mT is aligned to the measured NV center axis.

regions).

Although the depth of the majority of these NV centers is unknown, in average,
NV centers at the sample area show much longer T_2 times in comparison to the
reference area. A careful analysis of the histogram reveals that NV centers at
the sample area show T_2 times that can be classified into two groups: the first
group with values $< 60\,\mathrm{\mu s}$ and the second group with values $85\,\mathrm{\mu s} < T_2 < 160\,\mathrm{\mu s}$.
This characteristic spreading of T_2 times is attributed to the formed NV centers
within the ion stopping (shorter T_2 times, closer to the diamond surface) and ion
channeling (longer T_2 times, deeper) ranges, respectively.

It should be highlighted that this behavior is observed in several diamond sub-

strates fabricated under similar conditions, with small deviations due to variations in crystal quality. As an example, the upper case of the histogram in figure A.12 presents T_2 times of created NV centers in a second fabricated diamond substrate. The thickness of the boron-doped layer is initially 30 nm. Similarly as in the first fabricated diamond substrate, the boron-doped film thickness is set to match the tail of the ion stopping range according to CTRIM simulations (see the discussion of figure 4.11 c). In this case, molecular nitrogen ion ($^{14}N_2^+$) implantation with 30 keV of energy and an ion fluence of 4×10^9 atoms cm^{-2} is performed, followed by thermal annealing and WCO treatment, as previously described. For this implantation event, an incident angle of 7° is set to reduce the probability of ion channeling. These measurements are performed on the bare oxygen-terminated surface after the final plasma etching step of 34 nm (etching performed on both regions).

As seen in figure A.12, T_2 times of NV centers at the sample area of both fabricated diamond substrates are much longer in comparison to the corresponding reference areas. This assures the reproducibility of the technique and the observed enhancements presented in Chapter 4. These results further highlight the manipulation of the charge-state of implantation defects as a versatile tool, even if experimental conditions must be adapted to fulfill the requirements of different NV center-based applications, i.e. higher implantation energies for the creation of deeper NV centers in the crystal. Moreover, the T_2 times of NV centers at the reference areas of both fabricated diamond substrates are comparably low. This indicates that residual implantation defects are indeed the dominant source of spin decoherence in the case of conventional nitrogen implantation followed by thermal annealing.

From all the NV centers initially measured in the first fabricated diamond substrate (lower part of figure A.12), only those that fulfill the criteria of (i.) having a spin contrast (i.e. Rabi oscillations) above 15% and (ii.) showing stable photon emission during all three rounds of measurements for the depth calibration (bare surface - layer of Gd^{3+} ions - cleaned surface, see Appendix G.2) are taken into account. The majority of the NV centers at the reference area (approximately 70%) and a parcel of the NV centers at the sample area (approximately 20%) demonstrated low spin contrast and/or photoluminescence blinking. These two features result in a low SNR, leading to a low precision and longer integration times in the relevant spin measurements, specially in the T_1 times (if measurable at all).

The blinking behavior and/or low spin contrast are attributed to the presence of electronic states in the band gap induced by lattice defects that would change the charge-state of nearby NV centers. These defects might be generated not only by

the implantation and annealing processes, but also by the surface polishing [260] and during the crystal growth. The T_1 and T_2 times of NV centers that fulfill the above-mentioned criteria are shown in the main results of Chapter 4 (figure 4.11).

It must be emphasized that, although the measured T_2 times at the reference area of NV centers at depths of $\sim 3\,\mathrm{nm}$ (figure 4.11 a) are extremely short, T_1 times of a few milliseconds are still observed (figure 4.11 b). This behavior is a typical signature of electron spins in the vicinity of NV centers [36, 271]. Electron spin flip-flops produce a typical magnetic noise power spectral density with maximum values in the kHz-MHz frequency range (where the T_2 times measured by Hahn-echo scheme are sensitive), but with negligible values at the GHz range (where the T_1 times are sensitive). This reinforces the attribution that electron spins of di-vacancy and small vacancy chains are a dominant source of spin decoherence, as discussed in Chapter 4.
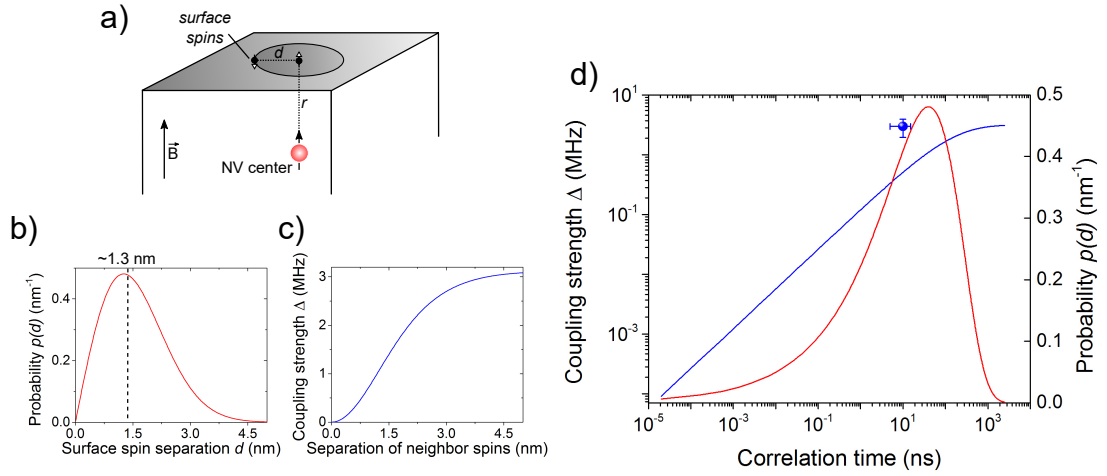
J. Estimation of the effect of surface spins on near-surface NV centers

As discussed in Chapter 4 (section 4.4), the observed scaling of the power spectral density with the distance to the diamond surface for NV centers at the sample area is attributed mainly to electron spins on the diamond surface. Such spins are related to localized electronic states at the diamond surface with a density of $\rho_{\mathrm{ss}} = 10^{13}\,\mathrm{spins.cm^{-2}}$ (i.e. 1 spin per $10\,\mathrm{nm^2}$), as derived from the presented experimental results. Here, a simple analytical model to address the experimental results such as the amplitude and correlation time of the sensed magnetic noise by NV centers is derived[4]. For simplicity, the analysis is restricted to NV centers and surface spins with a quantization axis perpendicular to the surface. The modeled system is sketched in figure A.13 a).

Figure 4.12 a) (in section 4.4) presents the power spectral density of an NV center located at $r = 3.2\,\mathrm{nm}$ below the diamond surface at the sample area. Within this depth range, NV centers are expected to interact significantly with surface spins covering an area of about $10\,\mathrm{nm^2}$ [124]. Moreover, the interaction strength decreases to zero for surface spins located at the magic angle, which encircles an area of about $80\,\mathrm{nm^2}$. Thus, the average number of strongly-coupled surface spins to the NV center spin is roughly one.

---

[4]Collaboration with Dr. Philipp Neumann.

Figure A.13.: Analytical estimation of the surface spin bath characteristics. a) Sketch of the modeled system, consisting of an individual NV center (depth of r) with the main axis perpendicular to the surface (aligned to the external magnetic field **B**), and surface electron spins with a density ρ_{ss} (mean separation of d). **b)** The probability distribution of surface spins is shown as a function of the mean spin separation. The maximum probability of near-neighbor spins related to the experimentally-extracted $\rho_{ss} \sim 10^{13}$ spins.cm^{-2} occurs for a separation of approximately 1.3 nm. **c)** The calculated coupling strength of the NV center to surface spins is shown as a function of the mean separation of near-neighbor surface spins (d). **d)** The calculated coupling strength of the NV center to surface spins (blue line, left axis) and probability distribution of near-neighbor surface spins (red line, right axis) are shown versus the corresponding noise correlation time. The blue dot represents the experimentally-extracted value of coupling strength and correlation time for the NV center with 3.2 nm of depth at the sample area, as shown in figure 4.12 (section 4.4). The error bars correspond to the standard deviation of the data fit.

In the presented analysis, the strongly-coupled surface electron spin is placed right above the NV center, whereas a second spin is placed with a distance d (see figure A.13 a). This configuration mimics an alternating signal at the NV center position due to mutual surface spin flip-flops. The flip-flop rate γ corresponds to the mutual magnetic dipole coupling and scales as $\gamma \approx 50\,(\text{MHz.nm}^3).d^{-3}$ for the considered arrangement. The corresponding noise correlation time is hence $\tau = \gamma^{-1}$. For a given surface spin density, the probability distribution to find a nearest neighbor surface spin located at distance d is deduced as [124]:

$$p(d) = 2\pi d\rho_{ss}e^{-\pi\rho_{ss}d^2}, \tag{A.14}$$

with the normalization condition of $\int_0^\infty p(d)dd = 1$. As seen in figure A.13 b), a

density of surface spins of $\rho_{ss} = 10^{13}$ spins.cm^{-2} results in the maximum probability for a spin separation of $d \approx 1.3$ nm. Moreover, stochastic alternating magnetic fields by surface spin flip-flops are generated by anti-parallel aligned surface spin pairs and their total coupling Δ to the NV center, thus decreasing for smaller mutual distances d as:

$$\Delta(r, \theta) \approx \frac{50 \,(\mathrm{MHz}\,\mathrm{nm}^3)}{r^3} \left(3 \cos^5 \theta - \cos^3 \theta - 2 \right), \qquad (A.15)$$

where the angle θ depends on d and r as $\tan \theta = d/r$, as sketched in figure A.13 a). The calculated noise coupling strength of the sampled NV center and surface spins as a function of d is shown in figure A.13 c).

The expected behavior of the noise coupling strength (Δ) and the corresponding correlation time (τ) can be estimated from the above-presented results, as presented in figure A.13 d) (blue line). In addition, the described probability distribution of surface spins is shown as a function of the noise correlation time (red line). The analytical values reproduce satisfactorily the experimentally-obtained values of correlation times of ~ 10 ns for NV centers at the sample area (see the blue dot in figure A.13 d), but underestimates the noise coupling strength. Potential reasons for this deviation can be the imposed restrictions by the orientation of the NV center, by including only two surface spins in the calculations, and additional noise components such as residual P1 centers in the fabricated diamond substrate lattice.

List of Publications

Publications in scientific journals

Main contribution:

1. Fávaro de Oliveira, F.; *et al.*, Tailoring spin defects in diamond by lattice charging; Nature Communications **8**, 15409 (2017) DOI:10.1038/ncomms15409

2. Fávaro de Oliveira, F.; *et al.*, On the efficiency of combined ion implantation for the creation of near-surface nitrogen-vacancy centers in diamond; Physica Status Solidi (a) **213**, 8 (2016) DOI:10.1002/pssa.201600326

3. Fávaro de Oliveira, F.; *et al.*, Toward Optimized Surface δ-Profiles of Nitrogen-Vacancy Centers Activated by Helium Irradiation in Diamond; Nano Letters **16**, $2228 - 2233$ (2016) DOI:10.1021/acs.nanolett.5b04511

4. Fávaro de Oliveira, F.; *et al.*, Effect of low-damage inductively coupled plasma on shallow nitrogen-vacancy centers in diamond; Applied Physics Letters **107**, 073107 (2015) DOI:10.1063/1.4929356

Co-authorship:

5. Schlipf, L.; *et al.*, Molecular quantum spin network controlled by a single qubit; ArXiv eprints. arXiv: 1703.08248 (2017)

6. Pfender, M.; *et al.*, Protecting a diamond quantum memory by charge state control; ArXiv eprints. arXiv: 1702.01590 (2017)

7. Häberle, T.; *et al.*, Nuclear quantum-assisted magnetometer; Rev. Sci. Instrum. **88**, 013702 (2017) DOI:10.1063/1.4973449

8. Schreyvogel, C.; *et al.*, Active and fast charge-state switching of single NV centres in diamond by in-plane Al-Schottky junctions; E. Beilstein J. Nanotechnol. **7**, $1727 - 1735$ (2016) DOI:10.3762/bjnano.7.165

9. Jakobi, I.; *et al.*, Efficient creation of dipolar coupled nitrogen-vacancy spin qubits in diamond; J. Phys.: Conf. Ser. **752**, 012001 (2016) DOI:10.1088/1742−6596/752/1/012001

10. Chejanovsky, N.; *et al.*, Structural Attributes and Photodynamics of Visible Spectrum Quantum Emitters in Hexagonal Boron Nitride; Nano Lett., **16** (11), 7037 − 7045 (2016) DOI:10.1021/acs.nanolett.6b03268

11. Momenzadeh, S. A.; *et al.*, Thin circular diamond membrane with embedded nitrogenvacancy centers for hybrid spin-mechanical quantum systems; Phys. Rev. Applied **6**, 024026 (2016) DOI:10.1103/PhysRevApplied.6.024026

12. Momenzadeh, S. A.; *et al.*, Nanoengineered Diamond Waveguide as a Robust Bright Platform for Nanomagnetometry Using Shallow Nitrogen Vacancy Centers; Nano Lett., **15** (1), 165 − 169 (2015) DOI:10.1021/nl503326t

Bibliography

1. Schrödinger, E. Quantisierung als Eigenwertproblem. *Annalen der Physik* **385,** 437–490 (1926).

2. El-Kareh, B. *Silicon Devices and Process Integration* (Springer US, 2009).

3. Moore, G. E. *et al.* Cramming more components onto integrated circuits. *Proceedings of the IEEE* **86,** 82–85 (1998).

4. Fuechsle, M. *et al.* A single-atom transistor. *Nat Nano* **7,** 242–246 (2012).

5. DiVincenzo, D. P. The Physical Implementation of Quantum Computation. *Fortschritte der Physik* **48,** 771–783 (2000).

6. Knill, E., Laflamme, R. & Milburn, G. J. A scheme for efficient quantum computation with linear optics. *Nature* **409,** 46–52 (2001).

7. Aspuru-Guzik, A. & Walther, P. Photonic quantum simulators. *Nat Phys* **8,** 285–291 (2012).

8. Cirac, J. I. & Zoller, P. Quantum Computations with Cold Trapped Ions. *Phys. Rev. Lett.* **74,** 4091–4094 (1995).

9. Kielpinski, D., Monroe, C. & Wineland, D. J. Architecture for a large-scale ion-trap quantum computer. *Nature* **417,** 709–711 (2002).

10. Blatt, R. & Roos, C. F. Quantum simulations with trapped ions. *Nat Phys* **8,** 277–284 (2012).

11. Jaksch, D., Briegel, H.-J., Cirac, J. I., Gardiner, C. W. & Zoller, P. Entanglement of Atoms via Cold Controlled Collisions. *Phys. Rev. Lett.* **82,** 1975–1978 (1999).

12. Brennen, G. K., Caves, C. M., Jessen, P. S. & Deutsch, I. H. Quantum Logic Gates in Optical Lattices. *Phys. Rev. Lett.* **82,** 1060–1063 (1999).

13. Kane, B. E. A silicon-based nuclear spin quantum computer. *Nature* **393,** 133–137 (1998).

14. Maurer, P. C. *et al.* Room-Temperature Quantum Bit Memory Exceeding One Second. *Science* **336,** 1283–1286 (2012).

15. Dutt, M. V. G. *et al.* Quantum Register Based on Individual Electronic and Nuclear Spin Qubits in Diamond. *Science* **316,** 1312–1316 (2007).

16. Waldherr, G. *et al.* Quantum error correction in a solid-state hybrid spin register. *Nature* **506,** 204–207 (2014).

17. Degen, C. L., Reinhard, F. & Cappellaro, P. Quantum sensing. *ArXiv e-prints.* arXiv: `1611.02427` `[quant-ph]` (2016).

18. Wrachtrup, J. & Finkler, A. Single spin magnetic resonance. *Journal of Magnetic Resonance* **269,** 225 –236 (2016).

19. Jelezko, F. & Wrachtrup, J. Single defect centres in diamond: A review. *physica status solidi (a)* **203,** 3207–3225 (2006).

20. Balasubramanian, G. *et al.* Ultralong spin coherence time in isotopically engineered diamond. *Nat Mater* **8,** 383–387 (2009).

21. Fujimori, N., Ikegaya, A., Imai, T., Ota, N. & Shibata, T. *Chemical vapor deposition method of high quality diamond* US Patent 6,162,412. 2000.

22. Gruber, A. *et al.* Scanning Confocal Optical Microscopy and Magnetic Resonance on Single Defect Centers. *Science* **276,** 2012–2014 (1997).

23. Ofori-Okai, B. K. *et al.* Spin properties of very shallow nitrogen vacancy defects in diamond. *Phys. Rev. B* **86,** 081406 (2012).

24. Chang, Y.-R. *et al.* Mass production and dynamic imaging of fluorescent nanodiamonds. *Nat Nano* **3,** 284–288 (2008).

25. Sonnefraud, Y. *et al.* Diamond nanocrystals hosting single nitrogen-vacancy color centers sorted by photon-correlation near-field microscopy. *Opt. Lett.* **33,** 611–613 (2008).

26. Tisler, J. *et al.* Fluorescence and Spin Properties of Defects in Single Digit Nanodiamonds. *ACS Nano* **3,** 1959–1965 (2009).

27. Staudacher, T. *et al.* Nuclear Magnetic Resonance Spectroscopy on a (5-Nanometer)^3 Sample Volume. *Science* **339,** 561–563 (2013).

28. Müller, C. *et al.* Nuclear Magnetic Resonance Spectroscopy with single spin sensitivity. *Nature Communications* **5,** 4703 (2014).

29. Mamin, H. J. *et al.* Nanoscale Nuclear Magnetic Resonance with a Nitrogen-Vacancy Spin Sensor. *Science* **339,** 557–560 (2013).

30. Häberle, T., Schmid-Lorch, D., Reinhard, F. & Wrachtrup, J. Nanoscale nuclear magnetic imaging with chemical contrast. *Nat Nano* **10,** 125–128 (2015).

31. Shi, F. *et al.* Single-protein spin resonance spectroscopy under ambient conditions. *Science* **347,** 1135–1138 (2015).

32. Clark, C. D., Ditchburn, R. W. & Dyer, H. B. The Absorption Spectra of Natural and Irradiated Diamonds. *Proceedings of the Royal Society of London A: Mathematical, Physical and Engineering Sciences* **234,** 363–381 (1956).

33. Meijer, J. *et al.* Generation of single color centers by focused nitrogen implantation. *Applied Physics Letters* **87,** 261909 (2005).

34. Rabeau, J. R. *et al.* Implantation of labelled single nitrogen vacancy centers in diamond using N^{15}. *Applied Physics Letters* **88,** 023113 (2006).

35. Pezzagna, S, Naydenov, B, Jelezko, F, Wrachtrup, J & Meijer, J. Creation efficiency of nitrogen-vacancy centres in diamond. *New Journal of Physics* **12,** 065017 (2010).

36. Myers, B. A. *et al.* Probing Surface Noise with Depth-Calibrated Spins in Diamond. *Phys. Rev. Lett.* **113,** 027602 (2014).

37. Kim, M. *et al.* Decoherence of Near-Surface Nitrogen-Vacancy Centers Due to Electric Field Noise. *Phys. Rev. Lett.* **115,** 087602 (2015).

38. Widmann, M. *et al.* Coherent control of single spins in silicon carbide at room temperature. *Nat Mater* **14,** 164–168 (2015).

39. Kornher, T. *et al.* Production yield of rare-earth ions implanted into an optical crystal. *Applied Physics Letters* **108,** 053108 (2016).

40. Wellstood, F. C., Urbina, C. & Clarke, J. Low-frequency noise in dc superconducting quantum interference devices below 1 K. *Applied Physics Letters* **50,** 772–774 (1987).

41. Wolf, S. A. *et al.* Spintronics: A Spin-Based Electronics Vision for the Future. *Science* **294,** 1488–1495 (2001).

42. Schenkel, T. *et al.* Electrical activation and electron spin coherence of ultralow dose antimony implants in silicon. *Applied Physics Letters* **88,** 112101 (2006).

43. De Sousa, R. Dangling-bond spin relaxation and magnetic 1/f noise from the amorphous-semiconductor/oxide interface: Theory. *Phys. Rev. B* **76,** 245306 (2007).

44. Samsonenko, N. D., Zhmykhov, G. V., Zon, V. S. & Aksenov, V. K. Characteristic features of the electron paramagnetic resonance of the surface centers of diamond. *Journal of Structural Chemistry* **20,** 951–953 (1979).

45. Pate, B. The diamond surface: atomic and electronic structure. *Surface Science* **165,** 83 –142 (1986).

46. Osipov, V. Y., Shames, A. & Vul', A. Y. Exchange coupled pairs of dangling bond spins as a new type of paramagnetic defects in nanodiamonds. *Physica B: Condensed Matter* **404.** Proceedings of the 25th International Conference on Defects in Semiconductors, 4522 –4524 (2009).

47. Laraoui, A., Hodges, J. S. & Meriles, C. A. Nitrogen-Vacancy-Assisted Magnetometry of Paramagnetic Centers in an Individual Diamond Nanocrystal. *Nano Letters* **12,** 3477–3482 (2012).

48. Kaviani, M. *et al.* Proper Surface Termination for Luminescent Near-Surface NV Centers in Diamond. *Nano Letters* **14,** 4772–4777 (2014).

49. Howe, J. Y. *The oxidation of diamond* PhD thesis (Alfred University, 2001), 203. ISBN: 0493094075; 9780493094076.

50. Kawabata, Y., Taniguchi, J. & Miyamoto, I. XPS studies on damage evaluation of single-crystal diamond chips processed with ion beam etching and reactive ion beam assisted chemical etching. *Diamond and Related Materials* **13,** 93 –98 (2004).

51. Kim, M. *et al.* Effect of oxygen plasma and thermal oxidation on shallow nitrogen-vacancy centers in diamond. *Applied Physics Letters* **105,** 042406 (2014).

52. Cui, S. *et al.* Reduced Plasma-Induced Damage to Near-Surface Nitrogen-Vacancy Centers in Diamond. *Nano Letters* **15,** 2887–2891 (2015).

53. Denisenko, A., Romanyuk, A., Pietzka, C., Scharpf, J. & Kohn, E. Surface damages in diamond by Ar/O2 plasma and their effect on the electrical and electrochemical characteristics of boron-doped layers. *Journal of Applied Physics* **108,** 074901 (2010).

54. Ovartchaiyapong, P., Lee, K. W., Myers, B. A. & Jayich, A. C. B. Dynamic strain-mediated coupling of a single diamond spin to a mechanical resonator. *Nat Commun* **5,** 4429 (2014).

55. Momenzadeh, S. A. *et al.* Nanoengineered Diamond Waveguide as a Robust Bright Platform for Nanomagnetometry Using Shallow Nitrogen Vacancy Centers. *Nano Letters* **15,** 165–169 (2015).

56. Momenzadeh, S. A. *et al.* Thin Circular Diamond Membrane with Embedded Nitrogen-Vacancy Centers for Hybrid Spin-Mechanical Quantum Systems. *Phys. Rev. Applied* **6,** 024026 (2016).

57. Appel, P. *et al.* Fabrication of all diamond scanning probes for nanoscale magnetometry. *Review of Scientific Instruments* **87,** 063703 (2016).

58. Steinert, S. *et al.* High sensitivity magnetic imaging using an array of spins in diamond. *Review of Scientific Instruments* **81,** 043705 (2010).

59. Martin, J., Wannemacher, R., Teichert, J., Bischoff, L. & Köhler, B. Generation and detection of fluorescent color centers in diamond with submicron resolution. *Applied Physics Letters* **75,** 3096–3098 (1999).

60. Waldermann, F. *et al.* Creating diamond color centers for quantum optical applications. *Diamond and Related Materials* **16,** 1887–1895 (2007).

61. Aharonovich, I. *et al.* Producing optimized ensembles of nitrogen-vacancy color centers for quantum information applications. *Journal of Applied Physics* **106,** 124904 (2009).

62. Huang, Z. *et al.* Diamond nitrogen-vacancy centers created by scanning focused helium ion beam and annealing. *Applied Physics Letters* **103,** 081906 (2013).

63. McCloskey, D. *et al.* Helium ion microscope generated nitrogen-vacancy centres in type Ib diamond. *Applied Physics Letters* **104,** 031109 (2014).

64. Ohno, K. *et al.* Engineering shallow spins in diamond with nitrogen delta-doping. *Applied Physics Letters* **101,** 082413 (2012).

65. Ohashi, K. *et al.* Negatively Charged Nitrogen-Vacancy Centers in a 5 nm Thin 12C Diamond Film. *Nano Letters* **13,** 4733–4738 (2013).

66. Osterkamp, C. *et al.* Stabilizing shallow color centers in diamond created by nitrogen delta-doping using SF6 plasma treatment. *Applied Physics Letters* **106,** 113109 (2015).

67. Vikharev, A. L. *et al.* Novel microwave plasma-assisted CVD reactor for diamond delta doping. *physica status solidi (RRL)* **10,** 324–327 (2016).

68. Lobaev, M. *et al.* Influence of CVD diamond growth conditions on nitrogen incorporation. *Diamond and Related Materials* **72,** 1–6 (2017).

69. Balmer, R. S. *et al.* Chemical vapour deposition synthetic diamond: materials, technology and applications. *Journal of Physics: Condensed Matter* **21,** 364221 (2009).

70. Davies, G. & Evans, T. Graphitization of Diamond at Zero Pressure and at a High Pressure. *Proceedings of the Royal Society of London A: Mathematical, Physical and Engineering Sciences* **328,** 413–427 (1972).

71. Ohno, K. *Nanometer-scale engineering of shallow spins in diamond* PhD thesis (University of California, Santa Barbara, 2014).

72. Choi, W., Lahiri, I., Seelaboyina, R. & Kang, Y. S. Synthesis of Graphene and Its Applications: A Review. *Critical Reviews in Solid State and Materials Sciences* **35,** 52–71 (2010).

73. Mohs, F. Grundriß der mineralogie. Zweite Theil. Physiographie. Mit 10 Kupfertafeln. *Dresden, in der Arnoldischen Buchhandlung* (1824).

74. Ekimov, E. A. *et al.* Superconductivity in diamond. *Nature* **428,** 542–545 (2004).

75. Kalish, R. Diamond as a unique high-tech electronic material: difficulties and prospects. *Journal of Physics D: Applied Physics* **40,** 6467 (2007).

76. Paoletti, A., Tucciarone, A. & italiana di fisica, S. *The Physics of Diamond* ISBN: 9781614992202 (IOS Press, 1997).

77. Malshe, A., Park, B., Brown, W. & Naseem, H. A review of techniques for polishing and planarizing chemically vapor-deposited (CVD) diamond films and substrates. *Diamond and Related Materials* **8,** 1198–1213 (1999).

78. Collins, A. T. & Kiflawi, I. The annealing of radiation damage in type Ia diamond. *Journal of Physics: Condensed Matter* **21,** 364209 (2009).

79. Zaitsev, A. M. *Optical Properties of Diamond* First (Springer-Verlag Berlin Heidelberg, Reading, Massachusetts, 2001).

80. Borst, T. & Weis, O. Electrical characterization of homoepitaxial diamond films doped with B, P, Li and Na during crystal growth. *Diamond and Related Materials* **4,** 948–953 (1995).

81. Han, Q.-G., Li, M.-Z., Jia, X.-P., Ma, H.-A. & Li, Y. Modeling of effective design of high pressure anvils used for large scale commercial production of gem quality large single crystal diamond. *Diamond and Related Materials* **20,** 969–973 (2011).

82. Ferro, S. Synthesis of diamond. *J. Mater. Chem.* **12,** 2843–2855 (2002).

83. Zhigadlo, N. Spontaneous growth of diamond from MnNi solvent-catalyst using opposed anvil-type high-pressure apparatus. *Journal of Crystal Growth* **395,** 1–4 (2014).

84. Burns, R. C. *et al.* HPHT growth and x-ray characterization of high-quality type IIa diamond. *Journal of Physics: Condensed Matter* **21,** 364224 (2009).

85. Balmer, R. S. *et al.* Chemical vapour deposition synthetic diamond: materials, technology and applications. *Journal of Physics: Condensed Matter* **21,** 364221 (2009).

86. Bednarski, C., Dai, Z., Li, A.-P. & Golding, B. Studies of heteroepitaxial growth of diamond. *Diamond and Related Materials* **12.** 13th European Conference on Diamond, Diamond-Like Materials, Carbon Nanotubes, Nitrides and Silicon Carbide, 241–245 (2003).

87. Decker, T., Lundie, G., Pappas, D., Welty, R. & Parent, C. *Amorphous diamond coating of blades* US Patent 5,799,549. 1998.

88. Mizuochi, N. *et al.* Coherence of single spins coupled to a nuclear spin bath of varying density. *Phys. Rev. B* **80,** 041201 (2009).

89. Yamamoto, T. *et al.* Extending spin coherence times of diamond qubits by high-temperature annealing. *Phys. Rev. B* **88,** 075206 (2013).

90. Aleksov, A *et al.* Diamond diodes and transistors. *Semiconductor Science and Technology* **18,** S59 (2003).

91. Goss, J. P., Jones, R., Breuer, S. J., Briddon, P. R. & Öberg, S. The Twelve-Line 1.682 eV Luminescence Center in Diamond and the Vacancy-Silicon Complex. *Phys. Rev. Lett.* **77,** 3041–3044 (1996).

92. Rogers, L. J. *et al.* Electronic structure of the negatively charged silicon-vacancy center in diamond. *Phys. Rev. B* **89,** 235101 (2014).

93. Rogers, L. J. *et al.* All-Optical Initialization, Readout, and Coherent Preparation of Single Silicon-Vacancy Spins in Diamond. *Phys. Rev. Lett.* **113,** 263602 (2014).

94. Iwasaki, T. *et al.* Germanium-Vacancy Single Color Centers in Diamond. *Scientific Reports* **5,** 12882 (2015).

95. Rogers, L. J. *et al.* Multiple intrinsically identical single-photon emitters in the solid state. *Nature Communications* **5,** 4739 (2014).

96. Davies, G. & Hamer, M. F. Optical Studies of the 1.945 eV Vibronic Band in Diamond. *Proceedings of the Royal Society of London A: Mathematical, Physical and Engineering Sciences* **348,** 285–298 (1976).

97. Doherty, M. W. *et al.* Measuring the defect structure orientation of a single NV-centre in diamond. *New Journal of Physics* **16,** 063067 (2014).

98. Michl, J. *et al.* Perfect alignment and preferential orientation of nitrogen-vacancy centers during chemical vapor deposition diamond growth on (111) surfaces. *Applied Physics Letters* **104,** 102407 (2014).

99. Lenef, A. & Rand, S. C. Electronic structure of the N-V center in diamond: Theory. *Phys. Rev. B* **53,** 13441–13455 (1996).

100. Aslam, N, Waldherr, G, Neumann, P, Jelezko, F & Wrachtrup, J. Photo-induced ionization dynamics of the nitrogen vacancy defect in diamond investigated by single-shot charge state detection. *New Journal of Physics* **15,** 013064 (2013).

101. Grotz, B. *et al.* Charge state manipulation of qubits in diamond. *Nature Communications* **3,** 729 (2012).

102. Hauf, M. V. *et al.* Chemical control of the charge state of nitrogen-vacancy centers in diamond. *Phys. Rev. B* **83,** 081304 (2011).

103. Rogers, L. J. *et al.* Singlet levels of the NV - centre in diamond. *New Journal of Physics* **17,** 013048 (2015).

104. Pfender, M. *et al.* Protecting a diamond quantum memory by charge state control. *ArXiv e-prints.* arXiv: `1702.01590` `[quant-ph]` (2017).

105. Maze, J. R. *et al.* Properties of nitrogen-vacancy centers in diamond: the group theoretic approach. *New Journal of Physics* **13,** 025025 (2011).

106. Rogers, L. J., Armstrong, S, Sellars, M. J. & Manson, N. B. Infrared emission of the NV centre in diamond: Zeeman and uniaxial stress studies. *New Journal of Physics* **10,** 103024 (2008).

107. Goldman, M. L. *et al.* Phonon-Induced Population Dynamics and Intersystem Crossing in Nitrogen-Vacancy Centers. *Phys. Rev. Lett.* **114,** 145502 (2015).

108. Goldman, M. L. *et al.* State-selective intersystem crossing in nitrogen-vacancy centers. *Phys. Rev. B* **91,** 165201 (2015).

109. Kurtsiefer, C., Mayer, S., Zarda, P. & Weinfurter, H. Stable Solid-State Source of Single Photons. *Phys. Rev. Lett.* **85,** 290–293 (2000).

110. Waldherr, G. *et al.* Dark States of Single Nitrogen-Vacancy Centers in Diamond Unraveled by Single Shot NMR. *Phys. Rev. Lett.* **106,** 157601 (2011).

111. Acosta, V. M. *et al.* Temperature Dependence of the Nitrogen-Vacancy Magnetic Resonance in Diamond. *Phys. Rev. Lett.* **104,** 070801 (2010).

112. Chen, X.-D. *et al.* Temperature dependent energy level shifts of nitrogen-vacancy centers in diamond. *Applied Physics Letters* **99,** 161903 (2011).

113. Neumann, P. *et al.* High-Precision Nanoscale Temperature Sensing Using Single Defects in Diamond. *Nano Letters* **13,** 2738–2742 (2013).

114. Rondin, L *et al.* Magnetometry with nitrogen-vacancy defects in diamond. *Reports on Progress in Physics* **77,** 056503 (2014).

115. Neumann, P. *et al.* Single-Shot Readout of a Single Nuclear Spin. *Science* **329,** 542–544 (2010).

116. Balasubramanian, G. *et al.* Nanoscale imaging magnetometry with diamond spins under ambient conditions. *Nature* **455,** 648–651 (2008).

117. Smeltzer, B., McIntyre, J. & Childress, L. Robust control of individual nuclear spins in diamond. *Phys. Rev. A* **80,** 050302 (2009).

118. Dréau, A., Maze, J.-R., Lesik, M., Roch, J.-F. & Jacques, V. High-resolution spectroscopy of single NV defects coupled with nearby ^{13}C nuclear spins in diamond. *Phys. Rev. B* **85,** 134107 (2012).

119. Neumann, P. *et al.* Multipartite Entanglement Among Single Spins in Diamond. *Science* **320,** 1326–1329 (2008).

120. Bloch, F. Nuclear Induction. *Phys. Rev.* **70,** 460–474 (1946).

121. Nielsen, M. & Chuang, I. *Quantum Computation and Quantum Information* ISBN: 9780521635035 (Cambridge University Press, 2000).

122. Dréau, A. *et al.* Avoiding power broadening in optically detected magnetic resonance of single NV defects for enhanced dc magnetic field sensitivity. *Phys. Rev. B* **84,** 195204 (2011).

123. Jarmola, A., Acosta, V. M., Jensen, K., Chemerisov, S. & Budker, D. Temperature− and Magnetic−Field−Dependent Longitudinal Spin Relaxation in Nitrogen-Vacancy Ensembles in Diamond. *Phys. Rev. Lett.* **108,** 197601 (2012).

124. Rosskopf, T. *et al.* Investigation of Surface Magnetic Noise by Shallow Spins in Diamond. *Phys. Rev. Lett.* **112,** 147602 (2014).

125. Staudacher, T. *et al.* Enhancing the spin properties of shallow implanted nitrogen vacancy centers in diamond by epitaxial overgrowth. *Applied Physics Letters* **101,** 212401 (2012).

126. Aharonovich, I. *et al.* Homoepitaxial Growth of Single Crystal Diamond Membranes for Quantum Information Processing. *Advanced Materials* **24,** OP54–OP59 (2012).

127. Maze, J. R. *et al.* Free induction decay of single spins in diamond. *New Journal of Physics* **14,** 103041 (2012).

128. Staudacher, T. *Nuclear magnetic resonance spectroscopy on a nanoscopic sample volume* PhD thesis (3. Physikalisches Institut der Universität Stuttgart, 2015).

129. Taylor, J. M. *et al.* High-sensitivity diamond magnetometer with nanoscale resolution. *Nat Phys* **4,** 810–816 (2008).

130. Hahn, E. L. Spin Echoes. *Phys. Rev.* **80,** 580–594 (1950).

131. Childress, L. *et al.* Coherent Dynamics of Coupled Electron and Nuclear Spin Qubits in Diamond. *Science* **314,** 281–285 (2006).

132. Osterkamp, C. *et al.* Increasing the creation yield of shallow single defects in diamond by surface plasma treatment. *Applied Physics Letters* **103,** 193118 (2013).

133. Maier, F., Ristein, J. & Ley, L. Electron affinity of plasma-hydrogenated and chemically oxidized diamond (100) surfaces. *Phys. Rev. B* **64,** 165411 (2001).

134. Maier, F., Riedel, M., Mantel, B., Ristein, J. & Ley, L. Origin of Surface Conductivity in Diamond. *Phys. Rev. Lett.* **85,** 3472–3475 (2000).

135. Schreyvogel, C., Polyakov, V., Wunderlich, R., Meijer, J. & Nebel, C. E. Active charge state control of single NV centres in diamond by in-plane Al-Schottky junctions. *Sci Rep* **5,** 12160 (2015).

136. Romach, Y. *et al.* Spectroscopy of Surface-Induced Noise Using Shallow Spins in Diamond. *Phys. Rev. Lett.* **114,** 017601 (2015).

137. Campbell, B. & Mainwood, A. Radiation Damage of Diamond by Electron and Gamma Irradiation. *physica status solidi (a)* **181,** 99–107 (2000).

138. Davies, G., Lawson, S. C., Collins, A. T., Mainwood, A. & Sharp, S. J. Vacancy-related centers in diamond. *Phys. Rev. B* **46,** 13157–13170 (1992).

139. *Element Six* http://www.e6.com/en/Home. Accessed: 2017-02-15.

140. Fu, K.-M. C., Santori, C., Barclay, P. E. & Beausoleil, R. G. Conversion of neutral nitrogen-vacancy centers to negatively charged nitrogen-vacancy centers through selective oxidation. *Applied Physics Letters* **96,** 121907 (2010).

141. Steinert, S. *et al.* Magnetic spin imaging under ambient conditions with sub-cellular resolution. *Nature Communications* **4,** 1607 (2013).

142. Cherepov, E. *et al.* Redistribution of nitrogen implanted in the crystals of synthetic diamond. *Nuclear Instruments and Methods in Physics Research Section B: Beam Interactions with Materials and Atoms* **183,** 301 –304 (2001).

143. Pezzagna, S., Rogalla, D., Wildanger, D., Meijer, J. & Zaitsev, A. Creation and nature of optical centres in diamond for single-photon emission - overview and critical remarks. *New Journal of Physics* **13,** 035024 (2011).

144. Nastasi, M. A. & Mayer, J. W. *Ion implantation and synthesis of materials* (Springer Berlin, 2006).

145. Ziegler, J. F., Ziegler, M. & Biersack, J. SRIM - The stopping and range of ions in matter (2010). *Nuclear Instruments and Methods in Physics Research Section B: Beam Interactions with Materials and Atoms* **268.** 19th International Conference on Ion Beam Analysis, 1818 –1823 (2010).

146. Posselt, M. & Biersack, J. P. Computer simulation of ion implantation into crystalline targets. *Nucl. Instr. Meth. Phys. Res. Sec. B* **64,** 706–710 (1992).

147. Antonov, D. *et al.* Statistical investigations on nitrogen-vacancy center creation. *Applied Physics Letters* **104,** 012105 (2014).

148. Yamamoto, T. *et al.* Isotopic identification of engineered nitrogen-vacancy spin qubits in ultrapure diamond. *Phys. Rev. B* **90,** 081117 (2014).

149. Kalish, R. & Prawer, S. Graphitization of diamond by ion impact: Fundamentals and applications. *Nuclear Instruments and Methods in Physics Research Section B: Beam Interactions with Materials and Atoms* **106,** 492 –499 (1995).

150. Uzan-Saguy, C. *et al.* Damage threshold for ion-beam induced graphitization of diamond. *Applied Physics Letters* **67,** 1194–1196 (1995).

151. Forneris, J. *et al.* Creation and characterization of He-related color centers in diamond. *Journal of Luminescence* **179,** 59–63 (2016).

152. Naydenov, B. *et al.* Enhanced generation of single optically active spins in diamond by ion implantation. *Applied Physics Letters* **96,** 16 (2010).

153. Schwartz, J, Michaelides, P, Weis, C. D. & Schenkel, T. In situ optimization of co-implantation and substrate temperature conditions for nitrogen-vacancy center formation in single-crystal diamonds. *New Journal of Physics* **13,** 035022 (2011).

154. Ohno, K. *et al.* Three-dimensional localization of spins in diamond using 12C implantation. *Applied Physics Letters* **105,** 052406 (2014).

155. McLellan, C. A. *et al.* Patterned Formation of Highly Coherent Nitrogen-Vacancy Centers Using a Focused Electron Irradiation Technique. *Nano Letters* **16,** 2450–2454 (2016).

156. Degen, C. L. Scanning magnetic field microscope with a diamond single-spin sensor. *Applied Physics Letters* **92,** 243111 (2008).

157. Maze, J. R. *et al.* Nanoscale magnetic sensing with an individual electronic spin in diamond. *Nature* **455,** 644–647 (2008).

158. Loretz, M., Pezzagna, S., Meijer, J. & Degen, C. L. Nanoscale nuclear magnetic resonance with a 1.9-nm-deep nitrogen-vacancy sensor. *Applied Physics Letters* **104,** 033102 (2014).

159. Mott-Smith, H. M. History of "Plasmas". *Nature* **233,** 219–219 (1971).

160. Tonks, L. & Langmuir, I. A General Theory of the Plasma of an Arc. *Phys. Rev.* **34,** 876–922 (1929).

161. Poulsen, R. G. Plasma etching in integrated circuit manufacture − A review. *Journal of Vacuum Science and Technology* **14,** 266–274 (1977).

162. Taylor, S, Zhang, J. F. & Eccleston, W. A review of the plasma oxidation of silicon and its applications. *Semiconductor Science and Technology* **8,** 1426 (1993).

163. Abe, H., Yoneda, M. & Fujiwara, N. Developments of Plasma Etching Technology for Fabricating Semiconductor Devices. *Japanese Journal of Applied Physics* **47,** 1435 (2008).

164. Maluf, N. & Williams, K. *Introduction to microelectromechanical systems engineering* (Artech House, 2004).

165. Lieberman, M. A. & Lichtenberg, A. J. *Principles of Plasma Discharges and Materials Processing* (New York: John Wiley & Sons, Inc, 2005).

166. Tsukanov, A. V. Nanoelectromechanical diamond structures in quantum informatics. Part I. *Russian Microelectronics* **45,** 77–90 (2016).

167. Landau, L. Kinetic equation for the Coulomb effect. *Phys. Z. Sowjetunion* **10,** 154 (1936).

168. Vlasov, A. A. The Vibrational Properties of an Electron Gas. *Soviet Physics Uspekhi* **10,** 721 (1968).

169. Bellan, P. *Fundamentals of Plasma Physics* ISBN: 9781139449731 (Cambridge University Press, 2008).

170. Freidberg, J. P. Ideal magnetohydrodynamic theory of magnetic fusion systems. *Rev. Mod. Phys.* **54,** 801–902 (1982).

171. Freidberg, J. *Plasma Physics and Fusion Energy* ISBN: 9781139462150 (Cambridge University Press, 2008).

172. Debye, P & Hückel, E. De la theorie des electrolytes. I. abaissement du point de congelation et phenomenes associes. *Physikalische Zeitschrift* **24,** 185–206 (1923).

173. Sandhu, G. S. & Chu, W. K. Reactive ion etching of diamond. *Applied Physics Letters* **55,** 437–438 (1989).

174. Vivensang, C., Turban, G., Anger, E. & Gicquel, A. Reactive ion etching of diamond and diamond-like carbon films. *Diamond and Related Materials* **3,** 645–649 (1994).

175. Lee, C., Gu, E., Dawson, M., Friel, I. & Scarsbrook, G. Etching and micro-optics fabrication in diamond using chlorine-based inductively-coupled plasma. *Diamond and Related Materials* **17,** 1292–1296 (2008).

176. Bello, I *et al.* Effects at reactive ion etching of CVD diamond. *Thin Solid Films* **368,** 222–226 (2000).

177. Shpilman, Z., Gouzman, I., Grossman, E., Akhvlediani, R. & Hoffman, A. Hydrogen plasma and atomic oxygen treatments of diamond: Chemical versus morphological effects. *Applied Physics Letters* **92,** 234103 (2008).

178. Hausmann, B. J. *et al.* Fabrication of diamond nanowires for quantum information processing applications. *Diamond and Related Materials* **19,** 621 –629 (2010).

179. Leech, P. W., Reeves, G. K. & Holland, A. Reactive ion etching of diamond in CF4, O2, O2 and Ar-based mixtures. *Journal of Materials Science* **36,** 3453–3459 (2001).

180. Egitto, F. D., Emmi, F., Horwath, R. S. & Vukanovic, V. Plasma etching of organic materials. I. Polyimide in O2-CF4. *Journal of Vacuum Science & Technology B: Microelectronics Processing and Phenomena* **3,** 893–904 (1985).

181. Ding, G. *et al.* Micromachining of CVD diamond by RIE for MEMS applications. *Diamond and Related Materials* **14,** 1543 –1548 (2005).

182. Janssen, W. & Gheeraert, E. Dry etching of diamond nanowires using self-organized metal droplet masks. *Diamond and Related Materials* **20,** 389 – 394 (2011).

183. Tran, D., Fansler, C., Grotjohn, T., Reinhard, D. & Asmussen, J. Investigation of mask selectivities and diamond etching using microwave plasma-assisted etching. *Diamond and Related Materials* **19.** Proceedings of Diamond 2009, The 20th European Conference on Diamond, Diamond-Like Materials, Carbon Nanotubes and Nitrides, Part 2, 778–782 (2010).

184. Sze, S. *Semiconductor Devices: Physics and Technology* ISBN: 9780470873670 (John Wiley & Sons Singapore Pte. Limited, 2012).

185. Hittorf, W. Über die Electricitätsleitung der Gase. *Annalen der Physik* **257,** 90–139 (1884).

186. Okumura, T. Inductively Coupled Plasma Sources and Applications. *Physics Research International* **2010,** 164249 (2011).

187. Khanaliloo, B. *et al.* Single-Crystal Diamond Nanobeam Waveguide Optomechanics. *Phys. Rev. X* **5,** 041051 (2015).

188. Khanaliloo, B., Mitchell, M., Hryciw, A. C. & Barclay, P. E. High-Q/V Monolithic Diamond Microdisks Fabricated with Quasi-isotropic Etching. *Nano Letters* **15,** 5131–5136 (2015).

189. Reznik, A., Richter, V. & Kalish, R. The re-arrangement of broken bonds in damaged diamond: Graphitization versus annealing back to diamond. *Diamond and Related Materials* **7,** 317–321 (1998).

190. Graupner, R., Maier, F., Ristein, J., Ley, L. & Jung, C. High-resolution surface-sensitive C1*s* core-level spectra of clean and hydrogen-terminated diamond (100) and (111) surfaces. *Phys. Rev. B* **57,** 12397–12409 (1998).

191. Kuznetsov, V. L., Zilberberg, I. L., Butenko, Y. V., Chuvilin, A. L. & Segall, B. Theoretical study of the formation of closed curved graphite-like structures during annealing of diamond surface. *Journal of Applied Physics* **86,** 863–870 (1999).

192. Fujishima, A. *Diamond Electrochemistry* ISBN: 9780444519085 (BKC, 2005).

193. *NIST X-ray Photoelectron Spectroscopy Database* https://srdata.nist.gov/xps/. Accessed: 2017-02-15.

194. Yagi, I., Notsu, H., Kondo, T., Tryk, D. A. & Fujishima, A. Electrochemical selectivity for redox systems at oxygen-terminated diamond electrodes. *Journal of Electroanalytical Chemistry* **473,** 173–178 (1999).

195. Denisenko, A., Romanyuk, A., Pietzka, C., Scharpf, J. & Kohn, E. Electronic surface barrier properties of fluorine-terminated boron-doped diamond in electrolytes. *Surface Science* **605,** 632–637 (2011).

196. Chandran, M., Shasha, M., Michaelson, S., Akhvlediani, R. & Hoffman, A. Incorporation of nitrogen into polycrystalline diamond surfaces by RF plasma nitridation process at different temperatures: Bonding configuration and thermal stabilty studies by in situ XPS and HREELS. *physica status solidi (a)* **212,** 2487–2495 (2015).

197. Santori, C., Barclay, P. E., Fu, K.-M. C. & Beausoleil, R. G. Vertical distribution of nitrogen-vacancy centers in diamond formed by ion implantation and annealing. *Phys. Rev. B* **79,** 125313 (2009).

198. Dolde, F. *et al.* Room-temperature entanglement between single defect spins in diamond. *Nat Phys* **9,** 139–143 (2013).

199. Roth, J., Gähler, F. & Trebin, H.-R. A Molecular Dynamics Run with 5180116000 Particles. *Int. J. Mod. Phys. C: Computational Physics & Physical Computation* **11,** 317 (2000).

200. Stadler, J, Mikulla, R & Trebin, H.-R. IMD: A software package for molecular dynamics studies on parallel computers. *Int. J. Mod. Phys. C* **8,** 1131–1140 (1997).

201. Tersoff, J. New empirical approach for the structure and energy of covalent systems. *Phys. Rev. B* **37,** 6991–7000 (1988).

202. Tersoff, J. Empirical Interatomic Potential for Carbon, with Applications to Amorphous Carbon. *Phys. Rev. Lett.* **61,** 2879–2882 (1988).

203. Tersoff, J. Empirical interatomic potential for silicon with improved elastic properties. *Phys. Rev. B* **38,** 9902–9905 (1988).

204. Tersoff, J. New empirical model for the structural properties of silicon. *Phys. Rev. Lett.* **56,** 632–635 (1986).

205. Tersoff, J. Modeling solid-state chemistry: Interatomic potentials for multi-component systems. *Phys. Rev. B* **39,** 5566–5568 (1989).

206. De Brito Mota, F., Justo, J. F. & Fazzio, A. Structural properties of amorphous silicon nitride. *Phys. Rev. B* **58,** 8323–8328 (1998).

207. Ziegler, J., Biersack, J. & Littmark, U. *SRIM, the Stopping and Range of Ions in Matter* (Pergamon Press, 1985).

208. Chan, H. *et al.* The effect of interatomic potential in molecular dynamics simulation of low energy ion implantation. *Nucl. Instr. Meth. Phys. Res. Sec. B: Beam Interactions with Materials and Atoms* **228,** 240–244 (2005).

209. Deák, P., Aradi, B., Kaviani, M., Frauenheim, T. & Gali, A. Formation of NV centers in diamond: A theoretical study based on calculated transitions and migration of nitrogen and vacancy related defects. *Phys. Rev. B* **89,** 075203 (2014).

210. Goss, J. P., Briddon, P. R., Papagiannidis, S. & Jones, R. Interstitial nitrogen and its complexes in diamond. *Phys. Rev. B* **70,** 235208 (2004).

211. Breuer, S. J. & Briddon, P. R. *Ab initio* investigation of the native defects in diamond and self-diffusion. *Phys. Rev. B* **51,** 6984–6994 (1995).

212. Mainwood, A. Nitrogen and nitrogen-vacancy complexes and their formation in diamond. *Phys. Rev. B* **49,** 7934–7940 (1994).

213. Field, J. *The Properties of natural and synthetic diamond* (Academic Press, 1992).

214. Twitchen, D. J., Newton, M. E., Baker, J. M., Anthony, T. R. & Banholzer, W. F. Electron-paramagnetic-resonance measurements on the divacancy defect center $R4/W6$ in diamond. *Phys. Rev. B* **59,** 12900–12910 (1999).

215. Yang, W. & Liu, R.-B. Quantum many-body theory of qubit decoherence in a finite-size spin bath. *Phys. Rev. B* **78,** 085315 (2008).

216. Sze, S. & Ng, K. *Physics of Semiconductor Devices* ISBN: 9780470068304 (Wiley, 2006).

217. http://www.silvaco.com/. *SILVACO* 2000. (2016).

218. Farrer, R. G. & Vermeulen, L. A. Photoconductivity in irradiated diamond. *Journal of Physics C: Solid State Physics* **5,** 2762 (1972).

219. Collins, A. T. Diamond electronic devices-a critical appraisal. *Semiconductor Science and Technology* **4,** 605 (1989).

220. Vogel, T., Meijer, J. & Zaitsev, A. Highly effective p-type doping of diamond by MeV-ion implantation of boron. *Diamond and Related Materials* **13,** 1822 –1825 (2004).

221. Bernholc, J., Antonelli, A., Del Sole, T. M., Bar-Yam, Y. & Pantelides, S. T. Mechanism of self-diffusion in diamond. *Phys. Rev. Lett.* **61,** 2689– 2692 (1988).

222. Schwartz, J, Aloni, S, Ogletree, D. F. & Schenkel, T. Effects of low-energy electron irradiation on formation of nitrogen-vacancy centers in single-crystal diamond. *New Journal of Physics* **14,** 043024 (2012).

223. Silverman, A., Adler, J. & Kalish, R. Dynamics of the Formation of the Nitrogen-Vacancy Center in Diamond. *Communications in Computational Physics* **19,** 380–392 (2016).

224. Kalish, R., Uzan-Saguy, C., Philosoph, B., Richter, V. & Prawer, S. Loss of electrical conductivity in boron-doped diamond due to ion-induced damage. *Applied Physics Letters* **70,** 999–1001 (1997).

225. Kubo, Y. *et al.* Strong Coupling of a Spin Ensemble to a Superconducting Resonator. *Phys. Rev. Lett.* **105,** 140502 (2010).

226. Spinicelli, P *et al.* Engineered arrays of nitrogen-vacancy color centers in diamond based on implantation of CN-molecules through nanoapertures. *New Journal of Physics* **13,** 025014 (2011).

227. Neumann, P. *et al.* Quantum register based on coupled electron spins in a room-temperature solid. *Nat Phys* **6,** 249–253 (2010).

228. Yamamoto, T. *et al.* Strongly coupled diamond spin qubits by molecular nitrogen implantation. *Phys. Rev. B* **88,** 201201 (2013).

229. Pezzagna, S. *et al.* Creation of colour centres in diamond by collimated ion-implantation through nano-channels in mica. *physica status solidi (a)* **208,** 2017–2022 (2011).

230. Scarabelli, D., Trusheim, M., Gaathon, O., Englund, D. & Wind, S. J. Nanoscale Engineering of Closely-Spaced Electronic Spins in Diamond. *Nano Letters* **16,** 4982–4990 (2016).

231. Jakobi, I *et al.* Efficient creation of dipolar coupled nitrogen-vacancy spin qubits in diamond. *Journal of Physics: Conference Series* **752,** 012001 (2016).

232. Lee, J. C. *et al.* Deterministic coupling of delta-doped nitrogen vacancy centers to a nanobeam photonic crystal cavity. *Applied Physics Letters* **105,** 261101 (2014).

233. Acosta, V. M. *et al.* Diamonds with a high density of nitrogen-vacancy centers for magnetometry applications. *Phys. Rev. B* **80,** 115202 (2009).

234. Edmonds, A. M. *et al.* Production of oriented nitrogen-vacancy color centers in synthetic diamond. *Phys. Rev. B* **86,** 035201 (2012).

235. Novotny, L. & Hecht, B. *Principles of Nano-Optics* ISBN: 9781139452052 (Cambridge University Press, 2006).

236. Orwa, J. *et al.* An upper limit on the lateral vacancy diffusion length in diamond. *Diamond and Related Materials* **24,** 6–10 (2012).

237. Skokov, S., Weiner, B. & Frenklach, M. Elementary Reaction Mechanism for Growth of Diamond (100) Surfaces from Methyl Radicals. *The Journal of Physical Chemistry* **98,** 7073–7082 (1994).

238. Tallaire, A., Kasu, M., Ueda, K. & Makimoto, T. Origin of growth defects in CVD diamond epitaxial films. *Diamond and Related Materials* **17,** 60–65 (2008).

239. Okushi, H., Watanabe, H., Ri, S., Yamanaka, S. & Takeuchi, D. Device-grade homoepitaxial diamond film growth. *Journal of Crystal Growth* **237-239, Part 2,** 1269 –1276 (2002).

240. Kaukonen, M. *et al.* Effect of N and B doping on the growth of CVD diamond $(100) : H(2 \times 1)$ surfaces. *Phys. Rev. B* **57,** 9965–9970 (1998).

241. Yiming, Z., Larsson, F. & Larsson, K. Effect of CVD diamond growth by doping with nitrogen. *Theoretical Chemistry Accounts* **133,** 1432 (2013).

242. Müller-Sebert, W., Wörner, E., Fuchs, F., Wild, C. & Koidl, P. Nitrogen induced increase of growth rate in chemical vapor deposition of diamond. *Applied Physics Letters* **68,** 759–760 (1996).

243. Yan, C.-S. & Vohra, Y. K. Multiple twinning and nitrogen defect center in chemical vapor deposited homoepitaxial diamond. *Diamond and Related Materials* **8,** 2022–2031 (1999).

244. Watanabe, H. *et al.* Formation of Nitrogen-Vacancy Centers in Homoepitaxial Diamond Thin Films Grown via Microwave Plasma-Assisted Chemical Vapor Deposition. *IEEE Transactions on Nanotechnology* **15,** 614–618 (2016).

245. Chandran, M., Michaelson, S., Saguy, C. & Hoffman, A. Fabrication of a nanometer thick nitrogen delta doped layer at the sub-surface region of (100) diamond. *Applied Physics Letters* **109,** 221602 (2016).

246. Chandran, M., Shasha, M., Michaelson, S., Akhvlediani, R. & Hoffman, A. Incorporation of nitrogen into polycrystalline diamond surfaces by RF plasma nitridation process at different temperatures: Bonding configuration and thermal stabilty studies by in situ XPS and HREELS. *physica status solidi (a)* **212,** 2487–2495 (2015).

247. Häberle, T. *et al.* Nuclear quantum-assisted magnetometer. *Review of Scientific Instruments* **88,** 013702 (2017).

248. Webb, R. H. Confocal optical microscopy. *Reports on Progress in Physics* **59,** 427 (1996).

249. Stamnes, J. J. Focusing of a perfect wave and the airy pattern formula. *Optics Communications* **37,** 311–314 (1981).

250. Kimble, H. J., Dagenais, M. & Mandel, L. Photon Antibunching in Resonance Fluorescence. *Phys. Rev. Lett.* **39,** 691–695 (1977).

251. Beveratos, A. *et al.* Room temperature stable single-photon source. *The European Physical Journal D - Atomic, Molecular, Optical and Plasma Physics* **18,** 191–196 (2002).

252. Watts, J. & Wolstenholme, J. *An Introduction to Surface Analysis by XPS and AES* ISBN: 9780470847121 (Wiley, 2003).

253. Harris, L. A. Analysis of Materials by Electron-Excited Auger Electrons. *Journal of Applied Physics* **39,** 1419–1427 (1968).

254. Fadley, C. S. Angle-resolved x-ray photoelectron spectroscopy. *Progress in Surface Science* **16,** 275–388 (1984).

255. Briggs, D. & Seah, M. *Practical Surface Analysis, Auger and X-ray Photoelectron Spectroscopy* ISBN: 9780471920816 (Wiley, 1990).

256. Cui, S. & Hu, E. L. Increased negatively charged nitrogen-vacancy centers in fluorinated diamond. *Applied Physics Letters* **103,** 051603 (2013).

257. Widmann, C. J., Giese, C., Wolfer, M., Kono, S. & Nebel, C. E. F- and Cl-terminations of (100)-oriented single crystalline diamond. *physica status solidi (a)* **211,** 2328–2332 (2014).

258. Rietwyk, K. J. *et al.* Work function and electron affinity of the fluorine-terminated (100) diamond surface. *Applied Physics Letters* **102,** 091604 (2013).

259. Bendavid, A., Martin, P., Randeniya, L., Amin, M. & Rohanizadeh, R. The properties of fluorine-containing diamond-like carbon films prepared by pulsed DC plasma-activated chemical vapour deposition. *Diamond and Related Materials* **19,** 1466–1471 (2010).

260. Volpe, P.-N. *et al.* Defect analysis and excitons diffusion in undoped homoepitaxial diamond films after polishing and oxygen plasma etching. *Diamond and Related Materials* **18,** 1205–1210 (2009).

261. Muchnikov, A. B. *et al.* Homoepitaxial growth of CVD diamond after ICP pretreatment. *physica status solidi (a)* **212,** 2572–2577 (2015).

262. Uzan-Saguy, C. *et al.* Hydrogen diffusion in B-ion-implanted and B-doped homo-epitaxial diamond: passivation of defects vs. passivation of B acceptors. *Diamond and Related Materials* **10,** 453–458 (2001).

263. Chevallier, J *et al.* Hydrogen in n-type diamond. *Diamond and Related Materials* **11,** 1566–1571 (2002).

264. Stacey, A. *et al.* Depletion of nitrogen-vacancy color centers in diamond via hydrogen passivation. *Applied Physics Letters* **100,** 071902 (2012).

265. Ballutaud, D. *et al.* Hydrogen diffusion and stability in polycrystalline CVD undoped diamond. *Diamond and Related Materials* **10,** 405–410 (2001).

266. Zhen, C., Liu, X., Yan, Z., Gong, H. & Wang, Y. Characteristics of Au/Ti/p-diamond ohmic contacts prepared by r.f. sputtering. *Surface and Interface Analysis* **32,** 106–109 (2001).

267. Abramowitz, M. & Stegun, I. A. *Handbook of Mathematical Functions with Formulas, Graphs, and Mathematical Tables* (Dover, New York, 1964).

268. Cywiński, L., Lutchyn, R. M., Nave, C. P. & Das Sarma, S. How to enhance dephasing time in superconducting qubits. *Phys. Rev. B* **77,** 174509 (2008).

269. Biercuk, M. J., Doherty, A. C. & Uys, H. Dynamical decoupling sequence construction as a filter-design problem. *Journal of Physics B: Atomic, Molecular and Optical Physics* **44,** 154002 (2011).

270. Álvarez, G. A. & Suter, D. Measuring the Spectrum of Colored Noise by Dynamical Decoupling. *Phys. Rev. Lett.* **107,** 230501 (2011).

271. Bar-Gill, N. *et al.* Suppression of spin-bath dynamics for improved coherence of multi-spin-qubit systems. *Nat. Commun.* **3,** 858 (2012).

272. Meiboom, S. & Gill, D. Modified Spin-echo Method for Measuring Nuclear Relaxation Times. *Review of Scientific Instruments* **29,** 688–691 (1958).

273. Pelliccione, M., Myers, B. A., Pascal, L. M. A., Das, A. & Bleszynski Jayich, A. C. Two-Dimensional Nanoscale Imaging of Gadolinium Spins via Scanning Probe Relaxometry with a Single Spin in Diamond. *Phys. Rev. Applied* **2,** 054014 (2014).

274. Schmid-Lorch, D. *et al.* Relaxometry and Dephasing Imaging of Superparamagnetic Magnetite Nanoparticles Using a Single Qubit. *Nano Letters* **15,** 4942–4947 (2015).